THE UNIVERSITY OF CHICAGO

DETECTING AND INTERPRETING THE DYNAMICAL EVOLUTION OF TRANSITING MULTIPLANET SYSTEMS

A DISSERTATION SUBMITTED TO
THE FACULTY OF THE DIVISION OF THE PHYSICAL SCIENCES
IN CANDIDACY FOR THE DEGREE OF
DOCTOR OF PHILOSOPHY

DEPARTMENT OF ASTRONOMY AND ASTROPHYSICS

BY

SEAN MARTIN MILLS

CHICAGO, ILLINOIS

AUGUST 2017

Copyright © 2017 by Sean Martin Mills

All Rights Reserved

For my parents

L'hypothèse qu'il existe des planètes plus éloignées du Soleil que celles que nous connaissons, estelle donc neuve? ... qu'un corps qui traverse des régions aussi éloignées pourrait être soumis â des forces totalement inconnues, telles que l'action de planètes, trop distantes pour être jamais aperçues.

Esperons seulement, ques les astres dont parle Clairaut ne seront pas tous invisibles.

The hypothesis that there are planets more distant from the sun than those we know, is it new? ... that a body traversing such distant regions could be subjected to forces totally unknown, such as the action of planets too distant to be ever seen.

Let us hope only that the stars of which are spoken will not all be invisible.

Urbain J. Le Verrier

Recherches sur les mouvements d'Uranus, 1846

TABLE OF CONTENTS

LIST OF FIGURES

LIST OF TABLES

ACKNOWLEDGMENTS

It is a pleasure to thank the many people who have been essential to my education throughout my life, including the completion of this dissertation.

My advisor Daniel Fabrycky's endless ideas, and insight into my own ideas, were a continuous source of scientific inspiration. I particularly appreciated his foresight on which of these thoughts would be most worthwhile and interesting to pursue. His patience and flexibility made my five years go smoothly, and his guidance made it to go successfully. I feel lucky to have had such a mentor as a grad student, and continue to look forward to conversations with him as fresh insight always awaits. And I can't help but mention his remarkable talent to maintain a flourishing personal life along with a successful professional one, which heartened me about the future.

I thank Jacob Bean, Fred Ciesla, and Fausto Cattaneo for their time on my thesis committee, and from whom I received excellent advice about my present research as well as future career plans. Thanks to Don York, Mike Gladders and Rich Kron for extra effort making the graduate academic experience as excellent as possible. Thanks also to Arieh Königl, Fausto Cattaneo, Peter Vandervoort, Dan Hooper, Scott Dodelson, Ed Kibblewhite, and all of the UChicago Astronomy professors for stimulating classes, lectures, and a dose of history.

I thank all of my collaborators, especially Tsevi Mazeh, Bill Welsh, Eric Ford, Jerry Orosz, Eric Agol, and Jack Lissauer, who went out of their way to help me understand something new. Bill in particular showed great kindness and encouragement in getting me involved in CBP research.

I thank Laticia Rebeles, Jennifer Smith, and Randy Landsberg for practical help and using astronomy to get me involved with the Chicago community. I also thank Titos Matsakos for good conversation and advice, as well as numerous other UChicago graduate students and postdocs, especially the five others who shared the corner TAAC office.

I thank Bill Borucki and the entire *Kepler* team for their vision and hard work making

the *Kepler* mission a success. Without it, nearly all of this work would have been impossible.

Thanks to Bill Savage, whose unique and engaging teaching piqued my interest in math at a young age, and to Jim Fox and Mike Kennedy who, along with many others, helped keep it going.

I thank my friends for years of welcome distractions continuing from high school to today. I thank my Ricketts compadres for getting me through long nights of sets. I thank the UChicago and Elevate ultimate communities for giving me an outlet for my energy.

Finally, I thank my Mom, Dad, and Megan, whose endless sacrifices and support have given me these opportunities. And I thank Evaline for love and patience these past five years, and for making my life that much better.

ABSTRACT

The dynamical interactions of our Solar System have been studied in depth since Isaac Newton recognized that the planets may not be stable to each others gravitational perturbations. Recently, the discovery of exoplanet systems, including approximately a thousand planet candidates in systems of more than two bodies, has opened an extremely vast and diverse laboratory for planetary dynamics. In this dissertation, I describe techniques for measuring the dynamical, post-Keplerian interactions of planetary systems. Such signals often require numerical N-body analysis and photodynamic techniques combined with Bayesian statistics to correctly determine the properties of the planetary systems causing them. By simultaneously fitting the entire lightcurve data set at once, I am able to extract low signal-to-noise effects such as the resonance dynamics of a very faint system (Kepler-223), the slow orbital precession of a giant planet system (Kepler-108), and transit timing variations among very small and low mass planets (Kepler-444). I use these analyses to gain physical insight into the systems history, such as Kepler-108's potentially chaotic, violent past. Kepler-223's present structure indicates a migration origin for at least some close-in, sub-Neptune planets, which I explore in terms of tidal dissipation, smooth and stochastic migration, and secular evolution. I also analyze circumbinary systems including the newly discovered KIC 10753734. Taken together, these results provide insight into planetary formation in a broad array of environments for planet from compact sub-Neptune systems to Jupiters and circumbinary planets.

CHAPTER 1

INTRODUCTION

The modern scientific study and interpretation of the orbits of the Solar System planets began approximately 500 years ago with the circulation of Copernicus' "Little Commentary" on Heliocentrism (Copernicus, 1514). In the next century, the Copernican model was refined and improved by observers such as Tycho Brahe and theorists such as Johannes Kepler (Kepler et al., 1627; Kepler, 1618). However, a successful explanation of the planets' trajectories was first presented by Newton, with his idea of mutual gravitation (Newton, 1687). Newton may be considered the first planetary dynamicist, because he realized that using his model, the N-body interactions among all of the planets naturally led to instabilities in the Solar System (Newton, 1717). While he attributed the planets' relative longevity to divine intervention, it has since been shown that imprecise orbital measurements, masses, and approximations were the cause of Newton's conclusions of short-term instability (Laplace, 1779; Lagrange, 1778; Poisson, 1809)[1]. Once the contemporary Solar System configuration had been determined, and considering its uncertain future, the question of its origin followed naturally. In the mid-18$^{\text{th}}$ century, Immanuel Kant developed the Nebular Hypothesis – the idea that the planets' orbits are nearly coplanar and all prograde relative to the spin of the star because they all formed in a single gas and dust disk which collapsed into a flat, rotating geometry due gravitational attraction and the conservation of angular moment (Kant, 1755). This has proven to be the longest-standing theory of planet formation which is still considered correct in a fundamental way; however, modern researchers have considerably improved upon our understanding of the details of this process.

1. Nonetheless, it has recently been shown that our Solar System is indeed on the verge of instability (Laskar & Gastineau, 2009).

1.1 Planet Formation and Migration

Planets are generally thought to form via core-accretion, a process where solids in a protoplanetary disk grow larger and larger due to successive collisions[2]. Planets are thus expected to contain signatures of their formation environment, such as their growth rate depending on their composition and their compositions reflecting the available materials in their neighborhood. For instance, water- or ice-rich bodies are more likely to be found beyond the 'snow line,' the distance away from the sun where it is cool enough that water ice does not sublimate allowing small bodies to more easily aggregate (Hayashi, 1981; Armitage, 2010). Planets which grow massive before the dissipation of the protoplanetary disk are expected to contain large quantities of H and He as accretion may be runaway (Pollack et al., 1996; Lissauer et al., 2009). But protoplanets are also subject to movement within the disk and will not generally remain in their formation locations.

In the presence of a gas disk, very small ($\lesssim$ km-sized) objects experience significant gas drag as they orbit, resulting in the rapid decay of their semi-major axes (Weidenschilling, 1977). However, for objects as large as planets, the effects of gas drag are small. Low-mass ($\lesssim 30M_{\oplus}$) planets in a quiescent disk experience Type I migration (Goldreich & Tremaine, 1979, 1980, 1982). In this scenario, the structure of the massive protoplanetery disk is perturbed minimally by the comparatively small planet. The planet feels significant torques primarily from deflected disk particles in Lindblad Resonances with the planet, which lie very close to integer ratios of the planet's orbital period (see, e.g., Binney & Tremaine, 2008; Lubow & Ida, 2010, for discussions of Lindblad resonances). The torques the particles produce at these locations exhibit slight asymmetries attributed primarily to the outer Lindblad resonance residing slightly closer to the planet than the inner resonance. This causes the planet to

2. However, there are other formation mechanisms proposed for different types of planets including gravitational instability for massive planets (Kuiper, 1951; Toomre, 1964; Boss, 1997) or pebble accretion of rocky bodies in density traps in the protoplanetary disk (Cuzzi et al., 2001; Lambrechts & Johansen, 2012; Levison et al., 2015). For an overview of planet formation theories, see, e.g., Armitage (2010), Chambers (2010), or D'Angelo et al. (2010).

migrate inward as it loses angular momentum in exchanges with disk particles (Ward, 1997). The torque causes a planet's semi-major axis to decrease on a timescale inversely proportional to its mass because larger planets interact more strongly with the disk. The timescale of migration is quite small compared to the lifetime of the disk, and therefore large-scale planet migration may be expected (Ward, 1997). On the other hand, if a planet grows very massive ($\gtrsim 50 M_\oplus$), it is able to clear its orbit of disk material, and enters into the regime of Type II migration (Lin & Papaloizou, 1986). This results in migration timescales nearly independent of the planet's mass, but still inwards excepting rare cases.

After the protoplanetary disk dissipates, a second phase of planet formation and evolution may occur. In some cases there are many miniature proto-planets (called planetesimals, oligarchs, or embryos depending on their size and state), which emerge from the disk and may collisionally merge to form larger planets (Kokubo & Ida, 1998; Chambers & Wetherill, 1998; Agnor et al., 1999). Their merging is expedited by the disk's dissipation because there is no longer a medium to damp orbital eccentricities – thus crossing orbits may be more easily achieved and maintained. This is the process which is conjectured to have formed the inner Solar System including the Earth (Wetherill, 1985; Chambers & Wetherill, 1998; Morbidelli et al., 2000; Walsh et al., 2011; Izidoro et al., 2014). On the other hand, some planets may emerge from the dissipating disk essentially fully formed, as the large H and He envelopes on the giant planets suggest occurred in the outer regions of our Solar System. These planets are not immune to drastic orbital changes, however, as the removal of the damping disk may result in instabilities on thousand to billion year timescales depending on their exact spacing (Wisdom, 1980; Duncan et al., 1989; Gladman, 1993; Chambers et al., 1996; Zhou et al., 2007; Quillen, 2011; Pu & Wu, 2015; Laskar & Petit, 2017). Migration may also still occur by the interaction with left-over planetesimals (Fernandez & Ip, 1984), via planet-planet scattering (Rasio & Ford, 1996), by tidal forces (Rasio et al., 1996; Delisle et al., 2012), or by interactions with nearby stars (Mazeh et al., 1997; Holman et al., 1997; Fabrycky & Tremaine, 2007). Which formation pathways are important for different classes

of planets remains an open question.

1.2 Mean Motion Resonances

In multi-planet systems, pairs of planets migrating at different rates naturally sweep through a range of different orbital period ratios. Therefore, for migration lasting a sufficient length of time, it is virtually certain that a pair of planets reaches a configuration where their orbital periods are near integer ratios of each other, e.g., 2:1, 3:2, etc. Such a configuration is known as a mean motion resonance (MMR). Two planets in an MMR have periods that are related to each other via

$$\frac{P_2}{P_1} = \frac{n_1}{n_2} \approx \frac{k+j}{k}, \tag{1.1}$$

where j and k are small positive integers and P_i and n_i are the orbital period and mean motion ($n_i = 2\pi/P_i$) of the i^{th} planet. The value of j is the order of the resonance, and k is the rank.

For such a configuration, successive conjunctions (passages of closest approach) of the planets will occur in nearly the same location in the orbits. For circular orbits, if a conjunction occurs at time $t_0 = 0$, the next conjunction will occur when the inner (faster) planet catches up to the outer one again at

$$t_1 = \frac{2\pi}{n_1 - n_2} = \frac{2\pi}{n_1 \frac{k}{k+j} - n_1} = \frac{k+j}{j} P_1 \left(= \frac{(k+j)2\pi}{jn_1} \right) \tag{1.2}$$

or equivalently

$$t_1 = \frac{k}{j} P_2 \left(= \frac{2\pi k}{jn_2} \right). \tag{1.3}$$

For instance, define a reference line which passes through a pair of planets in a circular 2:1 first-order resonance orbit at conjunction (the first conjunction thus occurs at $\lambda_2 = 0$). The mean longitude λ of the outer planet will follow $\lambda_2 = n_2 t \mod 2\pi$. Then the next

conjunction will occur at

$$\lambda_2 = \frac{2\pi}{P_2} t_1 \bmod 2\pi = \frac{2\pi}{P_2}\frac{1}{1} P_2 \bmod 2\pi = 2\pi \bmod 2\pi = 0, \tag{1.4}$$

i.e., the same place in the orbit.

For eccentric planets ($e \neq 0$) the longitude of the periastron (ϖ), and its precession ($\dot{\varpi}$) must also be considered since the precession of the periastron may change the relative position of the conjunction in the orbits. In that case, the resonant angle (ϕ) may be generally written

$$\phi = l_1\lambda_1 + l_2\lambda_2 + l_3\varpi_1 + l_4\varpi_2, \tag{1.5}$$

where the l_is are integers[3]. For an exact resonance, the value of ϕ is constant. However, the resonance has a non-zero width, and thus in general the angle is subject to libration (oscillation) around a constant value. In resonance, this angle will vary slowly compared to the λ angles which compose it. Note that if we take the derivative of Eq. 1.5 for the case of circular restricted orbits in exact resonance, we recover Eq. 1.1:

$$\begin{aligned} \dot{\phi} &= l_1\dot{\lambda}_1 + l_2\dot{\lambda}_2 \\ \Leftrightarrow 0 &= l_1(\dot{n_1 t}) + l_2(\dot{n_2 t}) \\ \Leftrightarrow 0 &= l_1 n_1 + l_2 n_2 \\ \Leftrightarrow \frac{n_1}{n_2} &= \frac{-l_2}{l_1}, \end{aligned} \tag{1.6}$$

where $l_1 = k$ and $l_2 = -(k + j)$ and without loss of generality we use a coordinate system where the mean longitude at conjunction is 0. However in a physical system, both orbiting bodies can not maintain zero eccentricity as their interactions force a minimum eccentricity,

3. A more general form may be written involving the longitudes of the ascending nodes, Ω_1 and Ω_2; however, we restrict our discussion here to coplanar planets where $\Omega_1 = \Omega_2 = \dot{\Omega}_1 = \dot{\Omega}_2 = 0$. Generally, the longitude of the periastron $\varpi_i = \omega_i + \Omega_i$. In the coplanar case where we set $\Omega_i = 0$, $\varpi_i = \omega_i$ and Eq. 1.5 is equivalent with either ω or ϖ on the right hand side. We continue using ϖ as is convention. For a complete discussion including non-coplanar resonances, see Murray & Dermott (1999).

and therefore the ϖ terms must be included.

d'Alambert's rule states that the sum of the integer coefficients (l_is) in Eq. 1.5 is zero. This property can be derived by an expansion of the 3-body Newtonian gravitational equations in terms of orbital elements (see, e.g., Murray & Dermott, 1999, §6.3). But it can be demonstrated easily, because the libration angle is a physical property of the system which must not depend on our choice of coordinate system. If we change the reference angle in our coordinate system by an angle ϵ such that all of our longitude measurements are changed by that amount, we see that

$$\begin{aligned} & \phi_\epsilon = l_1(\lambda_1 + \epsilon) + (l_2\lambda_2 + \epsilon) + l_3(\varpi_1 + \epsilon) + l_4(\varpi_2 + \epsilon) \\ \Leftrightarrow\ & \phi_\epsilon = l_1\lambda_1 + l_2\lambda_2 + l_3\varpi_1 + l_4\varpi_2 + \epsilon(l_1 + l_2 + l_3 + l_4) \\ \Leftrightarrow\ & \phi_\epsilon = \phi + \epsilon(l_1 + l_2 + l_3 + l_4). \end{aligned} \tag{1.7}$$

Since ϵ may take any value, this implies $\sum_i l_i = 0$.

For systems of three (or more) planets, one may consider the resonances between each pair of planets:

$$\begin{aligned} \phi_1 &= l_1\lambda_1 + l_2\lambda_2 + l_3\varpi_1 + l_4\varpi_2 \\ \phi_2 &= l_5\lambda_2 + l_6\lambda_3 + l_7\varpi_2 + l_8\varpi_3. \end{aligned} \tag{1.8}$$

However, there is also the possibility that all three (or more) planets are involved in a resonance. In this case, the 3-body resonant angle will be a combination of the λs of all 3 planets, and can be structured to remove the resonant angle's dependence on ϖ. This makes observational determination of the resonance angle much more tenable, because a planet's λ is often far easier to precisely measure (e.g., via transit times) than its eccentricity vector. As an example of a 3-body resonance, consider three planet whose period ratios are near a 4:2:1 resonant chain (sequence of resonances). This is the classic case of the three interior

Galilean moons of Jupiter. We may take

$$\phi_1 = 1\lambda_1 - 2\lambda_2 + 1\varpi_2 \tag{1.9}$$

and

$$\phi_2 = 1\lambda_2 - 2\lambda_3 + 1\varpi_2. \tag{1.10}$$

and construct the 3-body resonance angle by subtracting ϕ_2 from ϕ_1:

$$\phi_3 = \phi_1 - \phi_2 = 1\lambda_1 - 3\lambda_2 + 2\lambda_3, \tag{1.11}$$

which still obeys d'Alembert's Law and does not depend on any ϖ.

One of the most important dynamical aspects of MMRs is the stability of resonance to small perturbation. There are two ways to show this, the first shown below is an examination of the equations of motion of the bodies directly.

Following Murray & Dermott (1999), we can define a coordinate system with a fixed origin and multiple massive bodies. Each body has a position $\vec{R}_i$ relative to the origin and mass m_i. We designate one body ($i = 0$) as the primary (star) and allow it to be the origin of a new coordinate system. At an instant in time, the i^{th} body is located at position $\vec{r}_i$ relative to the primary at a distance $|\vec{r}_i| = r_i = (x_i^2 + y_i^2 + z_i^2)^{1/2}$. By Newton's law of gravitation, we see that the accelerations relative to the fixed origin are

$$m_0 \ddot{\vec{R}}_0 = Gm_0 \sum_{i=1}^{N} m_i \frac{\vec{r}_i}{r_i^3} \tag{1.12}$$

and

$$m_i \ddot{\vec{R}}_i = -Gm_i m_0 \frac{\vec{r}_i}{r_i^3} + Gm_i \sum_{\substack{j=1 \\ j\neq i}}^{N} m_j \frac{\vec{r}_j - \vec{r}_i}{|\vec{r}_j - \vec{r}_i|^3}. \tag{1.13}$$

To convert to the coordinate system centered on the primary body, we subtract the the primary's position or acceleration from the i^{th} body's, i.e., $\ddot{\vec{r}}_i = \ddot{\vec{R}}_i - \ddot{\vec{R}}_0$. Clearly in the

stellar-centric coordinate system the primary has no acceleration since it is fixed at the origin. Subtracting Eq. 1.12 from Eq. 1.13, and dividing by their respective masses, we see that the equations of motion of the N body system around the primary at the origin are governed by

$$\ddot{\vec{r}}_i = \underbrace{-G(m_0+m_i)\frac{\vec{r}_i}{r_i^3}}_{\text{2-body term}} + \underbrace{G\sum_{j=1}^{N}\left(\frac{\vec{r}_j-\vec{r}_i}{|\vec{r}_j-\vec{r}_i|^3}-\frac{\vec{r}_j}{r_j^3}\right)m_j}_{R}. \tag{1.14}$$

The first term on the right hand side of of Eqn. 1.14 is the gradient of the two-body potential. The second term (R) is the gradient of a function known as the 'disturbing function' since it acts as a perturbation away from the Newtonian two-body trajectory. This function may be expanded using Legendre polynomials and written in terms of orbital elements[4].

For the case of two planets, with the inner much more massive than the eccentric outer body, the disturbing function (R) averaged over the fast (orbital longitude) frequencies ($\bar{R}$) may be written:

$$\bar{R} = \frac{Gm}{a_1}\left(\frac{a_1}{a_2}R_{\rm sec} + e_1^{|l_3|}e_2^{|l_4|}s_1^{|l_5|}s_2^{|l_6|}F\big(\frac{a_1}{a_2}\big)\cos\phi\right), \tag{1.15}$$

where $R_{\rm sec}$ is the secular (low frequency) contribution to the disturbing function and is dependent on $e_{1,2}$, $s_{1,2}$, and Laplace coefficients, $s = \frac{1}{2}\sin i$ with i the inclination, and $F\big(\frac{a_1}{a_2}\big)$ is a function of Laplace coefficients of the semi-major axis ratio of the two planets. If the inner body's eccentricity is small, and requiring the planets be coplanar (the likely scenario in disk-damped migration), we are left with

$$\bar{R} = \frac{Gm}{a_1}\left(\frac{a_1}{a_2}R_{\rm sec} + e_2^{|l_4|}F\big(\frac{a_1}{a_2}\big)\cos\phi\right). \tag{1.16}$$

We then consider Eq. 1.16 with libration angle

$$\phi = l_1\lambda_1 + l_2\lambda_2 + l_4\varpi_2. \tag{1.17}$$

4. We do not undertake to show the expansion here because it has been carried out many times (see Murray & Dermott, 1999, §6 for example) and is more algebraically tedious than physically informative.

Taking the time derivative of ϕ and using the fact that $\lambda_i = n_i t + \epsilon_i$ where ϵ is the mean longitude at the given epoch, yields

$$\dot{\phi} = l_1(\dot{n}_1 t + n_1 + \dot{\epsilon}_1) + l_2(\dot{n}_2 t + n_2 + \dot{\epsilon}_2) + l_4\dot{\varpi}_2. \tag{1.18}$$

Since the inner planet is much more massive than the outer planet in our scenario, we may neglect variations of the inner planet due to perturbations from the outer planet ($\dot{n}_1 \approx 0$). We also define the mean longitude of epoch in a new way: $\dot{\varepsilon} = \dot{\epsilon} + t\dot{n}$, and thus $\lambda = \int n\, dt + \varepsilon$. This is convenient as it removes the direct t dependence from time derivatives of ϕ. We are left with

$$\dot{\phi} = l_1 n_1 + l_2 n_2 + l_2\dot{\varepsilon}_2 + l_4\dot{\varpi}_2. \tag{1.19}$$

Taking a further time derivative yields

$$\ddot{\phi} = l_2\dot{n}_2 + l_2\ddot{\varepsilon}_2 + l_4\ddot{\varpi}_2. \tag{1.20}$$

Both $\ddot{\varepsilon}_2$ and $\ddot{\varpi}_2$ are proportional to $(m_1/M_\star)^2$, and thus can be neglected as small compared to $\dot{n}_2$ in most cases (the exception being when e is also very small). We are left with

$$\ddot{\phi} \approx l_2\dot{n}_2. \tag{1.21}$$

Lagrange's planetary equation of motion for a is given by[5]

$$\dot{a} = \frac{2}{na}\frac{\partial \bar{R}}{\partial \lambda}, \tag{1.22}$$

5. This equation is found by rewriting Eq. 1.14 as $\frac{\partial^2 \vec{r}}{\partial t^2} = \nabla U$, where ∇U is the right hand side Eq. 1.14, noting that $\frac{\mathrm{d}\vec{r}}{\mathrm{d}t} = \sum_{i=1}^{6} \frac{\partial \vec{r}}{\partial \alpha_i}\frac{\mathrm{d}\alpha_i}{\mathrm{d}t} + \frac{\partial \vec{r}}{\partial t} \Rightarrow \frac{\mathrm{d}^2\vec{r}}{\mathrm{d}t^2} = \sum_{i=1}^{6} \frac{\partial \dot{\vec{r}}}{\partial \alpha_i}\frac{\mathrm{d}\alpha_i}{\mathrm{d}t} + \frac{\partial^2 \vec{r}}{\partial t^2}$ for $\vec{\alpha} = \{a,\, e,\, i,\, \omega,\, \Omega,\, T_0\}$, and completing the coordinate conversion $\{\vec{r}, \dot{\vec{r}}\} \rightarrow \vec{\alpha}$. For a full derivation see, e.g., Roy (1988) §6.7-6.10.

which implies

$$\dot{n} = -\frac{3}{a^2}\frac{\partial \bar{R}}{\partial \lambda}, \tag{1.23}$$

using $n^{-2} = a^3$. Inserting Eq. 1.16 for $\bar{R}$, we see that

$$\dot{n} = C \sin \phi, \tag{1.24}$$

where the value C consists of a combination of Laplace coefficients, e_2, and the semi-major axes and masses of the planets. Combinging Eqs. 1.21 and 1.24 yields

$$\ddot{\phi} \approx C \sin \phi, \tag{1.25}$$

the equation of a simple harmonic oscillator with the frequency determined by the orbital parameters and masses of the planets. The restorative nature of the force causes ϕ to be stable to perturbations around the mean value, with libration as a natural consequence.

Following Peale (1976) we now consider a physical description of the restorative nature of resonance torques which complements the above mathematical approach and may be more intuitive. We consider the same case discussed above, with two coplanar planets (p_1 and p_2) near 2:1 resonance with at least the outer planet (p_2) possessing significant eccentricity. Should a conjunction of the two planets occur near, but just before, the apocenter of p_2 then the force the planet feels before and after transit will be asymmetric due to the asymmetry of the orbit's geometry. This geometry is shown in Fig 1.1, with the positions of planets p_1 (red) and p_2 (blue) in conjunction at time A, indicated by the dashed line showing the distance of closest approach. Black arrows indicate orbital velocities of the two planets – p_1 travels faster than p_2 due to its interior orbit, and p_2 is traveling most slowly at apocenter. We see that just before conjunction (A'), the planets are closer together compared to just after (A'') due to the eccentricity. Furthermore, while p_1 has a constant velocity which is more rapid than p_2's velocity at all times, the velocity of p_2 is lower at time A'' compared to A'. Therefore

the velocity difference between the planets is greater at A'', and thus the planets are near each other for a smaller amount of time. Both the distance and velocity difference cause planet p_2 to feel a stronger force before conjunction at A' compared to afterwards at A''. The force felt at A' has a component anti-parallel to p_2's velocity since p_1 is slightly behind it, whereas the force felt by p_2 at A'' has a component in the direction of the tangential velocity since p_1 is slightly ahead of it. Since the force felt at A' is greater than A'', the net force in the direction of the orbital velocity is negative, i.e., it is in the opposite direction of the velocity. This slight decrease in orbital velocity results in a loss of angular momentum and a correspondingly shorter and more rapid orbit. The increased speed of the p_2 means that p_1 will catch it later in its orbit at the next conjunction – closer to the pericenter (marked ϖ'). This effect will continue until the conjunction occurs at ϖ', at which point the exact symmetry of the conjunction causes no net force on the next conjunction. This is the stable equilibrium in a 2:1 resonance: conjunction at the apocenter, or $\phi = 180°$. If the conjunctions progress further, the opposite situation occurs (see time B in Fig. 1.1). In this case the force is greater at B', implying a net force in the direction of the orbital velocity of p_2, an increased orbital velocity, a gain of angular momentum, and therefore a larger, slower orbit once again moving conjunction towards ϖ'[6]. This oscillation and stability of ϕ to small changes in the orbital period of the outer planet is exactly what is expressed in Eqs. 1.21 and 1.25. Thus we again establish by physical reasoning the oscillations of a conjunction around a stable point, and the resistance of planets in resonance to changes in orbital period ratio.

For small eccentricities ($\lesssim 0.01$), the contribution of $\dot{\varpi}$ and $\ddot{\varpi}$ becomes important since it is relatively easier for small perturbations to change the direction of the eccentricity vector. In this case, a pair of planets in resonance may have successive conjunctions at different locations in inertial space, however the motion of ϖ causes a planet's apocenter or pericenter

6. This somewhat counterintuitive effect of the planet slowing down in its orbit when a force is applied in the direction of its motion is sometimes referred to as the "Donkey Effect," because evidently donkeys are rather stubborn and the harder you pull on their reigns while leading them, the harder they pull back and slow down (Lynden-Bell & Kalnajs, 1972).

Figure 1.1: Geometry of Eccentric 2-body Resonance

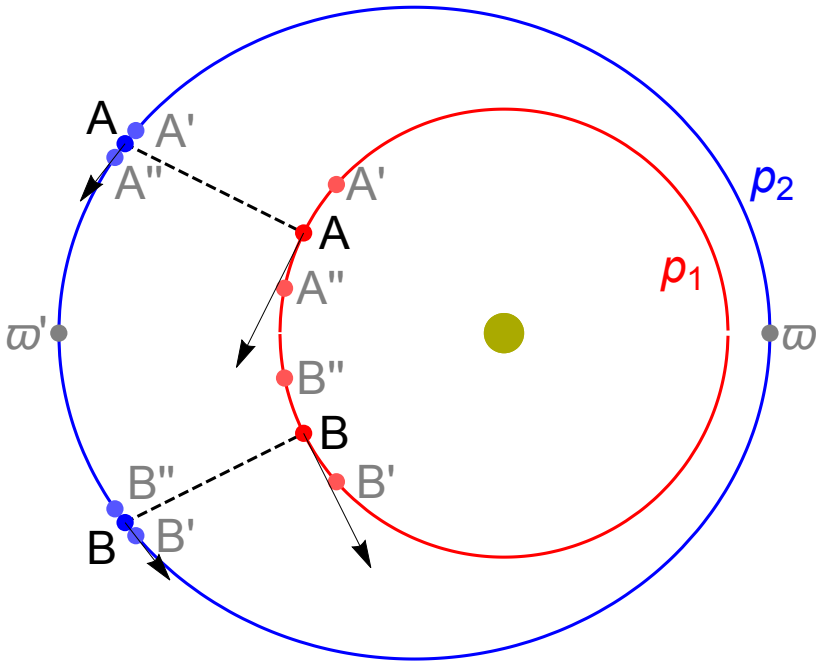

The orbital geometry of a pair of planets (p_1 and p_2), with the outer (p_2) displaying significant eccentricity. Periastron (gray ϖ) and apastron (gray ϖ') of the outer planet are indicated. The positions of both planets are shown at two distinct conjunctions (A and B). Black arrows represent the planets' velocities.

to librate about conjunctions (Sinclair, 1972; Greenberg et al., 1972). For very small e (and thus large $\dot{\varpi}$), this may result in resonance far from the nominal value of the period ratios as suggested in Eq 1.1; nonetheless, the resonance is still active. This regime of resonance is not described in detail here as it is not directly applicable to most of the systems studied here (for details, see e.g.,. Peale, 1976).

As planets migrate smoothly through a protoplanetary disk, differential migration rates cause pairs of planets to sweep through a large range of period ratios. Suppose the outer planet of a pair is migrating inwards faster than an interior planet due to a larger mass or local disk properties. In this case, after the planets encounter a first order resonance, further decrease in the period ratio may be prevented as the resonance traps them into libration which prevents further period ratio change. In this case, they may continue migration together in lock-step at constant period ratio (Melita & Woolfson, 1996; Lee & Peale, 2002; Ferraz-Mello et al., 2003; Cresswell & Nelson, 2006; Terquem & Papaloizou, 2007). However, planets are not guaranteed to capture into resonance during disk migration. Rapid differential migration compared to the resonance libration time (Quillen, 2006; Ketchum et al., 2011), high eccentricities (Henrard, 1982; Borderies & Goldreich, 1984; Murray & Dermott, 1999), non-smooth/turbulent migration (Adams et al., 2008; Lecoanet et al., 2009; Ketchum et al., 2011; Batygin & Adams, 2017), divergent migration (e.g., Sinclair, 1972; Henrard & Lemaitre, 1983; Peale, 1986; Chiang et al., 2002; Tsiganis et al., 2005), and other effects (e.g., Goldreich & Schlichting, 2014; Zhang et al., 2014; Pan & Schlichting, 2017) may cause planet pairs to migrate past or escape resonances. Additionally, one would not expect that planets formed in situ via giant impacts or without significant migration to end up in resonance since the resonance width is small compared to phase space of orbital period ratios.

In our own Solar System, there is strong evidence of the migration of Neptune due to its resonance with the Plutinos (though the migration was likely caused by plantesimals rather than the protoplanetary disk; Fernandez & Ip, 1984; Malhotra, 1993, 1996), and possibly significant migration of Jupiter and Saturn while the disk was still present (Tsiganis et al.

2005; Walsh et al. 2011; Batygin & Laughlin 2015; however, cf. Minton & Malhotra 2009; Agnor & Lin 2012; Kaib & Chambers 2016). On the other hand, the planets of the inner Solar System are speculated to have formed in roughly their current orbits via giant impacts after the protoplanetary disk dissipated, with no mechanism for resonant capture (Wetherill, 1985; Chambers & Wetherill, 1998; Morbidelli et al., 2000). The Solar System planetary compositions are consistent with this picture. The large mass-fraction of Hydrogen, Helium, and volatile elements in the outer Solar System planets suggest they formed when the natal gas and dust disk was still present around the Sun. On the other hand, the lack of substantial gaseous atmospheres and relatively low fraction of volatiles on the inner planets suggests they may have formed after the gas and dust dissipated.

1.3 The Detection of Exoplanets

While the idea of planets outside our Solar System had no doubt been imagined by many (see, e.g., Bruno, 1584; Newton, 1687), Struve (1952) describes the likely methods of their detection with modern scientific instruments. He noted that if planets are in short period orbits (just as binary stars were found to be), they may produce an observable reflux motion on their host stars. This periodic motion of the star due to the planet could be measured with high precision spectrometry which provides precise radial velocities (RVs) of the star via measurement of the shifts of spectral lines. Additionally, Struve noted that as a planet transits in front of its host star, it may block enough of the stellar surface for precise stellar photometry to detect a drop in flux. This vision went unheralded for many years, but these two methods are now by far the most successful at exoplanet discovery and characterization.

The very first extrasolar planetary mass objects discovered were found in 1992 around the pulsar PSR1257+12 (Wolszczan & Frail, 1992). The $\sim 4M_{\oplus}$ planets of the initial discovery caused the observed interval between the star's millisecond pulses to change. Similar to the RV method, the pulsar timing changes are due to the gravitational reflex motion caused by the planets and the finite speed of light. Unfortunately, finding more planets around pulsars

has proven challenging, with only two or three more confidently detected in the past 25 years (Wolszczan, 1994; Thorsett et al., 1993; Ford et al., 2000; Bailes et al., 2011). Additionally, these planets have escaped widespread interest because one expects them to exist in an extreme environment unlike Solar System objects (because they orbit a neutron star rather than a main sequence star), and are expected to form through very different pathways.

The first planet around a main sequence star (51 Pegasi) was discovered in 1995 via the RV method (Mayor & Queloz, 1995; Mayor et al., 1995). This discovery opened the floodgates for thousands of observations in the following years, as well as provided impetus for countless new theories on planet formation. The vast majority of planet formation theory up until this point had been based on the Solar System architecture. The 51 Pegasi system looked wildly different than the Solar System, consisting of a single Jupiter-mass planet in a four day orbit. Such planets have subsequently been found around many stars – approximately 1% of stars are thought to host 'hot Jupiters' (Marcy et al., 2005; Mayor et al., 2011; Wright et al., 2012; Howard et al., 2012).

Observationally, it is easiest to detect large planets close to their host stars, and many more giant planets were discovered in the following years including the discovery of the first multi-planet exoplanet system (Butler et al., 1999). Specifically, the radial velocity change of the star induced by the planet is proportional to $M_{\rm p}/M_{\star}$, where $M_{\rm p}$ is the mass of the planet (Cumming et al., 1999). Searching for planets therefore requires extremely precise radial velocity measurements over a period of many orbits (weeks to years) to detect the periodic variations. This is accomplished by the use of reference lines as calibrations, historically by using an iodine or thorium-argon gas cell. The known locations of the atomic absorption lines are super-imposed on the spectra, making any stellar line shifts more readily detectable (Butler et al., 1996; Baranne et al., 1996). Improvements in technique allow for the RV detection of planets as small as a few Earth masses at present (e.g., Marcy et al., 2014), although astrophysical stellar noise often becomes a concern at that level (Lovis & Fischer, 2010; Dumusque et al., 2011b,a; Fischer et al., 2016). New technologies (e.g., Li

et al., 2008; Yi et al., 2016), observing strategies (e.g., Delfosse et al., 1998; Marcy et al., 1998; Kane et al., 2008; Plavchan et al., 2013), and improved data analysis techniques (e.g., Bonfils et al., 2007; Dawson & Fabrycky, 2010; Rajpaul et al., 2015) continue the push to lower mass planets. To date, successful RV surveys using a variety of spectrographs have identified hundreds of exoplanets from Jovian to super-Earth mass (e.g., HIRES, ELODIE, CORALIE, HARPS, Vogt et al., 1994; Baranne et al., 1996; Queloz et al., 2000; Mayor et al., 2003).

Follow-up photometric observations of known RV planets led to the first measured exoplanet transit by detection of the missing stellar flux blocked by the planet (Charbonneau et al., 2000). In the past 5 years, the number of exoplanets detected via transit have overtaken those discovered via RVs. Despite significant efforts by ground-based observers (HATNet and WASP, Bakos et al., 2004; Pollacco et al., 2006), the vast majority of discoveries have come as a result of space-based surveys (e.g., COROT and *Kepler*, Baglin, 2003; Borucki et al., 2010), which allow extremely stable photometric measurements over many years while avoiding atmospheric effects. NASA's *Kepler* mission has been the most fruitful, with over 2,000 confirmed planets and thousands more candidates to date (Morton & Johnson, 2011; Fressin et al., 2013; Coughlin et al., 2016; Morton et al., 2016).

Exoplanet transits directly provide information on many planetary orbital and physical properties, despite the inability to resolve the planet itself in transit. The timing between successive transits gives a precise planetary orbital period (P). The transit depth (δ) is approximately equal to the relative areas of the planet and star, $(R_{\rm p}/R_\star)^2$, where R is radius and the subscript p refers to a planet and $\star$ to the host star throughout. Fig. 1.2 identifies δ in a transiting lightcurve and several other quantities discussed below. Note that in the case Fig. 1.2 illustrates, δ is not exactly equal to $(R_{\rm p}/R_\star)^2$ due to non-uniform stellar surface brightness (limb darkening).

The duration of a transit reveals the ratio of the length of the transit chord across the surface of the star to the planet's velocity. The velocity is a function of the stellar mass and

the planet's semi-major axis (or period) and the planet's eccentricity. Therefore, a planetary transit directly determines the ratio of $a/R_\star$ (Winn, 2010, for precise relations, see). With independent information about the star, e.g., from spectra, the planet's semi-major axis and insolation may then be computed. Equivalently, making use of Kepler's third Law, the density of the planetary host star ($\rho_\star$) may be measured via transits:

$$\rho_\star \approx \frac{3\pi}{GP}\left(\frac{a}{R_\star}\right)^3 \tag{1.26}$$

(Seager & Mallén-Ornelas, 2003).

The curvature of the star relative to the planet's direction of travel at the location the planet begins and ends its transit affects the transit shape. Specifically, the ratio of the transit's total duration to the ingress and egress times (the proportion of the transit which the planet is not completely on the star, $T_{\rm ratio} = \frac{T_{\rm ingress}+T_{\rm egress}+T_{\rm fully\,transiting}}{T_{\rm fully\,transiting}}$) reveals the impact parameter (b) of the planet transit (Winn, 2010, and see Fig. 1.2). By creating a right triangle with a leg equal to the vertical height of the planet above the center of the star (h_p) and the hypotenuse as the distance from the center of the star to the planet (r_p), the planet's the inclination may be computed as

$$\begin{aligned} \cos i &= \frac{h_p}{r_p} \\ \Leftrightarrow \quad i &= \cos^{-1}\left(\frac{(b\times R_\star)}{(a(1-e^2)/(1+e\sin\omega))}\right) \\ \Leftrightarrow \quad i &= \cos^{-1}\left(b\times\left(\frac{R_\star}{a}\right)\times\frac{(1+e\sin\omega)}{(1-e^2)}\right). \end{aligned} \tag{1.27}$$

For small e, this is a straightforward computation of direct lightcurve observables.

Like with RV measurements, both the overall mass scale of the system and the angle of the planet's projected orbit on the sky plane is undetermined (without additional information such as stellar spectra modeling). Eccentricity constraints are also usually weak. Critically, and unlike RV measurements, for Keplerian transits of a single planet there is no signature

of the planet-to-star mass ratio in transits.

1.4 Orbital Properties of Exoplanets

RV surveys demonstrated that Jovian planets have a preference for low-order MMRs in multi-planet systems (Wright et al., 2011). Additionally, observed Jovian exoplanets often had larger eccentricities than Solar System planets (Marcy & Butler, 1996; Cochran et al., 1997), with giant exoplanets exhibiting a broad range in e extending above $e = 0.5$ (Tremaine & Zakamska, 2004; Wright et al., 2009; Winn & Fabrycky, 2015). The mechanism for the assembly of these systems is still unclear (see Wisdom, 1980; Duncan et al., 1989; Chambers et al., 1996; Mazeh et al., 1997; Lin & Ida, 1997; Malmberg et al., 2007), but some theories (e.g., Chatterjee et al., 2008) suggest that highly mutually-inclined systems should be expected. Such systems remain elusive to detection via RVs (albeit, see Nelson et al., 2016, for an RV detection of coplanarity). Additionally, low eccentricities and precise orbital period information are challenging to extract from RV data alone.

On the other hand, transit observation missions (particularly *Kepler*) have been much more successful to date at probing the detailed architectures of small exoplanet systems. *Kepler*'s photometric precision allowed for the detection of a wide range of exoplanet sizes, from Jupiters down to Mars-sized planets (see Coughlin et al., 2016; Morton et al., 2016). With injection and recovery tests to understand survey completeness, this enabled a population census of planets in our solar neighborhood including planet occurrence rates for planets larger than $\sim$1 $R_\oplus$. Planets with short orbital periods are very common, with $\sim$30% of Sun-like stars hosting a planet from 1-8$R_{\rm Earth}$ with periods less than 50 days (Howard et al., 2012; Petigura et al., 2013), of which roughly half have an $R = 2$-$4R_{\rm Earth}$ planet. The Solar System has no planet in this intermediate size range between that of Earth and Neptune, and does not possess very short period planets. It has since been statistically revealed that planets with $R \lesssim 1.5R_{\rm Earth}$ are likely to be rocky (scaled-up Earth-like planets called super-Earths), whereas those with $R \gtrsim 1.5R_{\rm Earth}$ are likely to have a significant gas envelope

Figure 1.2: Transit Geometry and Lightcurve

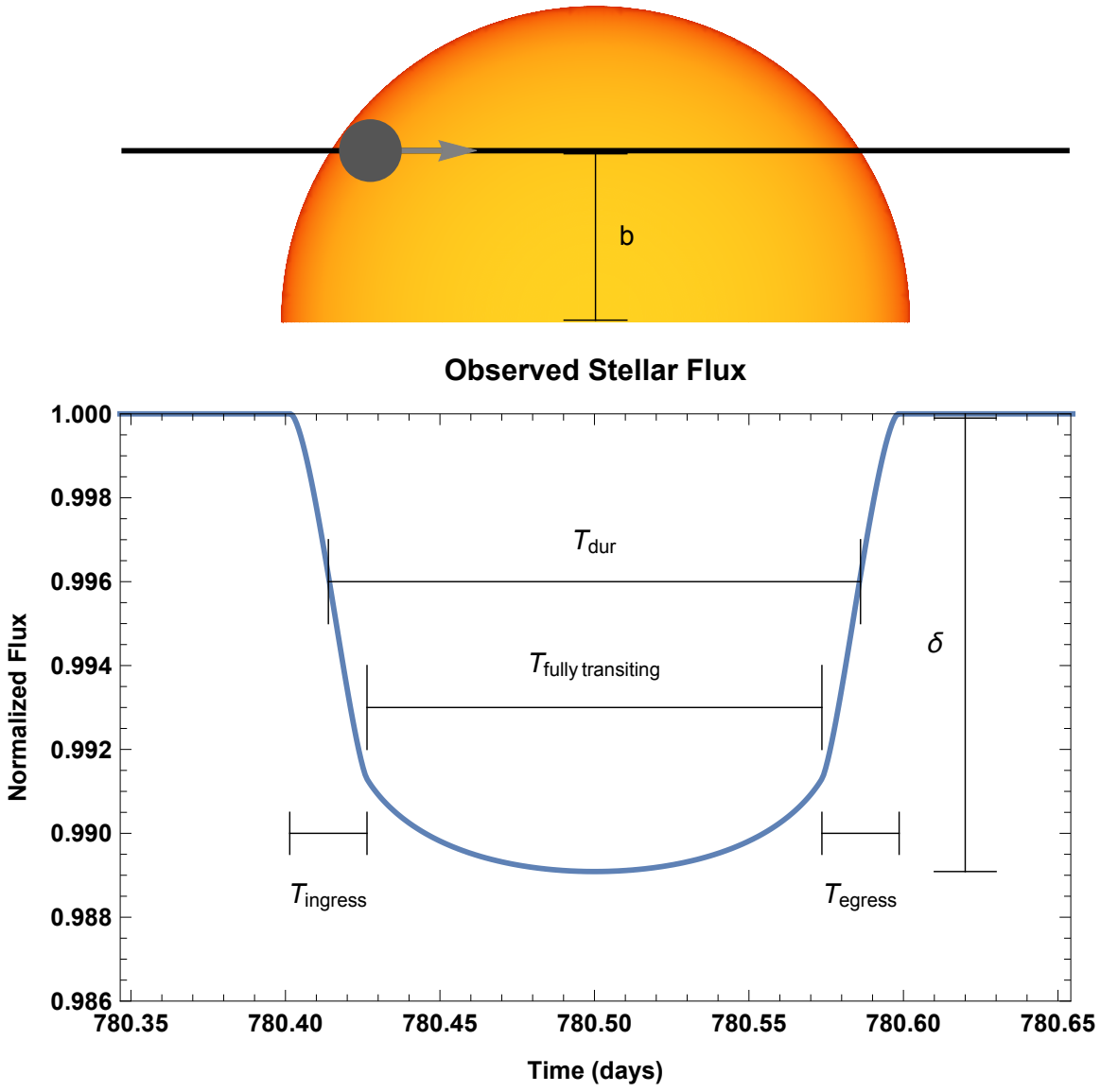

An example of a transiting planet's geometry and lightcurve with realistic limb darkening. Several observables defined in §1.3 are labeled. The planet (gray) has just entered the fully transiting geometry.

(scaled-down Neptune-like planets called sub-Neptunes) (Marcy et al., 2014; Rogers, 2015). This distinction is adhered to henceforth, with small, low-density (significant gas mass fraction) planets referred to as sub-Neptunes. These close-in planets with $R \lesssim 4R_{\rm Earth}$ are also often found in multiply transiting systems. Some of the first *Kepler* systems announced had high multiplicity (e.g., Steffen et al., 2010; Lissauer et al., 2011a), and hundreds of multiplanet systems of $R \lesssim 4R_{\rm Earth}$ have since been detected in systematic searches (Coughlin et al., 2016; Morton et al., 2016) and studied individually in great detail (e.g., Kepler-11, Lissauer et al., 2011a; Migaszewski et al., 2012; Lissauer et al., 2013; Mahajan & Wu, 2014; Bedell et al., 2017). Since Solar System models implicitly or explicitly avoided producing such planets, this new class of ubiquitous yet diverse planets has sparked a fresh inquiry into planet formation and evolution.

Kepler's transit observations also allow for precise measurements of the planets' orbital periods by virtue of the timing of their transits. Statistical studies of the period ratios of exoplanets revealed an intriguing feature: the period ratios between pairs of planets in the majority of multiplanet systems are drawn from a broad, random distribution; however, there are peaks in this distribution near MMRs, especially the 3:2 and 2:1 resonances, the latter of which also features a dearth just inside of the resonance (Fabrycky et al., 2014; Steffen & Hwang, 2015). This is illustrated in Fig. 1.3, an updated version of the seminal Figure 4 from Fabrycky et al. (2014) using *Kepler* Data Release 25 (Twicken et al., 2016)[7]. Additionally, deviations from perfectly periodic Keplerian transits have been detected. These transit timing variations (TTVs) reveal information about the masses and eccentricities of planetary systems (discussed in §1.5).

A period dependency of the orbital architectures of planets has also recently been demonstrated (Delisle & Laskar, 2014), suggesting tidal evolution of multiplanet systems. In general, planets that are sufficiently close to their host stars undergo tidal distortion due to their host star's gravitational potential. Therefore, if planets are not synchronously rotating, or

7. See also https://exoplanetarchive.ipac.caltech.edu/docs/Q1Q17-DR25-KOIcompanion.html

Figure 1.3: Period Ratio Distribution of *Kepler* Transiting Multiplanet Systems

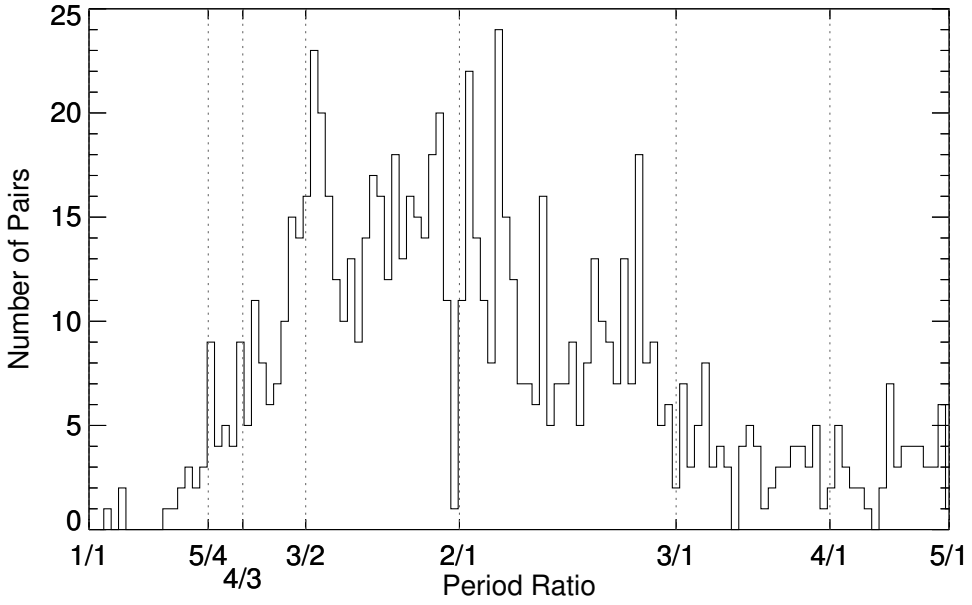

An update to Figure 4 from Fabrycky et al. (2014), this plot shows the distribution of period ratios of pairs of planets (confirmed and candidates) observed by *Kepler* from the Data Release 25 Kepler Object of Interest Catalog. Important MMRs are indicated with dashed lines. Significant features include the continuity of the distribution, as well as peaks just wide of several MMRs including 3:2 and 2:1. There is also a significant trough just inside 2:1 and peak at $\sim$2.17:1.

if they are on eccentric orbits, they will dissipate energy internally as they respond to their orientation changing relative to the tidal forces[8]. The effect of tides has a strong semi-major axis dependence, with an eccentricity damping timescale dependent on the 6.5 power of a:

$$\tau_e = \frac{4}{63}\frac{M_p a^{13/2} Q}{G^{1/2} M_\star^{3/2} R_p^5}, \tag{1.28}$$

where G is the universal gravitational constant and Q is the quality factor of the planet (Goldreich & Soter, 1966; Rasio et al., 1996), and an even stronger a^8 dependence for the semi-major axis decay timescale (Yoder & Peale, 1981; Rasio et al., 1996). Planets in multiple planet systems (particularly near or in MMR) force an eccentricity on each other (see, e.g., Murray & Dermott, 1999, §7.4), and are therefore naturally subject to tidal dissipation regardless of their initial conditions. This tidal dissipation will spread the planets away from resonance as their eccentricity is damped (Lithwick & Wu, 2012; Lee et al., 2013). This process may take Gyr and in some cases can substantially change the architectures of the planet systems. By estimating the distance planets have spread apart over their lifetimes, insight into the quality factor (Q) and therefore internal structure of the planets can be gleaned (Lee et al., 2013).

1.5 Transit Timing Variations

The Classical Planets including Mercury, Venus, Mars, Jupiter, and Saturn were known to astronomers since antiquity due to their easy visibility with the naked eye and their fast motion across the sky. William Herschel added to this list in 1780s with measurements of Uranus which demonstrated its planetary orbit as computed by Anders Lexell (Herschel &

8. Planets may also raise tides on their host stars; however, the dissipation from this is generally negligible given the small $M_p/M_\star$ ratio, and high stellar Q values (see Goldreich & Soter, 1966; Schlaufman et al., 2010; Penev et al., 2012).

Watson, 1781; Doig, 1950)[9]. The orbit of Uranus was subsequently followed-up by many observers, and its location in the past determined by vetting old star catalogs. Considering only the Keplerian orbit of Uranus was immediately insufficient to explain its trajectory across the sky – the gravity of the nearby giant planets Jupiter and Saturn perturbed the perfectly periodic orbit causing deviations from an elliptical path. However, Alexis Bouvard found that even after including these effects the observed path of Uranus was still discrepant from predictions (Bouvard, 1821), and perhaps another massive object needed to be considered. In the 1840s, John Couch Adams and Urbain Le Verrier working independently both calculated the likely mass and position of such an unobserved perturber (Adams, 1846; Le Verrier, 1846). In 1846, Johann Galle identified the object now known as Neptune in the same patch of sky both theorists had predicted (Galle, 1846)[10]. The discovery of Neptune demonstrated the predictive success of multi-body planetary dynamics at determining properties of unseen planets in our Solar System including position and mass.

In exoplanetary systems, it was recognized that the same principle could be applied to determine the properties of observed multi-planet systems. Shortly after the discovery of PSR1257+12 (Wolszczan & Frail, 1992), the orbital periods of its planets were predicted to perturb each other measurably within a few years (Rasio et al., 1992). Additionally, if the planets were in an exact MMR, the effect would be amplified considerably (Malhotra et al., 1992). These dynamical perturbations were indeed detected (along with a 3rd planet in the system) in the following two years, validating both the planetary interpretation of the periodic pulsar signal and the dynamical modeling (Wolszczan, 1994).

Similarly, it was recognized that the for transiting exoplanets the timing of the planet's passage in front of the star due to perturbations of other planets may be detectable (Dobro-

9. Uranus had been observed before, perhaps as early as 128BCE by Hipparchos (Bourtembourg, 2013), but certainly as early as the 1690s by John Flamsteed (Le Verrier, 1846). However, all observers prior to Herschel mis-categorized the object as a star due to its slow proper motion and faint apparent magnitude.

10. Like Uranus, Neptune had also been observed earlier on numerous occasions but was mistaken for a stationary star. The first definitive observation of Neptune was made by Gallileo in the early 1600s (Kowal & Drake, 1980).

volskis & Borucki, 1996; Miralda-Escudé, 2002), particularly if they are near MMR (Agol et al., 2005; Holman & Murray, 2005). This recognition paralleled work on multi-star systems going back many decades (e.g., Soderhjelm, 1975), and has since been explored in great analytic detail (e.g., Lithwick et al., 2012; Agol & Deck, 2016; Nesvorný & Vokrouhlický, 2016). Once measured, these variations in transit times allow for the extraction of the masses and orbital parameters of the planets that produce them (Nesvorný & Morbidelli, 2008; Nesvorný & Beaugé, 2010).

For pairs of planets near, but not in, resonance the dominant TTV frequency and its amplitude reveals a combination of the mass and eccentricity (Lithwick et al., 2012). Following the convention of binary-star observers, this frequency is commonly displayed in a plot of the difference of the observed transit times and transit times calculated using a constant period model (an 'Observed Minus Calculated' or O-C plot). Fig. 1.4 demonstrates this effect for a pair of $0.1 M_{\rm Jupiter}$ planets outside 2:1 MMR. The period of the signal (the TTV super-period) is to first order

$$P_{\rm TTV} = \frac{P_2}{(k+1)|\Delta|}, \tag{1.29}$$

where j and k are positive integers as in Eq. 1.1, and Δ is the offset from exact resonance: $\Delta = \frac{P_2}{P_1}\frac{j}{j+k} - 1$ (Lithwick et al., 2012). To first order in eccentricity, the amplitude is proportional to

$$A_{\rm TTV\,1,2} = \frac{P_{1,2}\mu_{2,1}}{|\Delta|}\left(1 + \frac{|Z_{\rm free}|}{|\Delta|}\right), \tag{1.30}$$

where μ_i is reduced mass ($\mu_i = \frac{M_i}{M_\star}$), the linear combination of the two planet's complex free eccentricity ($Z_{\rm free}$) can be approximated as $Z_{\rm free} \approx 2^{-1/2}(e_1 e^{i\varpi_1} + e_2 e^{i\varpi_2})$, and the subscripts $1, 2$ indicate which body's properties are appropriate for which TTV amplitude (Lithwick et al., 2012; Hadden & Lithwick, 2017). This equation illustrates the intrinsic mass-eccentricity degeneracy in measuring planet masses and orbital architectures with TTVs. However, with more precise data that allow for the determination of more frequencies in the TTV signal, this degeneracy may be broken via the so called synodic 'chopping' effect (Deck

& Agol, 2015, and see Fig. 1.4).

Eq. 1.29 approaches a singularity for planets in exact MMR, and a different expansion is valid (Nesvorný & Vokrouhlický, 2016):

$$P_{\rm TTV,MMR} \propto \frac{P_1 + P_2}{(\mu_1 + \mu_2)^{2/3}} \tag{1.31}$$

and

$$\frac{A_{\rm TTV,MMR,1}}{A_{\rm TTV,MMR,2}} \propto \frac{m_2}{m_1}\left(\frac{P_1}{P_2}\right)^{2/3} \tag{1.32}$$

where A_i is the TTV amplitude of planet i[11].

Both Eqs. 1.30 and 1.32 indicate the strong mass dependence of the planets on the size of any TTV signal. The most extreme case of a massive planet is the extrapolation from a Jupiter-mass planet to a brown dwarf or stellar companion. Those planets in orbit around both stars – circumbinary planets (CBPs) – are likely to exhibit large TTVs with amplitude of order days over a few year period because of the large motions of the stars due to the binary orbit with periods typically observed to be on order weeks (Welsh et al., 2015). Such systems have the largest observed TTVs to date (Doyle et al., 2011). Planets orbiting one of the two or more stars in a multiple star system are also not uncommon (Eggenberger et al., 2007; Roell et al., 2012; Ngo et al., 2017). However, they are likely to only exhibit small TTVs due to the other stars over a few year observing window because the binaries' orbits are generally 10s to 1,000s of years long.

1.6 This Work

This work explores the implications of individual planetary system architectures on their respective formation and evolution, and what they suggest about planet formation in general. In order to measure precise orbital configurations and masses in multi-planet systems,

11. The exact relations may be found in Nesvorný & Vokrouhlický (2016), but we only include the scalings here to illustrate the different dependence from non-resonant TTVs with straightforward expressions.

Figure 1.4: TTVs of a Pair of Planets Near 2:1 Resonance

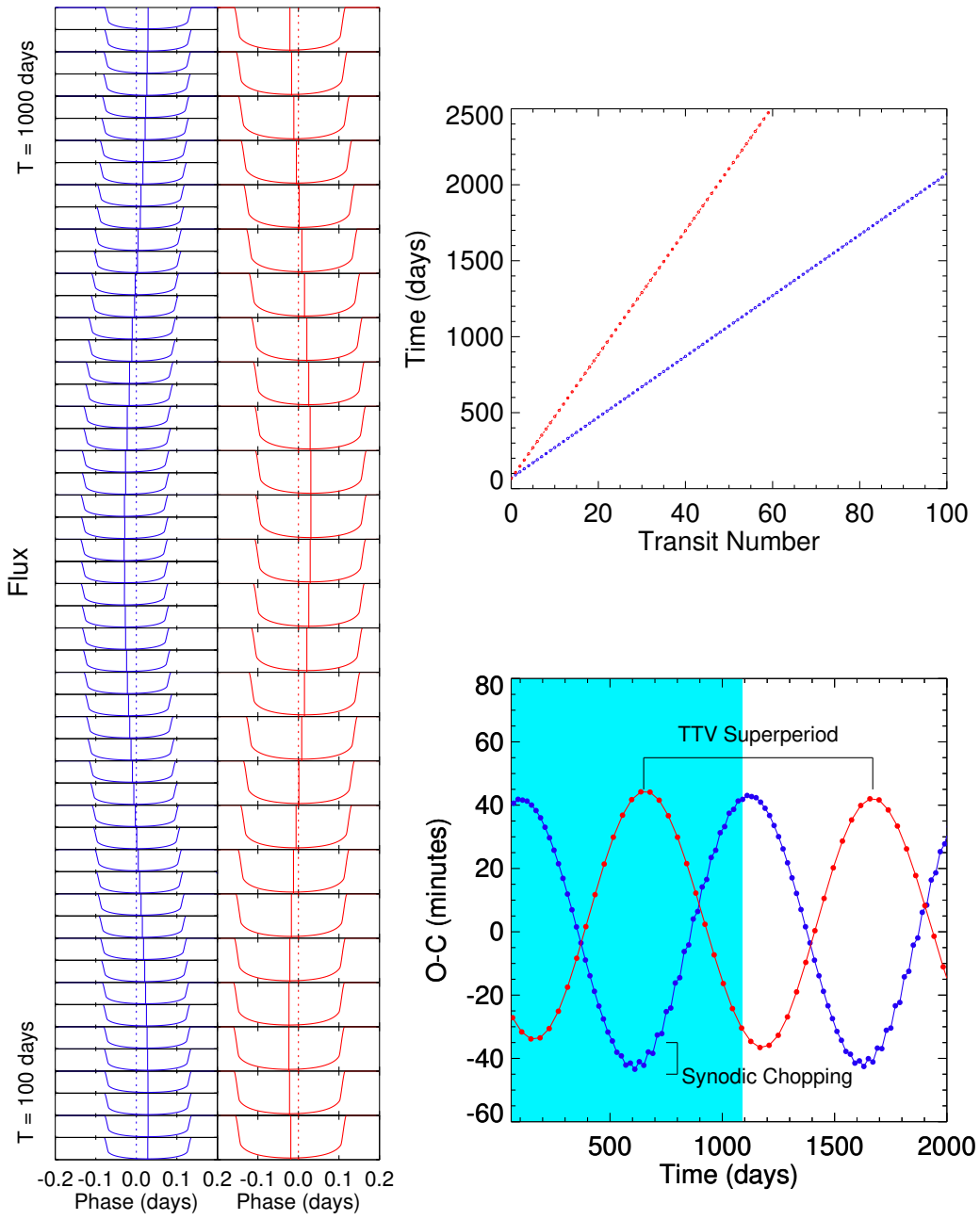

Simulated transit times for a pair of 0.1 $M_{\rm Jupiter}$ planets on nearly circular orbits just outside the 2:1 resonance ($P_1 = 20$ days and $P_2 = 40.8$ days). The upper right hand panel shows the transit times as open circles for the interior planet 1 (blue) and the exterior planet 2 (red) as a function of sequential transit number (the index is arbitrary). Both closely follow a linear relationship, with the best fit dashed line plotted almost directly atop the points. However, closer inspection shows residuals to the line: simulated photometry of the first 52 transits of the interior planet (blue) and first 26 of the exterior (red) are shown at left, phased at the best-fit constant linear period as plotted in the upper right panel. Because of the near 2:1 resonance, these span nearly the same time interval. The predicted linear transit time is shown as a vertical dashed line in the center of each panel. The observed transit photometry is seen to vary from this position and the actual transit midtime is plotted as a solid vertical line in each panel. A strong anti-correlation between the tran-

Figure 1.4 Continued: TTVs of a Pair of Planets Near 2:1 Resonance

sit timings of the two planets is readily visible. These transit time residuals may also be plotted as a function of observational time in an observed minus calculated (O-C) TTV figure as shown in the lower right panel. The transits shown on the left from bottom to top correspond to the shaded region of the plot. The same anti-correlated features are seen. Applying Eq. 1.29 to this planet configuration yields $P_{\rm TTV} = 1020$ days, very close to the observed N-body value in the lower right panel. Additionally, synodic chopping can be seen in the O-C TTVs, which would allow breaking the mass-eccentricity degeneracy if measured.

a photodynamic code was developed for the analysis of *Kepler* light curves and RV data. This code and its use are explained in §2. Kepler-223, a four sub-Neptune planet system around a distant star whose faintness had hitherto precluded proper characterization is then discussed. This system's resonant configuration suggests a smooth disk-migration origin – some of the first evidence that low mass (sub-Neptune) planets migrate into resonance. Kepler-108, a pair of giant planets which exhibit a high mutual inclination which induces a secular precession observable as transit duration variations is then presented. This is the first confidently detected large mutual inclination between transiting planets. A description of mass measurements of Mars-sized planets in the compact Kepler-444 system follows in §5. The architectures of both this system and Kepler-108 suggest departures from a pure disk-migration origin and imply a wide variety of different planet formation/evolution mechanisms. The dynamical detection and interpretation of planets around binaries is considered next. These CBPs represent planets from a potentially distinct birth environment, where different physical processes than in single-star planetary systems may be important or dominant, and the detailed characterization of a few members of this population is discussed. Lastly two brief population statistical studies are presented. The first is an updated mass-radius relationship fit, where the differences between RV and transit detections are considered. The second expands on Rein (2012), attempting to understand the origin of the observed muli-transiting planet period ratio distribution.

This work draws heavily, and often directly, from several papers published over the course of my graduate studies. The photodynamic code in §2 has been used in much of my published work. The Kepler-223 section is a more detailed exposition of Mills et al. (2016). The Kepler-

108 and Kepler-444 chapters share much of the text from Mills & Fabrycky (2017a) and Mills & Fabrycky (2017b), respectively. §6 draws from Welsh et al. (2015) and ongoing work on KIC 10753734. §7 replicates content from Mills & Mazeh (2017) and presents ongoing work on stochastic migration.

CHAPTER 2

PHOTODYNAMIC ANALYSIS CODE

The purpose of this photodynamic model is to produce synthetic light curves given a transiting or eclipsing multiple planet or star system, and then compare it to *Kepler* time series photometry and other data including radial velocities (RVs) and spectroscopically determined stellar parameters. The photodynamic code takes as input the arrangement of a multiple star or planetary system at a specified time and integrates it forward and backward in time under the influence of gravity. A theoretical photometric light curve is produced by tracking the positions of the bodies as they pass in front of or behind each other from the perspective of a distant stationary observer[1]. This code can create a single synthetic light curve for a given system and set of observation times or, along with observed photometry, fit an initial guess at the solution through differential evolution Markov chain Monte Carlo (DEMCMC, explained below) to estimate best fits and uncertainties.

2.1 Parameter Setup

The flux from the central star is defined by five parameters: mass ($M_\star$), radius ($R_\star$), two limb darkening coefficients for the primary (c_1 and c_2), and a dilution factor (*dilute*). Following Mandel & Agol (2002), we model the stellar flux as a function of position on the projected stellar surface with a radially symmetric quadratic limb darkening law specifying intensity as a function of radial position by

$$I[\mu] = 1 - c_1(1-\mu) - c_2(1-\mu)^2, \tag{2.1}$$

1. The data released by the *Kepler* mission has already been converted into a barycentric solar system time scheme, barycentric Julian date (BJD).

where the two model parameters are the coefficients c_1 and c_2, and μ is given by

$$\mu = \mu[x, y] = (1 - (x^2 + y^2))^{1/2} \tag{2.2}$$

for a 2D Cartesian coordinate system centered on the disk of the star and normalized such that the stellar radius is unity. The dilution factor (*dilute*) is the fraction of observed light that is from a constant source outside the system. For an isolated stellar system dilution would be zero, but *Kepler* and other real data often have faint, unresolved background stars providing constant illumination of a few percent which affect apparent transit depth and therefore planet radius.

Each additional body requires either 8 or 11 parameters. Six parameters are required to specify a unique position and velocity of the object in three dimensions. These may inputted in Cartesian coordinates (x, y, z, v_x, v_y, v_z) or as orbital elements with the sky plane as the reference (period (P), time of conjunction (T_0), eccentricity (e), argument of periastron (ω), inclination (i), and nodal angle on the sky (Ω)) and converted internally to Cartesian coordinates. By default in the code and throughout this text unless otherwise specified, instantaneous Keplerian orbital elements are referred to the center of mass of all interior orbits, i.e., are Jacobian elements. To reduce correlation among eccentricity parameters, the eccentricity vectors $h = e \sin \omega$ and $k = e \sin \omega$ or $h_2 = \sqrt{e} \sin \omega$ and $k_2 = \sqrt{e} \sin \omega$ are generally used (the latter to naturally produce a flat prior on e in MCMC fitting). Every body also requires a radius (R) and mass (M). Three additional parameters are required only by bright (usually stellar) objects: the fraction of the system's intensity coming from this body ($f_{\rm frac}$) and two limb darkening coefficients ($c_{1,i}$ and $c_{2,i}$ for the $i^{\rm th}$ star) following the same prescription as the primary star. Priors in most parameters are generally uniform, however various e priors are also available including a Rayleigh distribution with any specified σ, or a maximum allowed e.

Additionally, since orbital elements and Cartesian coordinates change in time due to

dynamical interactions, the reference time when the inputs are specified is required. This time, $T_{\rm epoch}$, is generally chosen either near a specific transit event of interest or near the center of the data set.

The code computes a theoretical lightcurve for the system at a list of times specified by the user and will compute the χ^2 value of the model if given associated uncertainties. Both short and long cadence data, or a mix of both, can be given to the code. *Kepler*'s long cadence data are 30 minute photometric integrations, while short cadence data are 1 minute integrations. For short cadence points, the flux is calculated based on the positions of the system's bodies at the exact timestamp of the cadence. For long cadence data, the instantaneous flux at the time of the center of an observation may not sufficiently estimate the integrated flux over the entire time period (particularly during transit ingress and egress when the flux is changing considerably over time periods shorter than the integration time of the data point). Therefore, each long cadence point is divided into several evenly-spaced sub-points spanning the long cadence time interval (typically $\sim$20 points), and the flux values at each of these sub-points are averaged together to create a theoretical long cadence flux value.

2.2 Integration

A stellar-centric coordinate system is used in the code in which one of the bodies (called the primary hereafter) is considered to be centered at the origin at all times. The internal coordinates are Cartesian with the x-y plane being the plane of the sky and the positive z axis pointed away from the observer. Adapting Murray & Dermott (1999) to the many-body case, we define the coordinate system as described in §1.2 Eqs. 1.12-1.16. We integrate Eq. 1.16 to advance the positions of the bodies as a function of time.

The equations of motion of the initialized system are integrated using the GNU Scientific Library's (GSL) implementation of an explicit embedded Runge-Kutta Prince Dormand (8,9) method (for details see Galassi & Gough, 2009). This integrator is slightly slower than

sympleptic type integrators, but is more flexible for use from hierarchical to multiple star systems. Adjustable time boundaries are specified to include all of *Kepler*'s observational window, and any additional data such as RV. During the integration, if any body passes in front of any other body which has non-zero brightness, the exact time of mid transit is computed by applying the Newton-Raphson method to the sky projected separation of the two bodies in question (Fabrycky, 2010).

Two options exist for computing the light curve near a transit. The first assumes the relative velocity of the transiting body to the occulted star is constant. This is known as the rectilinear transit approximation. The instantaneous sky-projected relative velocity, $\vec{v}_{rel,mid}$, and position, $\vec{x}_{rel,mid}$ of the transiting body found from the Newton-Raphson method above is used to compute positions of the body near the transit time by the simple relationship $\vec{x}_{rel} = \vec{v}_{rel,mid}\Delta T + \vec{x}_{rel,mid}$. The positions are tracked for a time in both directions of at least $\frac{(R_s+R_p)}{v_{rel,mid}}$ where R_s and R_p are the transited and transiting bodies' radii respectively. The second method is to perform small integration steps to find the exact positions of the planets at each time of interest near a transit. This is computationally slower, but often necessary when several bodies are approximately the same mass in the system or otherwise have relative velocities changing on the timescale of a transit. In the most extreme case, a planet around a binary star system could theoretically have zero velocity relative to the star it is transiting at some point during transit. This would occur if the untransited star slows the rapid, sky-projected velocity of the transited star to the same speed as the planet at the time of transit. If this is near the zero point found by the Newton-Raphson method, an arbitrarily long transit may be erroneously computed using the rectilinear approximation.

At each time of interest near a transit event, the relative positions computed as described above of all bodies involved (usually two, but possibly several for mutual transit events) are passed to an adaptation of the Pál (2012) multi-body transit code. In order to save computation time, particularly for many-body systems, bodies at a large sky-projected distance from other bodies are not passed to the transit algorithm. The radii of the relevant bodies are

normalized such that the transited star furthest from the observer has a radius of unity. The relevant limb darkening parameters are applied to the transited body and the normalized amount of light blocked by the transiting bodies is computed. This amount is multiplied by the fractional brightness this individual star is contributing to the system. If there is more than one star being transited at the same time, this process is repeated for each star, keeping track only of bodies between successively closer stars and the observer.

2.3 Light Travel Time Effect

So far, only instantaneous planet positions have been discussed, but in real systems the timing of transits is affected by the finite speed of light (c). The model has an option to compute light curves and transit times either with an infinite speed of light (for simplicity and comparison with other models) and with the true value c. In both cases, the Newton-Raphson method is employed to find transit times.

In the stellar-centric coordinates of this model, the light time effect (LITE) is easily dealt with for a body occulting or being occulted by the primary star since the primary is always stationary. The time it takes for light to travel between the primary star and another body is simply $\frac{z_{\rm body}}{c}$ where $z_{\rm body}$ is the z coordinate of the other body, c is the speed of light in a vacuum, and we are interested only in the travel time of light towards the observer. Since we are interested in the times as they would appear to a distant observer with a constant clock, we must additionally compute the z distance from the primary star to the stationary barycenter: $z_{\rm bary} = \frac{\sum_0^N m_i z_i}{\sum_0^N m_i}$. We therefore adjust calculated transit times using the formula

$$t_{\rm true} = t_{\rm inst} - \frac{(2 \cdot z_{\rm bary} - z_{\rm body})}{c} \tag{2.3}$$

where $t_{\rm inst}$ is the time of events computed assuming and infinite speed of light, $t_{\rm true}$ is the time of events corrected for the LITE, and the factor of 2 in front of the arises from adjusting both the position of the primary star and the other body by the barycentric distance. By

moving the second term of right hand side of Eq. 2.3 to the left, we have a formula to compute the infinite speed of light model time necessary to find accurate relative positions of the two bodies at a given input time. Note that z_{body} and z_{bary} are both functions of time so this formulation will create an error by assuming that these values are essentially constant over the time $t_{\text{inst}} - t_{\text{true}}$, but this error is small due to the high speed of light relative to the velocities of bodies in the system and that, geometrically, most transits occur at times when the bodies' z velocities are low.

Computing the LITE for transits not involving the primary star (e.g., for in CBPs) is somewhat more complicated as both bodies are in motion in our coordinate system. Transit times are still computed iteratively using the Newton-Raphson method. We are now interested in the position of the background object's light after it has traveled a distance $z_{sep} = |z_{back} - z_{fore}|$, where z_{back} is the background object's z position and z_{fore} is the foreground object's z position. This corresponds to a light travel time of $t_{\text{LITE}} = \frac{z_{sep}}{c}$. We then find the time at which the foreground object's position at time $t_0 + t_{\text{LITE}}$ is closest to the background object's position at time t_0. The code does this to second order, making use of the position, velocity, and acceleration of the body in front over the time interval t_{LITE}. Once this time of minimum is found, the transit timing must again be corrected to the barycentric time by the formula

$$t_{\text{true}} = t_0 - \frac{(2 \cdot z_{\text{bary}} - z_{back} - z_{fore})}{c}. \tag{2.4}$$

2.4 Radial Velocities

Radial velocities for any object in the system can be computed in this model by advancing the equations of motion to any specified time and examining the velocities of the objects. The theoretical radial velocity in the Jacobian coordinate system is

$$v_{\text{rad}} = v_{\text{body,z}} - v_{\text{bary,z}} \tag{2.5}$$

where $v_{\rm bary} = \frac{\sum_i^N m_i v_{z,i}}{\sum_i^N m_i}$. Often RV measurements can only be made for the primary body. In this case, the formula reduces to $v_{\rm rad} = -v_{\rm bary,z}$ since the primary body is at the origin. The general form is useful for multiple star systems when RV measurements can be obtained for multiple stars (e.g. a double lined binary spectrum in a CBP system).

Times for radial velocity output are user-specified and, similar to photometry data, the code can take a list of times, radial velocities, and uncertainties to add to the total χ^2 from photometry. When fitting RV data, the code adds a floating offset value ($C_{\rm RV}$) to the measured RVs to account for the barycenter of the system traveling towards or away from the observers at a constant rate. The value is chosen to minimize the χ^2. RV data can also optionally be flagged to be from N different telescopes such that there are N different constant offsets. All data from the $i^{\rm th}$ telescope is given the same χ^2-minimizing offset, but that may differ from the offset for the $j^{\rm th}$ telescope, accounting for systematic instrument differences.

As the positions of the bodies in a system are advanced through time to check for transits for photometry, the RV times are also monitored and computed as necessary. This reduces computation time by only requiring one integration of the equations of motion for all components of the model.

2.5 Monte Carlo Simulations

Discussion thus far has been limited to describing a single run of the model. The full power of the code is realized by running it many times in Monte Carlo simulations to fit parameters and estimate uncertainties. We implement a differential evolution Markov chain Monte Carlo (DEMCMC) to better analyze the *Kepler* data. The advantages of differential evolution over traditional MCMC are speed of convergence and calculation for even highly linearly correlated parameters. A brief discussion of the DEMCMC with specifics relating to photodynamics will be discussed below, but for a complete discussion of the algorithm the

reader should consult Ter Braak (2005).

To initialize the system, an estimate by eye or using data from the *Kepler* Object of Interest (KOI) catalog is used. A characteristic spread of each parameter is estimated and the chains are initialized by adding to the initial guess of each parameter a draw from a Normal distribution with σ equal to the chosen spread. This initial clustered setup is used since gridding over the possible values of all parameters in a high dimensional space is computationally impractical as too much computation time is spent in high χ^2 areas early on and chains are in danger of becoming trapped in clearly incorrect local minima.

A DEMCMC evolves of a set of parameter vectors, $\{\vec{p}\}$, each of which is known individually as a chain, $\vec{p}_i$. Every time the DEMCMC is evolved, the chains are said to take a step to the next generation, adding a link to every chain. Every generation, each chain evolves all of its parameter values by proposing new values generated by adding the difference between two values of other randomly chosen chains, multiplied by a scale factor γ and a N($\mu = 0$, $\sigma = 0.1$) random variate R. Thus a single step would evolve the i^{th} chain's parameters like $p_{i,\alpha} \mathrel{+}= \gamma \cdot (1 + R) \cdot (p_{j,\alpha} - p_{k,\alpha})$ for all parameters α, where j and k are indices chosen with at random in the range $[1, N_{chains}]$ such that $i \neq j \neq k$, and γ is a mutable scalar discussed further below.

The χ^2 value for the proposed parameter values is computed: $\chi^2 = \sum_{i=1}^{N} \frac{(x_i - y_i)^2}{\sigma_i^2}$ where x_i are observed data points and y_i are computed model points. Following a thermodynamic Metropolis approach, new parameter values are accepted and recorded as the current values for a given chain with probability $min\big(e^{\frac{\chi^2_{old} - \chi^2_{new}}{2}}, 1\big)$. Lower χ^2 values represent a better match of all photometry and RV data weighted by the errors. This formulation means that new parameter sets are accepted by the system according to their relative likelihood compared to the previous parameters. Note that if the new χ^2 is less than the old value, the new parameter vector is guaranteed to be accepted. If the new χ^2 value is higher than the old value, the probability it is accepted reduces exponentially with the difference in values. If the proposed parameter values are not accepted, the chain's parameter vector is kept at

its old value. This allows the chains to explore the χ^2 surface, weighting regions of low χ^2 by probabilistically staying in them. Generally hundreds of thousands of steps are taken until the chains are sufficiently converged, with parameter values being recorded every k^{th} step, where k is an integer (in practice set to 1000 for highly correlated, slowly converging parameter sets). This is done to minimize the dependency of a given chain's recorded set of parameter values on its previous set and avoid wasting disc space by storing large quantities of highly correlated data. If we remove the initial set of parameter values from all chains before they were converged, we essentially eliminate the effect of the the handpicked guess as long as it was close enough to the global minimum that the chains could find that minimum. We may then use the remaining recorded parameter values from all chains to estimate the posterior parameter distribution and uncertainties even for very non-Gaussian parameter distributions.

The factor γ described above is adapted at each step to speed up convergence. Ideally, in each generation the fraction of chains which accept their new parameters proposal is near an optimal fraction, $f_{\rm opt}$, usually chosen to be 0.23 (Ter Braak, 2005). If a smaller fraction of the chains' proposals are accepted than $f_{\rm opt}$ at a given step, then γ is reduced by a multiplicative factor $(1 - q)$, where q is called the relaxation factor and generally chosen to be 0.1. This results in the next steps' proposals being on average less distant from the current parameters. If the fraction of chains which have proposals accepted exceeds $f_{\rm opt}$, γ is increased by $(1 + q)$ to more quickly probe the lowest regions of the χ^2 surface.

The code also allows us to easily fix any parameters desired in the DEMCMC. This is useful, for instance, to explore certain simplifying assumptions and models. *Kepler* data often provides little information about the coplanarity of an individual system (although statistically most systems can be shown to be nearly coplanar, Fabrycky et al., 2014), therefore the nodal angles are often fixed: $\Omega_i = 0 \; \forall \; i$. This may vastly reduce the size of parameter space which need be searched and therefore speed up DEMCMC convergence time, while simultaneously limiting the solution set to the phase space that is likely for a given multi-

transiting system (see, e.g., Lissauer et al., 2011a). Additionally, since the absolute nodal angle of bodies on the sky is undetermined by photometry or radial velocities and only relative angles can be constrained due to dynamical interactions or occasionally mutual transits (Masuda et al., 2013), $\Omega_1 = 0$ in all cases. Further, if data is limited and some parameters are too degenerate or there are strong priors (e.g. limb darkening coefficient degeneracies or stellar mass from asteroseismology), fixing certain additional parameters may be preferred.

Each run of the model completes a high-accuracy N-body numerical integration combined with the computation transit photometry, generally for thousands of observation times. A DEMCMC is often composed of dozens of chains thousands of generations long requiring the model to be run hundreds of thousands of times. Thus for accurate error estimates, we expect to call the model millions of times, which is very computationally expensive. To reduce the computation time, the code is written in C, with consideration given for speed. In particular, since each DEMCMC chain calls the model once per generation, but only interacts with other chains at the very beginning of the step through selecting new parameters and the model computation time for each chain is very similar, the code is amenable to parallelization. We implement MPI to run up to 140 chains simultaneously computing the model and χ^2. The code then waits for all chains to finish the computation before continuing to the next step. The speedup with this method is nearly linear in the number of chains.

2.6 Comparison to Conventional TTV Techniques

As discussed in §1.5, conventional TTV fitting relies on matching a model to the measurements of individual transit times. In some cases, particularly for small, short-period planets, a transiting planet is only robustly detected by stacking many transits to get the required S/N for detection. Individual transits may have low S/N and thus uncertain timings.

In the case of *Kepler* data, the minimum total S/N for a planet to be considered a candidate was chosen to be 7.1σ (Jenkins, 2002; Tenenbaum et al., 2013). Over *Kepler*'s $\sim$1500 day observing window, a planet with a 3-day period may transit 500 times. If the planet

clearly passes the *Kepler* threshold limit with a robust 10-σ detection, then each individual transit would be detected at only $10^2/500 = 0.2\sigma$ confidence. This means each transit would be well below the noise level, making accurate determination of individual transit times difficult if not impossible as the transit may overwhelmed in the data by noise. However, since the photodynamic model fits all of the transit data at once, a given transit's position may be constrained by a combination of the physical model, and its temporally neighboring transits. Thus the model effectively bins the transits and the TTVs with a physical model simultaneously to extract accurate TTVs (and the planetary orbital parameters they imply) even if individual transits are difficult to measure. Photodynamics also allows self-consistent transit shape modeling – often the transit shape is held fixed to a globally found phased-transit value; however, if TTVs are not simultaneously taken into account the shape of the transit may be inferred to be more 'V' shaped than the true shape (Kipping, 2014).

Additionally, detecting other effects rather than simply transit timing are important for determining orbital properties of the planets. Transit duration variations (TDVs) indicate the transit chord of the planet changing across the face of the star. These TDVs (or the lack thereof) may be used to constrain the elusive mutual inclinations of planets since they are usually attributed to precession effects (see Miralda-Escudé, 2002; Pál & Kocsis, 2008; Sanchis-Ojeda et al., 2012; Carter et al., 2012; Mills & Fabrycky, 2017a). Because of the limb-darkening on the face of the star, transit chord changes may also lead to transit depth changes. Therefore the conventional method of simply extracting transit times to fit to a dynamical model may inadvertently discard important physical information. Additionally the transit fits themselves may not be sufficient if the transit is assumed to be constant, whereas a photodynamic model is fully self-consistent and directly fits the changing transit shape (if any) to the observational data.

CHAPTER 3

KEPLER-223

Surveys have revealed many multi-planet systems containing super-Earths and Neptunes in orbits of a few days to a few months (Mullally et al., 2015). There is debate whether in situ assembly (Hansen & Murray, 2013) or inward migration is the dominant mechanism of the formation of such planetary systems. Simulations suggest that migration creates tightly packed systems with planets whose orbital periods may be expressed as ratios of small integers (resonances, see Melita & Woolfson, 1996; Lee & Peale, 2002; Terquem & Papaloizou, 2007), often in a many-planet series (chain, see Cresswell & Nelson, 2006). In the hundreds of multi-planet systems of sub-Neptunes, more planet pairs are observed near resonances than would generally be expected (Fabrycky et al., 2014), but no individual system has hitherto been identified that must have been formed by migration. Proximity to resonance enables the detection of planets perturbing each other (Agol et al., 2005). Here we report transit timing variations of the four planets in the Kepler-223 system, model these variations as resonant-angle librations, and compute the long-term stability of the resonant chain. The architecture of Kepler-223 is too finely tuned to have been formed by scattering, and our numerical simulations demonstrate that its properties are natural outcomes of the migration hypothesis. Similar systems could be destabilized by any of several mechanisms (Cossou et al., 2014; Pu & Wu, 2015; Terquem & Papaloizou, 2007; Chatterjee & Ford, 2015), contributing to the observed orbital-period distribution, where many planets are not in resonances. Planetesimal interactions in particular are thought to be responsible for establishing the current orbits of the four giant planets in the Solar System by disrupting a theoretical initial resonant chain (Levison et al., 2011) similar to that observed in Kepler-223.

This chapter describes a dynamical model of the Kepler-223 (also known as KOI 730 and KIC 10227020) system and discuss its implication for planet formation and evolution. The four planets orbit a slightly evolved ($6.4^{+1.9}_{-1.7}$ Gyr) sun-like star as shown in §3.1. During the *Kepler* observing window, the ratios of orbital periods average $P_c/P_b = 1.3336$, $P_d/P_c =$

1.5015, and $P_e/P_d = 1.3339$, where the planets are named in alphabetic order from the interior (beginning with b, Lissauer et al., 2014).

3.1 Stellar Properties

The Kepler-223 star is positioned at RA=298°.318359, dec=47°.279491. It has a reported *Kepler* magnitude of 15.344 (Brown et al., 2011). Several photometric estimates of the properties of Kepler-223 have been made as part of attempts to determine stellar properties for the entire *Kepler* target sample (Rowe et al., 2014; Huber et al., 2014). However, stellar properties such as mass and radius derived from broadband photometry from the Kepler Input Catalog (KIC) have large uncertainties which can be the primary contributor to uncertainty in planetary radii. For example, photometric radii from the Kepler Input Catalog are uncertain at at the ∼35% level (Brown et al., 2011; Batalha et al., 2013; Burke et al., 2014). Stellar age is virtually unconstrained using broadband photometry.

In order to improve our knowledge of the Kepler-223 system, collaborators Howard Isaacson and Erik Petigura obtained a spectrum of the host star on 10 April 2012 using the HIRES spectrometer (Vogt et al., 1994) at the Keck-1 10 m telescope and performed a spectral fit. This data is now publicly available on CFOP (cfop.ipac.caltech.edu). Our spectrum has S/N = 14/pixel and a resolution of ∼60,000 at 5500Å. After normalizing the continuum, we model the observed spectrum using synthetic spectra. Model spectra are synthesized by interpolating within a grid of synthetic spectra from Coelho et al. (2005) that span a range of effective temperatures, $T_{\rm eff}$; surface gravities, $\log(g) = \log_{10} g$, where g is the surface gravity in cgs units; and metallicities, [Fe/H] (the logarithm of the ratio of iron to hydrogen in the star relative to that ratio in the sun). $T_{\rm eff}$, $\log(g)$, and [Fe/H] are adjusted in the model spectrum until it best matches the target spectrum in a χ^2 sense. We have assessed the precision of our spectral analysis technique by analyzing standard stars with well-measured properties from Huber et al. (2013a) and Valenti & Fischer (2005). The resulting spectroscopic parameters for Kepler-223 are $T_{\rm eff} = 5821 \pm 123$ K, $\log(g) = 4.070 \pm 0.096$ dex, and

[Fe/H] $= 0.060 \pm 0.047$ dex.

To determine an age and mass (and therefore radius and density combined with $\log(g)$) of the star, we match the measured properties to Y^2 isochrones (Demarque et al., 2004). The Y^2 isochrones give $\log(g)$ and $T_{\rm eff}$ as a function of age, mass, [Fe/H], $[\alpha/Fe]$, and Z (the fraction of metals in the star). We assume $[\alpha/Fe]$ is 0, i.e. that the enhancement of metals in Kepler-223 is similar to the Sun in composition, but not necessarily in total quantity. If we choose a value of [Fe/H] with fixed $[\alpha/Fe]$, Z is determined, so we are left with a vector-valued function of three variables: $f(age, M_\star, [\mathrm{Fe/H}]) = (\log(g), T_{\rm eff}, [\mathrm{Fe/H}])$. We use the interpolater provided with the Y^2 isochrones to form a grid in age from 0.01 to 15.00 Gyr with 0.01 Gyr steps for a given [Fe/H]. We then use a 2D linear interpolation of the grid to run a 2-parameter, 8-chain MCMC to estimate age and mass for that specific [Fe/H]. At each generation of the chain, the new values were accepted with a probability proportional to $\exp[((\chi^2_{\log(g)} + \chi^2_{T_{\rm eff}})_{old} - (\chi^2_{\log(g)} + \chi^2_{T_{\rm eff}})_{new})/2]$, where $\chi_i = (\mathrm{data_i} - \mathrm{model_i})/\mathrm{error_i}$. This formulation assumes a relatively smooth function compared to the grid size, but allows for the exploration of parameter space near the best-fit value in order to obtain uncertainty estimates.

$[\mathrm{Fe/H}]_i$ is gridded with a spacing of 0.01 to span several $[\mathrm{Fe/H}]_{err} = 0.047$ to ensure that we take into account the effects of [Fe/H] over its range of likely values. In order to obtain the final parameter distribution, we interpolate across the grid points in [Fe/H]. To do this, the relative importance of the distribution at each point in [Fe/H] space must be determined. A common method of determining the marginal likelihood of different models is to compare the harmonic means of the likelihoods of each distribution. This method is susceptible to failure in some cases due to the large variance of the harmonic mean, so we adopt a similar method which does not have this drawback (see eqn. 16 in Newton & Raftery, 1994). The

distribution at each [Fe/H] point is given a weight equal to

$$p_4 = \frac{\delta m/(1-\delta) + \sum_{i=1}^{m} \exp(-\chi_T^2/2)/(\delta p_4 + (1-\delta)\exp(-\chi_T^2/2))}{\delta m/(1-\delta)p_4 + \sum_{i=1}^{m} (\delta p_4 + (1-\delta)\exp(-\chi_T^2/2))^{-1}} \tag{3.1}$$

where m is a large integer, $\chi_T^2 = \chi_{T_{\rm eff}}^2 + \chi_{\log(g)}^2 + \chi_{\rm [Fe/H]}^2$ is computed from the MCMC run, δ is small, and p_4 is solved for iteratively. We compare this method with the 'Ratio Estimator' described in Ford & Gregory (2007), which is a method for computing marginal likelihoods based on importance sampling, and get consistent results. We report best-fit values and 1-sigma uncertainties using the weighted medians of the resulting distribution and the weighted values 15.865% away from the most extreme values. Our analysis gives age $= 6.3^{+1.8}_{-1.7}$ Gyr and mass $= 1.125^{+0.095}_{-0.073} M_\odot$ (see Figs. 3.1 and 3.2). Combining with $\log(g)$, we measure $R_\star = 1.54^{+0.21}_{-0.18} R_\odot$.

To determine the size of model-dependent uncertainties, we compare our results with an independently developed, publicly available method for computing $M_\star$, $R_\star$, and age using the Dartmouth isochrones (available at: https://github.com/timothydmorton/isochrones). All three values are consistent within the 1-σ error bars, so we conclude that our measurements are robust and model-dependent errors are small compared to our quoted uncertainties.

We use a stellar population synthesis model, TRILEGAL (Girardi et al., 2005), with default galaxy stellar distribution and population as described therein, to determine the expected mass distribution of single stars within 1 square degree on the sky of Kepler-223 between 15 and 16 Kepler magnitudes. The expected mass distribution is approximately symmetric, centered on $\sim 1.1 M_\odot$, and significantly broader than the mass estimate from stellar parameters alone. As a result, the best fit mass and error bars described above are essentially unaffected by reasonable priors, so we keep flat priors in all parameters.

Additionally, we consider that whether or not a given star was selected as *Kepler* target was primarily a function by stellar radius and apparent luminosity: smaller, brighter stars

Figure 3.1: Kepler-223 Isochrone Fit

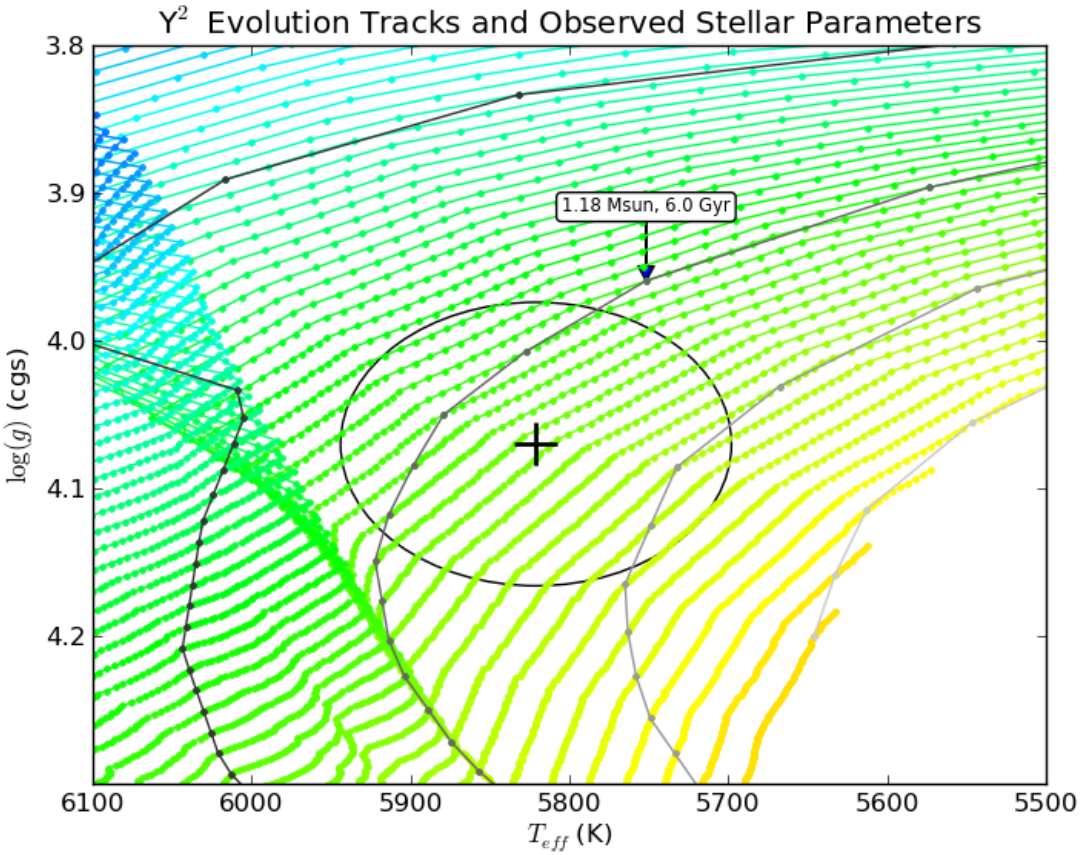

Yonsei-Yale Evolution Tracks with 0.01 Gyr increments marked with dots. Each color line corresponds to a different mass, in increments of 0.01 $M_{\odot}$ increasing from green to blue. Isochrones are over-plotted in 2 Gyr increments from 4 to 10 Gyr (dark gray in upper left to light gray in lower right) with each point representing a 0.01 $M_{\odot}$ increment. A point is labeled for reference. The best fit $T_{\rm eff}$ and $\log(g)$ value and 1-sigma uncertainty found from spectral matching are indicated with a black cross and oval. The stars in this area of parameter space have evolved off the main sequence.

Figure 3.2: Stellar Age and Mass Posteriors

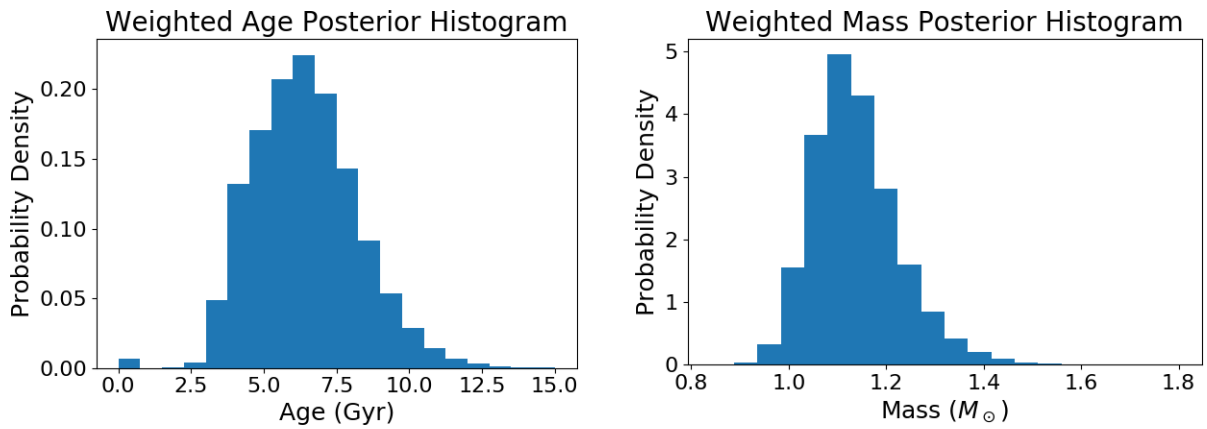

Age and mass posteriors obtained from fitting spectroscopically determined [Fe/H], $\log(g)$, and $T_{\rm eff}$ to Y^2 isochrone models.

were favored as they allow for easier detection of small planets (Batalha et al., 2010). Such selections were made with broadband photometry, notoriously poor at determining stellar radius (for instance Kepler-223 was estimated to be $\sim 30\%$ smaller than its true size (Brown et al., 2011)). We therefore hesitate to alter our stellar parameter posterior based on such effects, but point out that main sequence F, G, and K stars were the most common targets in the sample, and Kepler-223 lies in the middle of those spectral types, albeit slightly evolved. Thus we expect the prior to be at least moderately flat in the region of parameter space near Kepler-223 and don't expect dramatic changes in our stellar parameter posterior.

We derive an approximate distance of $2.29^{+0.34}_{-0.34}$ kpc to Kepler-223 by comparing our measurement of the star's intrinsic luminosity (based on spectroscopy and isochrone modeling) with its apparent V-band magnitude (Everett et al., 2012). Additionally, we use the computed intrinsic brightness distribution to estimate the flux received by the planets from the host star. We find $S_b = 492 \pm 47 S_0$, $S_c = 335 \pm 32 S_0$, $S_d = 195 \pm 19 S_0$, and $S_e = 133 \pm 13 S_0$, where $S_0 = 1377 W/m^2$ is the Earth's insolation.

3.2 Modeling Migration

Because of the low S/N and short observational window, the masses as well as the orbital parameters (especially the eccentricities and the arguments of pericenter) of Kepler-223's planets cannot be precisely constrained. Although the planets' periods are very near a chain of resonances, the part of the parameter space which corresponds to configurations acceptably fitting the data is much larger than that for stable, resonant systems. To demonstrate the plausibility of the physical existence of Kepler-223, we search for a formation scenario that results in a stable system which matches the data well.

We simulate the migration of 4 bodies which start outside of resonance into the 3:4:6:8 chain of periods that we observe following a simple model for incorporating planet-disk interactions into an N-body model (Goździewski & Migaszewski, 2014). Such a system is a natural outcome of disk migration: planets successively get trapped into resonant pairs as they migrate inward (Fig. 3.3). For this sequence of trapping to occur successfully, the planets must not migrate too fast to skip past the resonances, nor must the eccentricity excitation of a given resonance impede capture of successive ones or destabilize the system. The planetary migration is a physical process which depends on many parameters in a complex way. To model it realistically, one has to use sophisticated hydrodynamical codes (see, e.g., Masset & Snellgrove, 2001; Rein et al., 2010; Kley & Nelson, 2012). Such computations are time consuming and it is not yet possible to follow the evolution of a short-period, few-planet system in time-scales comparable to the disc lifetime, even for a single initial condition. Thus more computational tractable models are often used (Correa-Otto et al., 2013; Tadeu dos Santos et al., 2015).

As neither the initial orbits nor the disc properties which led to the currently observed configuration are known, one has to test many initial states. To do it effectively, we chose a simple model which has been employed before (Moore & Quillen, 2013). The drag force

Figure 3.3: Kepler-223 Resonant Configuration

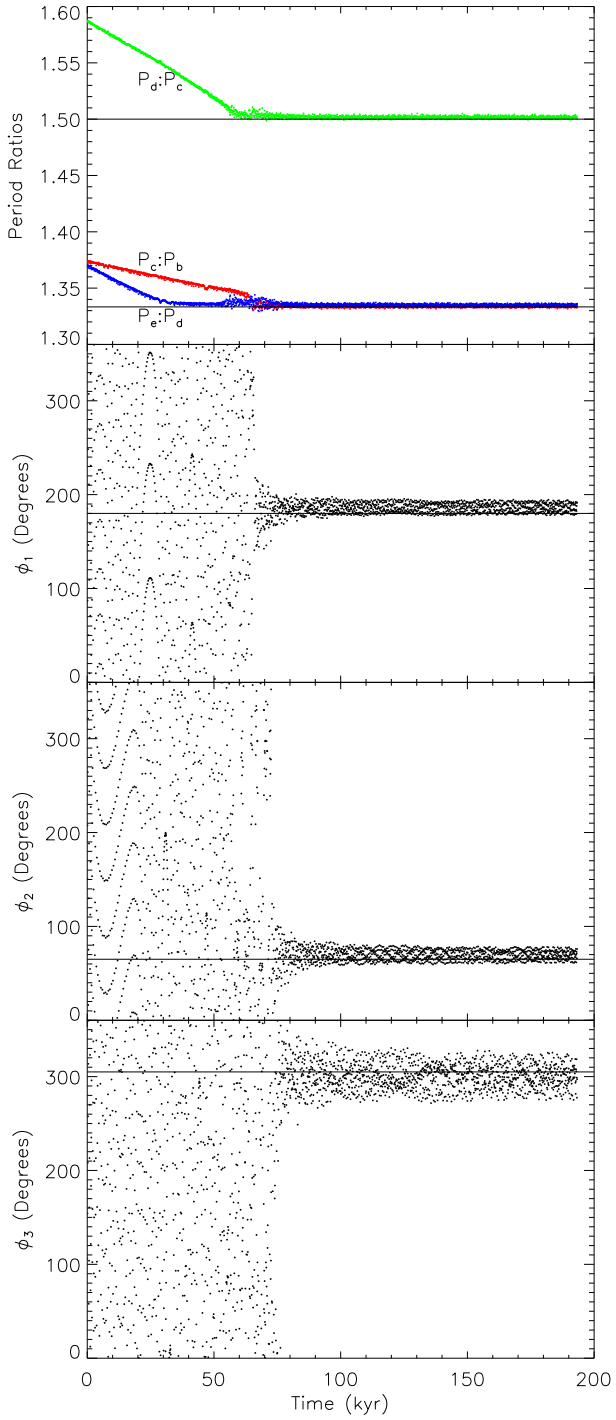

Top panel: Time evolution of period ratios of planets b and c (red), c and d (green) and d and e (blue). *Remaining panels:* Time evolution of the critical Laplace angles defined in the text.

acting on a planet moving with the astrocentric velocity $\vec{v}$ has the form

$$\vec{F} = -\frac{\vec{v}}{2\,\tau_a} - \frac{\vec{v} - \vec{v}_c}{\tau_e}, \tag{3.2}$$

where $\vec{v}_c$ is the velocity of the planet on a circular Keplerian orbit at a given radius r. The timescales of migration and circularization are denoted by τ_a and τ_e, respectively. In a physical treatment of the problem, they depend on disc properties as well as on the planets' masses and orbits. In the heuristic approach $\tau_e = K\,\tau_a$, where $K \in [1, 300]$ is a constant and

$$\tau_a = \tau_0 \left(\frac{m}{1\ M_\oplus}\right)^p \left(\frac{r}{1\,\mathrm{AU}}\right)^\alpha \exp\left(\frac{t}{T}\right), \tag{3.3}$$

where m is a planet mass, the power index p is either -1 (as in type I migration) or 0 (no mass dependence), $\alpha \in [-2, 0]$, t is time, and T is a time scale of disc depletion. Timescales are chosen from wide ranges, $\tau_0 \in [10^5, 10^7]\,\mathrm{yr}$, $T \in [10^6, 10^8]\,\mathrm{yr}$.

To start a single simulation, we choose values of the parameters described above from the following ranges. Masses of the planets are chosen from a range of $[1, 20]\,M_\oplus$. Initial orbits are circular, and the semi-major axes are chosen such that the periods ratios are above resonant values, i.e., initial P_2/P_1 and $P_4/P_3 \in [1.34, 1.4]$ and $P_3/P_2 \in [1.51, 1.6]$. The mean longitudes are chosen randomly from a whole range, $\lambda \in [0, 2\,\pi]$.

For an example initial system (e.g. Fig. 3.3), the migration of the planets is convergent, i.e., the period ratios of subsequent pairs of planets decrease in time. When P_{i+1}/P_i for a given pair reaches the resonant value, the planets get trapped in a MMR. When all three pairs are in 2-planet MMRs, ϕ_1, ϕ_2 and ϕ_3 start to librate. Using the fictitious force of Equation 3.2, it has been shown that continued migration may excite the liberation amplitudes of small planets and break the resonance (Goldreich & Schlichting, 2014). We do not commonly see such behavior in our migration simulations.

Once a given system fits the data qualitatively well (appropriate values of P_{i+1}/P_i and ϕ_i, $i = 1, 2, 3$), the formal measure of the goodness of the fit is computed. The simulation is done

in an arbitrary reference frame. To transform the orbits to the observational reference frame, one has to find an appropriate value of the argument of pericenter ω (all inclinations are $\pi/2$, and the longitudes of ascending nodes are 0), and the time in the simulation, t_0, which corresponds to a chosen reference epoch of the observations. Moreover, the sizes of orbits stemming from a simulation, $a_i^{(\mathrm{sim})}$, are, in general, different from the observational values, $a_i^{(\mathrm{obs})}$. Therefore, the system has to be scaled to best-fit the data. The three parameters to be fitted are ω, t_0 and $s \equiv a_i^{(\mathrm{obs})}/a_i^{(\mathrm{sim})}$. For each t_0 (varied with a step size equal to the period of the innermost planet), Powell's method is used to find (ω, s) which minimizes χ^2. The best-fitting solution matches the observed TTVs qualitatively well and is used as a starting point for the photodynamical modeling.

We also ran a series of migration simulations with more dispersed starting orbits ($a > 1$AU and $P_{i+1}/P_i > 2$). Our models found that for many starting conditions, planets got stuck in lower index, j, resonances than observed ($j = 1, 2$ instead of $j = 2, 3$ where the period ratio is specified by $(j+1)/j$). We then slightly expand our model by following Correa-Otto et al. (2013) to allow for planetary mass growth with time. With an appropriate choice of initial conditions and damping parameters, planets can frequently skip over such low resonances and become trapped in the 3:4:6:8 chain observed in Kepler-223 as their masses grow. As the disk forces exponentially decrease in the model we continue to integrate the equations of motion to ensure the system remains in resonance. We are able generate a stable system which approximately matches the observed transit timing variations.

We use the the critical Laplace angles to describe the behavior of the resonant chain: $\phi_1 \equiv -\lambda_b + 2\,\lambda_c - \lambda_d$ and $\phi_2 \equiv \lambda_c - 3\,\lambda_d + 2\,\lambda_e$ (for the mean longitudes, λ_i, for planets $i = b, c, d, e$) and for the whole system of four planets $\phi_3 \equiv 2\phi_2 - 3\phi_1 = 3\,\lambda_b - 4\,\lambda_c - 3\,\lambda_d + 4\,\lambda_e$. For the system to be considered a sufficient match to the data, the periods ratios must oscillate close to the nominal values, i.e., 4:3, 3:2, 4:3 for subsequent pairs of planets, and the resonant angles stay within a limited range around the values as seen in the observations (see Fig. 3.4) over a given time of a few hundred orbits. We find several migration solutions

that match this criteria (e.g., Fig. 3.3). In the simulations, these angles fluctuate on a range of timescales comparable to the length of the *Kepler* observing window, which can be observed as TTVs. We only briefly mention the feasibility of such a formation history here as a real planetary disk has much more complex disk structure, planet-disk interactions, and planet accretion physics involved that we do not examine in detail.

3.3 TTVs

Precise photometric data from *Kepler* has been used to identify this system in previous work (Borucki et al., 2011) although the low signal to noise at first caused an incorrect orbital period identification (Borucki et al., 2011; Lissauer et al., 2011b), and has hitherto precluded its detailed characterization. For this TTV analysis, we use *Kepler* long cadence (29.4 minute integrations) data, collected from March 2009 to May 2013. Given that Kepler-223 has planets in resonance, we strongly expect that it should exhibit time-variable transit times; however, no such detection has yet been reported. There are two possible reasons for this. First, many of the detections so far rely on planetary pairs that lie several percent off of resonance (Lithwick et al., 2012), such that the timescale of variation is smaller than the 4-year length of the *Kepler* dataset. In resonance, an analytic expression for the timescale of TTVs (Agol et al., 2005) predicts TTV signals to have a period of many years, so the variations over four years could be small enough to elude detection. Second, the small transit depth relative to the photometric uncertainties means post-Keplerian model parameters, such as variable transit times, are hard to constrain. Therefore, we first seek to characterize how the transit times vary over the dataset.

We begin by detrending the simple aperture photometry (SAP) flux data from the *Kepler* portal on the Mikulski Archive for Space Telescopes (MAST). For long-cadence data (*Kepler*

Figure 3.4: Long Term Period Ratio Distribution

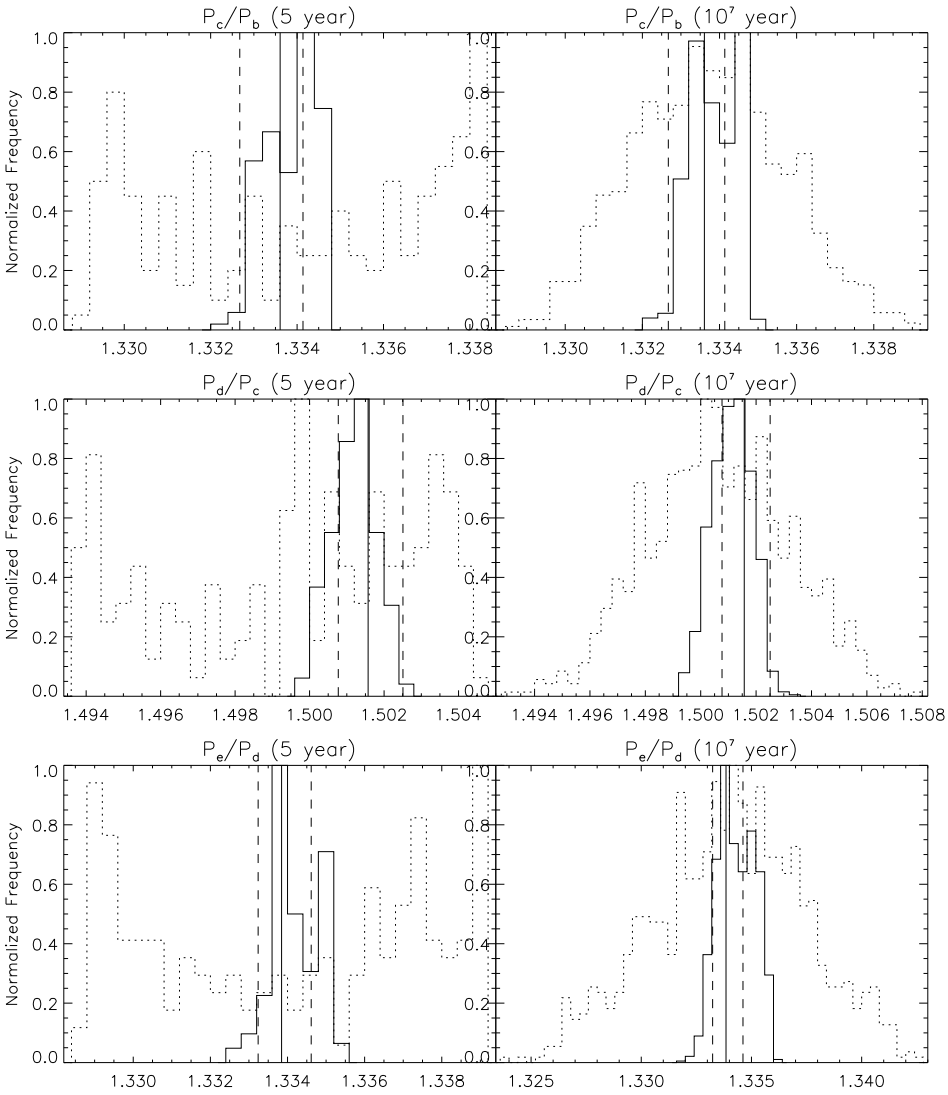

Left: The distribution of period ratios for each neighboring planet pair over a randomly selected 5 year window in the first 10^4 years for two 10^7-year stable parameter sets found in the $\mathcal{C}3$ DEMCMC posterior solution. The dotted histogram is for a solution which showed significant periods of Laplace angle circulation. The solid histogram is for a solution for which both ϕ_1 and ϕ_2 librate for 10^7 years. The mean period found in the data is represented by a vertical line, and dashed lines represent the highest and lowest quarter-to-quarter period measured. *Right:* The same as left panels, except over the entire 10^7 year interval. This demonstrates that the observed periods for the 4 planets match well with the expected range of observations for a resonant solution, even within only a relatively short observing window. Since the widths of the distributions of the resonant solution and the data is similar, we do not expect to see much larger TTV amplitudes than seen in the observing window, except if the planets enter an epoch of circulation.

quarters[1] 1-8), we fit the amplitudes of the first five cotrending basis vectors to determine a baseline. We discard points whose quality flag had a value greater than or equal to 16. For short-cadence data (*Kepler* quarters 9-17), cotrending basis vectors are not available; first we masked out the expected transit times, plus 20% of the full duration of each transit, intending to account for possible timing variations; then we fit a cubic polynomial model with a 2-day width centered within half an hour of each data point to determine its baseline. In both cases, the baseline is dominated by instrumental gains which are time-variable, thus we divide the flux by this baseline.

In computing TTVs and in the figures shown, we only use data for transits which do not overlap with another planetary transit, i.e., with two transit midtimes falling within 1 day of each other, according to a preliminary photodynamic model (see Fig. 3.5). The model shows that at the beginning of the dataset, planets b and e encroach on one another, which complicates every eighth transit of planet b and every third transit of planet e. Similarly, from the middle to the end of the dataset, planets c and d encroach on each other, compromising every third transit of planet c and every other transit of planet d. Even though data with overlapping transits is modeled directly by the photodynamic method described later; for now we remove it to ease the interpretation.

To determine transit times, we first fit transit parameters (P, T_0, $R_p/R_\star$, $T_{\rm dur}$, b, c_1, c_2) to the long-cadence dataset. Secondly, we divide the transit data into approximately 3 month segments based on the four observing quarters per year. We refit each quarter using the globally-determined values for all parameters except for T_0, which is solved for. Thus the whole dataset constrains the transit shape, whereas the model adjusts to fit the transit time locally. Thirdly, using these refined transit shape parameters, we slide the transit model in time through the data for each planet in each quarter, computing the goodness-

1. The *Kepler* data are divided into Q1-Q17. The star was dropped from the target list for Q4, but then the transiting planets were recognized and observations resumed. However, due to a failure of one of the CCD arrays, Q7, Q11, and Q15 are missing. Q1 and Q17 are shorter, and so we combine the data with their adjacent quarter for the analysis that is binned by quarter.

Figure 3.5: Model Quarterly Binned TTVs

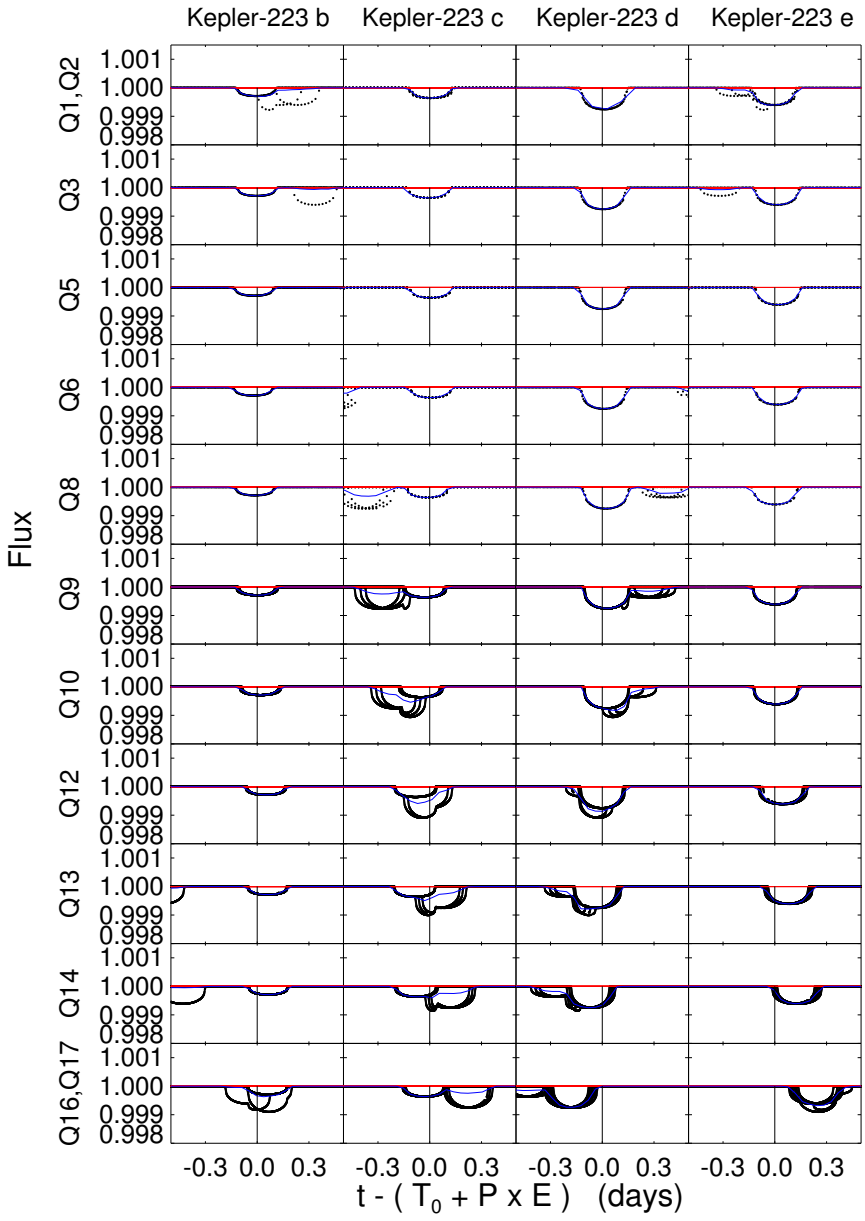

An example theoretical model of the lightcurve data shown in Fig. 3.6, broken down by quarter. Each panel is centered on the predicted transit time given a linear ephemeris matching that of Batalha et al. (2013); and the vertical black line under the red line indicates the mid-transit time in that case. We did not mask any transits for this example, showing that the transit shapes interfere with each other if they are not masked out; this led us to mask overlapping transits in Fig. 3.6.

of-fit statistic χ^2 in steps of 0.001 days. The values of that numerical χ^2 function which are within 1.0 of the minimum are fit with a parabola, the minimum of which we adopt as our best estimate of the mid-time. The time shift at which the χ^2 function rises to 1 and 9, evaluated on each side of the minimum, are adopted as narrow and conservative error bars. If the likelihood surface of the mid-time parameter were Gaussian, these values would correspond to 1-σ and 3-σ estimates. Table 3.1 reports the average time of the transits that were combined to make each measurement, the best-estimate, and uncertainty estimates of these time shifts. These data constitute our transit timing measurement, which does not depend of the photodynamical model we develop subsequently. We confirm the orbital periods are very close to true mean motion resonances, and detect clear TTVs (Figs. 3.6 and 3.7). Phase folding all of the long cadence data and removing TTVs allows the noisy transits to easily be identified by eye (Fig. 3.8).

These transit times are also represented graphically, in Fig. 3.6 as the horizontal error bar. We can see that the transits of planet d became almost half a duration earlier, whereas transits of planet e became more than half a duration later, during the dataset. Similarly, planet c has a clear fluctuation to earlier transits about midway through the dataset. These transit times guided our migration fits as described above. In order to make the connection, we take only the theoretical times which correspond to observed, non-overlapping transits used in the above analysis.

We use these transit times to estimate the Laplace critical angles (Quillen, 2011) and their evolution. To do so, note that for circular orbits the mean longitude λ is a linear function of time t, related to the transit period P and a specific mid-time T_0' as:

$$\lambda = 2\pi[1/4 + (t - T_0')/P]. \tag{3.4}$$

In place of T_0', we may use $T_0 + \Delta T_0$, where P and T_0 define the linear ephemeris on which

Figure 3.6: Measured Quarterly Binned TTVs

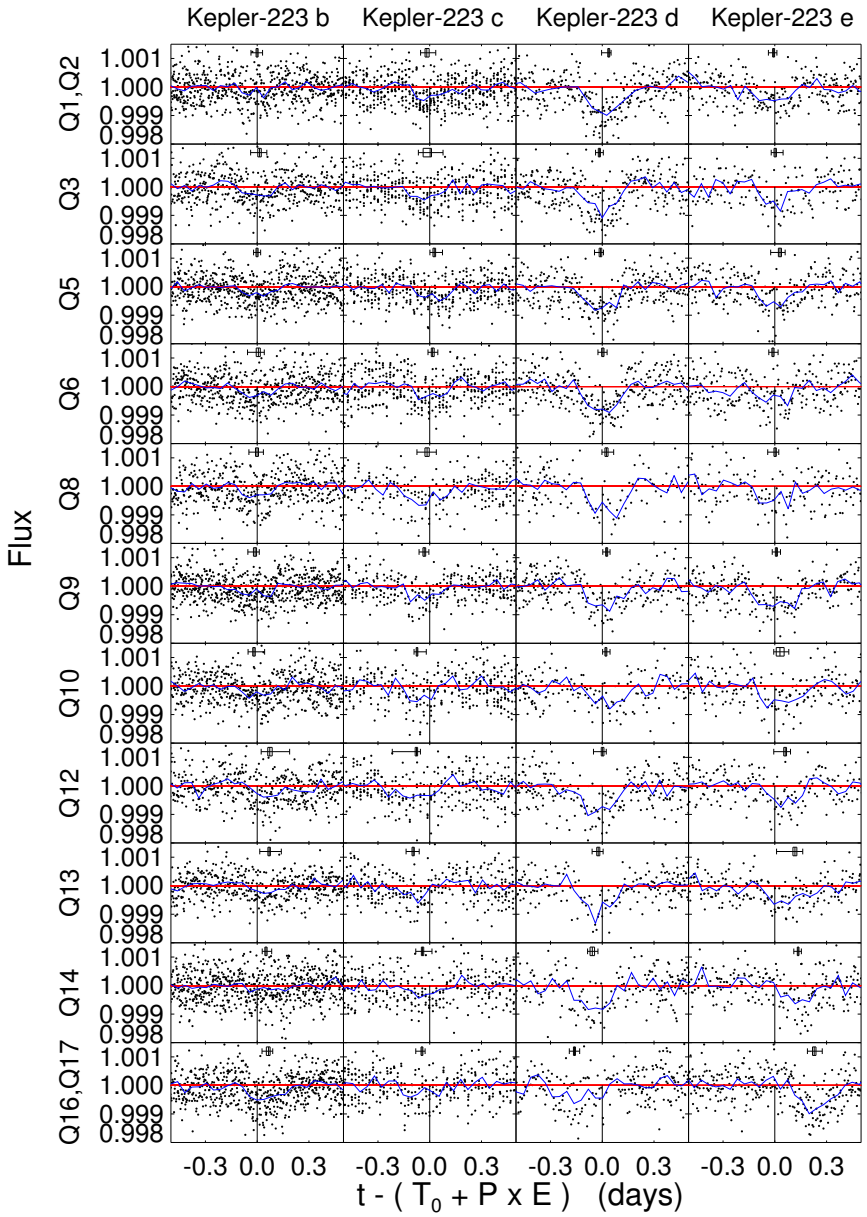

Long-cadence light curve for each planet, broken down by quarter. The data are binned together as the blue curve, to reduce the scatter and reveal the transits, against a horizontal red line showing no signal. Each panel is centered on the predicted transit time given a linear ephemeris matching that of Batalha et al. (2013); and the vertical black line under the red line indicates the mid-transit time in that case. On the other hand, the box and whisker error bars indicate the best-fit mid-transit time and estimates of 1 and 3 σ errors based on $\Delta\chi^2$ of 1 and 9. χ^2 values are computed by sliding an overall fit to the transit horizontally across the data and interpolating. Thus the difference in the placement of the vertical line and the box and whisker error bars shows the magnitude of the transit timing variations.

Figure 3.7: Photodynamically Measured TTVs

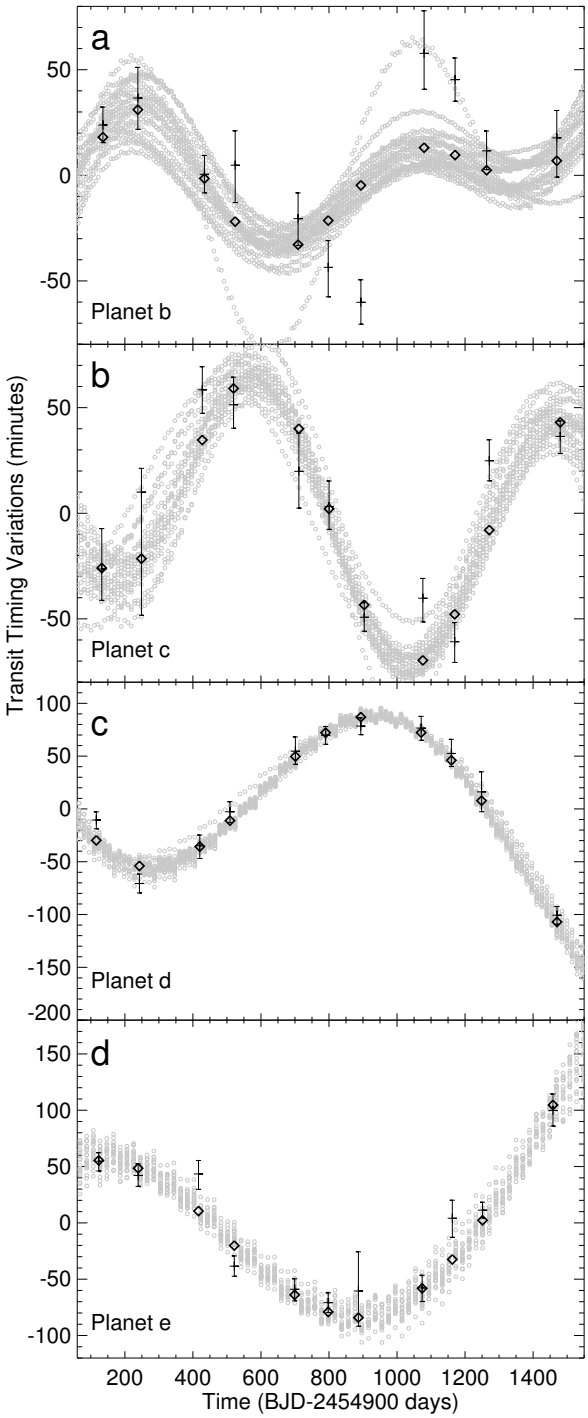

Transit timing variations for all four planets from innermost (panel a) to outermost (panel d) with respect to a linear ephemeris. Calculated transit times come from a linear regression of the best fit model transit times for the linear ephemeris and epoch. Open gray circles show the transit times from 20 different 10^7 year stable solutions drawn randomly from the $\mathcal{C}2$ DEMCMC posterior. Open black circles show the average of the gray circles. Black +s with 1-σ error bars indicate the TTVs found by fitting quarterly binned data (see Fig. 3.6), and black diamonds are the corresponding points for the black circle model binned in the same manner.

Figure 3.8: Kepler-223 Transits

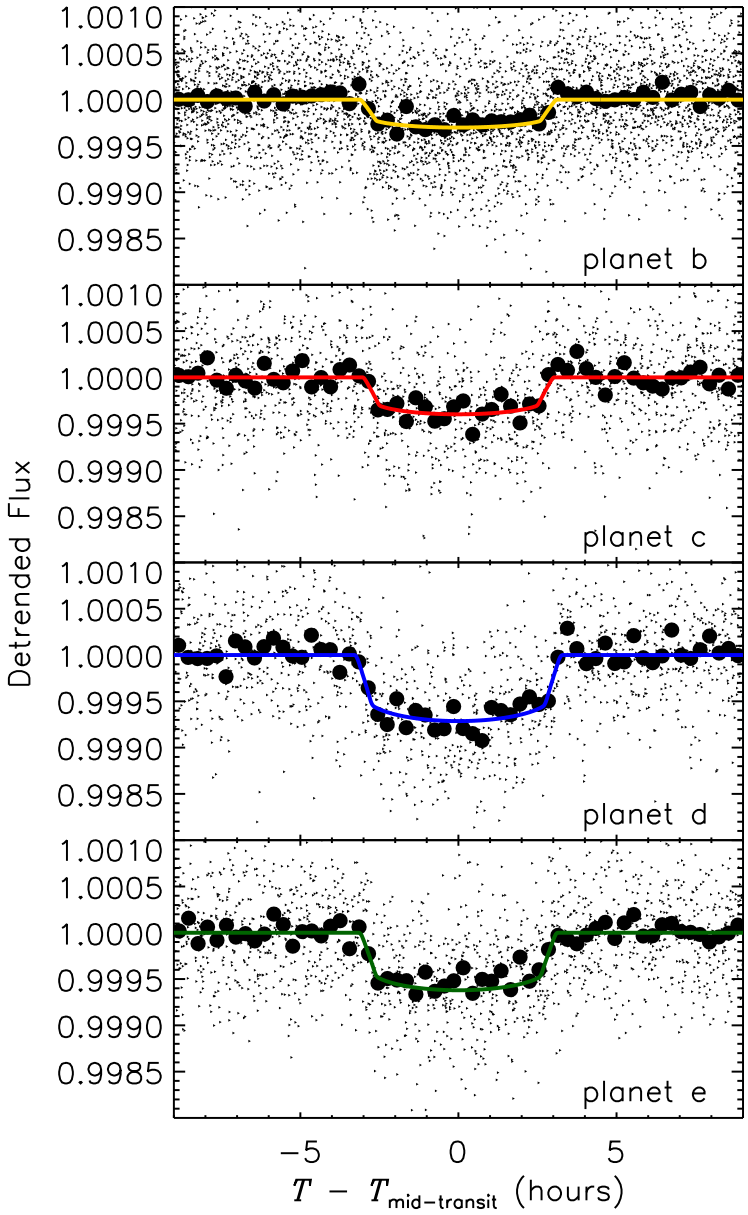

Transits of planet b (top) through e (bottom) binned together by phase-folding after removing the measured TTV for each quarter.

Table 3.1: Kepler-223 Quarterly Binned TTVs

$\bar{t} - 2454900$ (BJD)	-3σ	$-\sigma$	Best	$+\sigma$	$+3\sigma$
Kepler-223b: $P = 7.3840154$ *days,* $T_0 - 2454900$ *(BJD)* $= 70.49489$					
123.32662	-0.0354	-0.0058	-0.0006	0.0059	0.0316
239.02516	-0.0517	-0.0103	0.0137	0.0101	0.0423
416.51724	-0.0200	-0.0061	-0.0010	0.0062	0.0210
521.69775	-0.0628	-0.0123	0.0068	0.0113	0.0342
699.18988	-0.0470	-0.0088	-0.0010	0.0084	0.0370
797.79657	-0.0417	-0.0097	-0.0123	0.0088	0.0243
886.54260	-0.0343	-0.0072	-0.0187	0.0074	0.0617
1073.89526	-0.0500	-0.0118	0.0730	0.0140	0.1150
1162.64136	-0.0542	-0.0071	0.0692	0.0071	0.0708
1251.38745	-0.0217	-0.0062	0.0507	0.0065	0.0333
1458.46155	-0.0379	-0.0129	0.0659	0.0090	0.0241
Kepler-223c: $P = 9.8487130$ *days,* $T_0 - 2454900$ *(BJD)* $= 71.37624$					
116.10564	-0.0362	-0.0103	-0.0168	0.0133	0.0518
242.86336	-0.0683	-0.0405	0.0023	0.0077	0.0747
420.32413	-0.0254	-0.0077	0.0264	0.0076	0.0476
509.05453	-0.0266	-0.0077	0.0166	0.0090	0.0304
701.30371	-0.0585	-0.0121	-0.0155	0.0126	0.0535
790.03418	-0.0302	-0.0075	-0.0318	0.0084	0.0268
886.15869	-0.0173	-0.0046	-0.0737	0.0048	0.0537
1071.01367	-0.1404	-0.0078	-0.0766	0.0066	0.0226
1148.65283	-0.0411	-0.0067	-0.0959	0.0064	0.0349
1252.17163	-0.0392	-0.0067	-0.0418	0.0068	0.0548
1470.30054	-0.0361	-0.0056	-0.0449	0.0051	0.0179
Kepler-223d: $P = 14.7883997$ *days,* $T_0 - 2454900$ *(BJD)* $= 109.76775$					
132.10997	-0.0416	-0.0058	0.0376	0.0054	0.0134
248.65308	-0.0221	-0.0062	-0.0169	0.0063	0.0229
427.57138	-0.0351	-0.0084	-0.0099	0.0070	0.0169
519.49268	-0.0285	-0.0070	0.0035	0.0066	0.0245
711.54260	-0.0260	-0.0086	0.0240	0.0094	0.0420
800.18097	-0.0226	-0.0060	0.0256	0.0057	0.0194
898.66815	-0.0192	-0.0057	0.0212	0.0055	0.0238
1077.35193	-0.0530	-0.0080	0.0020	0.0077	0.0210
1169.50781	-0.0354	-0.0085	-0.0236	0.0093	0.0286
1271.27771	-0.0272	-0.0131	-0.0578	0.0132	0.0328
1483.43542	-0.0298	-0.0061	-0.1612	0.0057	0.0302
Kepler-223e: $P = 19.7213435$ *days,* $T_0 - 2454900$ *(BJD)* $= 68.10686$					
135.47421	-0.0303	-0.0060	-0.0067	0.0053	0.0187
238.21753	-0.0232	-0.0067	0.0022	0.0072	0.0458
433.78842	-0.0542	-0.0095	0.0302	0.0084	0.0298
524.27625	-0.0244	-0.0061	-0.0106	0.0063	0.0296
709.21222	-0.0432	-0.0071	0.0022	0.0065	0.0208
797.82037	-0.0240	-0.0060	0.0090	0.0061	0.0240
893.81256	-0.0357	-0.0216	0.0297	0.0242	0.0513
1079.88989	-0.0662	-0.0083	0.0602	0.0078	0.0308
1170.71301	-0.1067	-0.0118	0.1167	0.0110	0.0453
1263.01343	-0.0252	-0.0049	0.1352	0.0049	0.0188
1469.48169	-0.0393	-0.0097	0.2283	0.0100	0.0467

TTVs for each planet found by binning the data quarterly and iteratively solving for transit shape as described in the text. Mean transit time in the quarter is given in the first column followed by the measured TTV and uncertainties.

the quarterly ΔT_0 of Table 3.1 are based. Then for Laplace's critical angles we have:

$$\begin{aligned}
\phi_1 &= 2\lambda_c - \lambda_b - \lambda_d, && (3.5)\\
&= 2\pi\{\frac{-2T'_{0c}}{P_c} + \frac{T'_{0b}}{P_b} + \frac{T'_{0d}}{P_d} + t(\frac{2}{P_c} - \frac{1}{P_b} - \frac{1}{P_d})\}, && (3.6)\\
&= 2\pi\{0.4750 + 2.39834 \times 10^{-5}(t - 2454900BJD) - \frac{2\Delta T_{0c}}{P_c} + \frac{\Delta T_{0b}}{P_b} + \frac{\Delta T_{0d}}{P_d}\} && (3.7)
\end{aligned}$$

and similarly,

$$\begin{aligned}
\phi_2 &= \lambda_c - 3\lambda_d + 2\lambda_e, && (3.8)\\
&= 2\pi\{-\frac{T'_{0c}}{P_c} + \frac{3T'_{0d}}{P_d} - \frac{2T'_{0e}}{P_e} + t(\frac{1}{P_c} - \frac{3}{P_d} + \frac{2}{P_e})\}, && (3.9)\\
&= 2\pi\{0.1135 + 8.7366 \times 10^{-5}(t - 2454900BJD) - \frac{\Delta T_{0c}}{P_c} + \frac{3\Delta T_{0d}}{P_d} - \frac{2\Delta T_{0e}}{P_e}\} && (3.10)
\end{aligned}$$

These values are plotted in Fig 3.9. We see that assuming nearly circular orbits, the four years of data have recorded angle ϕ_1 performing nearly a full oscillation between the values $\sim 173^\circ$ and $\sim 190^\circ$, and ϕ_2 sweeping between $\sim 47^\circ$ and $\sim 75^\circ$. These specific values are sensitive to phase shifts due to eccentricity; the libration centers may be different by about 30° if the eccentricities are as high as 0.1.

The degree to which this transit analysis faithfully reproduces the actual Laplace angles was investigated using the migration simulations. In such simulations, we have access to the mean anomalies directly, and can compare the Laplace angles' true values (equations 3.5 and 3.8) with their transit-phase approximations (equations 3.6 and 3.9). We find that orbital eccentricity shifts the libration centers by about 30° for an eccentricity of 0.1, and the shift is linear in $e\cos\omega$. This is about the accuracy to which this method measures the libration centers. We also notice in Fig. 3.9 that a minimum and maximum value are obtained, suggesting the libration amplitudes have been measured to be $\sim 8^\circ$ and $\sim 14^\circ$ for ϕ_1 and ϕ_2 respectively. These particular values are subject to the assumption that the eccentricities of the planets have not precessed appreciably during the dataset. Indeed, we

Figure 3.9: Measured Quarterly Binned Laplace Angles

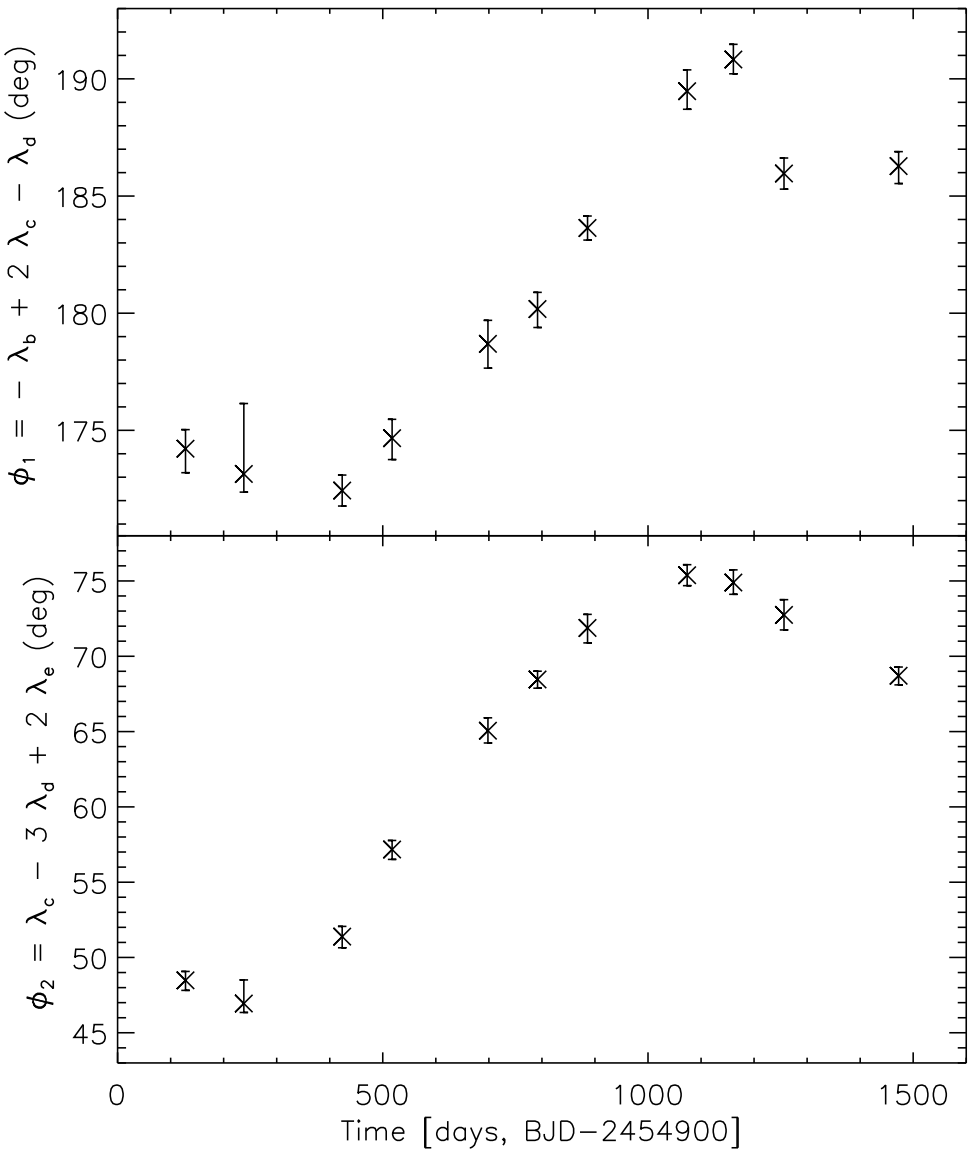

Laplace angle librations detected by binning transits into quarters and assuming 0 eccentricity. Almost an full libration cycle is observed in the ∼1500 day observing window.

expect the timescale of precession due to the resonance to considerably exceed the resonant libration timescale. Therefore we believe these amplitudes are good approximations of the true libration amplitudes.

3.4 Photodynamic Modeling

To improve the treatment of the TTV signal and to make a direct connection to planetary dynamics, we integrate the N-body equations of motion of the multi-planet system and directly model the photometric transit signals (Carter et al., 2012) using long and short cadence (58.8 second integrations) where available. We use a differential evolution Markov chain Monte Carlo (DEMCMC) coupled to this photodynamic model to estimate the parameters of the system. Such an approach allows chains of parameter values to probabilistically explore parameter space in order to converge on best-fit values with uncertainty estimates, even in the event of highly-correlated parameters (Ter Braak, 2005). We report system parameters of particular interest in Table 3.2, and describe our methodology below.

3.4.1 Fixed Parameters

Photodynamics can generally only determine densities and relative masses, except in cases where the very precise measurement of transit times allows the light travel time effect (LITE) to break the scale degeneracy. The low S/N of this system does not provide such accuracy. In order to prevent the DEMCMC chains from wandering unbounded as they adjusted the scale of the system, the mass of the star was held fixed. Masses, radii, and semi-major axes of all other bodies found by photodynamics can be scaled appropriately to the system once the true mass of any object (usually the star) is known from other means, such as radial velocity measurements, asteroseismology, or spectral fitting. That is, if the true mass of the star is different than the fixed value chosen, one need only scale the remaining parameters appropriately, and all discussion and stability arguments will still hold true. We report

Table 3.2: Select Kepler-223 Parameter Posteriors

Parameter Name (Unit)	DEMCMC Result
Spectroscopic Stellar Mass ($M_\odot$)	$1.125^{+0.094}_{-0.073}$
Stellar Radius ($R_\odot$)	$1.72^{+0.07}_{-0.14}$
Kepler-223 b Parameters:	
P (d)	$7.38449^{+0.00022}_{-0.00022}$
e	$0.078^{+0.015}_{-0.017}$
$\lvert i-90\rvert$ (°)	$0.0^{+1.8}$
M (M_{Earth})	$7.4^{+1.3}_{-1.1}$
R (R_{Earth})	$2.99^{+0.18}_{-0.27}$
ρ (g/cm^3)	$1.54^{+0.63}_{-0.35}$
Kepler-223 c Parameters:	
P (d)	$9.84564^{+0.00052}_{-0.00051}$
e	$0.150^{+0.019}_{-0.051}$
$\lvert i-90\rvert$ (°)	$0.0^{+1.3}$
M (M_{Earth})	$5.1^{+1.7}_{-1.1}$
R (R_{Earth})	$3.44^{+0.20}_{-0.30}$
ρ (g/cm^3)	$0.71^{+0.33}_{-0.20}$
Kepler-223 d Parameters:	
P (d)	$14.78869^{+0.00030}_{-0.00027}$
e	$0.037^{+0.018}_{-0.017}$
$\lvert i-90\rvert$ (°)	$2.06^{+0.26}_{-0.32}$
M (M_{Earth})	$8.0^{+1.5}_{-1.3}$
R (R_{Earth})	$5.24^{+0.26}_{-0.45}$
ρ (g/cm^3)	$0.31^{+0.12}_{-0.07}$
Kepler-223 e Parameters:	
P (d)	$19.72567^{+0.00055}_{-0.00054}$
e	$0.051^{+0.019}_{-0.019}$
$\lvert i-90\rvert$ (°)	$2.00^{+0.21}_{-0.27}$
M (M_{Earth})	$4.8^{+1.4}_{-1.2}$
R (R_{Earth})	$4.60^{+0.27}_{-0.41}$
ρ (g/cm^3)	$0.28^{+0.12}_{-0.08}$

Medians and 68% credible intervals for 2008 10^6-year stable solutions randomly drawn the $\mathcal{C}1$ DEMCMC posterior with the eccentricity prior as described in the text, $(e_{b,max}, e_{c,max}, e_{d,max}, e_{e,max}) = (0.212, 0.175, 0.212, 0.175)$, fixed $\Omega_j = 0$ for $j = b, c, d, e$. All values are valid at $T_{epoch} = 800.0$ (BJD-2454900). The stellar mass was held fixed in the DEMCMC simulation but uncertainties in planet mass were adjusted afterward to account for the quoted spectroscopic uncertainty in $M_\star$. See Table 3.3 for additional parameters.

values in Table 3.3 with the spectroscopic-best-fit stellar mass. We compute the expected spectroscopic radius, $R_\star = 1.54^{+0.21}_{-0.18} R_\odot$ as described above and add it as a data point to the DEMCMC since it better constrains the radius of the star for a fixed mass than transits alone.

The limb darkening coefficients were found to be degenerate given the low S/N of the transits; therefore, c_2 was held fixed while c_1 was allowed to float. The value for c_2 was chosen as 0.2 as this is near the median value for stars in the 4000K to 6500K range in the Kepler bandpass (Sing, 2010). It has been shown that having only one free limb darkening parameter is sufficient to match Kepler photometry reasonably well, although the best fit for the free parameter may differ from the value found if both c_1 and c_2 are allowed to float (Southworth et al., 2007; Southworth, 2008).

For practical reasons we do not attempt to constrain the differences in Ω through DEMCMC. Since the time span of the data is relatively short compared to the timescale of precession, the duration change even for highly misaligned planets is small, and the DEMCMC offers almost no constraint on mutual inclinations. If we do attempt to fit the Ωs, it takes the DEMCMC much longer to converge as there is a much larger and more complex volume of parameter space than the nearly coplanar case, and we are offered essentially no additional information about the system at the cost of vastly more computing time and real time. We note that the typical mean mutual inclination (MMI) of *Kepler* systems, $\sim 1.8°$, implies near coplanarity (Fabrycky et al., 2014). Additionally, multiplanet systems with higher mutual inclinations between planetary orbital planes are correlated with instability (Veras & Armitage, 2004), and we expect any observed system to be at least quasi-stable.

The low S/N also does not allow for photometric constraint of dilution of the primary star's light from contamination from nearby sources. Increased dilution is highly degenerate with an increase in the radius of all planets along with a slight change in limb darkening coefficients to alter the transits' shapes appropriately. Uncertainty in dilution is a major source of planet radius uncertainty in *Kepler* systems (Ciardi et al., 2015). United Kingdom

Table 3.3: Full Kepler-223 DEMCMC Posteriors

Parameter Name (Unit)	Eccentricity Prior ($\mathcal{C}1$)	Eccentricity Prior and Stability ($\mathcal{C}2$)	Laplace Angle Constraint ($\mathcal{C}3$)
Stellar Parameters:			
$R_\star(R_\odot)$	$1.716^{+0.077}_{-0.15}$	$1.72^{+0.07}_{-0.14}$	$1.622^{+0.078}_{-0.070}$
$M_\star(M_\odot)$	1.125 (fixed)	1.125 (fixed)	1.125 (fixed)
c_1	$0.54^{+0.10}_{-0.10}$	$0.54^{+0.10}_{-0.09}$	$0.57^{+0.11}_{-0.10}$
c_2	0.2 (fixed)	0.2 (fixed)	0.2 (fixed)
dilution	0.11202 (fixed)	0.11202 (fixed)	0.11202 (fixed)
Kepler-223 b Parameters:			
P (d)	$7.38454^{+0.00024}_{-0.00027}$	$7.38449^{+0.00022}_{-0.00022}$	$7.38453^{+0.00024}_{-0.00024}$
T_0 (BJD-2454900)	$801.5144^{+0.0044}_{-0.0046}$	$801.5155^{+0.0044}_{-0.0046}$	$801.5133^{+0.0042}_{-0.0045}$
$e \cdot \cos(\omega)$	$0.057^{+0.033}_{-0.029}$	$0.054^{+0.022}_{-0.022}$	$0.035^{+0.014}_{-0.016}$
$e \cdot \sin(\omega)$	$0.053^{+0.026}_{-0.12}$	$0.047^{+0.020}_{-0.039}$	$-0.004^{+0.029}_{-0.034}$
$\lvert i-90\rvert$ (°)	$0.0^{+1.7}$	$0.0^{+1.8}$	$0.0^{+1.4}$
Ω (°)	0.0 (fixed)	0.0 (fixed)	0.0 (fixed)
$M/M_\star$	$0.0000195^{+0.0000033}_{-0.0000030}$	$0.0000221^{+0.0000032}_{-0.0000031}$	$0.0000201^{+0.0000027}_{-0.0000026}$
$R/R_\star$	$0.01595^{+0.00053}_{-0.00053}$	$0.01597^{+0.00055}_{-0.00054}$	$0.01584^{+0.00052}_{-0.00053}$
Kepler-223 c Parameters:			
P (d)	$9.84582^{+0.00084}_{-0.00051}$	$9.84564^{+0.00052}_{-0.00051}$	$9.84613^{+0.00046}_{-0.00045}$
T_0 (BJD-2454900)	$800.1460^{+0.0049}_{-0.0040}$	$800.1459^{+0.0050}_{-0.0039}$	$800.1489^{+0.0061}_{-0.0047}$
$e \cdot \cos(\omega)$	$0.030^{+0.049}_{-0.045}$	$0.029^{+0.041}_{-0.038}$	$-0.010^{+0.019}_{-0.022}$
$e \cdot \sin(\omega)$	$0.135^{+0.026}_{-0.14}$	$0.139^{+0.021}_{-0.050}$	$0.060^{+0.033}_{-0.038}$
$\lvert i-90\rvert$ (°)	$0.0^{+1.4}$	$0.0^{+1.3}$	$0.0^{+1.5}$
Ω (°)	0.0 (fixed)	0.0 (fixed)	0.0 (fixed)
$M/M_\star$	$0.0000156^{+0.0000047}_{-0.0000037}$	$0.0000152^{+0.0000048}_{-0.0000033}$	$0.0000189^{+0.0000032}_{-0.0000033}$
$R/R_\star$	$0.01846^{+0.00054}_{-0.00055}$	$0.01842^{+0.00053}_{-0.00053}$	$0.01833^{+0.00056}_{-0.00057}$
Kepler-223 d Parameters:			
P (d)	$14.78881^{+0.00048}_{-0.00039}$	$14.78869^{+0.00030}_{-0.00027}$	$14.78862^{+0.00025}_{-0.00024}$
T_0 (BJD-2454900)	$804.8502^{+0.0022}_{-0.0023}$	$804.8504^{+0.0023}_{-0.0024}$	$804.8492^{+0.0022}_{-0.0023}$
$e \cdot \cos(\omega)$	$0.021^{+0.031}_{-0.029}$	$0.020^{+0.026}_{-0.024}$	$0.000^{+0.011}_{-0.013}$
$e \cdot \sin(\omega)$	$0.017^{+0.022}_{-0.069}$	$0.010^{+0.020}_{-0.032}$	$-0.001^{+0.015}_{-0.021}$
$\lvert i-90\rvert$ (°)	$2.02^{+0.29}_{-0.49}$	$2.06^{+0.26}_{-0.32}$	$1.68^{+0.30}_{-0.29}$
Ω (°)	0.0 (fixed)	0.0 (fixed)	0.0 (fixed)
$M/M_\star$	$0.0000201^{+0.0000040}_{-0.0000038}$	$0.0000240^{+0.0000039}_{-0.0000035}$	$0.0000225^{+0.0000032}_{-0.0000032}$
$R/R_\star$	$0.02791^{+0.00055}_{-0.00064}$	$0.02800^{+0.00052}_{-0.00059}$	$0.02756^{+0.00053}_{-0.00058}$
Kepler-223 e Parameters:			
P (d)	$19.72552^{+0.00068}_{-0.00070}$	$19.72567^{+0.00055}_{-0.00054}$	$19.72568^{+0.00054}_{-0.00048}$
T_0 (BJD-2454900)	$817.5230^{+0.0054}_{-0.0048}$	$817.5237^{+0.0055}_{-0.0051}$	$817.5231^{+0.0053}_{-0.0046}$
$e \cdot \cos(\omega)$	$0.017^{+0.042}_{-0.032}$	$0.017^{+0.026}_{-0.024}$	$0.013^{+0.014}_{-0.014}$
$e \cdot \sin(\omega)$	$0.045^{+0.031}_{-0.066}$	$0.039^{+0.023}_{-0.032}$	$0.033^{+0.016}_{-0.023}$
$\lvert i-90\rvert$ (°)	$1.95^{+0.24}_{-0.44}$	$2.00^{+0.21}_{-0.27}$	$1.69^{+0.25}_{-0.24}$
Ω (°)	0.0 (fixed)	0.0 (fixed)	0.0 (fixed)
$M/M_\star$	$0.0000101^{+0.0000043}_{-0.0000041}$	$0.0000145^{+0.0000039}_{-0.0000036}$	$0.0000130^{+0.0000031}_{-0.0000029}$
$R/R_\star$	$0.02448^{+0.00075}_{-0.00075}$	$0.02466^{+0.00074}_{-0.00076}$	$0.02421^{+0.00069}_{-0.00068}$

DEMCMC posterior probability estimates and uncertainties for all model parameters at $T_{epoch} = 800.0$ (BJD-2454900). Three parameter sets are given with fixed stellar mass: (1) DEMCMC results with eccentricity constraint $\mathcal{C}1$ as described in the text, (2) A subset of the $\mathcal{C}1$ DEMCMC results that only retain solutions stable for 10^6 years and (3) Laplace angle constraint $\mathcal{C}3$ as described in the text and fixed $\Omega_i = 0$ for $i = b, c, d, e$. The first column is similar to the table which appears in the main text, except with all parameters kept in ratio form.

Infrared Telescope (UKIRT) archives reveal that there are 2 objects within 2" of the position specified by the KIC (Brown et al., 2011). The brighter of the 2 objects has a distance < 0.2" from the KIC position and has a predicted *Kepler* magnitude of 15.4932, based on UKIRT's formula to convert their measured J band magnitudes to a *Kepler* magnitude (Howell et al., 2012). This value is 0.1492 magnitudes fainter than that reported in the KIC (15.344). The second object is 1.937" away from the KIC location, but is $\sim$8 times fainter. The sum of these two objects has a predicted intensity in the *Kepler* bandpass equal to 98.2% of the intensity of the object reported in the KIC. The next nearest object is part of a stellar pair which comprises KIC 10227024. Faulkes Telescope North (FTN) imaging confirms the dual nature of the Kepler 223 object, and the nearby KIC 10227024 pair (Brown et al., 2013). Speckle imaging done at WIYN observatory indicate no additional bodies between approximately 0.2" and 1.9" of the brighter object (Howell et al., 2011). The secondary source could be a distant background star or galaxy, faint foreground star, or could potentially be a gravitationally bound binary. The projected physical separation of two objects $\sim$2" apart at Kepler-223's distance is thousands of AU. If the fainter source was a binary companion with any modest eccentricity, it would not gravitationally perturb Kepler-223's planets significantly. While the hypothetical binary could in principle have high eccentricity ($e\sim0.99$), such an extreme configuation is unlikely and would probably now allow the observed tightly-packed system to remain stable. Therefore we do not include the dynamical effects of any additional stars, but do include the effects of its light in DEMCMC runs. The fainter of the two objects contributes approximately 11.202% of the light in the *Kepler* bandpass so we fix diluation at 0.11202 in the DEMCMC runs. This value has an uncertainty of several percent, but the error in determining true planet radius is dominated by uncertainties in stellar radius. Compared to an analysis without dilution included (dilution=0), the radii of the planets should be scaled by the factor $(1 - 0.11202)^{-1/2} \approx 1.06$. A small change in implied planet density would also result. The other values affected by ignoring the dilution measurement are only stellar limb darkening, which is essentially a nuisance parameter in

this analysis, and possibly impact parameter, i.e. inclination, which will have a negligibly small effect on predicted stellar radius due to its correlation in determining transit duration.

3.4.2 Consideration of the Planets' Host Star

Thus far we have assumed that the Kepler-223 planetary system's host star is the brighter of the two objects identified as KIC 10227020. Here we examine the possibility that the fainter star hosts the planets, and find it disfavored. Such an alternative would not alter our main conclusions about resonance, timing variations, and migration, but it would change the planetary masses and radii, altering our interpretation of the physical composition of the planets. The observed change in flux due to planetary transits must be constant regardless of which object the planets are transiting. Since the fraction of flux blocked by a planet transit is $(R_p/R_\star)^2$ and we know the ratio of the flux from the fainter object to the total flux, $c \approx 0.13$, we may write

$$\Big(\frac{r_A}{R_A}\Big)^2 = c\Big(\frac{r_B}{R_B}\Big)^2 \tag{3.11}$$

where R and r denote stellar and planet radii respectively and the subscripts A and B refer to the brighter and fainter of the two observe stars respectively. That is, the observed planet radii would differ from their currently inferred radius, r_A, by a factor $\sqrt{c} \cdot R_B/R_A$ if B is the true host star of Kepler-223's planets. The relative observed fluxes of the two stars implies

$$\frac{R_B^2 L_{Kep,B}}{d_B^2} = c\frac{R_A^2 L_{Kep,A}}{d_A^2} \tag{3.12}$$

where L_{Kep} is the luminosity in the *Kepler* bandpass and d is the distance to the star. We use standard mass-luminosity and mass-radius relations for main sequence (MS) stars and bolometric correction factors (Cox, 2000) and normalize the distances and radii to star A in order to get R_B as a function only of d_B, taking into account the fact that A is no longer on the main sequence and is ~ 2.5 times more luminous due to an increased radius. Thus for any given distance of the fainter star, there is a unique MS radius which matches the observations.

This method takes into account changes in both surface brightness and size of the stars. For instance, if the pair is bound and thus $d_A \approx d_B$, then $R_B/R_A \sim 0.6 \Rightarrow R_B \sim 1.0 R_\odot$. Such a radius for B implies a planetary radius larger by a factor of $0.6\sqrt{c} \sim 1.5$, while the mass of the planets would be marginally less since the planet-star mass ratios as found in our analysis would be unchanged, but smaller radii stars are lower in mass. Very low density planets with relatively small radii are uncommon (Weiss & Marcy, 2014). Therefore the scenario that A and B are a wide binary but the planets orbit the dimmer of the two stars is modestly disfavored. However, in the case the planets do orbit B, the scenario of gaseous/ice-rich planets migrating into resonance is unchanged.

Background stars would increase in radius and brightness as a function of distance to match observations and exacerbate the low-density planet problem. Therefore we more strongly disfavor star B as the planet host if it is a large background star. A small star in the foreground could potentially host similar or smaller radii planets than star A as its flux per unit area would be much greater than the distant star despite its cooler temperature. We use TRILEGAL with default galaxy parameters (Girardi et al., 2005) and a simple mass-radius scaling law ($R_\star = M_\star^{0.8}$ for $M < 1$ and $R_\star = M_\star^{0.57}$ for $M > 1$ in solar units) to determine that in the direction of Kepler-223 stars between the Kepler magnitudes 17 and 18 have a radius distribution $R = 0.92^{+0.12}_{-0.14} R_\odot$. This suggests that a foreground star is probably large enough that the planets of the Kepler-223 system would still need a massive gaseous atmosphere to match the observed transit depths, again keeping the low-density plnaet migration picture in tact. This analysis ignored evolved stars because evolved stars exist for only a fraction of the lifetimes of MS stars, except stellar remnants. However, to date, no planets have been found around white dwarfs (WDs), the only stellar remnant bright enough to fit the observations. Additionally, a protoplanetary disk necessary for migration into resonance is unlikely to be found around a WD. In summary, the most plausible option is that the planets do indeed orbit star A, the brighter of the two KIC 10227020 objects discussed throughout the paper, but the dynamics of the system are insensitive to this result

regardless.

3.4.3 Eccentricity Priors

Initial DEMCMC runs had unrestricted eccentricities with a uniform prior on $e\cos(\omega)$ and $e\sin(\omega)$ from 0 to 1. The chains in these DEMCMC runs explored low eccentricity parameter space relatively rapidly, but had occasional excursions to high eccentricity ($e \gtrsim 0.3$) parameter space. Some solutions with high eccentricity acceptably fit the observed data despite planetary orbits that crossed the semi-major axis of one or more neighboring planets. The *Kepler* data lone could not rule out such orbits since the observing window is much shorter than the lifetime of the system, and the resonant behavior prevents immediate destruction of the system by precluding close encounters on the time scale of the observations. Strong dependencies between masses, eccentricities, and pericenter angles on all planets resulted in slow parameter space exploration. The bulk of the volume of parameter space appeared to remain near lower eccentricities and a modest decrease in goodness of fit had to be overcome to reach high e space. But chains which reached high eccentricity lingered in a small area of parameter space for several 10^5 generations despite the existence of equal or better-fitting regions of parameter space, preventing DEMCMC convergence. If the total volume of high eccentricity parameter space is much less than low eccentricity parameter space, it may be ignored when quoting 68% confidence intervals as such a statistic does not take into account the behavior of the tails. However, proving that the volume of high eccentricity parameter space is small compared to low eccentricity requires convergence. Therefore we use a physical argument that high eccentricities that lead to orbital crossings are unlikely to be stable on Gyr timescales and remove that portion of parameter space by introducing a prior that no planet may cross the semi-major axis of another planet. This eccentricity cut-off was computed to be $(e_{b,max}, e_{c,max}, e_{d,max}, e_{e,max}) = (0.212, 0.175, 0.212, 0.175)$, with the symmetry of values due to the resonant chain structure of the periods. This limit is justified in retrospect as long-lived solutions rarely have high eccentricities (see §3.5 and Fig. 3.10).

Figure 3.10: Kepler-223 Stability Eccentricity Dependence

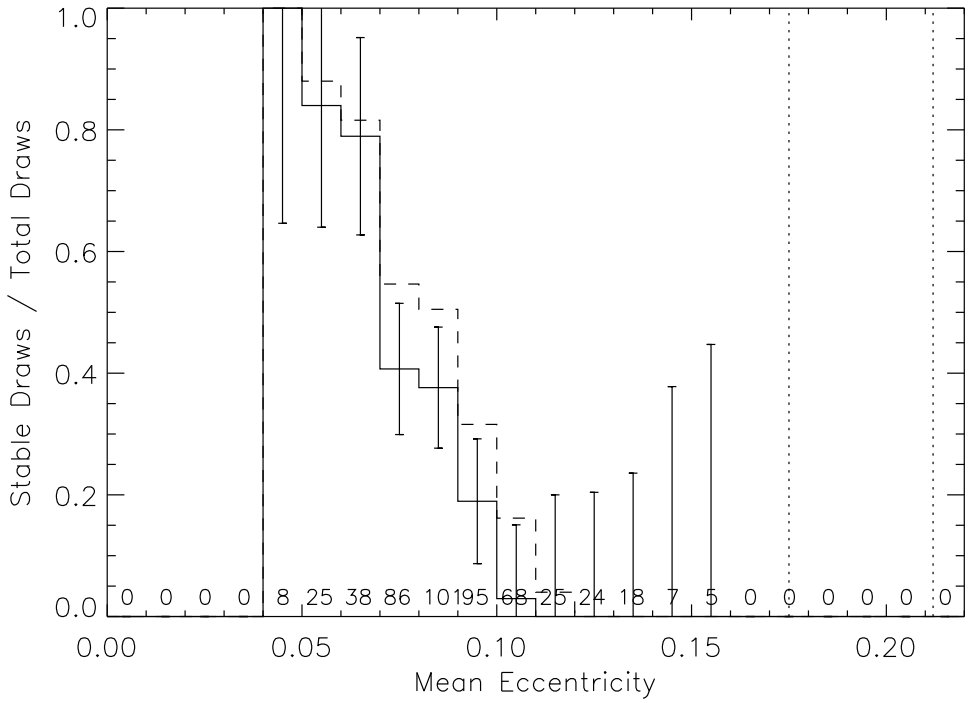

The fraction of 500 random draws from the $\mathcal{C}1$ posterior that survive for 10^7 years (solid line) and 10^6 years (dashed line) as a function of mean eccentricity of the four planets in bins of width 0.01. Dotted lines indicate the two e limits for the planets used in $\mathcal{C}1$: 0.175 and 0.212 for planets c and e and planets b and d respectively. Numbers represent the total number of draws in each eccentricity bin. The fraction of systems that last 10^7 years falls sharply and is consistent with 0 well below the eccentricity cuts imposed by $\mathcal{C}1$, implying such cuts did not remove any physical areas of parameter space. The similarity of the 10^6 year distribution and 10^7 year distribution indicates that using either as a proxy for stable solutions will yield comparable results.

With such a constraint (hereafter $\mathcal{C}1$), the DEMCMC was found approach convergence in a more computationally tenable timescale. We present posterior values subject to that restriction in Tables 3.2 and 3.3 with the caveat that it is, possible, if highly unlikely, that a stable, high eccentricity solution exists outside our assumed prior.

3.4.4 DEMCMC Results and Validation

The DEMCMC runs were considered to have converged when there was no longer any visible upward or downward trend in the parameters as a function of time and the distribution of parameters defined by the chains were constant for $\sim 10^6$ generations. Further, we compute

the autocorrelation of individual chains and note that on average there are greater than 17 autocorrelation timescales (defined as the minimum number of samples at which there is a zero in the autocorrelation function) in each chain, resulting in > 800 independent samples. Since we are quoting only 1-σ uncertainties, this is sufficient statistical accuracy. In total we run 48 chains 3.95×10^6 generations, discarding a burn-in of 3×10^5 generations. The slowest converging parameters are the eccentricity parameters, which occasionally reach the maximum values allowed by the eccentricity cuts and thus traverse essentially the whole of the allowed parameter space. We also test convergence with the Brooks-Gelman-Rubin $\hat{R}_c$ (Gelman & Rubin, 1992; Brooks & Gelman, 1998) and $\hat{R}_{interval}$ statistics (Brooks & Gelman, 1998) and by graphically monitoring their components. Although we do not start from a variety of different locations and our chains are not completely independent, checking whether or not the spread of each individual chain is comparable to the spread of the chains as a whole is still a useful test for non-convergence. Our more realistic estimate of parameter space ($\mathcal{C}2$ described below) involves taking the stable subset of such solutions, which lie in the well-explored, low-eccentricity area of parameter space.

In principle, if one runs a DEMCMC for a long enough time, eventually all of the chains will climb over any barriers in χ^2 space to escape a local minimum to find the global minimum and majority of the chains. As discussed, real world restrictions on computational resources and time prevent this, and even with an eccentricity prior we are forced to remove chains trapped in local minima by hand before performing our analysis. To do this, we simply plot a histogram of the distribution ofχ^2 values of the chains and discard those that are clearly in a higher region than others (often by $\Delta\chi^2 \sim 10^4$). We then proceed with all of the parameter sets from all remaining chains to determine parameter estimates. The uncertainties are computed by reporting the median and nearest 68.27/2% of values on either side of the median. We do not use the more common standard deviation as an approximation for Gaussian error bars because our parameter distributions are clearly non-Gaussian and often asymmetric. Table 3.3 lists the mean values and uncertainties found by the DEMCMC after

Table 3.4: Kepler-223 Best-Fit Solutions

	Planet			
Planet Parameters:	b	c	d	e
Period (d)	7.384720365879194	9.845453934132928	14.788902636701252	19.726218957815664
T_0 (BJD-2454900)	801.516262774051825	800.146170501596430	804.851045349929109	817.521944355066694
e	0.105758145660053	0.172729064427036	0.037330052890247	0.051464531998599
i (°)	90.701847866139545	90.301811036839879	92.189693102657941	92.056638725826986
Ω (°)	0.0	0.0	0.0	0.0
ω (°)	62.597372675420416	85.015828120049491	76.465729705828863	111.706814565803512
Mass ($M_{\rm Jup}$)	0.022730704097050	0.017312231285438	0.019623186719198	0.009576406850388
Radius ($R_p/R_\star$)	0.015954404145479	0.018346434846992	0.027674878130791	0.024759859857039
Stellar Parameters:	$M_\star$ ($M_\odot$):	1.125	$R_\star(R_\odot)$:	1.744528317200141
	c_1:	0.479330549583184	c_2:	0.2
	dilute:	0.11202		
Planet Parameters:	b	c	d	e
Period (d)	7.384583733215798	9.845639757204141	14.788880252356291	19.725687523818440
T_0 (BJD-2454900)	801.513943095097261	800.144691508369419	804.849755312464254	817.519383441790524
e	0.061453702027857	0.112391047984129	0.026604678672708	0.060783217179960
i (°)	91.105539095271382	91.085286013475226	91.966288309512123	91.806556478578258
Ω (°)	0.0	0.0	0.0	0.0
ω (°)	37.604238003695137	86.059011138583742	58.807213313926120	76.156009027159996
Mass ($M_{\rm Jup}$)	0.020503806935496	0.019192688432573	0.025560722351934	0.015467248730564
Radius ($R_p/R_\star$)	0.015793288256059	0.018609959659302	0.028232411829371	0.024265426463497
Stellar Parameters:	$M_\star$ ($M_\odot$):	1.125	$R_\star(R_\odot)$:	1.683974231305496
	c_1:	0.532243950638929	c_2:	0.2
	dilute:	0.11202		

Best fit solutions found by DEMCMC under $\mathcal{C}1$ (top) and $\mathcal{C}3$ (bottom) constraints at $T_{epoch} = 800.0$ (BJD-2454900) with $\chi^2 = 746480$ and 746489 respectively.

removing the burn in. The χ^2 of the best fit is 746480 for 783724 data points, yielding a reduced χ^2 of 0.95 (see Table 3.4).

In order to check that our parameter estimates and uncertainties were reasonable, we ran our fitting procedure on several mock data sets. To imitate the regime we were exploring, we used one of the preliminary migration results with best guess planetary radii to create a synthetic light curve at all data points in the Kepler-223 lightcurve. We masked out data near transits in the actual light curve and found the standard deviation of the remaining photometric points in both short and long cadence data. We used these values to add Gaussian noise to our synthetic light curve. We then used the photodynamic DEMCMC to attempt to find the injected planet parameters, but begin with a different solution found by migration with eccentricities and masses differing by factors of 1-3 and small variations in other parameters. This imitates our attempt to find the true Kepler-223 parameters by starting at a solution found by migration that generally matches the observed TTVs. The

parameters of the artificial injected data are quickly converged upon in the trial and after pruning a few DEMCMC chains that became stuck in clear local χ^2 minima, errors were found to be consistent with expectations, except the stellar radius which is overestimated. The injected model had $i = 90.0°$, but the low S/N does not allow for precise characterization of the transit shapes, meaning fitted inclinations varied by several degrees. To match the observed transit duration, the fitted stellar radius correlated with inclination. Since the impact parameter is positive definite, the mean b of the posterior is greater than zero, and thus the fitted $R_\star$ is found to be greater than the true value. Thus the stellar radius for Kepler-223 found by DEMCMC may also be slightly overestimated, but the spectroscopic density constraints make this effect quite small. Fixing one of the planets at 90° inclination for the injected parameter DEMCMC allows for recovery of the true stellar radius, but for the real system we do not know the inclination of a given planet a priori.

3.5 Planetary System Parameters and Stability

The density of the star is constrained by the photometric transit lengths and shapes, in addition to spectroscopic constraints on stellar mass and radius. The transit depths determine the ratio of the planets' radii to the star's. Since the star is evolved and somewhat larger than the Sun, the planet radii are ∼2.5-5.5 $R_\oplus$.

The TTV signal (Fig. 3.7) is sensitive to the strength of gravitational interactions among the planets. Combined with transit shape information, this constrains eccentricities and provides significant, non-zero mass detections for all bodies between 3 and 9 $M_\oplus$. The planets are thus a large fraction of Neptune in size, but a factor of a few lower than Neptune in mass. Such planets require non-negligible gas in their composition to reach the observed radii, particularly the lowest mass planet, e (see, e.g., Lopez & Fortney, 2014). It is notable that the density of the planets decreases with semi-major axis, consistent with scenarios involving atmospheric loss due to stellar irradiation or formation in increasingly gas-poor areas nearer the star.

The planets possess low to moderate ($\lesssim 0.15$) eccentricity. A planet's eccentricity is only loosely negatively correlated with mass from the TTVs in the data, so small changes in allowed eccentricity will have only a small effect on the posterior mass estimate. Additionally, since higher eccentricities do loosely correspond to lower masses, removing the maximum eccentricity constraints would have the effect of decreasing density of the planets, i.e., making them slightly more gaseous. Though the eccentricities are comparable to those in the Solar System, they are slightly higher than other compact systems of sub-Neptunes such as Kepler-11 (Lissauer et al., 2011a). The eccentricities may be excited and stabilized by the resonances, a property unique to Kepler-223. Periods near a 3:4:6:8 chain are maintained in all the stable, data-fitting solutions. Even in solutions where resonance is observed to occur in both Laplace angles for millions of years, the planets' periods are not instantaneously precisely integer multiples of each other. Because of the planet-planet interactions, the periods oscillate and therefore so do the period ratios, but remain close to the nominal resonant values. The range of period ratios implied by the observed TTVs are typical for the range of period ratios observed in a resonant system (Fig. 3.4). On the other hand, long-lived ($\gtrsim$10Myr) solutions which experience long epochs of Laplace angle circulation generally have a wider range of period ratios on the timescale of the observations. This suggests that the system is currently in a state of libration, although it can not be definitively ruled out that the libration is temporary and periods of Laplace angle circulation may have occurred previously or may occur in the future for this system (Ketchum et al., 2013).

Although we could find parameters which matched the data well over the observing window, we want to ensure that such solutions are physical by considering their long-term stability. We expect that, even with non-crossing orbits, tightly-packed systems with higher eccentricities are likely to be unstable. To assess the stability of the solutions in the posterior distribution, we selected 500 random draws from the posterior parameters sets obtained by the DEMCMC. We numerically integrated each of these solutions for 10^7 years, more than 10^8 orbits of the outermost planet. We use the MERCURY symplectic integrator (Chambers

& Migliorini, 1997) and stop integration if a close encounter between any two bodies occurs. 40% of systems lasted the entire 10^7 year integration. We also explore whether stability is correlated with eccentricity. Since the eccentricities of the planets are correlated, we reduce the eccentricity parameters for the planets into a single dimension: the mean eccentricity of the planets. It is notable that although 27% of the draws from parameter space had a mean eccentricity > 0.1, $< 1\%$ of those solutions remained stable for 10^7 years, compared to the $\sim 80\%$ which remained stable with mean $e < 0.06$. Thus we may broadly say higher eccentricities are correlated with instability in this resonant configuration and thus our orbit-crossing eccentricity cuts are unlikely to have removed much stable area of parameter space (see Fig. 3.10). We also note that after 10^6 years the general structure of the stability region is well defined, with most high eccentricity solutions going unstable before that (Fig. 3.10). Using that fact, we draw 5,000 parameter sets at random from the posterior of DEMCMC and run them for 10^6 years. We use the 2,008 stable ones to define the "long-lived" posterior constraint $\mathcal{C}2$ in Table 3.2 and Table 3.3. We recognize that such a cut potentially allows many solutions which go unstable on a timescale greater than 10^6 years but less than the age of the system (few billion years), but testing all solutions for billions of years is not computationally feasible. Therefore these constraints are permissive, allowing a slightly larger area of parameter space than may be stable (particularly at high eccentricity) but we do not expect this to change any of our conclusions.

In our photodynamic code, we do not include the effects of general relativity (GR) because its precession effects are well below the observational noise level. GR precession is known to affect long-term secular evolution of planetary systems (Laskar & Gastineau, 2009), potentially altering the stability of systems compared to a purely Newtonian analysis. To test if neglecting GR for Kepler-223 is a reasonable approximation in our Myr integrations, we modify MERCURY by introducing a simple potential which approximates GR precession

suitable for a planetary system dominated by the mass of the central star:

$$U_{GR} = -3\left(\frac{GM_\star}{c\,r}\right)^2, \tag{3.13}$$

where c is the speed of light and r is the distance from a planet to the star (Lissauer et al., 2011b). We randomly draw 100 parameter sets from the posterior $\mathcal{C}1$ and run them with this GR modification and without it. We find that there is no change in stability for any of the 100 draws and neglecting GR is justified. This is likely because the planet-planet interactions dominate the precession effects of GR because of their strong interactions due resonance.

3.5.1 DEMCMC Stability Heuristic

In order to further explore parameter space which was more likely to be stable, we ran an additional DEMCMC with a constraint that encouraged (but doesn't guarantee) stability. We first considered using the Mean Exponential Growth Number (MEGNO), which is a proxy of the Lyapunov Exponent and may predict future instability of the system (Goździewski et al., 2001). Two problems exist with such an indicator. The first is that near orbital resonances regions of 'stable chaos' exist in which some stability indicators, such as the MEGNO, may indicate instability, whereas other indicators, such as Frequency Map Analysis in frequency space, suggest long-term stability may remain (Mahajan & Wu, 2014). This would cause the MEGNO to be an overly strict constraint. More concerning is the fact that the MEGNO number may stay quite low (< 2) and be well-behaved for fairly long integration times $\gtrsim 10^5$ days before experiencing an abrupt upward trend as the system begins to go unstable. Integrating the divergence of paths on a timescale long enough to constrain stability for $> 10^6$ years is untenable at each step in DEMCMC, so we pursued an alternative option.

Kepler-223 is a system of resonant planets with what appears to be two librating Laplace

Figure 3.11: Migration Model Libration Angles

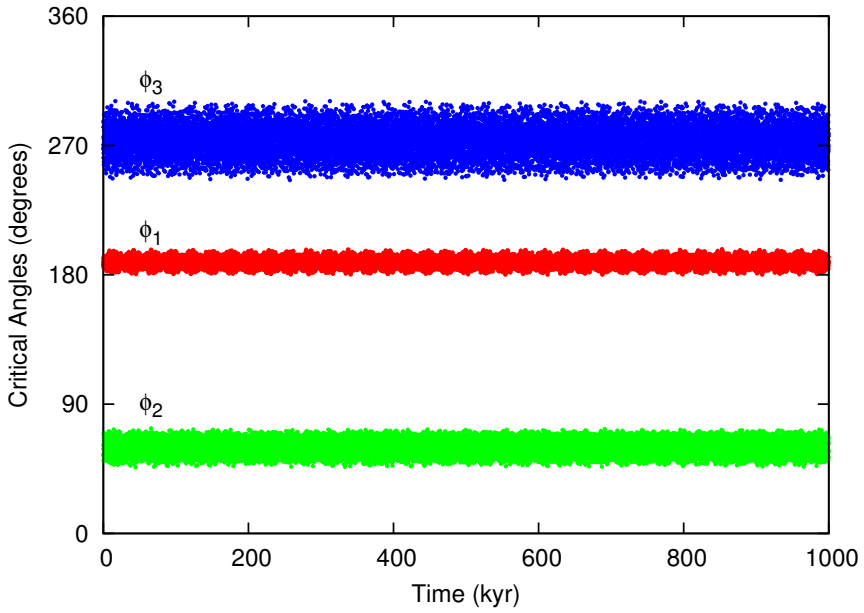

Evolution of the critical angles for the best-fitting migration solution.

angles between the inner 3 and outer 3 planets, as discussed earlier. Migration simulations suggest that very large Laplace angle libration amplitude is unlikely in stable solutions (see Fig. 3.11 for a typical resonant libration). Further, in stable solutions in the $\mathcal{C}2$ posterior, we note long-lived Laplace angle libration is likely to occur (occasionally stably for $> 10^5$yr). Numerical integrations revealed that the characteristic pericenter precession secular period of the system is $\sim$17 years, largely independent of the exact mass values chosen for the system. In order to a stable set of the system's parameters while balancing computational efficiency, at every step in the DEMCMC we integrate the parameter initial conditions for 100 years ($\gtrsim$5 secular cycles) and penalize Laplace angle oscillation amplitudes that grew too large, in addition to fitting the *Kepler* photometry.

Our Laplace angle criteria penalize both large libration amplitudes and the speed at which the amplitudes grow. If the total variation in ϕ_1 or ϕ_2 exceeds a cutoff value K_1 over the integration time (T_{max} in years), then the time at which that occurred is recorded ($T_{runaway}$). A value $-1 + (T_{runaway}/T_{max})^{-2}$ is added to the χ^2. All χ^2 values were also penalized by an amount $(\Delta\phi_i - V_i)^2$ for each $\Delta\phi_i > V_i$ and 0 if $\Delta\phi_i < V_i$ for angles V_i

$(i = 1, 2)$ and with $\Delta\phi = \phi_{max} - \phi_{min}$. This way if the Laplace angles were well enough behaved not to run away, but either or both still grew in amplitude above specified values for each angle V_1 and V_2, then a χ^2 penalty was assigned and the parameter set was less likely to be accepted. We impose no direct eccentricity constraint. We report a version with $(T_{max}, K_1, V_1, V_2) = (100\text{yr}, 170^\circ, 30^\circ, 50^\circ)$, hereafter $\mathcal{C}3$, where the numbers are roughly based on the results of migration and DEMCMC results which had long-term libration.

This methodology of penalizing χ^2 based on Laplace angles in a short time is essentially a method of requiring some of short term stability diagnostic to be passed for the chain's proposed parameters to be accepted. It should be emphasized that this method neither guarantees to reject all unstable systems, as they may pass this test, nor include all stable ones, as some Gyr-stable systems may fail. It guides the chains to stable solutions, primarily by ensuring eccentricities do not grow excessively large so that close encounters in the immediate future upset the Laplace resonances. The DEMCMC posterior constrained by the above Laplace angle prescription prefers smaller values of eccentricity than the posterior with no stability indicator, even though there is no eccentricity cutoff imposed on the DEMCMC with the Laplace angle constraint.

We initialize the DEMCMC from the same stable solution found from migration as before, but with this additional constraint. We run for 4.25×10^5 generations and throw away a 5×10^4 generation burn-in. This is significantly shorter than the $\mathcal{C}1$ runtime since a simpler and more compact region of parameter space could be explored with this constraint. Each chain on average experiences > 25 autocorrelation timescales, and we ensure for all parameters that $\hat{R}_{interval} \leq 1.01$, which is suitable for our non-Gaussian distributions. Running a similar stability check as before by choosing 300 chains from the posterior distribution then resulted in 100% of the parameter sets lasting 10^7 years. Posteriors of all parameters are reported in Table 3.3. We conservatively report values from $\mathcal{C}2$ in Table 3.2 of the main text to avoid removing any non-librating, physical (stable) solutions that fit the data, but suggest $\mathcal{C}3$ parameters more closely reflect the true planet values due to the likelihood that

the planets are stable and in a long-lived resonance.

3.6 Resonance

In both for parameters taken from the explicitly libration-constrained DEMCMC posterior ($\mathcal{C}3$) and that with only the eccentricity constraint ($\mathcal{C}1$), some libration of the Laplace angles is observed in all stable solutions. In these stable solutions the inner Laplace angle (ϕ_1) generally shows oscillations around 180° with amplitudes $\lesssim 40°$ on $\sim 10^5$year intervals. Occasionally the Laplace angle circulates, then begins oscillation around a different value, or 'nodding' (Ketchum et al., 2013). Such chaos in multi-resonant systems does not preclude stability and is not unique to this system (Batygin et al., 2015). The outer Laplace angle (ϕ_2) often switches modes with lengthy periods of circulation between, even in stable solutions (see Fig. 3.12), although it also occasionally maintains $\sim 10^5$ year oscillations. Such mode switching does not preclude the system from being a true resonance, but rather indicates that the best fit solution lies close to a separatrix.

For stable systems, two body resonances are observed to occur between adjacent pairs of bodies and for the 2:1 resonances. Drawing a set of planet parameters from the posterior found by the $\mathcal{C}3$ DEMCMC which shows both ϕ_1 and ϕ_2 oscillations for 10^7 years (see Fig. 3.13), we investigate the 2-body angle behavior. We define the resonance angles $\phi_{bc,in} = 3\lambda_b - 4\lambda_c + \varpi_b$, $\phi_{bc,out} = 3\lambda_b - 4\lambda_c + \varpi_c$, $\phi_{cd,in} = 2\lambda_c - 3\lambda_d + \varpi_c$, $\phi_{cd,out} = 2\lambda_c - 3\lambda_d + \varpi_d$, $\phi_{de,in} = 3\lambda_d - 4\lambda_e + \varpi_d$, $\phi_{de,out} = 3\lambda_d - 4\lambda_e + \varpi_e$, $\phi_{bd} = \lambda_b - 2\lambda_c + \varpi_b$, and $\phi_{ce} = \lambda_c - 2\lambda_e + \varpi_c$. Their libration centers are approximately -3, 179, 16, 155, 24, 177, 7, and -50 degrees respectively.

3.7 Tidal Dissipation

Whereas Kepler-223 is consistent with being in resonance, most *Kepler* systems near resonances lie slightly outside of a true resonance (Fabrycky et al., 2014). Although several

Figure 3.12: Chaotic Longterm Laplace Angle Example

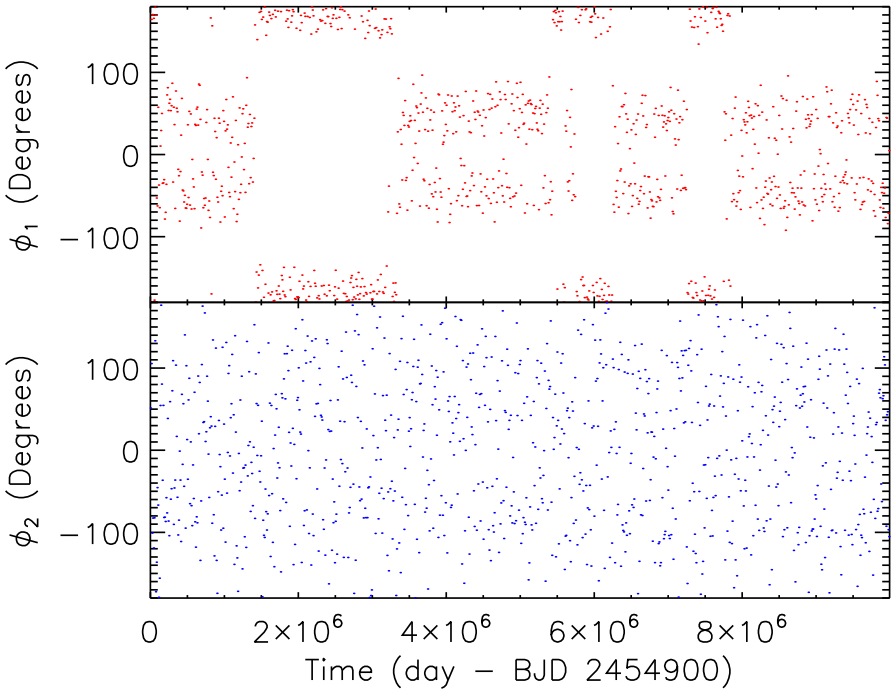

The two Laplace angles for a 10^7 year stable sample drawn from the $\mathcal{C}3$ DECMCMC posterior. The inner Laplace angle, ϕ_1, librates near the observed value initially but quickly switches to other libration centers. The center changes chaotically among 3 values. Some solutions librate around the observed angle for much longer time periods (see, e.g., Fig. 3.13), but nodding is not uncommon. Despite the constraint on the outer Laplace angle, ϕ_2, there are long periods of circulation with intermittent libration.

Figure 3.13: Periodic Longterm Laplace Angle Example

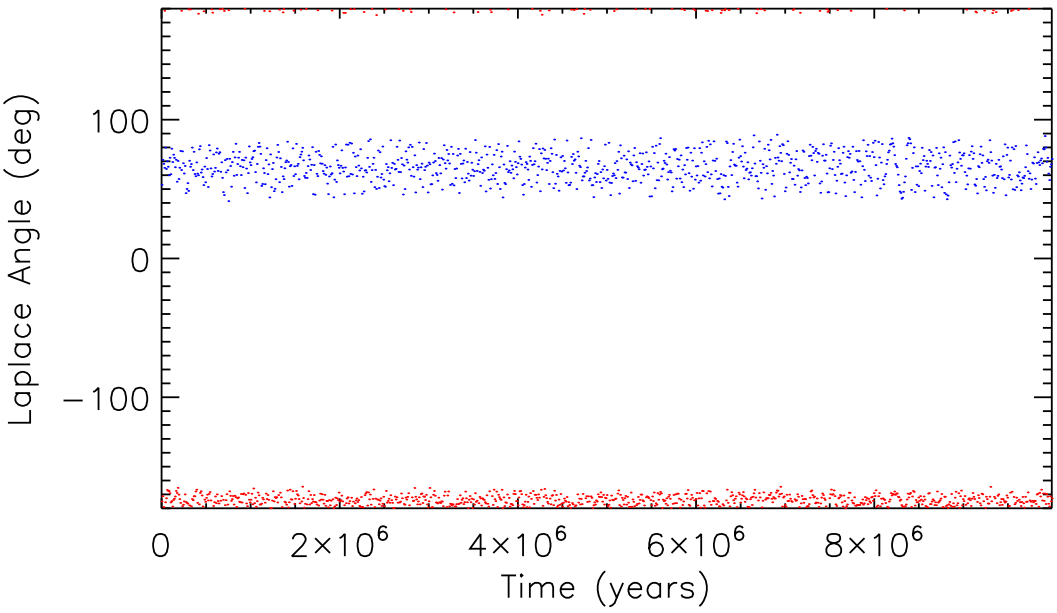

The librating Laplace angles, ϕ_1 (red) and ϕ_2 (blue), for a 10^7 year stable solution found in the $\mathcal{C}3$ DEMCMC posterior. Laplace angles librate over the entire 10^7 years. The period distribution in Fig. 3.4 is taken from this model.

dissipation mechanisms exist to move planets off resonances, some suggest the *Kepler* data implies that the surplus of periods exterior to resonances is a signature of tidal dissipation disrupting resonant pairs, since the pile-up outside of resonance is strongly dependent on planetary semi-major axis (Batygin & Morbidelli, 2013; Delisle & Laskar, 2014). Kepler-80 is a system with 4 confirmed planets that is similar to Kepler-223, as it also demonstrates a series of near-resonant pairs (Xie, 2013). However, the planets of the Kepler-80 system are closer to its host star than Kepler-223's, and each resonant pair sits noticeably wide of the resonance. We therefore suggest that Kepler-80 may have started in a resonant chain, but eventually lost its resonance from tidal dissipation that spread throughout the system due to the resonant couplings of the planet (as subsequently studied by MacDonald et al., 2016). If otherwise stable, Kepler-223 may be destined for the same fate in the distant future. The fact that tidal effects on resonance is not seen can be used to constrain the tidal dissipation parameter, Q, of the planets.

Although there is very large uncertainty in tidal dissipation rates, one may write the tidal circularization timescale as a result of tides raised on the planet by the star, t_e as

$$t_e = \frac{4}{63} \frac{m_p a_p^{13/2}}{(GM_\star^3)^{1/2} R_p^5} Q'_p \text{ yr}, \tag{3.14}$$

with M_p, R_p, and a_p the planet's mass, radius and semi-major axis respectively, and Q'_p a dissipation parameter $= \frac{3Q_p}{2k_2}$ (Goldreich & Soter, 1966). Q_p is the specific dissipation function of the planet and k_2 is the dimensionless Love number representing the ratio of additional potential produced by the redistribution of mass due to tides to the initial deforming potential. In the solar system, Q'_p is approximately bounded by $\sim [10, 500]$ for rocky bodies, and $\sim [10^4, 10^6]$ for ice and gas giants (Goldreich & Soter, 1966; Peale, 1999). In the case of Kepler-223, eccentricity damping because of tides raised on the star by the planet (Goldreich & Soter, 1966) is many orders of magnitude less strong and therefore is neglected here. Using characteristic masses of the star ($M_\star = 1.125 M_\odot$) and planet b ($M_b = 7.4 M_\oplus$)

from our fits, we find that the tidal dissipation time of planet b is $t_{e,b} \approx 3.7 \times 10^5\ Q'_p$ years. If the Q'_p values of Solar System objects are similar to extrasolar systems and the innermost planet of Kepler-223 were rocky that planet would have $t_e \approx 10^6$ to 10^8 year, while if it were gaseous the timescale would be $\gtrsim 10^9$ years.

To compute the approximate time that it would take to move the inner planet away from resonance, we follow Lee et al. (2013). Their prescription is for 2 planets in resonance, but we apply it to the resonance of the inner two planets, b and c, of Kepler-223, expecting a similar result. Interaction between all of the planets would allow tidal dissipation to push all of the planets away from resonance, not just the inner two. To alter the period ratio of planets b and c a distance δ away from resonance requires time $t_\delta = \delta^3 t_e / D_j$, for the $j : (j-1)$ resonance, where

$$D_j = \frac{9j^2}{(j-1)^3}\left(\frac{M_1}{M_\star}\right)^2 \beta(1+\beta)C_1^2. \tag{3.15}$$

Here $\beta = (M_2/M_1)(j/(j-1))^{1/3}$, C_1 is a numerical constant depending on the particular resonance ($C_1 = -1.190$ for a 2:1 resonance, $C_1 = -2.025$ for a 3:2 resonance, and $C_1 = -2.840$ for a 4:3 resonance), and M_1 and M_2 are the masses of the first and second planets respectively.

Again using characteristic masses of the star ($M_\star = 1.125 M_\odot$), planet b ($M_b = 7.4 M_\oplus$), and planet c ($M_c = 5.1 M_\oplus$), we compute for the $4:3$ resonance of the inner two planets $D_4 = 2.2 \times 10^{-8}$. This means the amount of time it takes for planet b to move a distance δ away from its resonant period is approximately $1.6 \times 10^{13}\ Q'_p \delta^3$yr. Based on the distribution of periods in Fig 3.4, we would expect to confidently notice that the planets are not in resonance if the shift in period ratios is on order 3/1000. Spectroscopic constraints put the age at $6.4^{+1.9}_{-1.7}$ Gyr, but with fairly large tails (see §3.1 and Fig. 3.2). There is no star spot signal for Kepler-223, and thus no age estimate can be made from gyrochronology, but the lack of spots implies that the star is not extremely young. Therefore we conservatively

expect that the time in which any shift took place to be at least 10^9 years assuming the system's current state is about as old as the star. Solving for Q'_p, we see that $Q'_p \gtrsim 2 \times 10^3$, which places the tidal dissipation of Kepler-223 b consistent with a gaseous planet, but rules out the low Q'_p observed in rocky Solar System bodies. We repeat this analysis considering the 2:1 resonance between Kepler-223 d and Kepler-223 b, and find a similar, but slightly higher, lower limit of $Q'_p \gtrsim 6 \times 10^3$. Thus if this interaction dominates over the closer 4:3 resonance, our results are essentially unchanged. We conclude that the current resonance, combined with the spectroscopically determined stellar age, rule out $Q \lesssim 1000$, consistent with the planets being gaseous mini-Neptunes rather than rocky (Peale, 1999) – matching the results determined photodynamically. In order to place additional constraints on the inner planet's composition, this result can be expanded to multi-layer planetary models with a solid or astrophysical ice core and a gaseous envelope (Remus et al., 2012; Storch & Lai, 2015). We leave as future work a complete, self-consistent tidal analysis of the system in which all planets are simultaneously experiencing dissipation and interacting rather than considering pairs of planets one at a time.

3.8 Implications for Planet Formation

Because (i) the orbital parameters of Kepler-223 are consistent with it being in a resonant state, (ii) solutions that are stable for 100 Myr exist within the parameter posteriors, and (iii) resonance greatly helps a system this compact to remain stable, we conclude that the system is probably a true resonant chain. Planetary migration in a disk has been extensively studied and often leads to resonant chains of planets (Melita & Woolfson, 1996; Lee & Peale, 2002; Terquem & Papaloizou, 2007; Cresswell & Nelson, 2006). We find that four planets starting well wide of resonance migrate inwards and converge to the 3:4:6:8 chain of periods that we observe with certain choices of simulation parameters (Fig. 3.3). Thus the Kepler-223 system is a plausible outcome of disk migration, but the full set of disk migration parameters and initial conditions that would lead to this system remains an open question.

In a migration scenario, systems trapped in resonances for which the orbital semi-major axes are small (less than about 0.5 au) can potentially be used to constrain the rate of disk photoevaporation and the lifetimes of disks, because a gaseous disk must exist in the 0.02–0.2 au range long enough for planets of moderate mass to migrate. It also provides constraints on turbulence and magnetic fields in the disk (see §7.2 and, e.g., Adams et al., 2008), and the structure of the disk that causes the planets to stop migrating (Masset et al., 2006; Liu et al., 2017). An alternative to gas-disk migration for trapping planets into resonances is migration via planetesimal scattering (Fernandez & Ip, 1984; Raymond et al., 2009; Minton & Levison, 2014). It is possible for planetesimal scattering to migrate two planets in a convergent manner, establishing a resonance. However, this convergent migration would excite the eccentricities of the planetesimal population, which would probably prevent additional planets from joining the resonance (Ormel et al., 2012; Chatterjee & Ford, 2015). The presence of a large volatile later (greater than about 10% H/He by mass; Lopez & Fortney, 2014) layer on the outer planets also suggests that the planets formed in the presence of a gas-containing disk at cool temperatures, further suggesting large-scale migration (Inamdar & Schlichting, 2015; Lee & Chiang, 2016).

Several other exoplanet systems have (GJ 876; Nelson et al., 2016), or are speculated to have (HR 8799; Goździewski & Migaszewski, 2014), resonant chains, but these are composed of planets that are substantially more massive and have much greater orbital distances; hence, these observations may not be relevant to the formation of systems of close-in sub-Neptunes. Several Kepler systems are probably in a true resonance (as opposed to near resonance; for example, the 6:5 system Kepler-50 and the 5:4:3 system Kepler-60; Goździewski et al., 2016); however, owing to the large number of known multi-planet systems, even if the orbital-period ratios of planets are essentially random, consistent with in situ, giant-impact formation, we would expect to observe some systems whose period ratios were near enough to integer values that they entered true dynamical resonances. By contrast, the precise conditions for the four-planet resonant chain of Kepler-223 cannot be accounted for by random selection

of period ratios (Fabrycky et al., 2014), and the system is probably too fragile to have been assembled by giant impacts (Raymond et al., 2008).

The dynamical fragility of Kepler-223 suggests that resonant chains were precursors to some of the more common, non-resonant systems and that planet–planet scattering post-formation is probably an important step in creating the observed period distribution (Pu & Wu, 2015). A model of the formation of the Solar System that has parallels with observed exoplanets involves the four giant planets entering a series of resonances, reaching their current configuration only after destabilization hundreds of millions of years later (Levison et al., 2011). Numerical simulations for Kepler-223 indicate that only a small mass of orbit-crossing planetesimals is needed to move Kepler-223 off resonance (Moore et al., 2013), but that it could escape this fate if intrinsic differences in protoplanetary disks resulted in the lack of such a planetesimal population. In fact, various mechanisms including disk dissipation (Cossou et al., 2014), planet–planet scattering (Pu & Wu, 2015), tidal dissipation (Terquem & Papaloizou, 2007) and planetesimal scattering (Chatterjee & Ford, 2015) could break migration-induced resonances in the majority of exoplanet systems. It has been suggested that some multi- resonant systems (for example, Kepler-80, which has planetary pairs near, but not in, two-body resonances) might have undergone resonant disruption as a result of tidal dissipation, which would explain most of the period ratios that are slightly greater than resonant values in Kepler data (Batygin & Morbidelli, 2013; Delisle & Laskar, 2014). It is possible that the Kepler-223 resonance has survived as a result of its relatively more distant innermost planet. Overall, we suggest that substantial migration of planets, including epochs of resonance that are typically only temporary, rather than in situ formation, leads to the final, observed planetary orbits for many close-in sub-Neptune systems.

3.9 Future Observations

Further measurements could much more tightly constrain the parameters of Kepler-223. Since less than one libration cycle has been observed so far, uncertainties in transit times

grow rapidly with time (see Fig. 3.14). For reference we predict future transit times and uncertainties by using the 152 10^7-year-stable solutions from the $\mathcal{C}1$ posterior, integrating them forward for several years, and averaging the resulting predicted transit times from the models. We report transit times quarterly for 10 years including over the *Kepler* observing window in Tables 3.5, 3.6, 3.7, and 3.8.

3.10 Acknowledgements

We thank Eric Agol, Jack Lissauer, and Jacob Bean for helpful comments on the manuscript. This material is based upon work supported by NASA under Grant Nos. NNX14AB87G (D.C.F.), NNX12AF73G (E.B.F.) and NNX14AN76G (E.B.F.) issued through the *Kepler* Participating Scientist Program. E.B.F received support from NASA Exoplanet Research Program award NNX15AE21G. D.C.F received support from the Alfred P. Sloan Foundation. C.M. was supported by the Polish National Science Centre MAESTRO grant DEC-2012/06/A/ST9/00276. The Center for Exoplanets and Habitable Worlds is supported by the Pennsylvania State University, the Eberly College of Science, and the Pennsylvania Space Grant Consortium. Computer simulations were run using the following facilities: the cluster "HAL9000" of the Faculty of Mathematics and Physics at the University of Szczecin; the cluster "Reef" installed in the Poznan Supercomputer Centre PCSS (computational grant No. 195); and the "Midway" cluster at University of Chicago Research Computing Center. Much of the data presented in this paper were obtained from the Mikulski Archive for Space Telescopes (MAST). STScI is operated by the Association of Universities for Research in Astronomy, Inc., under NASA contract NAS5-26555. Support for MAST for non-HST data is provided by the NASA Office of Space Science via grant NNX13AC07G and by other grants and contracts. The United Kingdom Infrared Telescope (UKIRT) is supported by NASA and operated under an agreement among the University of Hawaii, the University of Arizona, and Lockheed Martin Advanced Technology Center; operations are enabled through the cooperation of the Joint Astronomy Centre of the Science and Technology Facilities Council

Figure 3.14: Transit Timing Variation Future Uncertainties

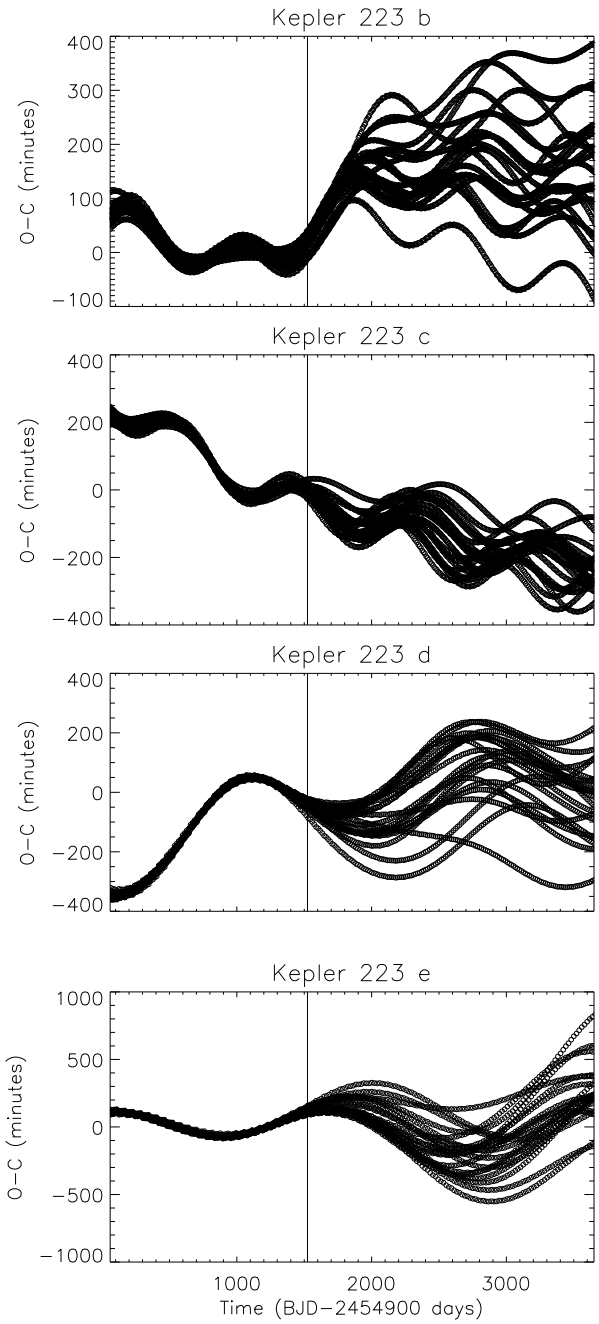

Transit timing variations over a 10 year period beginning with *Kepler*'s first observations for 20 parameter sets drawn randomly from the $\mathcal{C}1$ DEMCMC which are stable for 10^7 years. All solutions are very similar during the epoch of data collection (to the left of the vertical line), but diverge quickly afterwards indicating the variety of system architectures consistent with the data. These are a subset of the draws used to predict future transit times and errors found in Tables 3.5 to 3.8.

Table 3.5: Kepler-223 b Transit Times

Transit Number	Time (BJD-2454900)	1-Sigma Uncertainty (d)
-100	63.0887	0.0090
-87	159.1056	0.0082
-75	247.7220	0.0086
-63	336.3269	0.0080
-50	432.3078	0.0071
-38	520.9068	0.0072
-25	616.8956	0.0075
-13	705.5094	0.0064
-1	794.1301	0.0048
0	801.5152	0.0048
13	897.5250	0.0063
25	986.1462	0.0084
37	1074.7620	0.0087
50	1170.7562	0.0073
62	1259.3647	0.0067
74	1347.9759	0.0078
87	1443.9784	0.0097
99	1532.6046	0.0126
112	1628.6229	0.0176
124	1717.2574	0.0234
136	1805.8886	0.0294
149	1901.8986	0.0369
161	1990.5140	0.0449
173	2079.1234	0.0541
186	2175.1148	0.0647
198	2263.7253	0.0750
210	2352.3415	0.0863
223	2448.3486	0.1002
235	2536.9742	0.1144
248	2632.9840	0.1304
260	2721.6049	0.1450
272	2810.2207	0.1584
285	2906.2177	0.1702
297	2994.8290	0.1777
309	3083.4439	0.1815
322	3179.4500	0.1823
334	3268.0776	0.1810
346	3356.7097	0.1789
359	3452.7288	0.1766
371	3541.3596	0.1751
384	3637.3711	0.1747
396	3725.9939	0.1752
408	3814.6150	0.1760
421	3910.6233	0.1768
433	3999.2493	0.1778
445	4087.8797	0.1805
458	4183.8997	0.1865
470	4272.5348	0.1960
482	4361.1688	0.2090
495	4457.1861	0.2259
507	4545.8143	0.2423
520	4641.8253	0.2587
532	4730.4507	0.2714
544	4819.0767	0.2816
557	4915.0896	0.2911
569	5003.7167	0.2995
581	5092.3423	0.3090
594	5188.3495	0.3209

Transit times and uncertainties for Kepler-223 b. Transits times and errors are estimated from integrations of the randomly selected 10^7year-stable chains from the $\mathcal{C}1$ posterior. Transit times

Table 3.5 Continued: Kepler-223 b Transit Times

are listed quarterly to conserve space (the nearest transit every 3 months) and extend for 10 years past the end of the *Kepler* mission. The transits are indexed from 0 at BJD 2455700, the data epoch used in our fits.

of the U.K. When the data reported here were acquired, UKIRT was operated by the Joint Astronomy Centre on behalf of the Science and Technology Facilities Council of the U.K. This work makes use of observations from the Las Cumbres Observatory Global Telescope Network, the Kepler Community Follow-up Observing Program (CFOP), and NASA's Astrophysics Data System (ADS). We thank NASA Exoplanet Science Institute (NExScI) and the University of California Observatories at University of California Santa Cruz for their administration of the Keck Observatory. We extend special thanks to those of Hawaiian ancestry on whose sacred mountain of Mauna Kea we are privileged to be guests.

Author Contributions: Here I clarify what portion of the work described in this chapter was done by each author (including myself) in the original Mills et al. (2016) paper. S.M.M. performed the photodynamic, stability, tidal dissipation and spectral evolution analyses and led the paper authorship. D.C.F. designed the study, performed TTV and Laplace-angle libration analysis, and assisted writing the paper. C.M. performed the migration analysis, assisted in initial data fitting and contributed to the writing of the paper. E.B.F. advised on the DEMCMC analysis and paper direction. E.P. and H.I. obtained and analysed the spectra. All authors read and edited the manuscript.

Table 3.6: Kepler-223 c Transit Times

Transit Number	Time (BJD-2454900)	1-Sigma Uncertainty (d)
-75	61.5205	0.0108
-65	159.9930	0.0087
-56	248.6329	0.0102
-47	337.2847	0.0103
-38	425.9405	0.0083
-28	524.4408	0.0064
-19	613.0752	0.0066
-10	701.6938	0.0062
-1	790.3012	0.0048
0	800.1461	0.0047
10	898.5969	0.0047
19	987.2140	0.0058
28	1075.8474	0.0057
38	1174.3478	0.0055
47	1263.0059	0.0062
56	1351.6619	0.0065
65	1440.3070	0.0065
75	1538.7846	0.0103
84	1627.4012	0.0160
93	1716.0133	0.0205
102	1804.6307	0.0231
112	1903.1082	0.0265
121	1991.7538	0.0319
130	2080.4096	0.0386
140	2178.9176	0.0463
149	2267.5663	0.0545
158	2356.2017	0.0659
167	2444.8241	0.0792
177	2543.2857	0.0922
186	2631.9022	0.1007
195	2720.5283	0.1064
204	2809.1678	0.1111
214	2907.6683	0.1162
223	2996.3251	0.1202
232	3084.9789	0.1241
242	3183.4735	0.1293
251	3272.1091	0.1338
260	3360.7395	0.1358
269	3449.3713	0.1334
279	3547.8608	0.1260
288	3636.5121	0.1183
297	3725.1732	0.1116
306	3813.8398	0.1060
316	3912.3571	0.1008
325	4001.0181	0.0975
334	4089.6725	0.0963
344	4188.1723	0.0972
353	4276.8218	0.0981
362	4365.4757	0.0977
371	4454.1364	0.0963
381	4552.6567	0.0950
390	4641.3287	0.0954
399	4730.0003	0.0976
408	4818.6680	0.1014
418	4917.1799	0.1073
427	5005.8348	0.1139
436	5094.4859	0.1206
445	5183.1356	0.1264

Predicted TTVs as in Table 3.5, but for planet c.

Table 3.7: Kepler-223 d Transit Times

Transit Number	Time (BJD-2454900)	1-Sigma Uncertainty (d)
-50	65.4447	0.0072
-44	154.1447	0.0047
-38	242.8598	0.0044
-32	331.5817	0.0042
-26	420.3152	0.0037
-19	523.8387	0.0034
-13	612.5824	0.0032
-7	701.3208	0.0028
-1	790.0609	0.0024
0	804.8496	0.0023
6	893.5815	0.0022
13	997.0849	0.0023
19	1085.7975	0.0023
25	1174.4962	0.0027
31	1263.1929	0.0032
37	1351.8803	0.0041
43	1440.5709	0.0048
50	1544.0418	0.0067
56	1632.7313	0.0111
62	1721.4245	0.0188
68	1810.1174	0.0302
74	1898.8123	0.0455
80	1987.5064	0.0647
87	2090.9840	0.0922
93	2179.6785	0.1188
99	2268.3760	0.1489
105	2357.0723	0.1795
111	2445.7696	0.2115
118	2549.2464	0.2471
124	2637.9368	0.2750
130	2726.6220	0.2993
136	2815.3015	0.3205
142	2903.9760	0.3371
148	2992.6468	0.3513
155	3096.0946	0.3626
161	3184.7651	0.3687
167	3273.4360	0.3741
173	3362.1111	0.3749
179	3450.7875	0.3756
185	3539.4691	0.3729
192	3642.9321	0.3726
198	3731.6211	0.3709
204	3820.3123	0.3733
210	3909.0089	0.3759
216	3997.7067	0.3824
223	4101.1912	0.3894
229	4189.8933	0.3953
235	4278.5902	0.4036
241	4367.2873	0.4094
247	4455.9766	0.4173
253	4544.6648	0.4232
260	4648.1247	0.4338
266	4736.8036	0.4412
272	4825.4789	0.4512
278	4914.1553	0.4604
284	5002.8312	0.4712
291	5106.2912	0.4814
297	5194.9768	0.4888

Predicted TTVs as in Table 3.5, but for planet d.

Table 3.8: Kepler-223 e Transit Times

Transit Number	Time (BJD-2454900)	1-Sigma Uncertainty (d)
-38	68.0961	0.0084
-34	146.9947	0.0052
-29	245.6060	0.0045
-25	324.4947	0.0051
-20	423.0960	0.0054
-15	521.7036	0.0053
-11	600.5790	0.0048
-6	699.1903	0.0046
-1	797.7976	0.0051
0	817.5244	0.0051
4	896.4141	0.0058
9	995.0482	0.0062
13	1073.9507	0.0068
18	1172.5999	0.0072
23	1271.2455	0.0076
27	1350.1725	0.0074
32	1448.8244	0.0092
37	1547.4801	0.0182
41	1626.4056	0.0318
46	1725.0591	0.0566
51	1823.7144	0.0904
55	1902.6306	0.1256
60	2001.2820	0.1764
64	2080.1989	0.2253
69	2178.8518	0.2901
74	2277.5047	0.3626
78	2356.4352	0.4209
83	2455.1002	0.4967
88	2553.7756	0.5692
92	2632.7191	0.6235
97	2731.4064	0.6847
101	2810.3580	0.7279
106	2909.0518	0.7709
111	3007.7434	0.8016
115	3086.6969	0.8204
120	3185.3800	0.8305
125	3284.0570	0.8349
129	3362.9868	0.8261
134	3461.6404	0.8156
138	3540.5478	0.7970
143	3639.1727	0.7767
148	3737.7784	0.7475
152	3816.6534	0.7261
157	3915.2343	0.6929
162	4013.8034	0.6596
166	4092.6588	0.6342
171	4191.2188	0.6010
175	4270.0718	0.5771
180	4368.6341	0.5480
185	4467.2088	0.5270
189	4546.0679	0.5101
194	4644.6591	0.5010
199	4743.2570	0.4967
203	4822.1446	0.5026
208	4920.7617	0.5152
213	5019.3859	0.5379
217	5098.2951	0.5610
222	5196.9309	0.5959

Predicted TTVs as in Table 3.5, but for planet e.

CHAPTER 4

KEPLER-108

The vast majority of well studied giant-planet systems, including the Solar System, are nearly coplanar which implies dissipation within a primordial gas disk. However, intrinsic instability may lead to planet–planet scattering, which often produces non-coplanar, eccentric orbits. Planet scattering theories have been developed to explain observed high eccentricity systems and also hot Jupiters; thus far their predictions for mutual inclination (I) have barely been tested. Here we characterize a highly mutually-inclined ($I = 24^{+11}_{-8}$ degrees), moderately eccentric ($e \gtrsim 0.1$) giant planet system: Kepler-108. This system consists of two approximately Saturn-mass planets with periods of approximately 49 and 190 days around a star with a wide ($\sim$ 300AU) binary companion in an orbital configuration inconsistent with a purely disk migration origin.

4.1 Introduction

NASA's *Kepler* mission has discovered thousands of planets and planet candidates (Coughlin et al., 2016; Morton et al., 2016). The periods, phases, and radii (relative to their host stars) of transiting planets are straightforwardly measured (e.g. Winn, 2010). Transits may only be seen if the orbital plane is nearly edge-on to the observer (i.e., the inclination, $i \approx 90°$). The impact parameter, the distance of closest projected approach between planet and star, can often be determined by the shape of the transit ingress/egress (Seager & Mallén-Ornelas, 2003)[1].

Of the numerous candidates identified, nearly half are found in multiple-transiting planet systems (Burke et al., 2014). The *Kepler* data set also has over 200 cases of planets with

1. However, it is usually difficult to distinguish an inclination of just above 90° from just below 90° (both nearly edge-on orbits) with the same impact parameters. In some many body systems it is possible to distinguish these through either dynamical interactions (Huber et al., 2013b) or overlapping mutual transits (Masuda et al., 2013).

time-varying orbital periods (Holczer et al., 2016). These variations are usually attributed to interplanetary gravitational perturbations. These perturbations lead to measurable transit timing variation (TTV) amplitudes for very massive planets, or if planets are close to low-order resonances (Agol et al., 2005), which many pairs of super-Earths or Neptunes are (Fabrycky et al., 2014). Measurements of TTVs can put tight constraints on planet masses and eccentricities (Nesvorný & Morbidelli, 2008).

The absolute nodal angle of bodies on the sky is undetermined by photometry and only relative angles can be constrained due to dynamical interactions (or, in rare cases, mutual transits, e.g., Hirano et al., 2012). Mutual inclinations can be measured by the change (or lack thereof) in transit duration and depth as a function of time due to orbital plane precession (Miralda-Escudé, 2002; Sanchis-Ojeda et al., 2012; Carter et al., 2012). Planetary orbits that are highly misaligned will cause rapid precession, causing the chord of the transit to move up or down the face of the star. As a result, the chord will lengthen or shrink as it passes through different projected widths of the star, changing the transit duration. Rapid apse precession with very high eccentricities may also cause transit duration and depth changes (Pál & Kocsis, 2008). Combining TTVs, ingress/egress information, and duration/depth changes gives full 3D information on the system, up to a rotation in the plane of the sky.

The vast majority of observed exoplanet systems are statistically consistent with having low ($\lesssim 5^\circ$) mutual inclinations (Fabrycky et al., 2014). Only a few giant–planet systems have individually measured mutual inclinations, and these are composed of nearly-coplanar, low eccentricity, often resonant orbits (e.g., GJ 876 (Rivera et al., 2010; Nelson et al., 2016), Kepler-30 (Sanchis-Ojeda et al., 2012), KOI-872 (Nesvorný et al., 2012), Kepler-56 (Huber et al., 2013b), and Kepler-119 (Almenara et al., 2015)), consistent with a disk migration origin (Goldreich & Tremaine, 1980; Lee & Peale, 2002). The giant planets of our own solar system are also nearly coplanar and potentially experienced disk migration (Tsiganis et al., 2005; Morbidelli et al., 2007). Stochastic behavior due to many-body interactions in the form of resonance overlap or secular chaos may disrupt the architectures of planetary

systems after formation and dissipation of the natal disk (e.g. Wisdom, 1980; Duncan et al., 1989; Chambers et al., 1996; Lin & Ida, 1997; Lithwick & Wu, 2011; Davies et al., 2013; Lithwick & Wu, 2014). This process can lead to highly eccentric and mutually-inclined orbits (e.g. Lin & Ida, 1997; Chatterjee et al., 2008; Laskar & Gastineau, 2009), and may be the cause of some of the observed hot Jupiters (Wu & Lithwick, 2011; Lithwick & Wu, 2014). Therefore theory suggests that we may expect to see the signatures of instability and planet–planet scattering in giant planet systems (e.g., Chatterjee et al., 2008). However, only two systems are observed to have significant, measured mutual inclinations to date[2]: Kepler-419 b and c are observed to have a marginally detected mutual inclination of $9^{\circ}{}^{+8}_{-6}$ from TTV and transit duration variation (TDV) constraints, which is very modest considering the planets' high eccentricities (Dawson et al., 2014), and Upsilon Andromeda c and d are reported to have a mutual inclination of $\sim 30^{\circ}$, based on astrometric measurements using the Hubble Space Telescope fine guidance sensor (McArthur et al., 2010).

Here we present a photodynamic analysis of Kepler-108 (also known as KOI-119 and KIC 9471974) (Rowe et al., 2014), a system of two giant planets (Kepler-108b and Kepler-108c, the inner and outer planets respectively) with a large mutual inclination detected through transit duration and depth changes over the *Kepler* observing window. In §4.2, we describe our methods for identifying the system as one of interest and analysis of its parameters. In §4.3-4.5, we summarize the results of the analysis, present the system parameters, and discuss what further constraints can be made on the system. We conclude in §4.6 with a discussion of the system's dynamics and a general outlook.

2. There are several known circumbinary systems where the planet is slightly mutually inclined to the binaries and exhibit spectacular precession effects (e.g. Kostov et al., 2014; Welsh et al., 2015), but all currently known systems have low ($\lesssim 5^{\circ}$) mutual inclinations (Doyle et al., 2011; Welsh et al., 2012; Orosz et al., 2012b,a; Schwamb et al., 2013; Kostov et al., 2014; Welsh et al., 2015). Additionally, as such systems are likely to have vastly different histories, here we consider only systems with a single star and multiple planets.

4.2 Methods

4.2.1 Identification of the System

To identify Kepler-108 as a mutually inclined system, we searched the Kepler Object of Interest (KOI) catalog for systems which exhibited possible transit duration variations (TDVs) using the first 13 quarters of data. We began by detrending the simple aperture photometry (SAP) flux data from the *Kepler* portal on the Mikulski Archive for Space Telescopes (MAST). For this initial search we used long-cadence (29.4 minute exposure) data. To determine a flux baseline, we used the amplitudes of the first five cotrending basis vectors (the largest magnitude vectors from a singular value decomposition of the photometry for a given CCD channel, which dominate the systematic effects as given at https://archive.stsci.edu/kepler/cbv.html). We discarded points whose quality flag had a value equal to or greater than 16. We fit the individual transits to a time-binned transit function (Mandel & Agol, 2002) using a Levenberg-Marquardt algorithm with the uncertainties for the data points as reported in the *Kepler* photometric data using a globally fit transit shape. In our search, we used the periods given in the KOI catalog and discarded any transits within 1 day of each other to avoid spurious signals caused by overlapping transits. We fit a cubic polynomial with a 1 day width to the light curve in order to take into account stellar variability and additional systematic effects. We then binned the data into *Kepler* observing quarters (approximately 3 months) by shifting the transits to the same phase in each quarter according to their fitted transit times. We refit these transits to the raw SAP data, allowing the duration and depth of the transits to vary between quarters. Using an entire quarter of data for each fit allowed lower signal-to-noise (S/N) transits to be fitted and the uncertainties to be small, while still allowing enough distinct data points to see if any duration trends were present. We computed a linear fit to the quarterly best fit durations and compare it to the uncertainty of the duration. Since our data are already subdivided by quarter we can determine by inspection if there are quarterly instrumental

issues causing spurious duration changes. We are not aware of any instrumental effects that could produce such a signature, but expect that if one were to exist it would repeat every four quarters. We see no such trend. Another concern is that in different observing seasons, a given pixel or group of pixels in the aperture sum might observe a slightly different group of stars causing the transit depth to change as the transit is diluted by background stars. Again, such effects are readily noticeable as spikes or dips occurring every four quarters. Several candidate systems were found in our search, with Kepler-108 being the most convincing, and exhibiting strong TDVs (Fig. 4.1), as well as TTVs (Fig. 4.2). We redid the analysis with several different detrending timescales and found little dependence on the result (Fig. 4.1) since the timescales are much longer than the transits' ingress and egress timescales. We continue using this timescale for detrending as it allows us to remove stellar variability without distorting the transit shape significantly.

We note that the TTV super-period, $P_{\rm sup}$, may be predicted analytically: $P_{\rm sup} := P_{\rm c}/(4|\Delta|) = 1416$ days, where $\Delta = P_{\rm c}/(4P_{\rm b}) - 1 = 0.0336$ is the distance from the 4:1 resonance for planets b and c in our case (Lithwick et al., 2012). This agrees very well with the observed TTV data (Fig. 4.2). On the other hand we may also consider the affects of stellar variability, particularly spots, on the measured TTVs and TDVs. Star spots are darker than surrounding areas on the face of the star. Thus planet transits which cross a star spot may bias the measured transit time or duration. Crossing star spots in the first half of the transit may cause the transit center time to appear later than the actual time and crossing spots in the second half may cause the transit to appear earlier than it actually occurs (see Holczer et al., 2015). Such an effect is generally small, but we consider it here. In order to reproduce the long-period sinusoidal TTVs present in the planets, the spots would have to be in nearly the same location for successive transits, only slowly moving over the course of the 4 year observing window. This implies that it is merely a coincidence that $P_{\rm sup}$ is well-matched by the data, and the observed TTVs are caused by a near-commensurability of the planets' orbital periods with the stellar rotation period or a multiple of it. This

Figure 4.1: Kepler-108 Transit Duration Variations

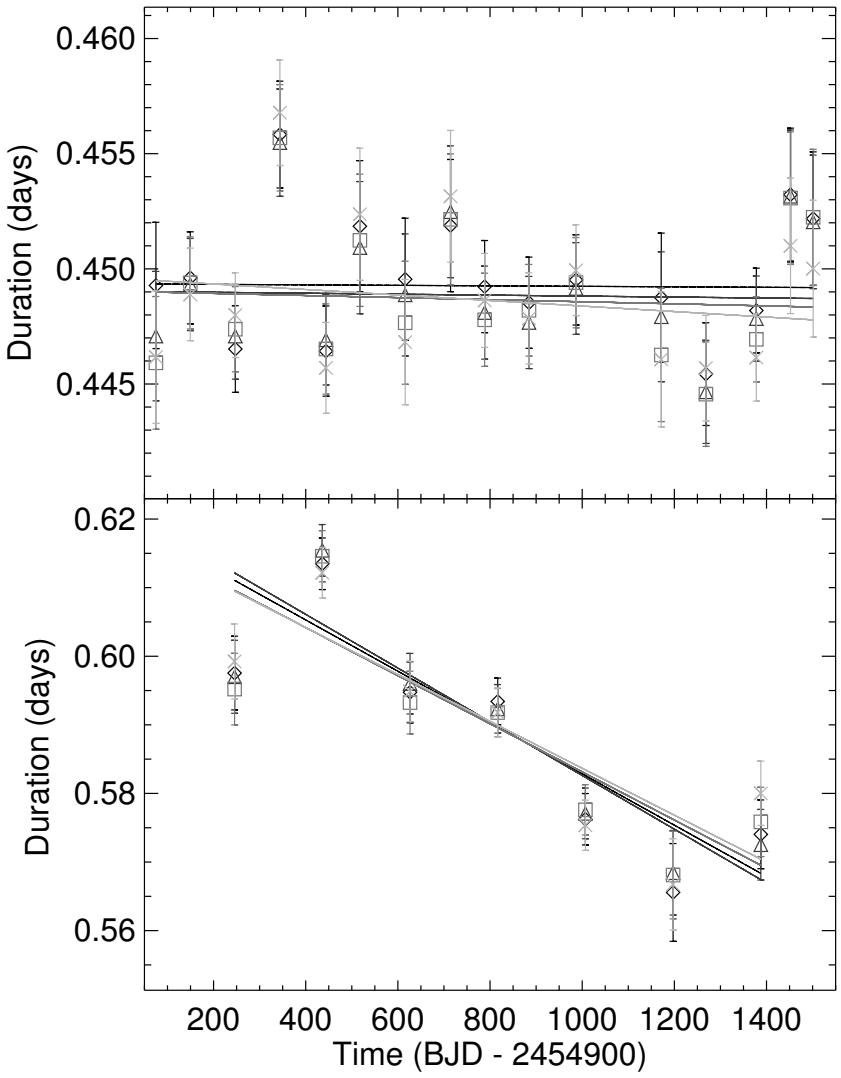

Transit durations and 1-σ uncertainties for planet b (top) and planet c (bottom) found by fitting the long-cadence data. The durations are measured using 4 different polynomial detrending lengths as described in the text from black to light gray: 7200 minutes (diamonds), 2880 minutes (triangles), 1440 minutes (squares), and 1000 minutes (xs). There is minimal variation among the different timescales, so we conclude that our choice of 1 day (1440 minute) detrending is justified. A clear trend appears in planet c.

Figure 4.2: Kepler-108 Transit Timing Variations

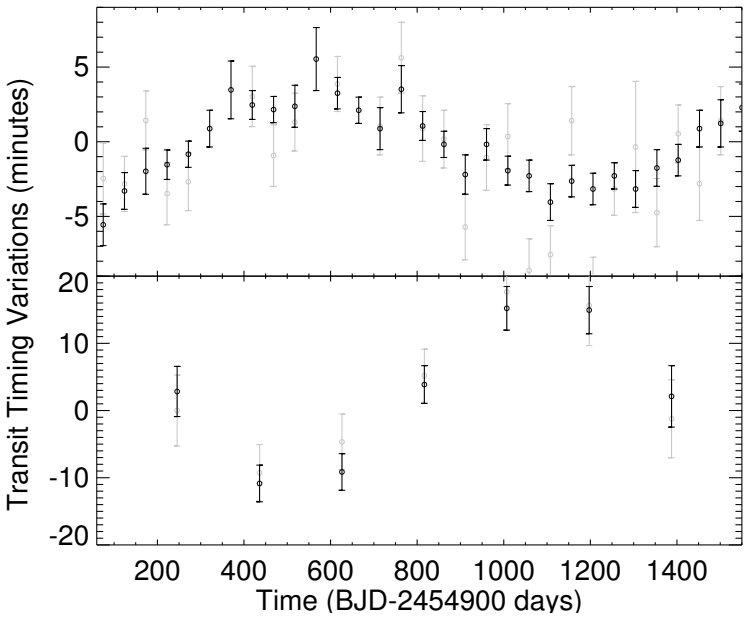

Individually measured TTVs with 1-σ uncertainties (gray). Plotted in black are the mean and variance for TTVs measured by taking 100 random draws from the posterior of photodynamical fit as described in §3. Therefore the black points combine the *Kepler* observational data with a physically possible N-body gravitational model to better constrain the TTVs.

does not make physical sense because the period ratios of the two planets have nearly a 4:1 commensurability yet their TTVs are anti-correlated, even in places where they transit very closely in time (e.g., $t_{\rm BJD} \approx 2455907 - 2455909$), indicating the effects of spots is small compared to the implied gravitational TTV effects. Durations may be similarly affected by star spot crossing, but we would predict that any star spots that would make ingress appear later or egress appear earlier would both cause the duration to decrease. For the duration to experience a net decrease as observed, it would require an increase in the number of spots as a function of time over the observing window regardless of location, but no signs of this are seen in the TTVs. We would expect the durations to decrease when the TTVs are greatest in absolute value if caused by star spots, and this correlation is not observed in the data. Thus we rule out star spots as causing the observed TTV and TDV variations.

4.2.2 Analysis of Stellar Properties

An asteroseismology study conducted by Huber et al. (2013a) found Kepler-108's mass to be $1.377 \pm 0.089 M_{\odot}$. However, Kepler-108 has been the subject of several follow-up studies which have revealed that it is a binary star system. Adaptive optics (AO) measurements in the i (Law et al., 2014), J, and K bands (Wang et al., 2015) have revealed a companion star 1.05" from Kepler-108A, which is highly likely to be associated with the system (Wang et al., 2015). The binary nature of the star system is also seen in archival UKIRT images (Lawrence et al., 2007).

To determine which star is the planet host, we examine the *Kepler* pixel level data and the Data Validation Report (DVR) (Bryson et al., 2013). *Kepler*'s pixels are approximately 4 arcsec and thus the two sources are not resolved, but we may still determine where within a given pixel a planet's host star lies. Because the field is crowded (including by KIC 9471979, a star within 1 apparent magnitude of the target stars, located approximately 10 arcsec to the south and 3 arcsec to the east), detecting the centroid shift while the planets are in and out of transit is not effective at determining which member of the binary the planets are

transiting because the centroid is affected by these bright stars that are somewhat further away (Bryson et al., 2013). Finding the centroid of the flux difference image (the difference in flux between when the planets are in and out of transit) should reveal the true location of the star being transited, though this method is potentially more uncertain. The DVR indicates that the host star of both planets b and c is approximately 0.5 arcsec east and 0.15 arcsec south of the nominal KIC location at the 4.6-σ and 2.2-σ levels for each planet respectively. Since the KIC location reflects the combined light of the binary star, its reported position is in between the two observed stars (with the fainter, planet-hosting star lying to the southeast). This is confirmed by centroid fitting of the UKIRT J-band images with `find.pro` and `starfinder.pro` (Diolaiti et al., 2000) and explains why the centroid offset is only $\sim$0.5 arcsec, rather than the 1.05 arcsec separation reported by AO imaging (Law et al., 2014; Wang et al., 2015). We find that stars A and B are located at approximately ($\alpha_{\rm A} = 294°33'32".085, \delta_{\rm A} = 46°03'44.98$) and ($\alpha_{\rm B} = 294°33'33".390, \delta_{\rm B} = 46°03'44".43$) respectively, whereas the DVR indicates the star hosting planets b and c is located at ($\alpha_{\rm b} = 294°33'33".334 \pm 0.085, \delta_{\rm b} = 46°03'44".236 \pm 0.097$) and ($\alpha_{\rm c} = 294°33'33".352 \pm 0.155, \delta_{\rm c} = 46°03'44".267 \pm 0.359$) respectively. Thus the planets are consistent with each other and Kepler-108B, but not Kepler-108A. The position angles (PAs) from the KIC location of the host star of planets b and c are $125° \pm 12°$ and $111° \pm 37°$ respectively, matching the reported PA of the fainter binary companion of 118° in both AO images (Law et al., 2014; Wang et al., 2015), and 180° from what would be expected from the brighter star. In summary, this analysis reveals that the position of the planets' host star is consistent with the southeastern star of the binary pair (Kepler-108B), and rules out the brighter star to the northwest (Kepler-108A) at $\gtrsim 5\sigma$.

We use the publicly available Dartmouth stellar isochrone modeling package `isochrones` (Morton, 2015, available at: https://github.com/timothydmorton/isochrones) to characterize the stars based on the AO flux measurements. We have apparent system magnitudes (taken from https://cfop.ipac.caltech.edu) and the magnitude differences between the two

Table 4.1: Kepler-108 Stellar Properties

	Kepler-108 A	Kepler-108 B (Planet Host)
	Asteroseismology[a]	
$M_\star(M_\odot)$	1.377 ± 0.089	-
$R_\star(R_\odot)$	2.192 ± 0.121	-
	Photometry	
$\text{Kepler}_{\text{mag}}$[b]	12.654 (Both Stars Combined)	
i_{mag}[cd]	12.90 ± 0.22	13.77 ± 0.22
J_{mag}[ce]	12.087 ± 0.15	12.287 ± 0.15
K_{mag}[ce]	11.640 ± 0.15	11.840 ± 0.15
$M_\star(M_\odot)$[f]	$1.26^{+0.33}_{-0.23}$	$0.96^{+0.29}_{-0.16}$
$R_\star(R_\odot)$[f]	$1.45^{+0.73}_{-0.41}$	$0.97^{+0.56}_{-0.21}$

[a] Huber et al. (2013a)
[b] KIC Catalog
[c] https://cfop.ipac.caltech.edu
[d] Law et al. (2014)
[e] Wang et al. (2015)
[f] Morton (2015)

stars in the i (Law et al., 2014), J, and K (Wang et al., 2015) bands (Table 4.1). Based on these, we compute the magnitudes of both Kepler-108 stars to use as input parameters to the `isochrones` package. We find that stellar parameters from the AO color constraints are consistent within 1-σ of the asteroseismology for the brighter star Kepler-108A (the non-planet hosting star); however the isochrone method has uncertainties a factor of a few greater than asteroseismology. Lower accuracy is expected from the photometric method because asteroseismology is one of the most precise methods of determining stellar density, and thus masses and radii combined with stellar models, developed to date. Nonetheless, the agreement between the different methods of estimations confirms that photometry can determine the properties of the planet host star, albeit with large uncertainties. We suggest therefore that our results be interpreted more as broad priors on the scale of the system and stellar density rather than a precise stellar measurement. We summarize our inputs and fitted values in Table 4.1 and find that the planet-hosting star has $R_\star = 0.97^{+0.56}_{-0.21} R_\odot$ and $M_\star = 0.96^{+0.29}_{-0.16} M_\odot$.

4.2.3 Photodynamic Analysis

We followed up our initial analysis of Kepler-108 by applying a photodynamic model. The model integrates the 3-body Newtonian equations of motions for the central star and two planets, including the light–travel–time effect. When the planets pass between the star and the line of sight, a synthetic light curve is generated (Pál, 2012), which can then be compared to the data. For computational efficiency, we assume that the planets' velocities are changing negligibly over the face of the host star due to eccentricity effects. By neglecting the change in planet velocity, this approximation ignores asymmetries in the ingress and egress that are on the order of $\lesssim$1 second, translating to errors in the normalized light curve of only $\lesssim 10^{-6}$ (see, e.g., Winn, 2010), much less than the uncertainty on the data. For the photodynamics, we took advantage of the short-cadence (58.8 second exposure) data available in *Kepler* Quarters 5-8 and 12. Cotrending basis vectors are not available for short-cadence data. To detrend this data, first we masked out the expected transit times and then fit a cubic polynomial model with a 1 day width (as done for the long-cadence data) centered within half an hour of each data-point, to determine its baseline. We divided the flux by this baseline. We continued using long-cadence data where short-cadence was not available (*Kepler* Quarters 1-3, 9-11, and 13-17). We detrended that data identically as described above for the short-cadence data. We performed detrending with and without using the CBVs and found statistically negligable difference in the fitting results. We used the photodynamic model to produce theoretical normalized flux values at the timestamp of each short-cadence data point. For long-cadence data, we computed the flux value at 15 equally spaced points in time over a cadence's integration and averaged them together to produce the theoretical result. A small amount of correlated noise (fractional variations $\lesssim 10^{-4}$, with a peak in a Lomb-Scargle periodgram of the out-of-transit short-cadence data near 45 minutes) was still present in the data likely due to known spurious instrumental frequencies (García et al., 2011; Christiansen et al., 2013) and, more broadly, the stellar variability which allowed for asteroseismology measurements. Our detrending algorithm did not address this

short time-scale noise to avoid distorting the transit shapes, but its amplitude is far below the data uncertainties. We multiplied the quoted data uncertainties by a factor of 1.075 such that the reduced χ^2 of our best-fitting model was 1.0[3]. By increasing our uncertainties, we conservatively widen our posteriors to take into account the scatter introduced by unmodeled aspects of the system, such as star spots or instrumental noise, whose affects may be small but non-zero and bias our results. One of the planets, Kepler-108b, had only partial transits observed at ∼BJD 2455959, 2456106, and 2456204 due to pauses in data collection. Our detrending algorithm performs poorly on cases where there is not a baseline on both sides of the transit. Therefore the data within 1 day of these transits was removed from the fits to avoid incorrectly influencing the fit by changing the measured depths. Since the mid-time and duration measurements of these transits is highly uncertain due to having only either the ingress or egress, retaining them would add minimal information to our fits. To expedite the computation, we fit only data within 1.0 days from any transit, because the model of data far from transit is always a constant: the transit parameters do not affect it. In total we were left with 25,425 photometric data points.

The parameters for each planet in the differential evolution Markov chain Monte Carlo (DEMCMC, Ter Braak, 2005) fit are $\{P,\, T_0,\, e^{1/2}\cos(\omega),\, e^{1/2}\sin(\omega),\, i,\, \Omega,\, R_{\rm p}/R_\star,\, M_{\rm p}/M_\star\}$, where P is the period, T_0 is the mid-transit time, e is eccentricity, ω is the argument of periapse, i is inclination, Ω is nodal angle, and R and M are radius and mass respectively (with subscripts $p = b, c$ for the planets and $\star$ for the star). The star had five additional parameters: $\{M_\star,\, R_\star,\, c_1,\, c_2,\, \textit{dilute}\}$, where $\{c_i\}$ are the two quadratic limb-darkening coefficients and *dilute* is the amount of dilution from other nearby sources. We use flat priors in all parameters unless otherwise stated below, including uniform priors on $e^{1/2}\cos(\omega)$ and $e^{1/2}\sin(\omega)$, resulting in a flat prior in total e.

The relative flux from each star in the *Kepler* bandpass is uncertain, so we allowed the

3. A more careful treatment could, in principle, be done using Gaussian process noise modeling (e.g. Ambikasaran et al., 2014), however this was computationally untenable for our study since we have $\sim 6\times10^5$ data points for a model that needed to be run $> 10^9$ times to provide posteriors on all of our models.

fractional amount of flux from the non-host star to vary as a free parameter. We ran photodynamic fits assuming Kepler-108B is the host with the the stellar mass fixed at the value found as described in §2.2 because photometry alone can only determine the stellar density when $M_{\rm p} \ll M_\star$. Our DEMCMC fits also used the measured stellar radius and uncertainty ($R_\star = 0.97^{+0.56}_{-0.21} R_\odot$) as a data point along with the *Kepler* photometry. Since *dilute* is highly degenerate with the size of the planets ($R_{\rm p}/R_\star$), our planetary radii are significantly more uncertain than previously reported values, which did not take into account contamination from another blended source. The shape of the transit does offer some constraints on the dilution so it is not a completely degenerate parameter. We did not include the companion star in our photodynamic model directly because its great distance (at minimum, the measured sky-projected distance of 327 AU; Wang et al., 2015) prevents it from detectably influencing the Kepler-108 planets over the *Kepler* observing window. We discuss potential long-term effects in §6. Although it is disfavored, we also ran a second, nearly identical set of DEMCMCs assuming that the asteroseismologically measured star is the host star, and thus fixed stellar mass at $1.377 M_\odot$ and used the constraint $R_\star = 2.192 \pm 0.121 R_\odot$ (Huber et al., 2013a). We include these posteriors in the appendix.

To test whether our detection of changing transit durations and depths (and therefore mutual inclination) was robust, we ran 3 different DEMCMCs for each host star: ($\mathcal{MI}$ — "Mutually Incline") allowing the inclinations and relative nodal angle of the planets to vary independently; ($\mathcal{NC}$ — "Nearly Coplanar") allowing only the planets inclinations to vary independently and fixing both planets to a nodal angle of $\Omega = 0$; and ($\mathcal{CO}$ — "Coplanar") forcing the planets to be coplanar, i.e. fixing $\Omega = 0$ and $i_{\rm b} = i_{\rm c}$, but allowing the value of the inclination to vary.

Requiring strict coplanarity ($\mathcal{CO}$) results in a far worse fit to the data ($\Delta\chi^2 \gtrsim 100$) than the other two models ($\mathcal{MI}$ and $\mathcal{NC}$) regardless of host star, because each planet must have the same inclination. As a result, the impact parameter of both planets is determined by a single inclination, and the transit shapes and durations of both planets cannot be fit well

compared to the case where two different inclination values are allowed. We no longer discuss $\mathcal{CO}$ as a viable candidate model since with only one additional free parameter compared to $\mathcal{NC}$ we vastly improve the fit and provide a more realistic model.

The $\mathcal{NC}$ ($\Omega_{\rm b,c} = 0$) DEMCMC was initialized with the periods of the two planets as reported in the *Kepler* catalog (Batalha et al., 2013), and at a variety of eccentricities below 0.1 for both planets. The DEMCMC chains slowly explored increasingly higher eccentricities, with the chains preferring for the inner planet (b) to have $e > 0.7$. Once the DEMCMC chains found this high-eccentricity space, they did not travel back to lower eccentricities because high eccentricity allowed a better fit to the data. Restarting the DEMCMC from a variety of solutions with planet b having $e \sim 0.75$ and $\omega \sim 150^\circ$ (near the best fit found previously), resulted in none of the chains seeking lower-eccentricity regions. Therefore we conclude that for the nearly coplanar case ($\mathcal{NC}$), high-eccentricity solutions are robustly preferred. We ran a parallel 46-chain DEMCMC until the parameters appeared stationary; the chains were well mixed (> 50 autocorrelation time scales for every parameter for each chain on average), and their Rubin-Gellman $\hat{R}_{interval}$ statistic (Brooks & Gelman, 1998) was below 1.05 for every parameter. We recorded the parameters for each chain every 1000 generations for 5×10^6 generations to reduce correlation and required disk space, and threw out the first 2×10^5 generations of all chains as a burn-in. We thus obtained 2×10^5 samples of the posterior for each DEMCMC, of which at least $50 \times 46 = 2300$ are completely independent.

The $\mathcal{MI}$ DEMCMC was initialized similarly to $\mathcal{NC}$, with all eccentricities below 0.1. This DEMCMC also explored higher eccentricities for planet b, but rather than remain high as in $\mathcal{NC}$, eccentricities continually varied between high and low values ($0.0 \lesssim e \lesssim 0.7$). Concerned that this DEMCMC was not finding the same very high eccentricity parameter space found by $\mathcal{NC}$, we ran $\mathcal{MI}$ again but starting from solutions drawn from $\mathcal{NC}$. All chains in this case quickly found lower-eccentricity solutions and did not return to the very high-eccentricity starting conditions. We ran the ($\mathcal{MI}$) DEMCMC for 1.25×10^7 generations,

with a 2×10^5 generation burn-in. This DEMCMC was run much longer because the wide range of acceptable eccentricities caused slower convergence. When the DEMCMC was stopped, each parameter had experienced > 30 autocorrelation time scales (at least 1000 independent points) and had $\hat{R}_{interval}$ statistic below 1.1. These values are still acceptable for convergence and continuing running was not computationally feasible. The complex nature of the parameter space (see Figs. 4.3 and 4.4) slows down the convergence significantly, particularly at high eccentricity. DEMCMC runs with Kepler-108A as host have similar statistics.

Concerned that we could potentially miss additional minima distant from our initialization on the χ^2 surface, we also ran a 4-temperature parallel-tempered DEMCMC (Earl & Deem, 2005) with both the $\mathcal{MI}$ and $\mathcal{NC}$ constraints. This approach is similar to a traditional DEMCMC, but it allows some chains (those with high temperatures) to have a much higher probability chance of exploring high χ^2 regions of parameter space, allowing them to easily traverse local maxima. This is accomplished by multiplying the $\Delta\chi^2$ between a proposed step and the chain's current location by a given "temperature" value, which increases the probability that higher χ^2 proposals are accepted. We initialized this DEMCMC from our best-fit solutions, but the high-temperature chains rapidly spread out over a much broader range of parameter space than explored before. The high-temperature chains may swap with low temperature chains once near a sufficiently low χ^2 minima and allow for a more refined exploration of parameter space in that area. This allows for efficient discovery and exploration of multimodal posteriors (for further discussion, see Earl & Deem, 2005). We find very similar posteriors and no additional minima which would affect our fits with this method.

4.3 Photodynamic Results

The data generally allow for two classes of solutions which cause the observed duration and depth changes in the transits (see Fig. 4.5). The first case, explored by $\mathcal{MI}$, we will describe

Figure 4.3: Kepler-108 Planet Posteriors

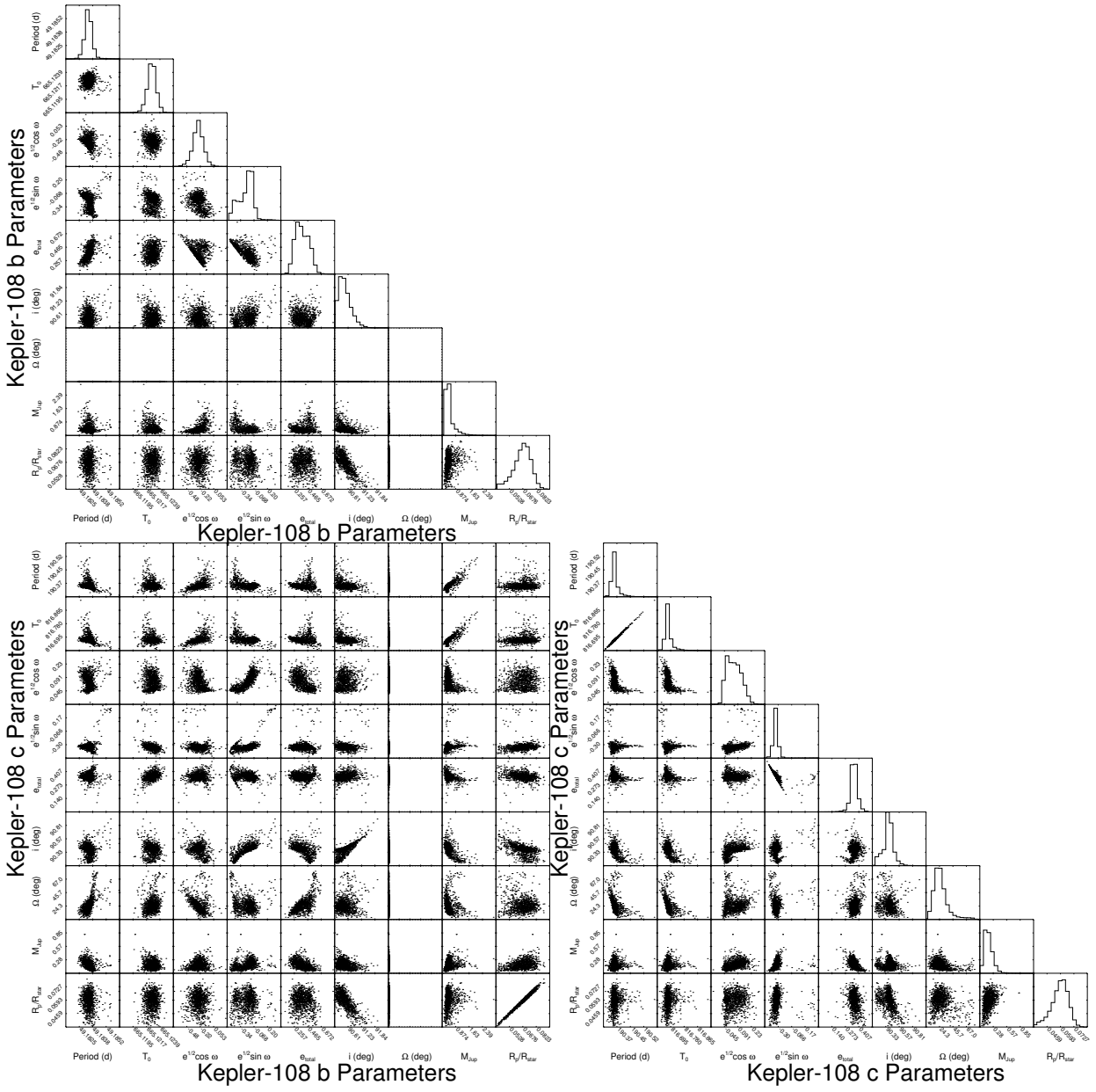

Correlations among all planetary parameters in $\mathcal{MI}$, the mutually inclined model. Where correlations would be between a parameter and itself, instead a histogram of the distribution of that parameter is shown.

Figure 4.4: Kepler-108 Stellar Posteriors

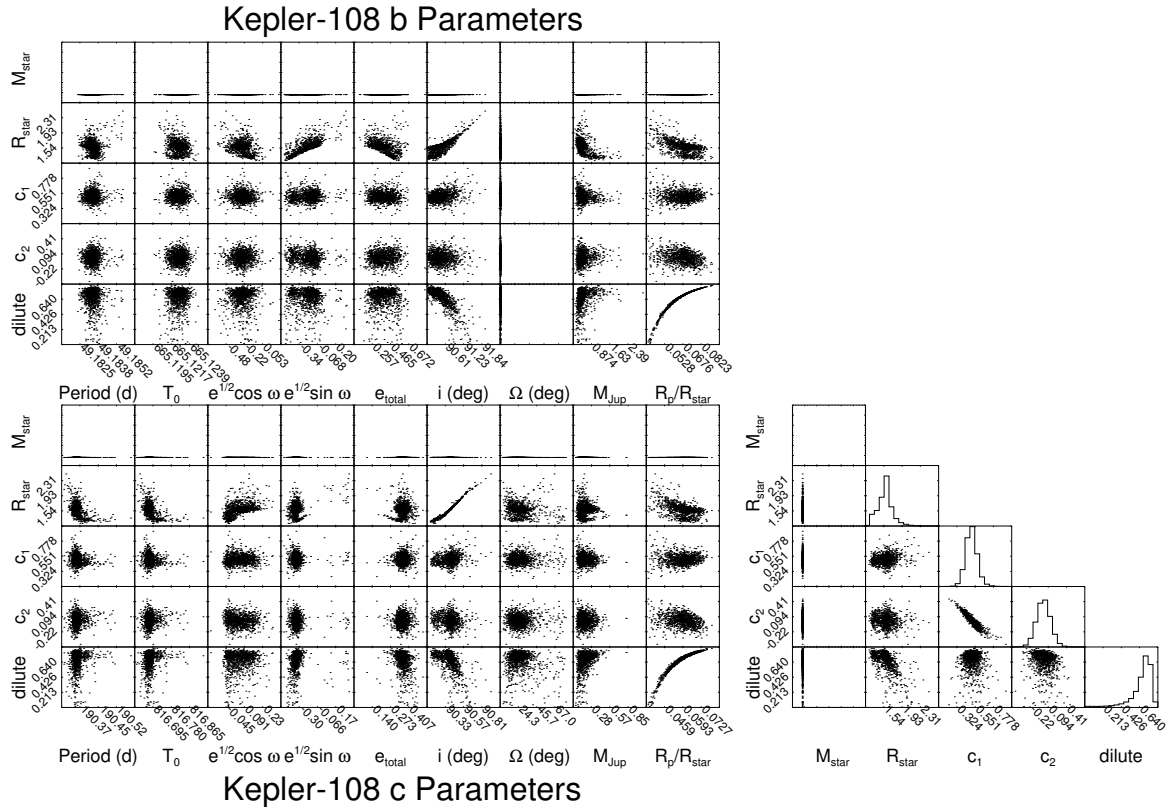

All correlations involving stellar parameters in $\mathcal{MI}$, the mutually inclined model. Where correlations would be between a parameter and itself, instead a histogram of the distribution of that parameter is shown.

as the low eccentricity, high mutual inclination case. The second case, explored by $\mathcal{NC}$, refers to the nearly coplanar, highly eccentric case. In this case, the mutual inclination between the planets is $\lesssim 1^\circ$. The very large (~ 0.75) eccentricity of the inner planet along with its increased mass causes faster precession of the node (and apse) of the outer planet. Along with the larger eccentricity of the outer planet, this results in similar transit duration and depth changes (see Fig. 4.6). DEMCMC posterior median values and 1- and 2-σ uncertainties at $T_{epoch} = 640.0$ (BJD-2454900) for the mutually inclined ($\mathcal{MI}$) and nearly coplanar ($\mathcal{NC}$) models are given in Table 4.2. Note that the distributions in many parameters are not Gaussian and the 2-σ interval is generally not twice as wide as the 1-σ interval. The distributions and correlations between parameters for $\mathcal{MI}$ are shown in Figs. 4.3 and 4.4. Correlations in other fits are similar. Confidence intervals higher than 2-σ are not given as the number of independent parameter values mean that there are relatively large fractional uncertainties on the confidence intervals of higher σ; however, the two sets of confidence intervals given are sufficient to understand the posteriors. Best-fit solutions found by DEMCMC under $\mathcal{MI}$ (top) and $\mathcal{NC}$ (bottom) constraints assuming Kepler-108B as the host star at $T_{epoch} = 640.0$ (BJD-2454900) are given in Table 4.3.

In a random sample of 100 draws from each posterior distribution, 99% were stable for $> 10^7$ years in $\mathcal{MI}$ and 100% were stable over the same time period in $\mathcal{NC}$, so stability alone can not easily rule out either regime.

The fixed nodal angle solution ($\mathcal{NC}$) around Kepler-108B had a best-fit $\chi^2 = 25407$ for 25,425 data points, and the system allowing non-zero mutual nodal angles ($\mathcal{MI}$) had $\chi^2 = 25435$. Since only 1 additional free parameter is added from the $\mathcal{NC}$ to $\mathcal{MI}$ models, we would expect an improvement of χ^2 of order unity if both models describe the data well, i.e. if it were true that large mutual inclination was not required to fit the data effectively (Akaike, 1974). The large difference in χ^2 suggests that the fit allowing large mutual inclinations is superior to the others by $> 4\sigma$ as follows.

Rigorously, we can define the F-ratio as the improvement in χ^2 normalized by the number

Figure 4.5: Phase-Folded Kepler-108 Transits

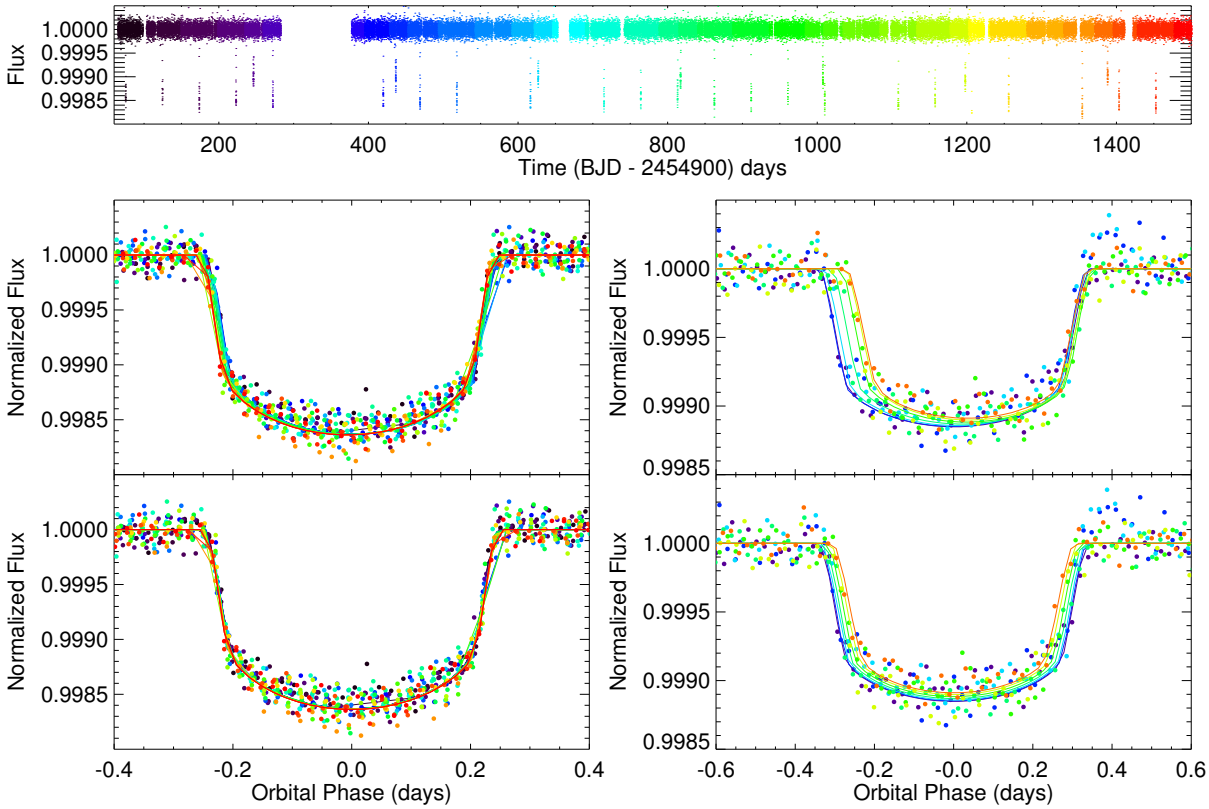

Top: Detrended flux over the Kepler observing window. The two planet transits appear clearly as periodic dips of different depth. Color is changed incrementally from violet to red such that each transit has a distinct color in the data. To reduce visual scatter, only long-cadence data is displayed although short-cadence data was used where available in the fitting procedure. *Bottom:* Left and Right columns are planets b and c respectively. The top panel shows the data (dots) and photodynamic best-fit model (line) phase-folded with a constant period (the best fit at $T_{\rm epoch} = 640.0$ (BJD-2454900), see Table 4.3). Bottom panels show the transits phase folded with the TTVs removed. This allows clear identification of the change in planet c's duration and depth with time (as indicated by color in the top panel). Model points are produced only where real data points are found and are connected by straight lines resulting in the apparent sharp corners on some of the transits.

Figure 4.6: Kepler-108 Transit Geometry

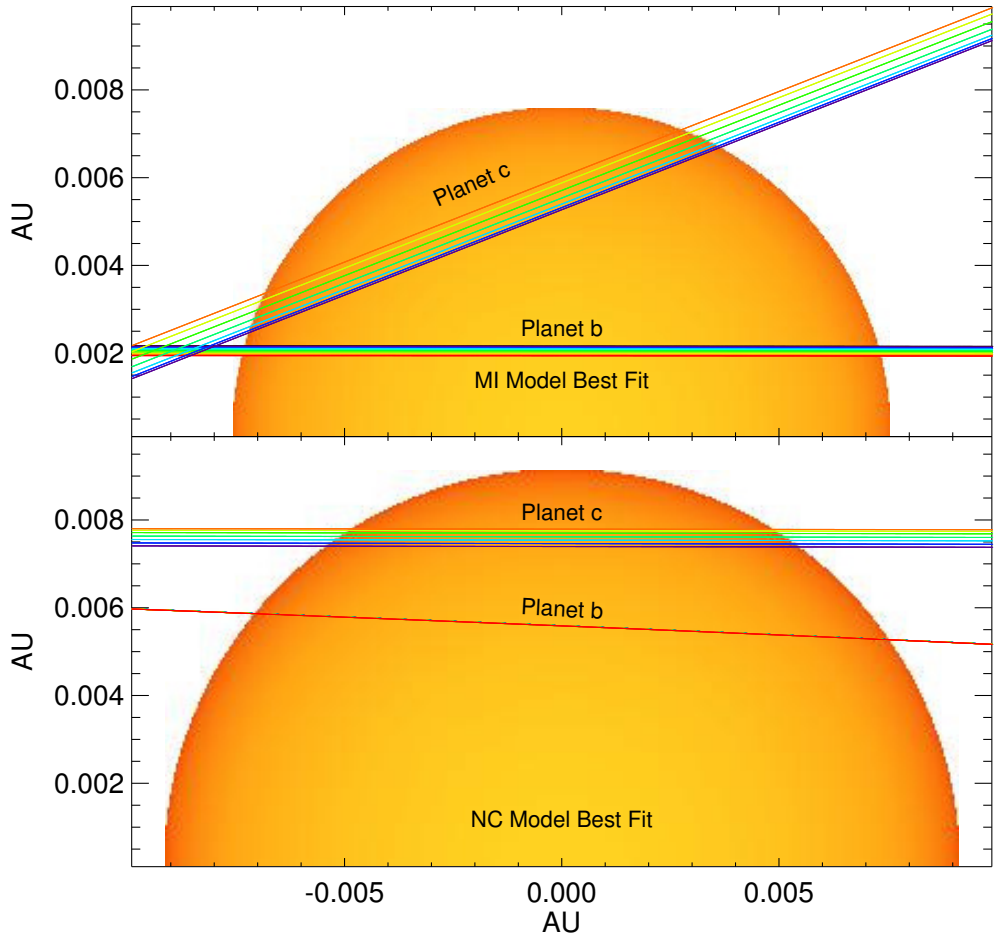

The chords of successive transits of the two planets over the face of the star using the same color scheme as in Fig. 4.5. *Top:* The best-fit favored, mutually inclined ($\mathcal{MI}$) case. *Bottom:* The disfavored, nearly coplanar ($\mathcal{NC}$) case. The physical distance the planets in this configuration can move across the face of the star is small, so planet c requires a high impact parameter to exhibit large duration changes. The stellar radius increase to ensure the transit duration is correct, and the difference in the ingress and egress shape due to these factors helps distinguish the two models.

Table 4.2: Kepler-108 Posteriors

	Host: Kepler-108B					
	$\mathcal{MI}$ - Mutually Inclined			$\mathcal{NC}$ - Nearly Coplanar		
Parameter Name (Unit)	Median	68.3% (1-σ) Uncertainties	95.4% (2-σ) Uncertainties	Median	68.3% (1-σ) Uncertainties	95.4% (2-σ) Uncertainties
Stellar Parameters:						
$R_\star(R_\odot)$	1.57	$^{+0.13}_{-0.16}$	$^{+0.38}_{-0.29}$	1.939	$^{+0.098}_{-0.11}$	$^{+0.96}_{-0.25}$
$M_\star(M_\odot)$	0.96	[a]		0.96	[a]	
c_1	0.503	$^{+0.069}_{-0.065}$	$^{+0.16}_{-0.13}$	0.54	$^{+0.10}_{-0.10}$	$^{+0.22}_{-0.21}$
c_2	0.01	$^{+0.12}_{-0.12}$	$^{+0.24}_{-0.24}$	0.02	$^{+0.14}_{-0.14}$	$^{+0.29}_{-0.28}$
dilute	0.699	$^{+0.062}_{-0.13}$	$^{+0.10}_{-0.50}$	0.22	$^{+0.19}_{-0.15}$	$^{+0.35}_{-0.21}$
Kepler-108 b Parameters:						
P (d)	49.18341	$^{+0.00033}_{-0.00033}$	$^{+0.00082}_{-0.00075}$	49.18356	$^{+0.00015}_{-0.00018}$	$^{+0.00026}_{-0.00038}$
T_0 (BJD-2454900 (d))	665.12253	$^{+0.00069}_{-0.00072}$	$^{+0.0014}_{-0.0016}$	665.1095	$^{+0.0035}_{-0.0068}$	$^{+0.0057}_{-0.024}$
$e^{1/2}\cos(\omega)$	-0.258	$^{+0.10}_{-0.10}$	$^{+0.22}_{-0.24}$	-0.758	$^{+0.012}_{-0.011}$	$^{+0.035}_{-0.023}$
$e^{1/2}\sin(\omega)$	-0.196	$^{+0.093}_{-0.22}$	$^{+0.18}_{-0.32}$	-0.483	$^{+0.026}_{-0.027}$	$^{+0.053}_{-0.078}$
e_{tot} [b]	0.135	$^{+0.11}_{-0.062}$	$^{+0.20}_{-0.094}$	0.810	$^{+0.023}_{-0.023}$	$^{+0.050}_{-0.047}$
i (°)	90.42	$^{+0.33}_{-0.22}$	$^{+0.75}_{-0.36}$	91.96	$^{+0.26}_{-0.29}$	$^{+0.54}_{-0.63}$
Ω (°)	0.0			0.0		
M ($M_{\rm Jup}$)	0.44	$^{+0.24}_{-0.11}$	$^{+0.91}_{-0.20}$	1.39	$^{+0.41}_{-0.32}$	$^{+0.96}_{-0.76}$
$R/R_\star$	0.0678	$^{+0.0081}_{-0.011}$	$^{+0.015}_{-0.024}$	0.0439	$^{+0.0061}_{-0.0034}$	$^{+0.014}_{-0.0047}$
Kepler-108 c Parameters:						
P (d)	190.353	$^{+0.017}_{-0.010}$	$^{+0.078}_{-0.024}$	190.540	$^{+0.11}_{-0.093}$	$^{+0.23}_{-0.21}$
T_0 (BJD-2454900 (d))	816.676	$^{+0.019}_{-0.012}$	$^{+0.087}_{-0.028}$	816.835	$^{+0.10}_{-0.090}$	$^{+0.22}_{-0.18}$
$e^{1/2}\cos(\omega)$	0.047	$^{+0.083}_{-0.073}$	$^{+0.15}_{-0.10}$	-0.2411	$^{+0.0085}_{-0.0075}$	$^{+0.019}_{-0.015}$
$e^{1/2}\sin(\omega)$	-0.347	$^{+0.035}_{-0.034}$	$^{+0.12}_{-0.086}$	-0.4528	$^{+0.0085}_{-0.0088}$	$^{+0.017}_{-0.020}$
e_{tot} [b]	0.128	$^{+0.023}_{-0.019}$	$^{+0.062}_{-0.052}$	0.2631	$^{+0.0062}_{-0.0060}$	$^{+0.014}_{-0.012}$
i (°)	90.379	$^{+0.069}_{-0.10}$	$^{+0.19}_{-0.22}$	90.557	$^{+0.041}_{-0.047}$	$^{+0.078}_{-0.11}$
Ω (°)	24	$^{+11}_{-8}$	$^{+40}_{-15}$	0.0		
M ($M_{\rm Jup}$)	0.169	$^{+0.095}_{-0.068}$	$^{+0.22}_{-0.11}$	0.0202	$^{+0.0055}_{-0.0051}$	$^{+0.011}_{-0.0099}$
$R/R_\star$	0.05946	$^{+0.0070}_{-0.0092}$	$^{+0.013}_{-0.021}$	0.0398	$^{+0.0056}_{-0.0031}$	$^{+0.013}_{-0.0043}$

[a] Note that the stellar mass is held fixed in these simulations so the values and uncertainties on the planets' masses may easily be scaled with future measurements of the stellar mass.

[b] e_{tot} is not actually a fitted parameter, rather it is derived from $e\cos(\omega)$ and $e\sin(\omega)$.

Table 4.3: Kepler-108B Best-Fit Solutions

	Planet	
Parameters:[a]	b	c
Period (d)	49.183083085839172	190.353737335237525
T_0 (BJD-2454900)	665.122619366413346	816.676288054934048
e	0.080502815440656	0.135150900332772
i (°)	90.447992776533482	90.402707451208229
Ω (°)	0.0	21.230171600736064
ω (°)	-151.443327788289849	-74.804240921039195
Mass ($M_{\rm Jup}$)	0.413341841865039	0.202792331316081
Radius ($R_{\rm p}/R_\star$)	0.067139110107278	0.059698074950235
$M_\star$ ($M_\odot$)	0.96	
$R_\star(R_\odot)$:	1.60826681434233	
c_1	0.519093256451504	
c_2	-0.021614974187020	
dilute	0.692460493291417	

	Planet	
Parameters:[a]	b	c
Period (d)	49.183505940179316	190.557066614127535
T_0 (BJD-2454900)	665.111210027200173	816.849801840698206
e	0.800786833080398	0.260953132882452
i (°)	91.960040412229276	90.557754765511007
Ω (°)	0.0	0.0
ω (°)	-147.461456894507307	-117.953198816245759
Mass ($M_{\rm Jup}$)	1.494038810020510	0.022840632640538
Radius ($R_{\rm p}/R_\star$)	0.042211249374808	0.038215416346983
$M_\star$ ($M_\odot$)	0.96	
$R_\star(R_\odot)$:	1.942786847021155	
c_1	0.520024994427787	
c_2	0.056552930588019	
dilute	0.155848582719487	

[a] Valid at $T_{epoch} = 640.0$ (BJD-2454900) for the mutually-inclined ($\mathcal{MI}$) model on top and nearly-coplanar ($\mathcal{NC}$) model below.

of new free parameters, DOF:

$$\Delta\chi^2/\Delta DOF = (25435 - 25407)/(18 - 17) = 28 \tag{4.1}$$

to the final reduced $\chi^2_{\rm f}$:

$$\chi^2_{\rm f}/\nu_{\rm f} = 25407/25425 = 0.999 \tag{4.2}$$

The F-test gives the probability (p-value) that the F-ratio is as high as observed by chance. In our case the p-value is 1×10^{-7}, so we may reject that the planets have the same nodal angle on the sky. We note that the χ^2 being slightly below 1.0 suggests we have overestimated our uncertainties and therefore only strengthens our reasoning.

To compare the entire distribution of parameters found by MCMC rather than just the best-fit solution, we computed the Bayes Factor, K, using Newton and Raftery's p_4 estimator (Newton & Raftery, 1994) and found the odds ratio to be $> 10^{10}$ in favor of $\mathcal{MI}$, i.e. large mutual inclination is strongly favored (Kass & Raftery, 1995).

Lastly, a physical argument can be made in support of $\mathcal{MI}$. The radii of the two planets of Kepler-108 differ by only $\sim$20% (in all scenarios). In the $\mathcal{MI}$ model, the planet masses differ by a significant, but reasonable, factor of $\sim$3. In the $\mathcal{NC}$ model, the masses must differ by a factor $\sim$70, implying that planet c, with a radius $R_{\rm c} \approx 0.7 R_{\rm Jupiter}$ has a mass of only $M_{\rm c} \approx 0.02 M_{\rm Jupiter}$, which implies a lower density than all but the most extreme sub-Neptune planets (Masuda, 2014).

Here we have compared the coplanar models only for the case where Kepler-108B is the planet host. However, we perform an identical analysis for the case with Kepler-108A as the planets' host, and this analysis also favors the mutually inclined case to a similar significance. Thus, even if there is some doubt regarding which star the planets orbit, we may say unambiguously that the planets are mutually inclined.

4.3.1 Mutual Inclination Discussion

The mutual inclination, I, between the orbital planets of two planets b and c is given by

$$I = \cos^{-1}\left(\cos i_{\rm b}\cos i_{\rm c} + \sin i_{\rm b}\sin i_{\rm c}\cos(\Omega_{\rm b} - \Omega_{\rm c})\right). \tag{4.3}$$

In our case we have defined $\Omega_{\rm b} = 0$ and both planets have $i \approx 90^\circ$ since they are both transiting. This means that the value of $I \approx \Omega_c$. Using the MCMC posteriors on the planets i and Ω values, we compute $I = 24.2^{\circ}{}^{+10.8}_{-7.8}$, with a 95% confidence interval of [9.6°, 64.4°]. This is a significant departure from the $\lesssim 5^\circ$ mutual inclination expected from a pure disk formation origin.

4.4 Observation Statistics

Since the planets in this system are precessing due to the high mutual inclination between them, they will eventually change their orientation so dramatically that they no longer transit. This has been observed in circumbinary systems (Kostov et al., 2014; Welsh et al., 2015), but never in a single-star planetary system. Few other known extrasolar systems are likely to exhibit large inclination variations due to self-excitation (Becker & Adams, 2016). To investigate the timescale of the precession in this system, we integrate the best-fit solution forward for 10^5 years (Table 4.3). We find that both planets periodically precess on and off the star (see Fig. 4.7). From our viewing perspective, this system has two planets transiting 3% of the time, one planet transiting 4% of the time, and no observable transits 93% of the time. The precession timescale, $P_{\rm prec}$, is found numerically to be on average ~ 5700 years, somewhat longer than an analytic prediction ~ 4100 years using the frequency for Ω and i oscillations found by applying the Laplace-Lagrange secular solution to first order in planet mass and second order in inclination (e.g. Murray & Dermott, 1999).

In order to better understand the statistics of observing systems like Kepler-108, we explore the likelihood that this system is observed as two transiting planets experiencing

Figure 4.7: Kepler-108 Impact Parameter Evolution

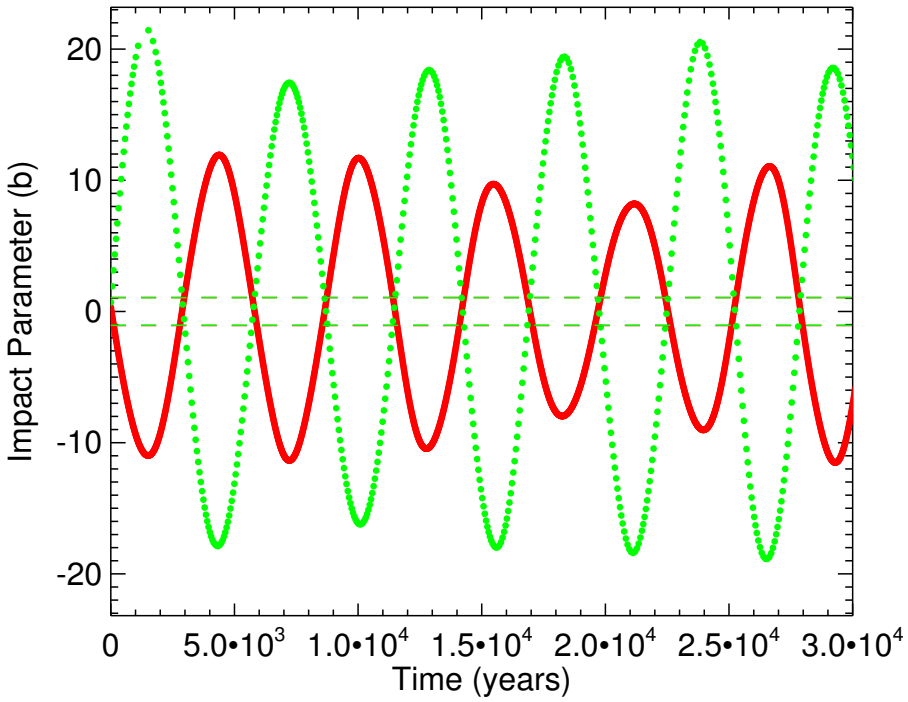

Evolution of the impact parameter (b) of both planets of Kepler-108 over 3×10^4 years. While b is usually reported as a positive definite quantity, we have assigned a negative value for b whenever the position of the planet at minimum b for a given transit is below the center of the star (negative y value). This allows us to visualize the planet moving up and down, on and off the star. Dashed lines show the maximum b where the planet will transit ($b_{\max} = (R_\star + R_i)/R_\star$, $i = b, c$). This data is taken from a portion of the 10^5 year run of the best-fit solution (see Table 4.3). The asymmetry with respect to $b = 0$ is due to the invariant plane being inclined to the observer.

TDVs from any orientation. We track the position in 3-dimensional space of both planets in our best-fit model every minute for one complete orbit of the outer planet at the beginning and end of the *Kepler* observing window. That is, we produce two $\vec{x}(t)$ functions for each planet ($\vec{x}_{\mathrm{b},1}(t)$, $\vec{x}_{\mathrm{b},2}(t)$, $\vec{x}_{\mathrm{c},1}(t)$, and $\vec{x}_{\mathrm{c},2}(t)$) each 190 days long and Δt ∼1300 days apart. We then randomly draw 10,000 different observing orientations and compute the impact parameter ($b_{\mathrm{j,k}}$, $j = b, c$, $k = 1, 2$) for each planet (b and c) in both windows (1 and 2) from each orientation. We compute the implied duration ($D_{\mathrm{j,k}}$) of the transit corresponding to each $b_{\mathrm{j,k}}$ using (Winn, 2010):

$$D_{\mathrm{j,k}} = \frac{P_{\mathrm{j}}}{\pi} \frac{\sqrt{1 - e_{\mathrm{j}}^2}}{1 - e_{\mathrm{j}} \sin(\omega)} \sin^{-1} \left(\frac{\sqrt{(R_\star + R_{\mathrm{j}})^2 - b_{\mathrm{j,k}}^2}}{a_{\mathrm{j}} \sin(i)} \right) \tag{4.4}$$

where the orbital elements come from the instantaneous position and velocity of the planets at the time of minimum b. This is a good approximation for the true duration. The change in duration over the observing window $(\Delta D)_{\mathrm{j}}$ is given by $D_{\mathrm{j},2} - D_{\mathrm{j},1}$. We establish as a detectability threshold $(\Delta D)_{\mathrm{j}} = 30$ minutes (the approximate limit of a confident detection of duration change in Kepler-108) and compute the fraction of observation angles for which $(\Delta D)_{\mathrm{j}}$ exceeds the threshold. We use the same threshold for both planets since they are approximately equal in radius, i.e. transit signal.

The results of this analysis are summarized in Table 4.4 which lists the fraction (and uncertainty) of randomly chosen viewing angles for which the Kepler-108 system would be observable as a two-planet system, one-planet system, and a no-planet system by the *Kepler* mission. Because the planets are highly mutually inclined, seeing a single planet transit does not guarantee that the second will be visible (see Fig. 4.8). The simulations demonstrate this as the two-planet observations are much fewer in number than the one-planet observations, which are dominated by the interior planet due to its closer orbit to the star. The second column shows the fraction of viewing angles for which Kepler-108 would appear to have duration variations in either planet of greater than 30 minutes (the approximate limit on a

Table 4.4: Kepler-108 Observational Likelihood

	Fraction of Viewing Angles With Planets Observed	Fraction with Planets and a Measurable Duration Drift
Two Planets	0.0006(2)	0.0005(2)
Single Planet	0.0439(21)	0.0080(9)
None Visible	0.9555(98)	n/a

confident detection of the duration change in Kepler-108). Approximately half of the cases where two planets are visible show measurable duration drift; however, in the case where only one planet is visible, measuring a duration drift will happen only ∼18% of the time.

It is clear from these statistics that our current viewing geometry is unusual. Since we have observed Kepler-108 as a 2-planet system exhibiting TDVs, it is probable that we have also observed similar systems in different viewing configurations. In other words, it is likely that some observed single-Jupiter systems may actually be members of mutually inclined multi-Jupiter systems. Thus, unless we are very unlucky, we expect that a close analysis of many systems with a single transiting Jupiter will reveal duration and depth changes in a few systems due to a non-transiting, mutually inclined companion. However, the measurement of a single planet's duration change gives very degenerate information about the perturbing planet's parameters, and it is more challenging to rule out systematics without a well-defined perturbing planet.

4.5 Future Observations

To assist potential future follow-up measurements, we predict TTVs and 1-σ uncertainties based on 100 random draws from the $\mathcal{MI}$ posterior up to 10 years after the end of *Kepler* data collection (Table 4.5).

4.5.1 Spin-Orbit Alignment

There is limited observable star spot activity on Kepler-108 in the *Kepler* data due to low S/N. Thus identifying the alignment of the stellar spin with the planets' orbits was not pos-

Figure 4.8: Projection of Transiting Geometry onto Celestial Sphere

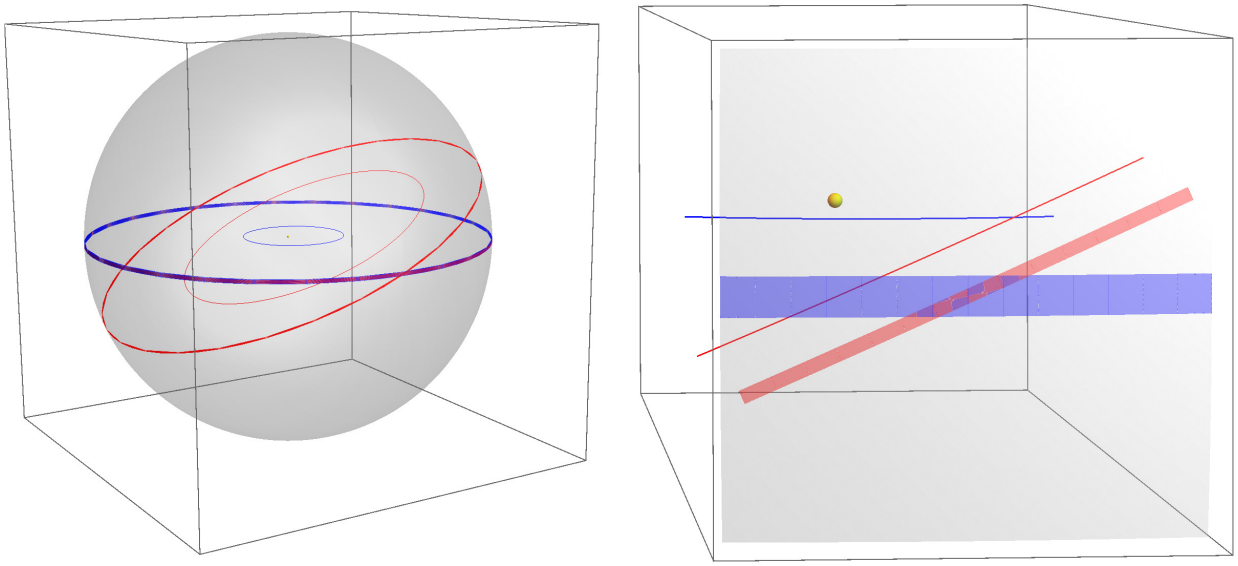

The orbits of Kepler-108 b and c are shown as thin blue and red lines respectively, to scale with the central star (yellow). The left hand panel shows a celestial sphere at 1AU (gray), with the blue and red bands indicating the regions of the sky where distant observers could view planets b and c in transiting geometries. Note that the surface area of these bands relative to the sphere is independent of the radius of the chosen sphere. The right hand panel shows a close-up of the section of the celestial sphere which is pointed towards the Earth. The small, approximately parallelogram-shaped overlap of red and blue is the only portion on the sky where both planets may be seen transiting simultaneously (like observed by *Kepler*).

Table 4.5: Kepler-108 Transit Times

	Kepler-108 b		Kepler-108 c	
n	Time (d)[a b]	Uncertainty (d)	Time (d)[a b]	Uncertainty (d)
-12	**74.908250**	**0.00096**		
-11	**124.09378**	**0.00085**		
-10	**173.27866**	**0.0010**		
-9	**222.46292**	**0.00069**		
-8	**271.64736**	**0.00059**		
-7	**320.83251**	**0.00085**		
-6	**370.01828**	**0.0013**		
-5	**419.20153**	**0.00066**		
-4	**468.38528**	**0.00061**		
-3	**517.56942**	**0.00099**	**245.68312**	**0.0025**
-2	**566.75554**	**0.0014**	**435.99272**	**0.0019**
-1	**615.93794**	**0.00075**	**626.31298**	**0.0019**
0	**665.12108**	**0.00060**	**816.64113**	**0.0019**
1	**714.30417**	**0.00098**	**1006.9681**	**0.0022**
2	**763.49001**	**0.0011**	**1197.2870**	**0.0023**
3	**812.67222**	**0.00069**	**1387.5972**	**0.0032**
4	**861.85535**	**0.00061**	1577.9021	0.0059
5	**911.03791**	**0.00091**	1768.2075	0.0092
6	**960.22324**	**0.00072**	1958.5204	0.010
7	**1009.4060**	**0.00068**	2148.8441	0.010
8	**1058.5897**	**0.00068**	2339.1728	0.0090
9	**1107.7724**	**0.00088**	2529.4974	0.0088
10	**1156.9574**	**0.00071**	2719.8132	0.010
11	**1206.1410**	**0.00067**	2910.1212	0.012
12	**1255.3256**	**0.00065**	3100.4256	0.016
13	**1304.5089**	**0.00086**	3290.7329	0.019
14	**1353.6939**	**0.00081**	3481.0495	0.020
15	**1402.8782**	**0.00069**	3671.3758	0.019
16	**1452.0636**	**0.00079**	3861.7039	0.018
17	**1501.2478**	**0.0011**	4052.0257	0.018
18	1550.4325	0.0011	4242.3386	0.020
19	1599.6171	0.0010	4432.6449	0.023
20	1648.8026	0.0013	4622.9495	0.027
21	1697.9878	0.0017	4813.2595	0.029
22	1747.1717	0.0015	5003.5798	0.029
23	1796.3560	0.0015	5193.9076	0.028
24	1845.5408	0.0018		
25	1894.7268	0.0022		
26	1943.9097	0.0018		
27	1993.0932	0.0017		
28	2042.2770	0.0019		
29	2091.4631	0.0022		
30	2140.6453	0.0017		
31	2189.8284	0.0016		
32	2239.0112	0.0017		
33	2288.1969	0.0018		
34	2337.3792	0.0015		
35	2386.5625	0.0015		
36	2435.7451	0.0015		
37	2484.9303	0.0015		
38	2534.1133	0.0014		
39	2583.2973	0.0015		

[a] BJD-2454900
[b] TTVS measured over the duration of the *Kepler* observing window are emboldened while future predicted TTVs are Roman.

Table 4.5 Continued: Kepler-108 Transit Times

	Kepler-108 b		Kepler-108 c	
n	Time (d)[a b]	Uncertainty (d)	Time (d)[a b]	Uncertainty (d)
40	2632.4801	0.0015		
41	2681.6651	0.0016		
42	2730.8490	0.0016		
43	2780.0339	0.0017		
44	2829.2174	0.0019		
45	2878.4024	0.0020		
46	2927.5869	0.0021		
47	2976.7723	0.0023		
48	3025.9569	0.0026		
49	3075.1414	0.0026		
50	3124.3259	0.0027		
51	3173.5113	0.0029		
52	3222.6968	0.0033		
53	3271.8804	0.0031		
54	3321.0644	0.0031		
55	3370.2489	0.0032		
56	3419.4350	0.0036		
57	3468.6176	0.0033		
58	3517.8009	0.0032		
59	3566.9843	0.0033		
60	3616.1703	0.0034		
61	3665.3525	0.0031		
62	3714.5356	0.0031		
63	3763.7183	0.0031		
64	3812.9037	0.0031		
65	3862.0863	0.0029		
66	3911.2698	0.0029		
67	3960.4523	0.0028		
68	4009.6375	0.0029		
69	4058.8207	0.0029		
70	4108.0051	0.0030		
71	4157.1881	0.0030		
72	4206.3731	0.0032		
73	4255.5572	0.0032		
74	4304.7423	0.0034		
75	4353.9262	0.0035		
76	4403.1110	0.0037		
77	4452.2956	0.0038		
78	4501.4811	0.0040		
79	4550.6660	0.0043		
80	4599.8502	0.0043		
81	4649.0346	0.0043		
82	4698.2198	0.0045		
83	4747.4055	0.0049		
84	4796.5888	0.0047		
85	4845.7725	0.0047		
86	4894.9566	0.0048		
87	4944.1428	0.0050		
88	4993.3252	0.0047		
89	5042.5083	0.0047		
90	5091.6915	0.0047		
91	5140.8773	0.0048		
92	5190.0576	0.0037		

[a] BJD-2454900
[b] TTVS measured over the duration of the *Kepler* observing window are emboldened while future predicted TTVs are Roman.

sible using star spot crossings (Nutzman et al., 2011). Previous spectroscopic measurements of Kepler-108 gave $v \sin(i_\star) = 5.3 \pm 0.6$ km s^{-1} where $i_\star$ is the inclination of the stellar spin axis to the line of sight and v is the star's rotational velocity (Huber et al., 2013a). For a star of radius $R_\star = 2.192 R_\odot$, this suggests a maximum rotation period ($i_\star = 90°$) of ∼22.4 days, but provides little information regarding the star's inclination relative to the observer. More importantly, it is not clear for which of the two stars in the binary this measurement is relevant.

The sky-projected angle between the stellar spin axis and the planets' orbit normals can be measured spectroscopically by identifying the change in apparent radial velocity of the stars as the planet crosses (known as the Rossiter-McLaughlin effect, see, e.g., Gaudi & Winn, 2007). The expected Rossiter-McLaughlin amplitude for the observed spin is $K_{\rm RM} = 6.9$ m s^{-1}, which is potentially observable (see e.g. Plavchan et al., 2015), though the transits are quite lengthy. These planets likely went through some chaotic destabilization event to get into mutually inclined orbits from their presumably coplanar, protoplanetary disk formation configuration. We therefore predict that the planets could be highly misaligned with the star's spin-axis[4].

4.5.2 Radial Velocity Constraints

Although we are confident that this system has a large mutual inclination, a small number of RV data points could help further constrain the system's parameters. RV measurements may be able to determine which star the planets are truly around and thus refine our fit significantly. Additionally, the RV curves are vastly different in shape between the $\mathcal{MI}$ and $\mathcal{NC}$ models due to the different eccentricities in the models. If the RV curve is observed to be saw-toothed, it would also give additional constraints on e and ω which are not well-measured in the photometry. Further, because the RV K amplitude is dependent on eccentricity (as

4. This would not be particularly abnormal, even without the large mutual inclination, because similarly massive stars commonly exhibit misalignment between planet orbits and stellar-spin (Winn et al., 2010; Mazeh et al., 2015b).

Figure 4.9: RV Signal Amplitudes

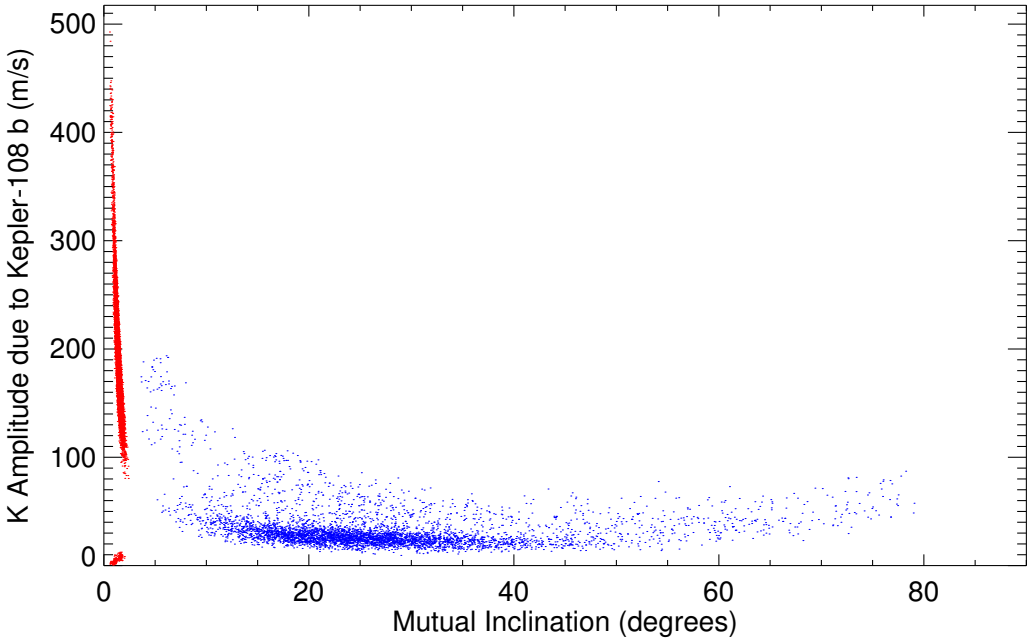

Theoretical K amplitude of the inner planet ($P \approx 49.2$ d) as a function of mutual inclination of the two planets for both $\mathcal{MI}$ (blue) and $\mathcal{NC}$ (red). Plotted are 10,000 randomly chosen points from both posteriors. Not only will a K amplitude give further weight to $\mathcal{MI}$, but it can also be seen that the $\mathcal{MI}$ region ($\gtrsim 7°$) has K dependence, implying RV measurements will better constrain mutual inclination there.

well as several other factors, Cumming et al., 1999),

$$K = \left(\frac{2\pi G}{P}(m_1 + m_2)\right)^{1/3} \frac{m_2}{(m_1 + m_2)} \frac{\sin(i)}{\sqrt{1 - e^2}}, \tag{4.5}$$

the overall amplitude of the RV signal will be drastically different in the nearly coplanar case $\mathcal{NC}$ compared to $\mathcal{MI}$, allowing for additional confirmation (Fig. 4.9). In addition, the K amplitude alone will help constrain the value of the mutual inclination in the highly mutually inclined case ($\mathcal{MI}$) since the K amplitude varies as a function of mutual inclination. A foreseeable challenge for RV measurements is that the two stars are only 1 arcsec apart, roughly the seeing limit for ground-based observations.

4.5.3 Non-transiting Planets

So far our discussion has included only the two planets observed in transit. The TTVs of the two observed planets can, in principle, put constraints on the orbits of non-transiting planets. Since the observed planets have moderate eccentricities and mutual inclinations, we must consider that any unobserved planet also may also have a substantial eccentricity and mutual inclination (which may be the cause of it not transiting). While constraints on non-transiting planets in systems where circular, coplanar orbits are assumed can be quite tight (Agol et al., 2005; Steffen & Agol, 2005; Agol & Steffen, 2007), considering eccentricity to first or higher orders vastly complicates this process (Agol & Deck, 2016). The addition of mutual inclinations will add further allowable TTV frequencies and amplitudes for unseen planets at a given period, and thus decomposing observed signals into the sums of transiting and hypothetical non-transiting planets to set upper limits on unseen planets of a given mass as a function of period becomes untenable.

Since the two planets completely explain the TTVs and the observed $P_{\rm sup}$ matches the expected result from two planets in the observed orbital periods (the residuals are consistent with no signal), we do not appeal to the existence of more planets. Additionally, more planets, particularly in a system of moderately high eccentricities and mutual inclinations, increases the chance that the system would be unstable.

The two known planets in Kepler-108 should both produce observable K amplitudes (Planet b: $\gtrsim 10$ m s^{-1}, Planet b: $\gtrsim 3$ m s^{-1}), and we expect that other Jovian-mass planets in the system with periods shorter than the outermost transiting planet ($P \approx 190.3$ days) may also be detectable through RV measurements. Since we speculate that this system experienced a planet–planet scattering event, it is likely that any other planets in the system may not be coplanar with the observed ones and thus only detectable through RVs, not transits. Small ($\lesssim 0.1 M_{\rm Jup}$) or longer period ($\gtrsim 200$d) planets would likely not be detectable by RVs.

4.6 Dynamical Discussion

We have presented a photodynamic analysis of the orbital parameters of the giant planet system Kepler-108. Planetary systems formed in disks are likely to be coplanar and nearly circular. However, the planets in Kepler-108 are shown to have a high mutually inclination ($I \gtrsim 10^\circ$) and eccentricity ($e_c \gtrsim 0.1$), not what one would expect from a purely disk formation origin. Instead, this system shows signs of a more violent, chaotic past as is predicted by theories of secular chaos and the formation of hot Jupiters, establishing an observational link between theoretical stages of planetary system evolution.

The presence of an additional companion star increases the richness of the dynamics of Kepler-108. Kozai-Lidov cycles from a distant companion have been suggested as a means of exciting eccentricities of planets, which may lead to strong planet–planet interactions including scattering and ejection (Malmberg et al., 2007). The timescale for Kozai-Lidov cycles is

$$\tau = \frac{2}{3\pi}\frac{P_\star^2}{P_\mathrm{p}}\frac{M_1 + M_2 + M_\mathrm{p}}{M_2(1-e_\star^2)^{3/2}} \tag{4.6}$$

(Kiseleva et al., 1998; Fabrycky & Tremaine, 2007), where 1 refers to the planet-hosting star, 2 the companion star, p the planet, and $P_\star$ refers to the binary star period. We do not know the period or eccentricity of the outer star, only its sky-projected distance, which is approximately 327 AU (Wang et al., 2015). The true distance is likely larger because this measurement ignores the separation of the stars along the axis in the direction of the observer. RV measurements could track the change in velocity as a function of time (i.e. a_z, where a is the acceleration and the subscript z represents the direction along the line of sight), which would allow an estimate of r_z, since M_2 and $r_\perp$ are known, where r is the distance between the objects and $\perp$ denotes the sky-plane direction, by solving the following for r_z:

$$a_\mathrm{z} = \frac{GM}{(r_\perp^2 + r_\mathrm{z}^2)^{3/2}} r_\mathrm{z} \tag{4.7}$$

However, even knowing the true separation of the stars would not reveal the period of the

companion star because the star's orbit may not be circular. Rather, the star may be near pericenter of much larger semi-major axis orbit or near apocenter of a much shorter, highly-eccentric orbit. Still, we desire to understand whether or not Kozai cycles from interactions with this companion star could be influencing the dynamics of Kepler-108 system.

If we assume the binary orbit is nearly circular and has a semi-major axis approximately equal to the sky-projected distance (327 AU), we derive $P_\star \sim 3900$ year and $\tau \sim 10$ Myr. This means that if the inclination of the companion star to the Kepler-108 c is large, it could potentially drive Kozai-Lidov oscillations and cause strong planet–planet interactions on this timescale. It is also entirely possible that the Kozai-Lidov timescale is longer than the age of the system (in large part because the timescale depends on the extremely uncertain $P_{\rm out}$ to the second power), or that the companion star is on a nearly coplanar orbit with the planets, in which case the Kozai-Lidov mechanism does not apply. Additionally, since the planet–planet precession interaction timescale is relatively short $P_{\rm prec} \ll \tau$, this can dominate the dynamics and prevent Kozai-Lidov cycles from occurring. To test this, we ran several realizations of the system by integrating forward in time the best-fit solution, with the additional companion star on a circular orbit at 327 AU, using the `MERCURY` integrator (Chambers, 2012). We run the simulations for 200 Myr, many times the expected Kozai-Lidov timescale of the system. The inclination of the companion star is varied by 10 degree intervals from 0 to 180 degrees. To ensure that the Kozai-Lidov mechanism works as expected in a three-body system, we also run the same set of simulations without the inner planet (Kepler-108 b). We find that the planet–planet interactions in the two-planet systems dominate and do not allow Kozai-Lidov eccentricity cycles to occur (see, e.g., Fig. 4.10). All two-planet systems tested remained stable for 2×10^8 years.

It is plausible that an additional planet at a much greater orbital period than of the observed 2 planets could have been subject to Kozai-Lidov oscillations shortly after dissipation of the natal disk, reached a high eccentricity, and caused a planet–planet scattering event. This could result in the large mutual inclination of the two observed planets. However, the

Figure 4.10: Kozai-Lidov Suppression

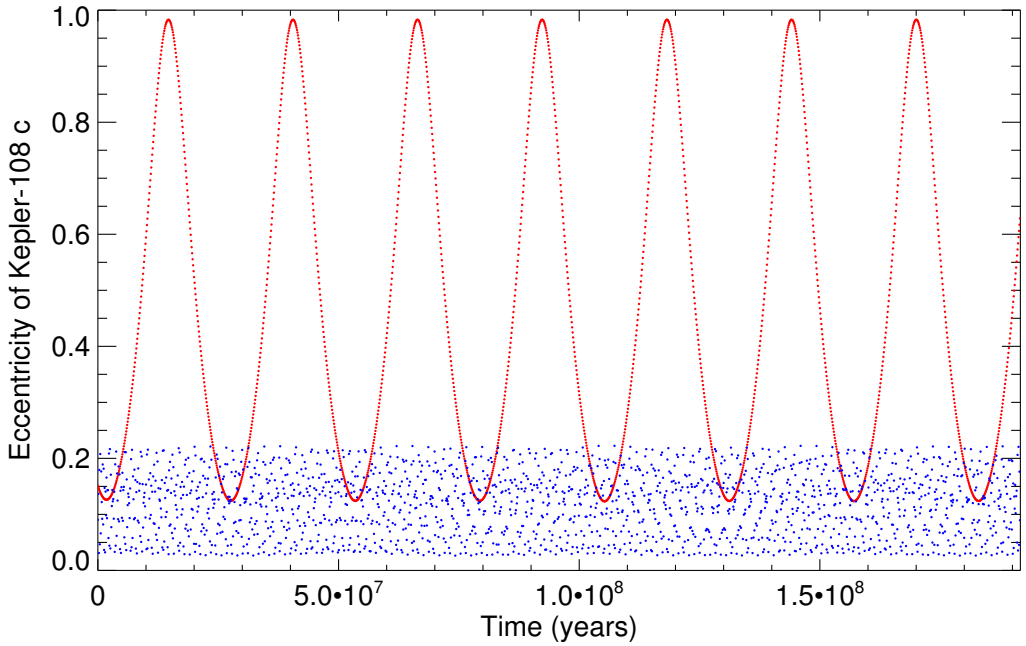

The eccentricity of Kepler-108 c as found by numerical simulation in the presence of a perturbing 1.377 $M_{\odot}$ star in a circular 327.5 AU orbit and $i = 10°$. The blue points represent the true 2-planet Kepler-108 system. The planet–planet interactions suppress the Kozai-Lidov oscillations and keep Kepler-108 c's eccentricities at moderate values. Kozai-Lidov oscillations driving Kepler-108 c are clearly present in a simulation with all other parameters identical, but not including the interior planet Kepler-108 b. These points are represented in red and show the very large and potentially destabilizing eccentricity swings that would result in Kepler-108 without taking the strong planet–planet interactions into account.

parameter space for unobserved, possibly-ejected, long-period planets is very large and we do not complete any numerical analysis of this scenario.

The rough similarity between the observed nodal precession timescales and the possible period of the binary star presents another intriguing possibility of the origin of this system: excitation of the planets' mutual inclination through a Laplace-Lagrange evection resonance (Touma & Sridhar, 2015). Studying the Kepler-108 system in this context may require additional data, particularly about the nature of the stellar binary's orbit, and theory, so we leave it to future work.

4.7 Summary

We have shown that the two gas giant planets in the Kepler-108 system in 49 and 190 day orbits are mutually inclined. A photodynamic TTV and TDV analysis produces a well-measured precession rate and reveals that a high mutual inclination model ($I = 24^{\circ}{}^{+11}_{-8}$) is strongly preferred by the data to a purely high eccentricity case with I less than a few degrees. We compute the likelihood of observing a system similar to Kepler-108 from any orientation and show that the probability of seeing it as a two-planet system with TDVs is very low, suggesting other similar systems exist but have not yet been identified as inclined multiplanet systems.

4.8 Appendix: Posteriors with Kepler-108A as the Planetary Host

Although it is strongly disfavored (see §4.2.2), for completeness we also report DEMCMC posteriors assuming Kepler-108 A is the stellar host (Tables 4.6 and 4.7).

Table 4.6: Disfavored Kepler-108A Posteriors

	Host: Kepler-108A					
	$\mathcal{MI}$ **- Mutually Inclined**			$\mathcal{NC}$ **- Nearly Coplanar**		
Parameter Name (Unit)	Median	68.3% (1-σ) Uncertainties	95.4% (2-σ) Uncertainties	Median	68.3% (1-σ) Uncertainties	95.4% (2-σ) Uncertainties
Stellar Parameters:						
$R_\star(R_\odot)$	2.13	$^{+0.12}_{-0.13}$	$^{+0.24}_{-0.25}$	2.21	$^{+0.080}_{-0.083}$	$^{+0.16}_{-0.17}$
$M_\star(M_\odot)$	1.377			1.377		
c_1	0.539	$^{+0.10}_{-0.092}$	$^{+0.21}_{-0.19}$	0.541	$^{+0.11}_{-0.10}$	$^{+0.22}_{-0.21}$
c_2	0.00	$^{+0.14}_{-0.14}$	$^{+0.28}_{-0.27}$	0.02	$^{+0.14}_{-0.14}$	$^{+0.28}_{-0.28}$
dilute	0.42	$^{+0.18}_{-0.22}$	$^{+0.31}_{-0.38}$	0.19	$^{+0.15}_{-0.13}$	$^{+0.28}_{-0.18}$
Kepler-108 b Parameters:						
P (d)	49.18336	$^{+0.00045}_{-0.00034}$	$^{+0.0022}_{-0.00075}$	49.183551	$^{+0.00015}_{-0.00018}$	$^{+0.00027}_{-0.00038}$
T_0 (BJD-2454900 (d))	665.12230	$^{+0.00070}_{-0.00075}$	$^{+0.0014}_{-0.0017}$	665.1099	$^{+0.0033}_{-0.0063}$	$^{+0.0053}_{-0.018}$
$e^{1/2}\cos(\omega)$	−0.270	$^{+0.094}_{-0.16}$	$^{+0.20}_{-0.34}$	−0.758	$^{+0.011}_{-0.011}$	$^{+0.023}_{-0.023}$
$e^{1/2}\sin(\omega)$	−0.116	$^{+0.060}_{-0.049}$	$^{+0.40}_{-0.23}$	−0.480	$^{+0.025}_{-0.025}$	$^{+0.050}_{-0.052}$
i (°)	91.06	$^{+0.18}_{-0.23}$	$^{+0.34}_{-0.51}$	92.01	$^{+0.21}_{-0.20}$	$^{+0.43}_{-0.42}$
Ω (°)	0.0			0.0		
M ($M_{\rm Jup}$)	0.48	$^{+0.25}_{-0.14}$	$^{+0.61}_{-0.22}$	1.93	$^{+0.45}_{-0.39}$	$^{+0.96}_{-0.71}$
$R/R_\star$	0.0504	$^{+0.0097}_{-0.0068}$	$^{+0.021}_{-0.010}$	0.0431	$^{+0.0044}_{-0.0028}$	$^{+0.0096}_{-0.0039}$
Kepler-108 c Parameters:						
P (d)	190.348	$^{+0.012}_{-0.015}$	$^{+0.027}_{-0.023}$	190.535	$^{+0.10}_{-0.087}$	$^{+0.22}_{-0.16}$
T_0 (BJD-2454900 (d))	816.669	$^{+0.013}_{-0.017}$	$^{+0.031}_{-0.036}$	816.831	$^{+0.10}_{-0.084}$	$^{+0.21}_{-0.15}$
$e^{1/2}\cos(\omega)$	0.081	$^{+0.078}_{-0.072}$	$^{+0.15}_{-0.13}$	−0.2408	$^{+0.0083}_{-0.0077}$	$^{+0.017}_{-0.015}$
$e^{1/2}\sin(\omega)$	−0.353	$^{+0.059}_{-0.036}$	$^{+0.66}_{-0.078}$	−0.4516	$^{+0.0083}_{-0.0085}$	$^{+0.017}_{-0.017}$
i (°)	90.542	$^{+0.053}_{-0.056}$	$^{+0.12}_{-0.11}$	90.567	$^{+0.030}_{-0.031}$	$^{+0.059}_{-0.063}$
Ω (°)	22	$^{+19}_{-9}$	$^{+36}_{-14}$	0.0		
M (M_{jup})	0.193	$^{+0.095}_{-0.074}$	$^{+0.20}_{-0.12}$	0.0295	$^{+0.0079}_{-0.0073}$	$^{+0.016}_{-0.014}$
$R/R_\star$	0.0449	$^{+0.0085}_{-0.0061}$	$^{+0.018}_{-0.0094}$	0.0391	$^{+0.0041}_{-0.0026}$	$^{+0.0088}_{-0.0037}$

The same format as Table 4.2, except with Kepler-108A as the host star, which is strongly disfavored (§4.2.2).

Table 4.7: Kepler-108B Best-Fit Solutions

	Planet	
Parameters:[a]	b	c
Period (d)	49.183166276551468	190.351354671141621
T_0 (BJD-2454900)	665.122980583247113	816.671779290328345
e	0.089986885710435	0.149122863867700
i (°)	91.010811057553170	90.522221912212288
Ω (°)	0.0	20.253567886356745
ω (°)	-154.480618347210282	-78.537503362093275
Mass ($M_{\rm Jup}$)	0.431852109916838	0.177045842528898
Radius ($R_{\rm p}/R_\star$)	0.051276491383251	0.045709799425805
$M_\star$ ($M_\odot$)	1.377	
$R_\star(R_\odot)$:	2.081902708396573	
c_1	0.548773346700056	
c_2	-0.020139937332240	
dilute	0.440556667838008	

	Planet	
Parameters:[a]	b	c
Period (d)	49.183540428579263	190.565864464644363
T_0 (BJD-2454900)	665.111007882649574	816.860367107108004
e	0.801635029977613	0.260981406054698
i (°)	91.977223010429583	90.561723018566155
Ω (°)	0.0	0.0
ω (°)	-147.861103185700557	-118.243316256653287
Mass ($M_{\rm Jup}$)	2.113070778746788	0.029094474876061
Radius ($R_{\rm p}/R_\star$)	0.043754954793284	0.039569609624921
$M_\star$ ($M_\odot$)	1.377	
$R_\star(R_\odot)$:	2.199762169565716	
c_1	0.540272159974162	
c_2	0.011661927881225	
dilute	0.213472272691092	

The same format as Table 4.3, except with Kepler-108A as the host star, which is strongly disfavored (§4.2.2). The χ^2 values here are 25409 and 25432 for the top and bottom parameters respectively.

4.9 Acknowledgements

We thank an anonymous reviewer and Titos Matsakos for helpful comments which greatly improved the quality of this manuscript. We thank Philip Lucas for assistance in understanding the UKIRT data and Thomas Barclay and Jason Rowe for helping us interpret *Kepler* systematics. This material is based upon work supported by NASA under Grant No. NNX14AB87G issued through the *Kepler* Participating Scientist Program. D.C.F received support from the Alfred P. Sloan Foundation. Computer simulations were run using the "Midway" cluster at University of Chicago Research Computing Center. Much of the data presented in this paper were obtained from the Mikulski Archive for Space Telescopes (MAST). STScI is operated by the Association of Universities for Research in Astronomy, Inc., under NASA contract NAS5-26555. Support for MAST for non-HST data is provided by the NASA Office of Space Science via grant NNX13AC07G and by other grants and contracts. The United Kingdom Infrared Telescope (UKIRT) is supported by NASA and operated under an agreement among the University of Hawaii, the University of Arizona, and Lockheed Martin Advanced Technology Center; operations are enabled through the cooperation of the Joint Astronomy Centre of the Science and Technology Facilities Council of the U.K. When the data reported here were acquired, UKIRT was operated by the Joint Astronomy Centre on behalf of the Science and Technology Facilities Council of the U.K. This work makes use of observations from the Las Cumbres Observatory Global Telescope Network, the Kepler Community Follow-up Observing Program (CFOP), and NASA's Astrophysics Data System (ADS).

CHAPTER 5

KEPLER-444

Kepler-444 is a five planet system around a host-star approximately 11 billion years old. The five transiting planets all have sub-Earth radii and are in a compact configuration with orbital periods between 3 and 10 days. Here we present a transit-timing analysis of the system using the full *Kepler* data set in order to determine the masses of the planets. Two planets, Kepler-444 d ($M_{\rm d} = 0.036^{+0.065}_{-0.020} M_{\oplus}$) and Kepler-444 e ($M_{\rm e} = 0.034^{+0.059}_{-0.019} M_{\oplus}$), have confidently detected masses due to their proximity to resonance which creates transit timing variations. The mass ratio of these planets combined with the magnitude of possible star-planet tidal effects suggests that smooth disk migration over a significant distance is unlikely to have brought the system to its currently observed orbital architecture without significant post-formation perturbations.

5.1 Introduction

Probing the mass-radius relationship for planets smaller than Earth is interesting to theorists as it may be used to constrain the formation and composition of these bodies, a topic of debate in the current literature (e.g Armitage, 2010; Chambers, 2010; Sinukoff et al., 2013; Chatterjee & Tan, 2014; Dupuy et al., 2016). A few planets in this size regime have been characterized (e.g. Sinukoff et al., 2013; Rappaport et al., 2013; Jontof-Hutter et al., 2015; Gillon et al., 2017); however, due to the small number of characterizable systems, little is yet known about the masses or compositions of the smallest ($\lesssim 1 R_{\oplus}$, $\lesssim 1 M_{\oplus}$) planets, despite them being among the most common in the galaxy (Malhotra, 2015).

Recent work has demonstrated the effectiveness of using photodynamic modeling to extract transit timing variations (TTVs) and planetary properties from systems with low S/N (e.g., Carter et al., 2012; Barros et al., 2015; Mills et al., 2016). This technique takes advantage of the many transits of short-period planets observed in the *Kepler* data by fitting

Table 5.1: Kepler-444 Planet Periods and Period Ratios

	Planet b	Planet c	Planet d	Planet e	Planet f
Period (d)	3.600105	4.545876	6.189437	7.743467	9.740501
Period Ratio		1.262707	1.361550	1.251078	1.257899
TTV Period (d)[a]		89.5	73.1	1780.3	308.5

[a] TTV super-period timescales calculated analytically based on the planet pair's distance from MMR (see, e.g., Lithwick et al., 2012).

the entire light curve and all transits simultaneously. Here, we apply this technique to Kepler-444.

Kepler-444's planets (b, c, d, e, and f from inside to out) range in radii from 0.4 to 0.8 $R_\oplus$ and in orbital period from 3.6 to 9.8 days (Rowe et al., 2015; Campante et al., 2015). Their period ratios are near, but not exactly on, mean motion resonances (MMRs; see Table 5.1). Despite the compact architecture of the system, it is around a star 11.2 ± 1.0 Gyr old (Campante et al., 2015) and therefore has likely been in a stable configuration for billions of years. A tight binary pair of M-dwarf stars also orbit together around Kepler-444 with a period of approximately 460 years and a distance of ~ 60 AU (Campante et al., 2015). Such a configuration poses a puzzle regarding the early history of the Kepler-444 system, as planetary formation and migration in a truncated protoplanetary disk in the presence of a very nearby binary star pair is not well understood, with several effects newly proposed (e.g., Touma & Sridhar, 2015; Xu & Lai, 2016). Recent studies have attempted to understand the possible histories of the system and use it to place constraints on formation mechanisms (Dupuy et al., 2016; Papaloizou, 2016). However, such studies were unable to use the actual compositions or masses of the Kepler-444 planets since they were hitherto unknown. In this paper, we use photodynamics to put constraints on the masses of the planets in the Kepler-444 system and report mass detections for two of the planets: $M_d = 0.036^{+0.065}_{-0.020} M_\oplus$ and $M_e = 0.034^{+0.059}_{-0.019} M_\oplus$.

5.2 Methods

We initially identified potential transit timing variations in the Kepler-444 system by simultaneously fitting the raw *Kepler* light curve with a planet transit model (Mandel & Agol, 2002) and a one-day wide polynomial to take into account systematic effects and stellar activity. Following Lithwick et al. (2012), we also compute the expected period of the TTV signal between each pair of planets analytically (Table 5.1), noting that period of the expected signal for planets d and e matches the TTV observations well (Fig. 5.1). We find statistically significant TTV between planets d and e, but the signal for all other planets is undetectably low as theoretically expected. The same conclusion was reached independently by (Hadden & Lithwick, 2017), a survey of many *Kepler* systems showing TTVs.

In order to perform a more robust, simultaneous fit for all planetary parameters, we first reprocessed the raw *Kepler* lightcurve data. We use short-cadence (58.8 second integration) data when it was available (*Kepler* observing quarters 4, 6, and 15-17) and long cadence data (29.4 minute integrations) otherwise. We first discarded points whose quality flag had a value equal to or greater than 16. We then detrended the light curves by masking out the expected transit times plus 20% of the transit duration to account for possible TTVs and then fit a cubic polynomial model with a 1000-minute width centered on photometric data points spaced by 30 minute intervals. We interpolated between these points to determine a baseline and divide the measured flux at each data point by these values. This detrending method produces two regions of extreme curvature in the lightcurve due to edge effects, so we discard the small regions with times BJD-2454900 = 1405.10 to 1405.18 days and 1490.88 to 1490.97 days. To account for certain Quarters showing higher noise levels than others despite all quarters having similar quoted uncertainties, we assign an uncertainty of 5.3030402e-05 to points in Quarter 12, 2.3470900e-04 in Quarter 16, and 6.5361999e-04 in Quarter 17, an increase over other regions by a factors of roughly 5, 4, and 11 respectively (the ratio of their out of transit standard deviation). Lastly, we increase the uncertainties in all points by a multiplicative factor of 1.38073 so that a fiducial fit to the light curve has a

$\chi^2 = 1.000$. This approach substantially increases the uncertainties on the fitted parameters compared to using the values reported by *Kepler*, allowing unmodeled noise to propagate to the final uncertainties on our parameter posteriors. We used data from *Kepler* Data Release 21 (DR21) for this analysis because there is less scatter in the DR21 data compared to the DR25.

Our photodynamic model integrates Newtonian equations of motions for the star and five planets including the light travel time effect (which in this case is negligible). When any of the planets pass in front of the star along the line of sight, a synthetic light curve is generated (Pál, 2012), which can then be compared to the data. The parameters we include for each planet in the differential evolution Markov chain Monte Carlo (DEMCMC; Ter Braak, 2005) fit are $\{P, T_0, e^{1/2}\cos(\omega), e^{1/2}\sin(\omega), i, \Omega, R_p/R_\star, M_p/M_\star\}$, where P is the period, T_0 is the mid-transit time, e is eccentricity, ω is the argument of periapse, i is inclination to the sky plane, Ω is nodal angle on that plane, and R and M are radius and mass respectively (with subscripts $p = b, c, d, e, f$ for the planets and $\star$ for the star). The star had five additional parameters: $\{M_\star, R_\star, c_1, c_2, dilute\}$, where c_i are the two quadratic limb-darkening coefficients and *dilute* is the amount of dilution from other nearby sources.

We put physically sensible, but permissive, minima ($\rho_p = 0.0$) and maxima ($\rho_p = \rho_{\rm Fe}$) on the bulk planet densities, where ρ_p is a planet's bulk density and $\rho_{\rm Fe}$ is the density of iron for a body of planet p's size. Taking values from (Seager et al., 2007), the maximum densities for the 5 planets from b to f respectively are (9.5, 9.7, 10.3, 10.5, 12.2) g/cm^3, differing due to the compressibility of iron. The prior on mass is otherwise flat between 0 and these values.

Since the mass and eccentricity implied by TTVs may be degenerate (Lithwick et al., 2012) and result in measured eccentricity values so high that the system go unstable on timescales much shorter than the age of the system (Pu & Wu, 2015), we use a Rayleigh prior on the eccentricity of all planets with width parameter $\sigma = 0.02$. This is consistent with the values measured in other tightly packed planetary systems (Hadden & Lithwick, 2014;

Fabrycky et al., 2014), and is consistent with long term stability because even moderate eccentricity has been shown to destabilize tightly packed systems (Pu & Wu, 2015).

The dilution is well-measured (Campante et al., 2015) so we fix $dilute = 0.0394$ since it would otherwise be highly degenerate with $R_p/R_\star$. This implies that the $R_p/R_\star$ value uncertainties may be slightly underestimated, but since (Campante et al., 2015) report $dilute = 0.0394 \pm 0.0001$, this will have only a very small effect on the reported posteriors. We also fix $\Omega_p = 0$ for all planets since we expect very small mutual inclinations between the planets because we see five planets transit (see, e.g., Lissauer et al., 2011a). Additionally, even modest values of Ω may greatly increase likelihood that the system becomes unstable over the system's lifetime due exchange of eccentricity and inclination on secular time scales. Since the transit information gives only the stellar density and planet-to-star mass ratio (via TTVs), we model with a fixed $M_\star = 0.758 M_\odot$, which sets the overall scale of the system. We use generic flat priors in all other parameters.

5.3 Results

Median values and 68.3% confidence intervals from the of photodynamic model are reported in Table 2. The full data set of the DEMCMC chains can be downloaded from the online version of this article. We ran a 64-chain DEMCMC for 900,000 generations recording every 1,000 generation, conservatively throwing out the first 50,000 generations as a burn-in. The autocorrelation timescale for the slowest converging parameters was approximately 60,000 generations, thus we are left with $\gtrsim$ 850 independent samples for each parameter. By numerically fitting the TTVs, the model produces mass constraints based on the *Kepler* data. Consistent with the measurement of individual transit times described in §5.2, planets b, c, and f do not induce significant TTVs on the other planets, which means their masses are not significantly detected. However, the TTVs in planets d and e are both significant enough to confidently place upper and lower bounds on the mass. The posteriors in mass are inconsistent with zero mass and fall off much more rapidly than the prior near $m = 0$.

Photodynamically measured TTVs are shown in Fig. 5.1, with the resulting mass constraints for planets d and e shown in Fig. 5.3 and reported for all planets in Table 5.2. Compared to the masses derived in Hadden & Lithwick (2017, $M_d = 0.2^{+0.5}_{-0.1} M_\oplus$ and $M_e = 0.1^{+0.2}_{-0.1} M_\oplus$), these new measurements ($M_\mathrm{d} = 0.036^{+0.065}_{-0.020} M_\oplus$ and $M_\mathrm{e} = 0.034^{+0.059}_{-0.019} M_\oplus$) are more precise. This is due in part to more a more restrictive and physical prior and in part to due to the photodynamic analysis method used in this study. We also compare individually measured 1-σ TTV posteriors from Holczer et al. (2016), to the photodynamic TTV posteriors in Fig. 5.2. We note that the relatively small error bars are a result of using the underlying physical model combined with the data of each transit and its neighboring transits to determine the best fit transit location and uncertainty. This dependence on neighboring transits due to model restrictions results in correlated measurements (unlike the independent Holczer et al. (2016) measurements), and therefore the quadratic sum of all of the points' distances from a nominal model normalized by their uncertainties may not be used to construct a simple χ^2 goodness of fit where independence is assumed.

We compute the posterior of $Z_{j+1,j}$ for each neighboring planet pair by approximating the value as $|z_{j+1} - z_j|/\sqrt{2}$ (see, e.g., Hadden & Lithwick, 2017, Eq. 4), where $z_j = e_j e^{i\omega_j}$ for each planet j and i is the imaginary unit. We find the median and 68% confidence intervals or upper limits $Z_{c,b} = 0.022^{+0.013}_{-0.011}$, $Z_{d,c} = 0.021^{+0.013}_{-0.010}$, $Z_{e,d} \leq 0.023$, $Z_{f,e} \leq 0.020$. We note that the interior planets are consistent with the prior alone, but the planet pair with detected masses (d and e) has a smaller value preferring low free eccentricity (Fig. 5.3). The absence of measurable TTVs induced by planet f on planet e also constrains $Z_{f,e}$. We compare these plots with similar M–$|Z|$ plots for all planets to demonstrate the full, joint mass-eccentricity constraints placed on planet f, and the unconstrained nature of planets b and c (Fig. 5.4). For completeness, we show the transits with TTVs removed in Fig. 5.5.

We also numerically integrate 100 draws from the DEMCMC posterior for 100 Myr to make sure we are exploring regions of parameter space stable for times comparable to a reasonable fraction of the system's age. 95% of the samples remain stable. Since approximately

Table 5.2: Photodynamic DEMCMC Posterior Median Values and 68.3% (1-σ equivalent) Uncertainties

Planet Parameters[a]

	Planet b	Planet c	Planet d	Planet e	Planet f
P (days)	$3.600105^{+0.000031}_{-0.000037}$	$4.545876^{+0.000030}_{-0.000031}$	$6.189437^{+0.000053}_{-0.000037}$	$7.743467^{+0.000060}_{-0.00010}$	$9.740501^{+0.000078}_{-0.000026}$
T_0 (days)	$815.08383^{+0.00052}_{-0.00055}$	$819.13903^{+0.00042}_{-0.00044}$	$816.70059^{+0.00072}_{-0.00072}$	$819.21772^{+0.00087}_{-0.00083}$	$817.89759^{+0.00038}_{-0.00032}$
$\sqrt{e}\cos\omega$	$-0.03^{+0.14}_{-0.10}$	$0.01^{+0.12}_{-0.13}$	$0.098^{+0.065}_{-0.12}$	$-0.035^{+0.12}_{-0.090}$	$-0.059^{+0.12}_{-0.078}$
$\sqrt{e}\sin\omega$	$0.048^{+0.099}_{-0.15}$	$-0.02^{+0.13}_{-0.11}$	$-0.014^{+0.10}_{-0.091}$	$0.038^{+0.074}_{-0.11}$	$0.052^{+0.075}_{-0.12}$
i (°)	$92.00^{+0.26}_{-0.30}$	$92.79^{+0.12}_{-0.11}$	$91.95^{+0.11}_{-0.10}$	$90.62^{+0.27}_{-0.35}$	$92.087^{+0.058}_{-0.054}$
Ω (°)	0 (fixed)	0 (fixed)	0 (fixed)	0 (fixed)	0 (fixed)
$M_p/M_\star$ ($\times 10^{-7}$)	$2.3^{+1.6}_{-1.6}$	$4.5^{+3.5}_{-3.2}$	$1.45^{+2.6}_{-0.81}$	$1.34^{+2.35}_{-0.74}$	$4.5^{+12}_{-3.5}$
$R_p/R_\star$ ($\times 10^{-3}$)	$4.967^{+0.070}_{-0.067}$	$6.380^{+0.090}_{-0.087}$	$6.613^{+0.079}_{-0.077}$	$6.799^{+0.078}_{-0.076}$	$9.39^{+0.13}_{-0.12}$

Stellar Parameters

$M_\star$ ($M_\odot$)[b]	$0.758\,(\pm 0.043)$
$R_\star$ ($R_\odot$)	$0.749^{+0.014}_{-0.013}$
c_1	$0.45^{+0.13}_{-0.14}$
c_2	$0.32^{+0.20}_{-0.19}$
dilute	0.0394 (fixed)

Planet Mass Posteriors Convolved with Stellar Uncertainties[b]

Planet	Radius ($R_\oplus$)	Median Mass ($M_\oplus$)	68.3% CI	95% CI	99% CI	Density (g cm^{-3})	68.3% CI	95% CI	99% CI
b	$0.406^{+0.013}_{-0.013}$		< 0.079	< 0.11	< 0.13		< 6.6	< 9.1	< 9.4
c	$0.521^{+0.017}_{-0.016}$		< 0.16	< 0.24	< 0.27		< 6.2	< 9.1	< 9.6
d	$0.540^{+0.017}_{-0.016}$	0.036	$[0.016, 0.10]$	$[0.0092, 0.20]$	$[0.0070, 0.27]$	1.27	$[0.56, 3.5]$	$[0.32, 7.2]$	$[0.25, 9.2]$
e	$0.555^{+0.018}_{-0.016}$	0.034	$[0.015, 0.093]$	$[0.0087, 0.19]$	$[0.0065, 0.25]$	1.08	$[0.48, 3.0]$	$[0.28, 6.1]$	$[0.21, 8.0]$
f	$0.767^{+0.025}_{-0.024}$		< 0.22	< 0.71	< 0.94		< 2.6	< 8.8	< 11

[a] Valid at $T_{\rm epoch} = 815$ (BJD - 2454900 days).

[b] $M_\star$ is held fixed at $0.758 M_\odot$ in the DEMCMC, but the posteriors are convolved with the uncertainties on stellar mass ($0.758 \pm 0.043 M_\odot$) from Campante et al. (2015) when determining uncertainties in physical units in the bottom panel.

Figure 5.1: Kepler-444 Photodynamic TTVs.

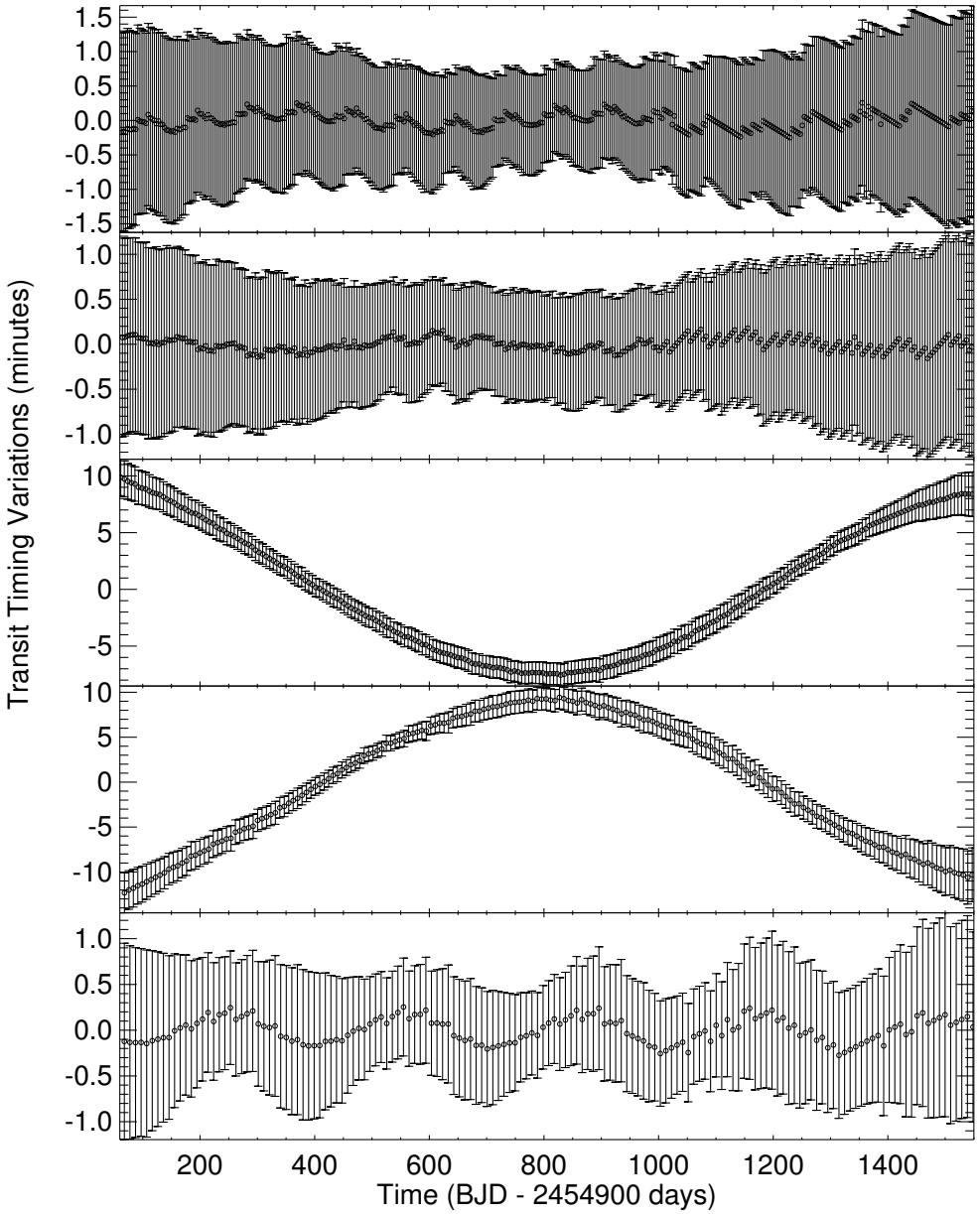

TTVs and uncertainties as measured by the photodynamic DEMCMC as described in §5.2. The values and error bars were generating by drawing from 100 parameter sets from the posterior and integrating the equations of motion to generate median and 1-σ uncertainties. The anti-correlated TTV signal between planets d and e with a $\sim$10 minute amplitude is readily visible by eye and results in a secure mass detection for both planets. All other TTV signals are below the noise level.

Figure 5.2: Comparison of Photodynamic and Individually Measured TTVs

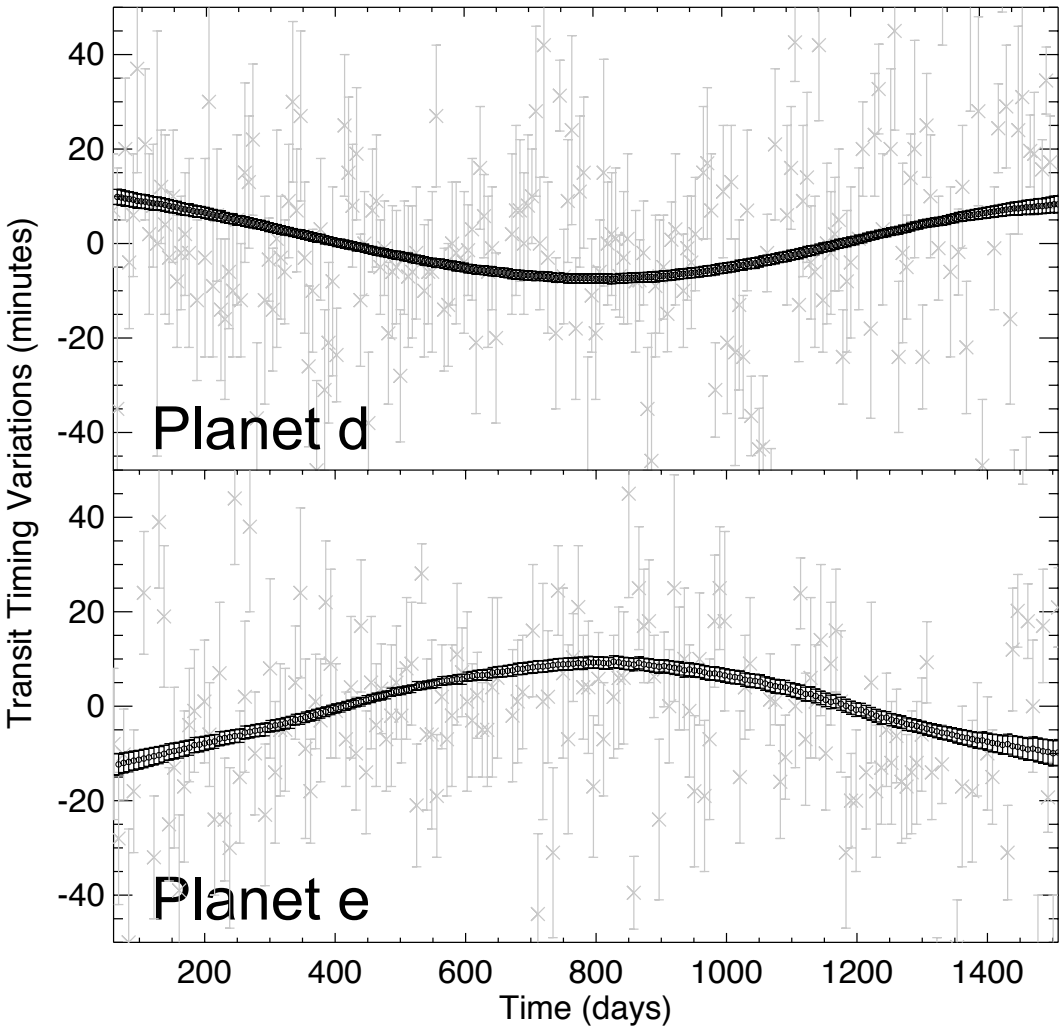

Photodynamic TTV posteriors for planets d and e (see Fig. 5.1) compared to individually measured TTVs in long cadence data from Holczer et al. (2016).

Figure 5.3: Planets d and e Mass and Eccentricity Posteriors

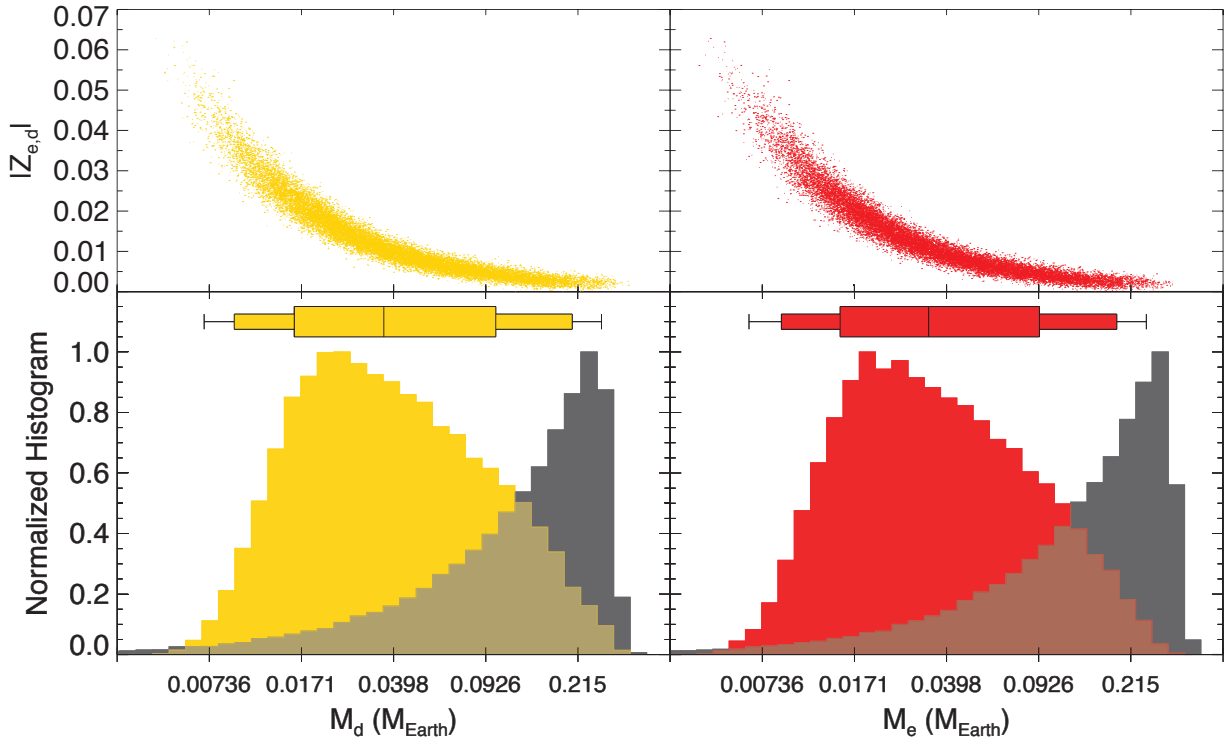

The posterior distributions of the masses of planets d (left, yellow) and e (right, red) against the $Z_{e,d}$ posterior (top) and marginalized over all parameters (bottom). The distribution of the mass prior for each planet is plotted in gray (note that the prior is flat in linear space). Box-and-whisker figures show the median, 68.3%, 95%, and 99% confidence intervals above the bottom panels. These panels illustrate how the posteriors cut off more rapidly than the prior at very low masses and also disfavor large masses because of the declining probability on the right hand of the distributions despite the increasing prior.

Figure 5.4: Planets b, c, and f Mass–Eccentricity Posteriors

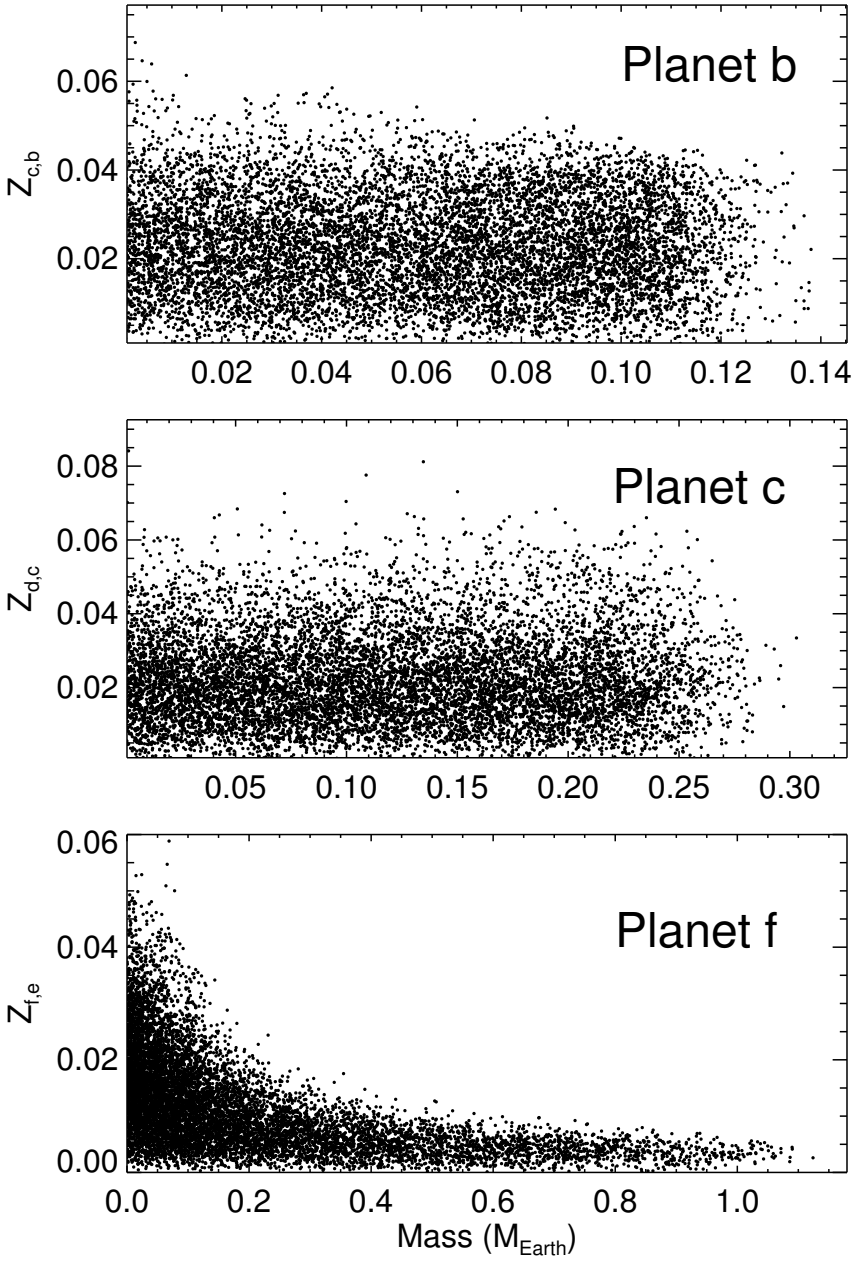

The mass–$|Z|$ posteriors for planets without confidently detected masses – note that posteriors extend continuously to $M = 0$. The top two panels indicate that the data show no preference away from the prior. However the lack of TTV in planet e sets a clear upper limit on the combination of mass and eccentricity in planet f. Note the different horizontal and vertical scales in each panel.

Figure 5.5: Kepler-444 Transit Lightcurves

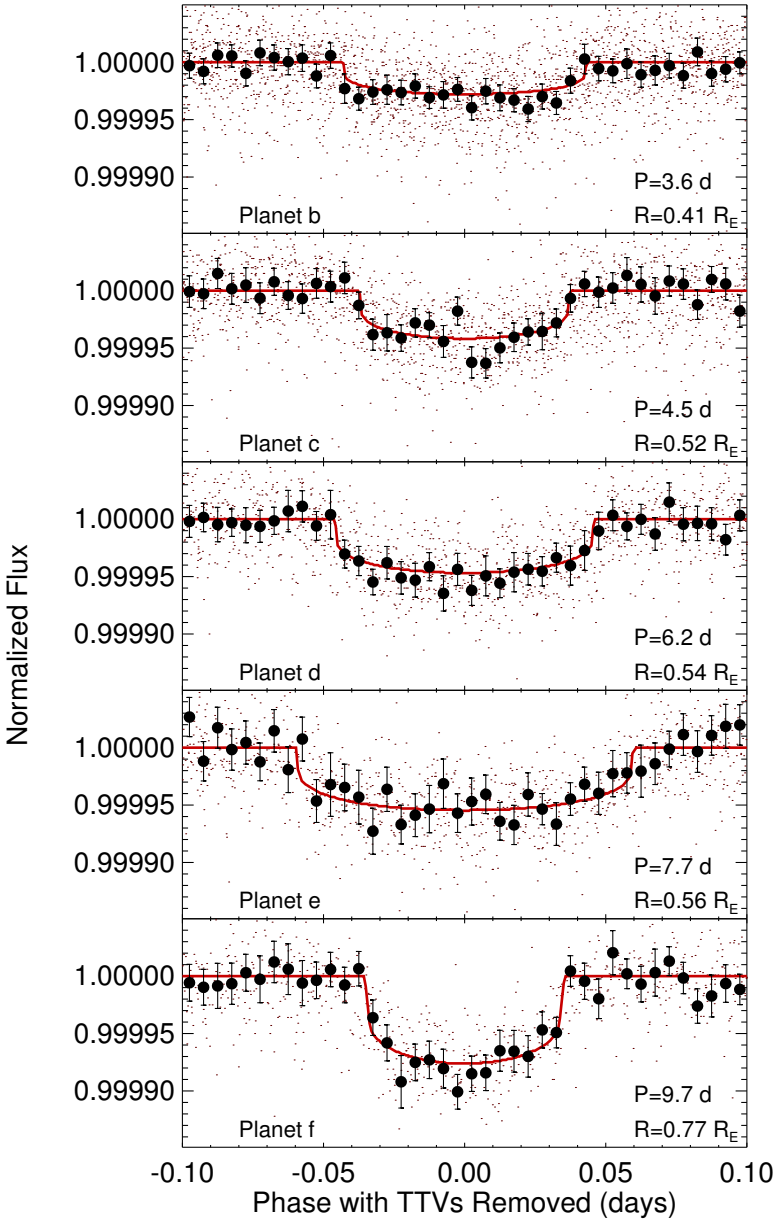

Transits are binned into 0.005 day intervals after phasing at the measured period and removing transit timing variations.

Figure 5.6: Planet Composition

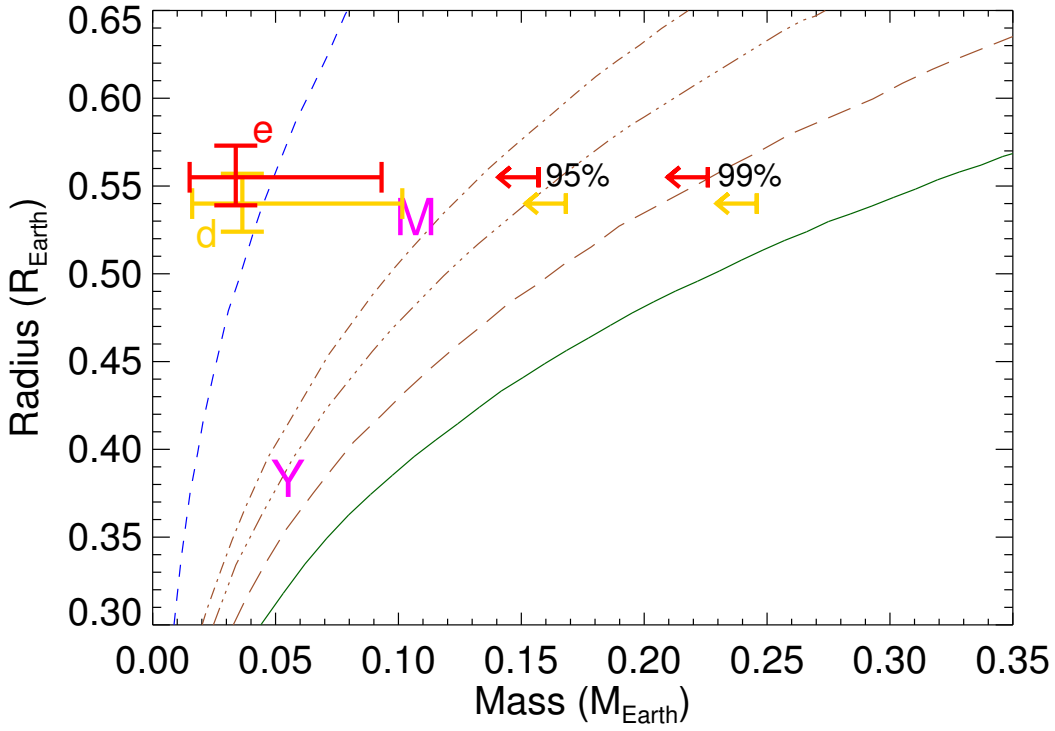

The mass and radius (and 1-σ uncertainties) of planets d (yellow) and e (red) are plotted on top of contours of constant composition taken from Seager et al. (2007). The solid green line represents pure iron planets, the brown lines pure rock ($MgSiO_3$), an Earth-like rock/iron ratio, and a Mercury-like rock/iron ratio from top to bottom, and the blue line represents a pure water planet. The vertical lines with arrows are the 95% and 99% upper bounds from the MCMC posterior, showing that the planets are inconsistent with a pure iron composition, and instead have a rockier composition consistent with the Solar System terrestrial planets. Mercury (Y) and Mars (M) are shown in pink.

equal numbers of systems are likely to go unstable in logarithmic bins of time (Pu & Wu, 2015), we expect $>$ 80% of our posterior to be stable for the measured system age of $\sim$11 Gyr.

Importantly, we note that at the 95% confidence level, both planets are inconsistent with being purely iron. Planet d requires a composition with a fraction of rock as least as great as Mercury ($\sim$30%), and, like Earth, planet e can be no more than 30% iron by mass. These measurements are plotted in Fig. 5.6 along with theoretical composition tracks taken from (Seager et al., 2007).

If we more speculatively suggest that the eccentricity of the planets is indeed very small ($|Z_{\rm e,d}| < 0.005$) as may be expected given tidal dissipation and a lack of strong external perturbations, then stricter mass constraints result (see Fig. 5.7). These constraints are more consistent with rocky bodies than those without a strict eccentricity upper bound, and are potentially more physically likely for such low-mass, highly-irradiated planets (e.g., Lopez & Rice, 2016).

5.4 Followup Observations

5.4.1 Radial Velocities

The radial velocity (RV) signal induced on a host star by a planet is given by (Cumming et al., 1999):

$$K = \left(\frac{2\pi G}{P}(M_\star + M_{\rm p})\right)^{1/3} \frac{M_{\rm p}}{(M_\star + M_{\rm p})} \frac{\sin(i)}{\sqrt{1-e^2}}, \tag{5.1}$$

where K is the RV amplitude, G the Newtonian gravitational constant, P the planet's period, $M_\star$ the stellar mass, and $M_{\rm p}$ the planet's mass. Inserting values for for Kepler-444 planets, we see that the expected K values range from ∼4-20 cm/s. This is below the current RV detection threshold (e.g., Plavchan et al., 2015).

5.4.2 PLATO

Because of the shallow transit depth, photometric follow-up is precluded for most existing instruments. However, the ESA's Planetary Transits and Oscillations of Stars Mission (PLATO) has recently received approval with operational dates of 2024-2020[1]. The precision goal for PLATO is 3.4×10^{-5} in 1 hour for stars with $m_{\rm V} \leq 11$. Since Kepler-444 is 2 magnitudes brighter, we may expect a factor of ∼10 times more photons and thus a precision of 1×10^{-5} per hour. Each planned 50 second exposure should therefore have a precision

1. See PLATO SCIRD - http://sci.esa.int/plato/42730-scird-for-plato/.

Figure 5.7: Low Eccentricity Mass Posteriors

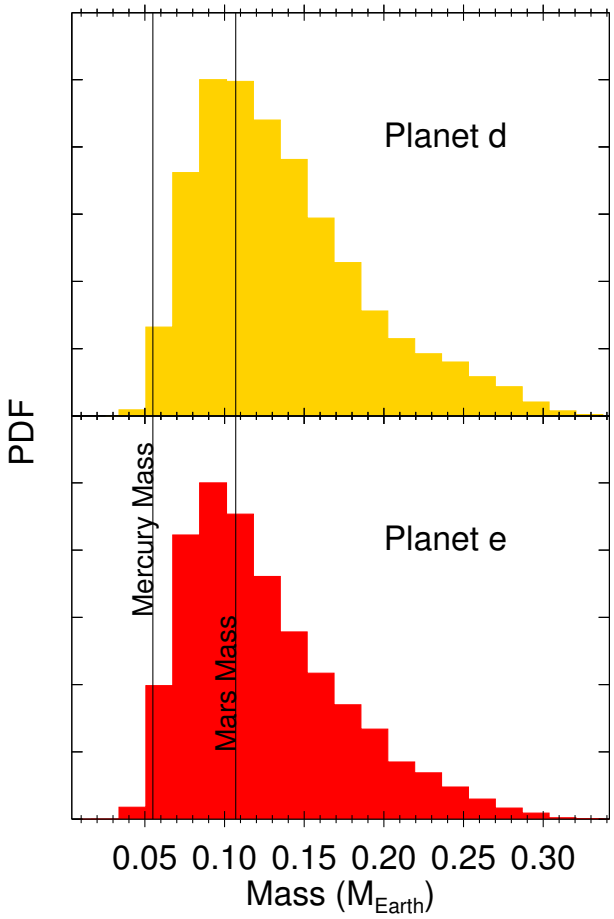

The distribution of mass posteriors for planets d and e when $|Z_{e,d}|$ is restricted to values below 0.005 assuming significant tidal dissipation. Due to the inverse correlation of mass and eccentricity, removing the high-eccentricity part of the posterior leaves only high mass values (see Fig. 5.3). Resulting 1-σ uncertainties are consistent with higher-density, rockier planets than suggested in Fig. 5.6.

of $\sqrt{3600/50} \times 10^{-5} \approx 8 \times 10^{-5}$. Taking several solutions from the *Kepler* data posteriors, based on the planned observing strategy we produce two-year sets of simulated PLATO transits beginning in 2025. We then add Gaussian noise to this data with $\sigma = 8 \times 10^{-5}$. Finally, we refit the combined actual *Kepler* data and simulated, noisy PLATO data to test how informative the PLATO measurements will be in further constraining the planet masses. We find that the mass constraints of planets d and e are improved to having ∼20% 1-σ uncertainties. Such a measurement may allow tight constraints on the fraction of the planet which is iron, rocky, or volatile, potentially distinguishing a water-rich planet from an Earth-like composition. Additionally, we find that in some cases Planet b (the smallest radius planet $R_b = 0.406 \pm 0.013 R_\oplus$) interacts with Planet c sufficiently to induce observable TTVs and a 99.7% confidence (3-σ equivalents) non-zero mass detection of Planet b. Such a measurement would make it (as of right now) the smallest exoplanet with a detected mass orbiting a main sequence star. To conclude, we note that the results in this section are dependent on the true noise properties and observing strategy of PLATO, which are currently uncertain.

5.5 Implications for Formation and Tidal Evolution

Papaloizou (2016, hereafter P16) performs an in-depth analysis of the possible migration history of the Kepler-444 system, considering both migration and circularization effects due to planet-disk interactions. Since the planets are very low mass, P16 assumes they are in the Type I migration regime with migration timescale, $\tau_{\rm mig} \propto M_{\rm p}^{-1}$. If the planets migrate at different rates (due to mass and local disk density), then one would expect them to approach MMRs with the other planets, at which point they would get trapped near those MMRs (Melita & Woolfson, 1996; Lee & Peale, 2002; Terquem & Papaloizou, 2007). An equilibrium would be reached where the resonant repulsion due to eccentricity damping is balanced by the differential migration rates of each pair of planets. Since the planets are up to 2% away from resonance, P16 speculates that significant relative contraction of the

planets did not occur, although significant migration as a unit might have. In order to match the observed period ratios, P16 assumes that planet e is significantly (by a factor of $\sim$3) more massive than d. This allows e to easily migrate more quickly than, and thus contract and approach resonance with, planet d while the other planets remain relatively more distant from resonances since they would not be as effective at overcoming the repulsive eccentricity damping force. Our photodynamical fit finds that $M_{\rm e}/M_{\rm d} = 0.93^{+0.14}_{-0.13}$, a significant departure from that assumption (see Fig. 5.8). This suggests that the present-day observed period ratios combined with smooth disk migration alone are generally insufficient for modeling specifics of the formation of the system. Many factors may have changed the migration of the planets while the disk was present, including local disk properties (Cossou et al., 2014) or turbulence in the disk (Oishi et al., 2007; Rein & Papaloizou, 2009). Alternately, the planets may have moved after the dispersal of the gas and dust disk, for instance via a combination of planetesimal crossings (Fernandez & Ip, 1984; Levison et al., 2007) or damping from tides raised by the star (Lee et al., 2013). Therefore, we caution against strict interpretations of observed exoplanet masses and architectures (or ensembles of these architectures) when it is likely that the systems have evolved substantially since their natal formation. We infer from the $M_{\rm e}/M_{\rm d}$ ratio that the system underwent significant orbital period changes after a migration formation, or formed in situ. We also note that very high, iron-like densities are disfavored, suggesting that large amounts of collisional stripping due to high velocity giant impacts likely did not occur (Marcus et al., 2010; Asphaug & Reufer, 2014).

Since the planets orbit very close to their host star, we consider the effects of tidal dissipation on the observed orbital period ratios. It is possible that tides on planets in or near a MMR causes their proximity to orbital resonance to change (generally spreading planets apart away from resonance) over Gyr timescales (Papaloizou, 2011; Lee et al., 2013). Following Papaloizou (2011, henceforth P11), we define δ_j as the distance from orbital resonance

Figure 5.8: Planet e to Planet d Mass Ratio

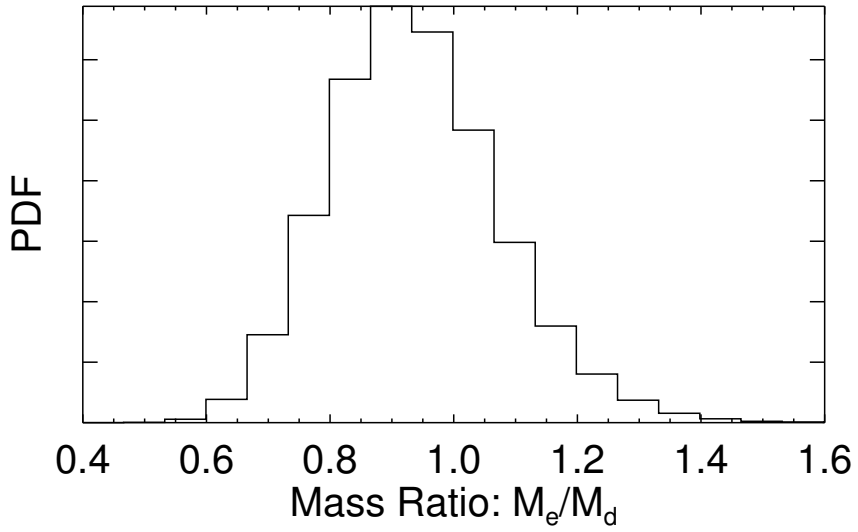

Photodynamic posteriors for the planet e to planet d mass ratio ($M_{\rm e}/M_{\rm d}$). This ratio is more tightly constrained than the individual planet masses.

by

$$\delta = \frac{n_j}{n_{j+1}} - \frac{(k+1)}{k}, \tag{5.2}$$

where n_j is the j^{th} planet's mean motion and k is the degree of the near first order resonance between planets j and $j+1$. P11 equation (40) gives the relation between the change in δ_j as a function of time and orbital parameters of the system. To determine analytically the amount tides would move planets away from exact resonance as a function of time P11 integrates Equation (40) from $t' = 0$ to $t' = t$ and assumes $\delta_{j,t=0} = 0$, i.e., the system begins in exact MMR (P11, Equation (42)). If, however, we integrate from $t' = 0$ to $t' = 11$ Gyr (the age of Kepler-444), and we know $\delta_{j,t=11Gyr}$ based on the observed system, we may solve for $\delta_{j,t=0}$ as a function of Q/k_2, the ratio of the tidal Q factor and the love number. This factor enters via the tidal circularization time

$$t_{c,j} = \frac{4}{63} \frac{M_j a_j^{13/2}}{(GM_\star^3)^{1/2} R_j^5} \frac{3Q}{2k_2}, \tag{5.3}$$

for the j^{th} planet (Goldreich & Soter, 1966; Rasio et al., 1996). We solve for the total change in distance from resonance since the planets' formation $\Delta_j = \delta_{j,t=11Gyr} - \delta_{j,t=0}$. For the inner pair of planets (b and c, $k = 4$), we find that $\Delta_1 \approx 7 \times 10^{-4} - 7 \times 10^{-7}$ for values of Q/k_2 ranging from 1 to 1000, using the approximation that $(Q/k_2)_b \approx (Q/k_2)_c$ which is reasonable given their similar size and proximity in the system. In the solar system, the rocky planets and large, rocky moons have $10 \lesssim Q/k_2 \lesssim 500$ (Goldreich & Soter, 1966). Since the observed $\delta_{1,t=11Gyr} = 1.27 \times 10^{-2}$, we see that tidal dissipation was insufficient to have moved the innermost pair a significant distance from its current period ratio and rules out tidal dissipation breaking a natal MMR. These findings are confirmed by long-term numerical N-body integrations, following (MacDonald et al., 2016).

The other pairs of planets have longer periods and, in the case of c and d, are further from resonance. They are thus generally less affected by tides. However, the period ratio of planets d and e are very close to resonance (Table 5.1) so even a small amount of dissipation may significantly impact their δ_3. Following Lee et al. (2013), we can set a limit on the tidal Q/k_2 factor for the innermost planet by using their equation (18) with the observed system age and planet parameters. We find $(Q/k_2)_d \gtrsim 12$. This limit is very near solar system values for rocky bodies, and possibly hints that the pair started in an exact MMR and was driven apart via this mechanism. This suggests that disk migration may have driven this pair of planets together, but the lack of tidally-broken commensurabilities among the other planets suggests the migration was not smooth or there were significant external perturbations after the disk dissipated.

5.6 Acknowledgements

We thank an anonymous referee for insightful comments which considerably added to the quality of this manuscript. This research is supported by Grant NNX14AB87G issued through NASA's *Kepler* Participating Science Program.

CHAPTER 6

CIRCUMBINARY PLANETS

To date there have been 11 planets identified orbiting two main sequence stars (circumbinary planets or CBPs; Doyle et al., 2011; Welsh et al., 2012; Orosz et al., 2012b,a; Schwamb et al., 2013; Kostov et al., 2014; Welsh et al., 2015; Kostov et al., 2016; Orosz et al., in prep.). While it is natural to speculate that the same processes that form planets around single stars would prevail in forming planets in circumbinary disks, new processes due to the second massive star may be important (e.g., Ford et al., 2000), or the relative importance of the processes may be different compared to single-star systems. To understand these differences requires a well-characterized sample of CBPs to match their single-star counterparts. Here I summarize a few key characteristics ascertained with the relatively small sample of CBPs thus far.

All of the CBPs discovered to date have low ($\lesssim 5^\circ$) mutual inclinations between the planets and their host binary. Additionally, the three planets of the only known multiplanet circumbinary system, Kepler-47, are coplanar to within 2° (Orosz et al., 2012a). Since dissipation in disks keeps planets coplanar, this suggests migration through a protoplanetary disk that was aligned with the binary pair brought the planets to their current positions (Foucart & Lai, 2013). However, this conclusion is affected by observational bias – planets aligned with their binary hosts are more likely to be observed as transiting eclipsing binaries (Borucki & Summers, 1984; Martin & Triaud, 2015). We await the completion of ongoing studies of non-transiting CBPs to understand the full distribution of binary-planet mutual inclinations (cf. Armstrong et al., 2014; Li et al., 2016).

The orbital periods of the first eight published CPBs were within a factor of 2 of the critical period (Welsh et al., 2015; Winn & Fabrycky, 2015),

$$P_{\rm crit} \approx \left(1.60 + 5.10 e_{\rm bin} - 2.22 e_{\rm bin}^2 + 4.12\mu - 4.27 e_{\rm bin}\mu - 5.09\mu^2 + 4.61 e_{\rm bin}^2\mu^2\right)^{3/2} P_{\rm bin}, \quad (6.1)$$

where $\mu = M_{\rm B}/(M_{\rm A} + M_{\rm B})$, below which planets go unstable (Eq. 3, Holman & Wiegert,

1999). This result is consistent with expectation based on planet migration (Pierens & Nelson, 2007, 2013; Kley & Haghighipour, 2014, 2015), although could also be in part due to observational bias (Armstrong et al., 2014; Winn & Fabrycky, 2015; Li et al., 2016). More recent results cast doubt on the robustness of the clustering, with Kepler-453 b's period more than a factor of two greater than the critical instability period (Welsh et al., 2015), and Kepler-4153 b's nearly a factor of 10 larger (Kostov et al., 2016).

Lastly, there are no Earth-like CBPs observed, with the smallest CBP to date having $R = 3R_{\rm Earth}$ (Orosz et al., in prep.). This result may also be attributed to observing bias from a combination of several factors. A single transit of a planet of a given radius will be less deep if it transits a star in a binary compared to the same transit across an isolated star. This is because the other star's light dilutes the transit depth. Additionally, conventional planetary transit search algorithms rely on the periodicity of the transits to bin together many transits to increase signal to noise of the detection. These searches generally work by phasing the data at a constant period throughout the data set and fitting a transit model. This approximation fails dramatically for CBPs where TTVs can exceed the transit duration by a large factor, thus smearing out the transits (Armstrong et al., 2013). Additionally, transits can start and stop over the course of the data set due to rapid precession induced by the binary (e.g., Kostov et al., 2014; Welsh et al., 2015). Eclipsing binary light curves have a lot of additional astrophysical signal which may mask transit events: in addition to the normal stellar noise and starspot signals, the stellar eclipses themselves are generally orders of magnitude deeper than planetary transits and can obscure them (e.g., Kostov et al., 2016).

In this chapter I will introduce KIC 10753734, a new addition to the CBP sample, and briefly review my contribution to the analysis of Kepler-453. This work is part of a community effort to characterize many individual systems with high precision so that physical models can be applied to individual systems as discussed above, and statistical studies may be begun. Additionally, these systems serve as probes to uncertain stellar physics which circumbinary planets can uniquely access (see, e.g., Orosz et al., 2012a; Boyajian et al.,

2012; Tal-Or et al., 2013)

6.1 KIC 10753734

This section describes the discovery of a planet in the binary star system KIC 10753734 and its initial modeling. This work is still in progress – for a complete analysis and final results see Mills et al. in prep.

6.1.1 Binary System

The KIC 10753734 stellar system is a known binary pair of of main sequence G dwarf stars with a 19.39220 day period (Prsa et al., 2011). We label the primary star A, the secondary B, and the planet p throughout. Radial velocity (RV) observations of KIC 10753734 were also obtained from BJD 2456504 to BJD 2456530 at the Hobby Eberly Telescope (HET), shortly after the *Kepler* observing window (Table 6.1). The spectra were double-lined, allowing RV measurements for each star in the system. The RV data are consistent with photometric measurements – a joint fit of eclipse times and RV data is show in Fig. 6.1, including a constant RV offset $C_{\rm RV}$ as a free parameter. The RV uncertainties quoted in the table were increased by a factor 5.1 so that our nominal model has $\chi^2_\nu = 1.00$.

Inspection of the *Kepler* lightcurve after the removal of systematics using the CBVs as discussed in §4.2.1 reveals large amplitude ($\sim$1%) variability in the flux from the KIC 10753734 binary away from eclipse (see Fig. 6.2). This is indicative of stellar rotation with starspot activity. The total observed flux decreases (increases) as the colder, darker starspots rotate into (out of) view. Variations in the shape of the eclipses confirm the starspots and reveal that both of the stars possess star spots and are rotating asynchronously with the orbit (since the location of the spots is changing). The bumps in the fit residuals indicate the passage of the eclipsing star over a spot on the background star, thus decreasing the

Table 6.1: KIC 10753734 RV Observations

Time (BJD-2454900)	RV (m s^{-1})	1-σ Uncertainty (m s^{-1})
KIC 10753734 A		
1604.8675950	-22045	692
1605.6377210	-20439	642
1606.6488530	-17080	700
1608.8633230	-6132	702
1609.6419980	1908	26291
1610.8373720	7532	828
1613.8455570	76649	741
1616.6215630	4134	26093
1617.8395860	-11013	433
1621.8319380	-25036	455
1622.8193050	-24325	422
1626.7271850	-15920	493
1630.8064110	17459	823
1633.6783800	86019	724
1634.7017760	60281	779
KIC 10753734 B		
1604.866813	30026	1574
1605.636940	27861	1542
1606.648071	24511	1347
1608.862542	11958	1473
1609.641217	1908	27178
1610.836590	-2737	1822
1613.844776	-78370	1720
1616.620781	4134	26093
1617.838804	18097	869
1621.831157	33595	1123
1622.818524	32709	1275
1626.726404	21823	1096
1630.805629	-12562	1027
1633.677599	-88072	706
1634.700994	-59097	1010

Figure 6.1: KIC 10753734 RV Model

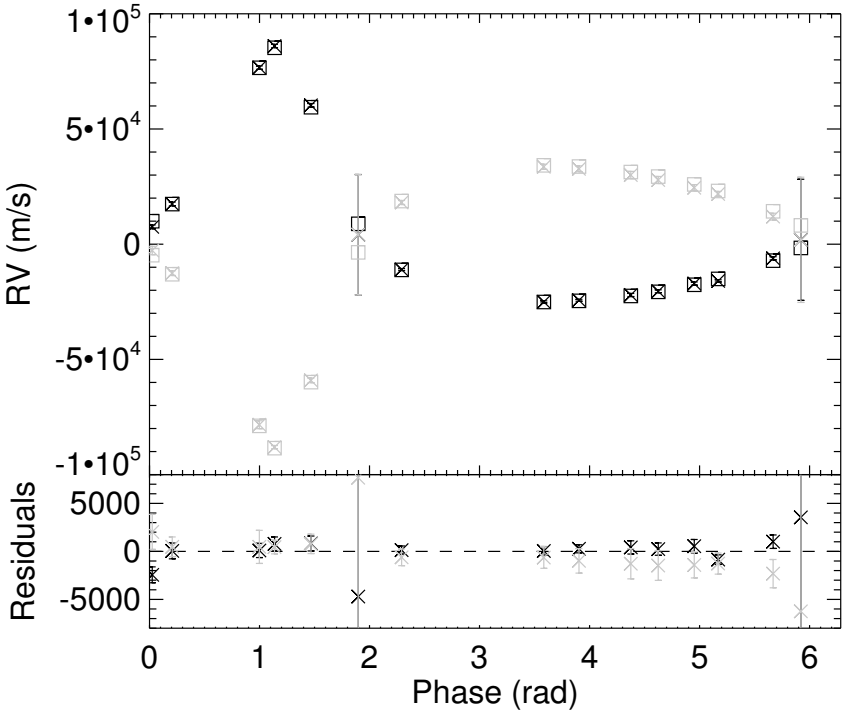

Measured RV data (×s with 1-σ uncertainties) phased at the binary orbital period compared to a joint eclipse timing and radial velocity fit model (open squares). The RV of the primary is shown in black, and the secondary in gray.

total flux blocked and causing a small apparent spike in intensity during the eclipse[1] (see Figs. 6.3 and 6.4).

The frequency of the star spot modulations reflects the stellar rotation periods. Since the eclipses reveal that both stars have spots we may expect two dominant frequencies, one at the rotation period of each star. We prepare the lightcurve for starspot frequency analysis by taking the *Kepler* photometric data set with CBV detrending (as shown in Fig. 6.2), and masking out the full duration plus a 10% buffer of every primary and secondary eclipse. We then apply a Lomb-Scargle (LS) periodogram (Lomb, 1976; Scargle, 1982) to this lightcurve. A dominant frequency peak (along with its first harmonic) is seen at $P \approx 8.6$ days in the periodogram (Fig. 6.5). Fig. 6.6 shows the autocorrelation function of the lightcurve taking into account missing data, which may be more effective at determining periods if the phase of the spots is changing or the spots are short-lived relative to the observing window. A single dominant mode is again present, suggesting a period of 8.8 days. This period does not match either the orbital period of the binary pair (19.4 days), nor the pseudo-synchronous rotation period (6.1 days), which may result if the stellar rotation rates are dominated by the binary pericenter passage speed where tides are strongest (Hut, 1981). The similar amplitude of the starspots in the eclipse measurements for both stars suggests that if both stars were rotating they should have similar amplitude effects on the lightcurve, and therefore two equally strong periods may be measured. The existence of a single dominant frequency tentatively suggests that both stars have a similar rotation period. This is indeed consistent with empirical and theoretical models of stellar rotation of main sequence stars, where stars that are nearly the same mass and likely the same age (due to binaries forming together from the same protostellar cloud) should have similar rotation periods (gyrochronology, see, e.g., Skumanich, 1972; Barnes, 2003; Mamajek & Hillenbrand, 2008; Angus et al., 2015; van Saders et al., 2016). However, in this case stellar tides have likely reduced the spin-down

1. In principle, faculae and other bright features may also be eclipsed resulting in downward spikes in transit, but this effect is generally smaller than the dimming caused by starspots for active and fast-rotating stars (Montet et al., 2017).

Figure 6.2: KIC 10753734 Lightcurve

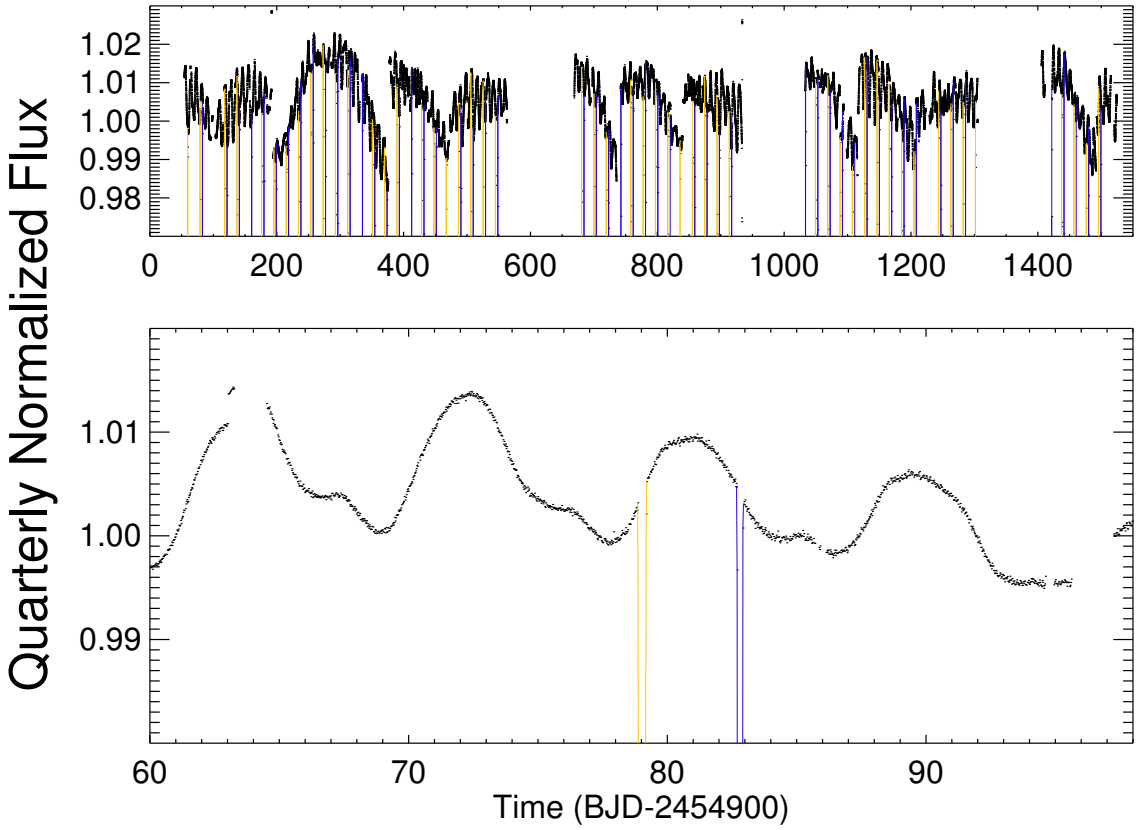

The KIC 10753734 lightcurve showing percent-level quasi-periodic variability due to starspots. The top panel shows the entire lightcurve, with the data in each observing quarter divided by the quarterly mean value to normalize the flux values. The lower panel focuses on a single observing quarter so that the detailed nature of the variation may be observed. In both panels primary eclipses are highlighted in blue and secondary in yellow, but the full depth is cut off to show detail in the out-of-eclipse lightcurve.

Figure 6.3: A Sample of Primary Eclipses

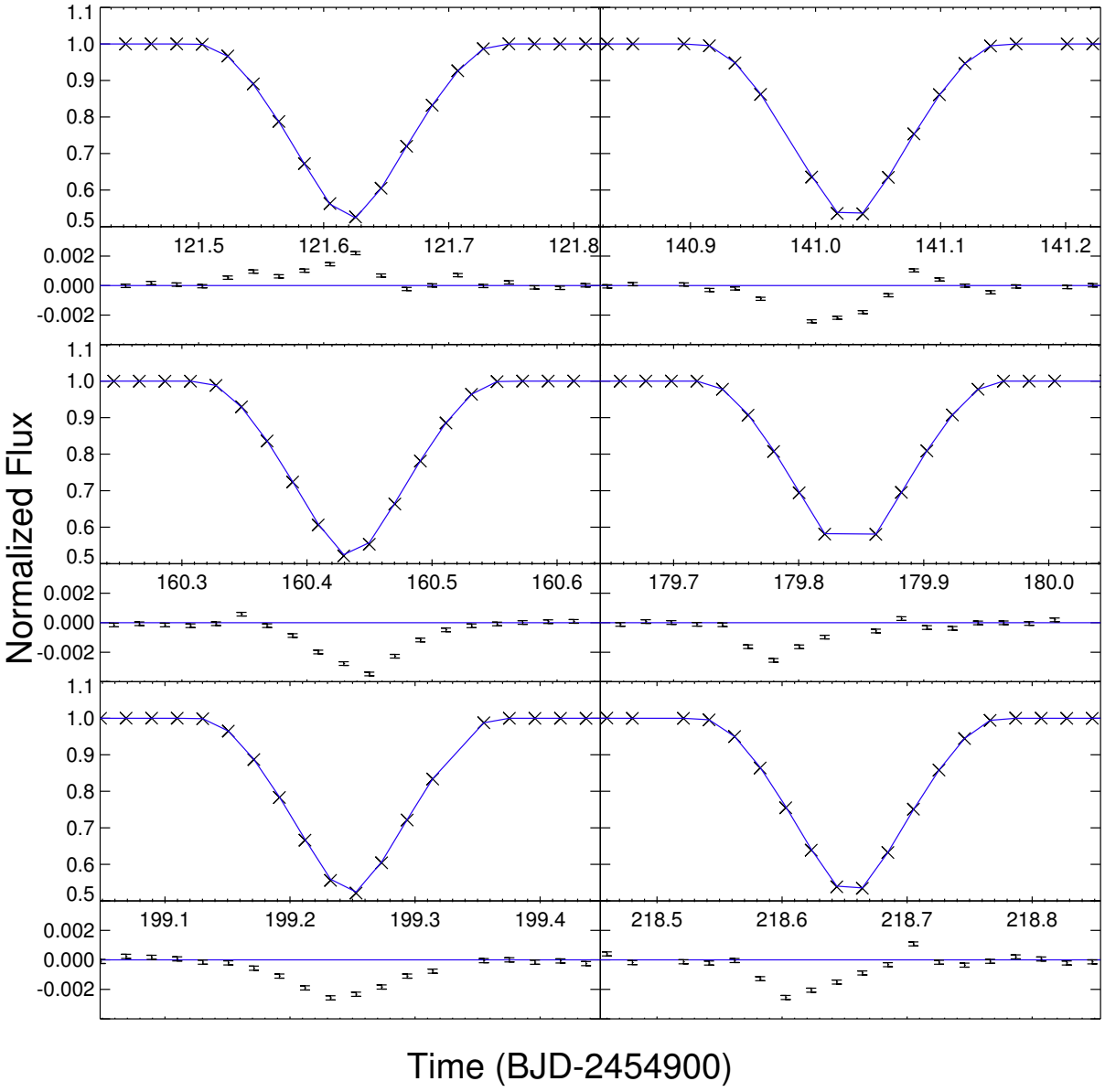

Six primary eclipse observations (black) and a naive global fit (blue), with residuals and uncertainties plotted below each eclipse. Outside of eclipse the residuals are relatively flat, but during eclipse their correlated nature suggests the presence of star spots on the primary star.

Figure 6.4: A Sample of Secondary Eclipses

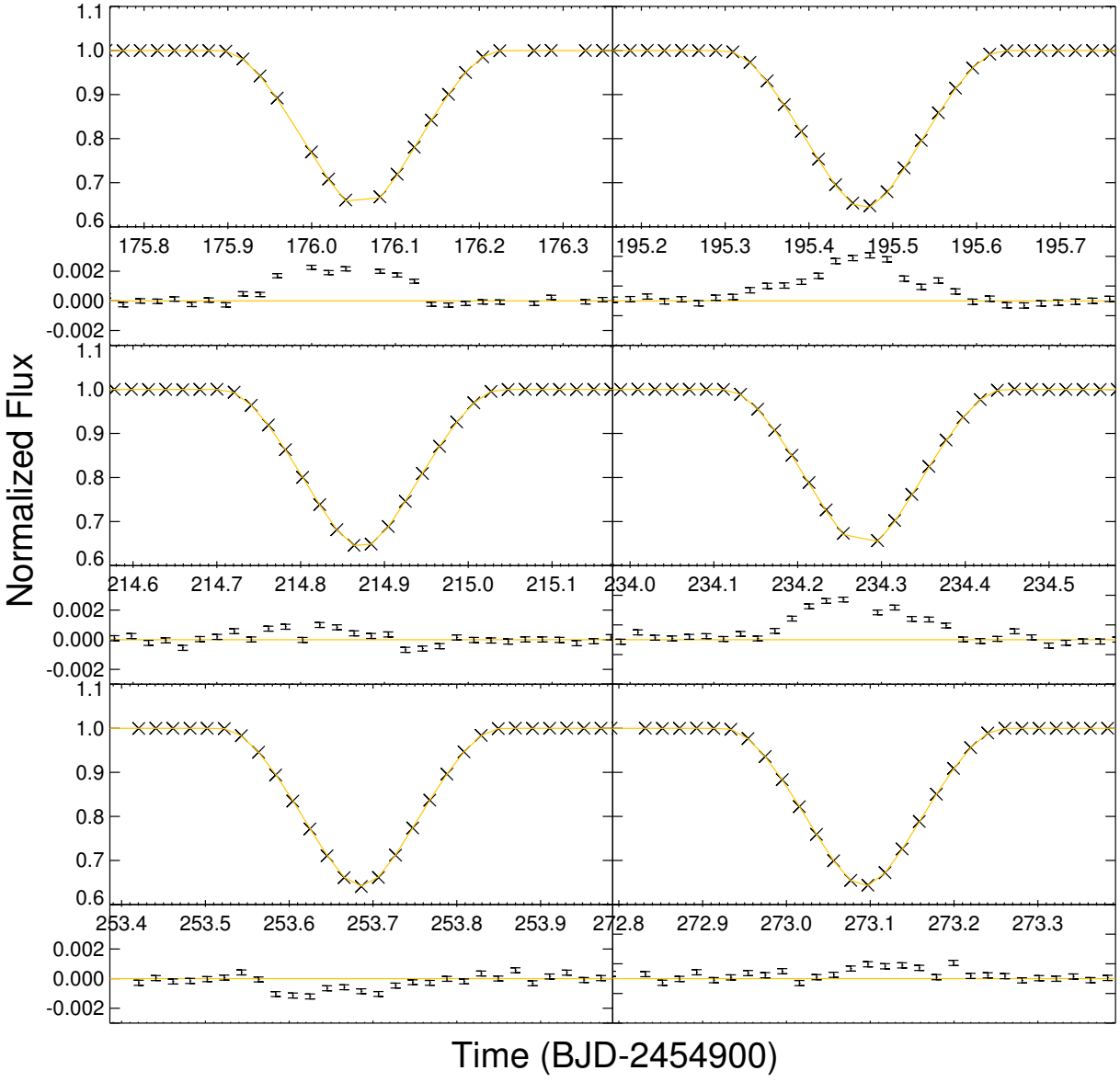

Similar to Fig. 6.3, but instead showing six secondary eclipse observations (black) and a naive global fit (yellow), with residuals and uncertainties plotted below each eclipse. Again, the out-of-eclipse data are consistent with a flat line, but inside their correlated nature suggests the presence of star spots on the secondary star as well.

Figure 6.5: Starspot LS Periodogram

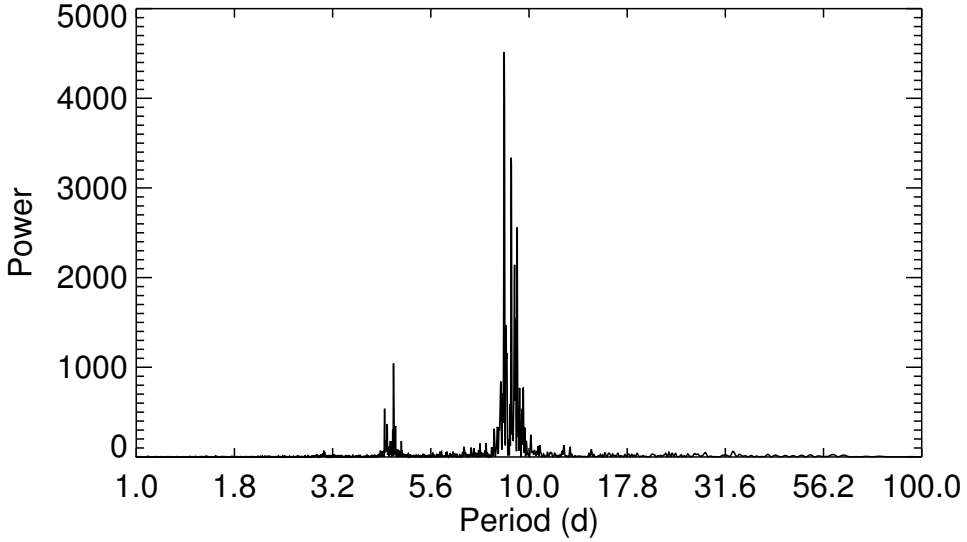

LS periodogram of the KIC 10753734 lightcurve after removing instrument systematics and masking out stellar eclipses, revealing a strong periodicity of 8.6 days and its first harmonic at 4.3 days.

(Hut, 1981).

6.1.2 Identification of Planetary Transits

Three planetary transits in KIC 10753734 were identified by visual inspection of the lightcurve. The first visually identified transit was detected at approximately BJD 2456137, roughly 1200 days into *Kepler*'s observing window (the transit marked by the dashed vertical line in the second panel from the bottom of Fig. 6.7). Two subsequent transits were identified when they occurred ∼250 days later separated by only ∼6.5 days (Fig. 6.7, bottom panel). This suggests a planet orbital period of ∼250 days, with the second pair of transits corresponding to transits of both stars during a single barycenter passage. A preliminary N-body transit model identified an additional transit location in the light curve: a small but statistically significant dip is indeed observed approximately 7 days prior to the first identified transit, bringing the total planet number of observed planetary transits to four.

Figure 6.6: Starspot Autocorrelation Function

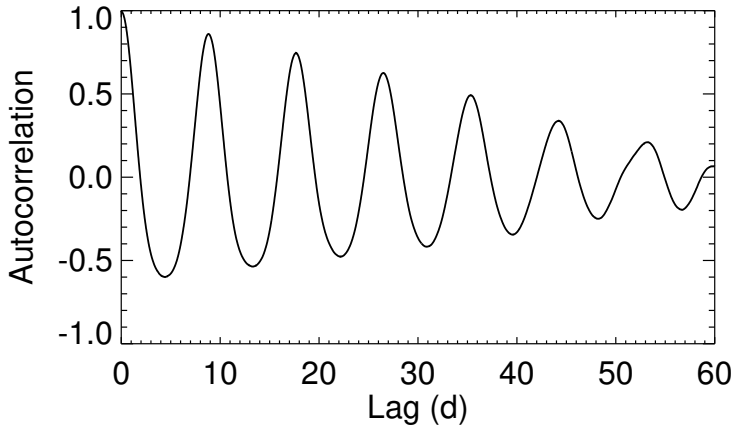

Autocorrelation function of the KIC 10753734 lightcurve after removing instrument systematics and masking out stellar eclipses, revealing a single decaying periodicity of 8.8 days.

We understand the lack of transits earlier in the data as due to a non-zero mutual inclination between the planet and the binary pair, causing the planet to only precess into a transiting geometry in the last few hundred days of the *Kepler* observing window. This is similar to the behavior observed in Kepler-413b (Kostov et al., 2014) and Kepler-453 b (Welsh et al., 2015). The following section describes the detailed modeling of the system to determine the full 3D architecture of the system.

6.1.3 N-body Modeling Procedure

The nominal model of spherical, radially symmetric stars as described in §2 is insufficient due to the prevalence of starspots. The starspots result in two primary effects: they (1) bias the eclipse depths and (2) affect the eclipse timings. The depths of the eclipse in large part determines the ratio of the stellar radii. When there are abundant, significant starspots, the large upward scatter at the bottom of the eclipse due to a star's occultation of the other's spots results in an average eclipse depth which is less than for a spotless background star (Fig. 6.8) (Oshagh et al., 2013). Therefore, we select a subset of eclipses to fit with our

Figure 6.7: Transits and Closest Stellar Approaches of KIC 10753734 b

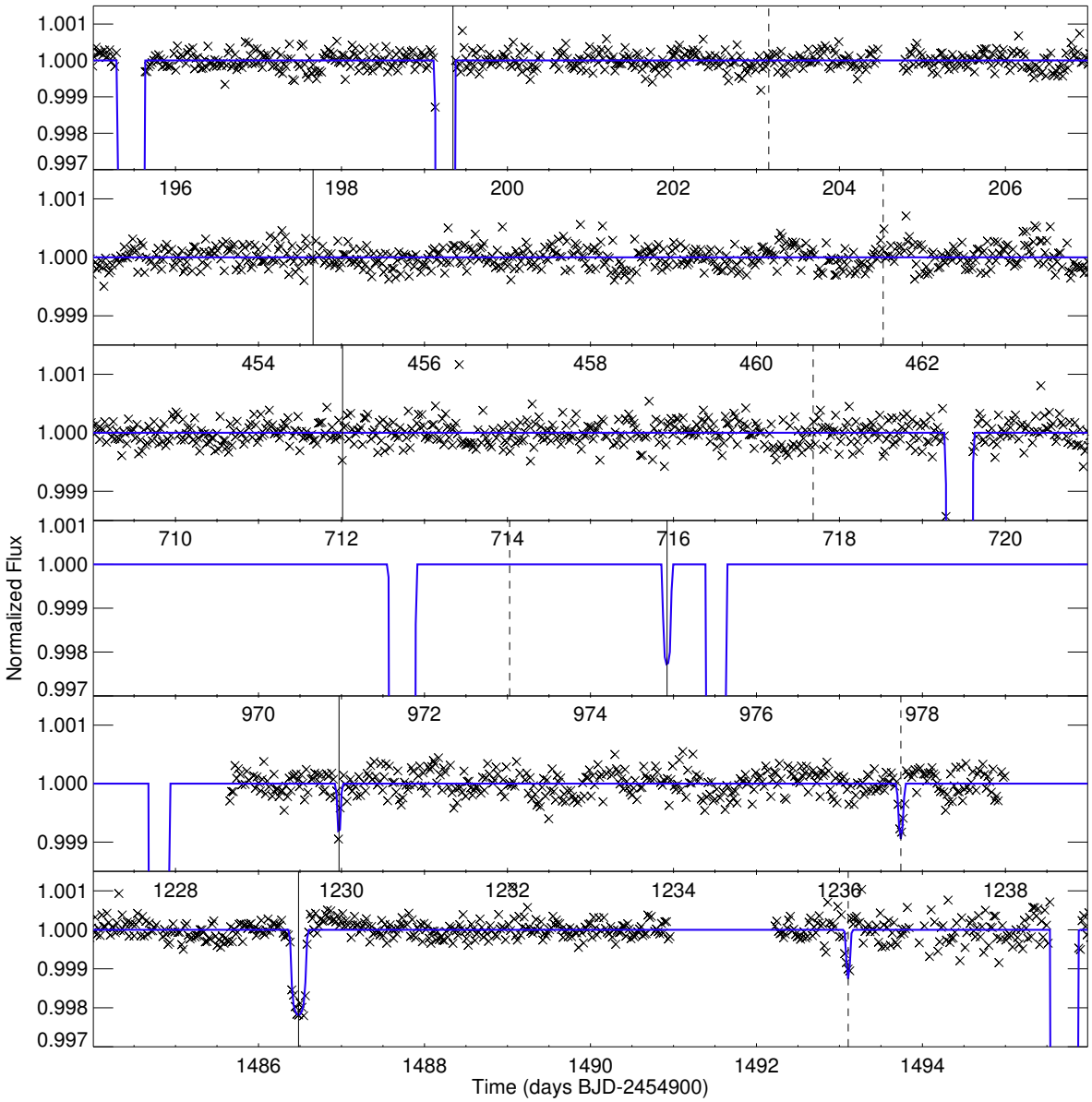

Twelve-day sections of the lightcurve near planet conjunction of the binary barycenter in chronological order as observed by *Kepler*. Times of closest approach between the planet and the primary (solid vertical line) and secondary star (dashed vertical line) are shown at each conjunction. In the bottom two panels, the most recent conjunctions in the *Kepler* observing window, transits of both host stars are visible. The third frame from the bottom has no data due to instrument malfunction, but our model predicts a single transit occurred in that window. No earlier conjunctions exhibit transits. Note that the vertical scale of the bottom and third from the bottom panels is compressed relative to the other panels to show the entire transit depth. Deep downward dips in flux that extend beyond the panel boundaries correspond to primary and secondary eclipses. To ensure no transits were missed, the twelve-day window was chosen well in excess of both the model's range of closest approaches and the ∼8 day theoretical maximum CBP TTV range computed analytically following Armstrong et al. (2013).

Figure 6.8: Phased Eclipses and Best Fit Nominal Model for All Eclipses

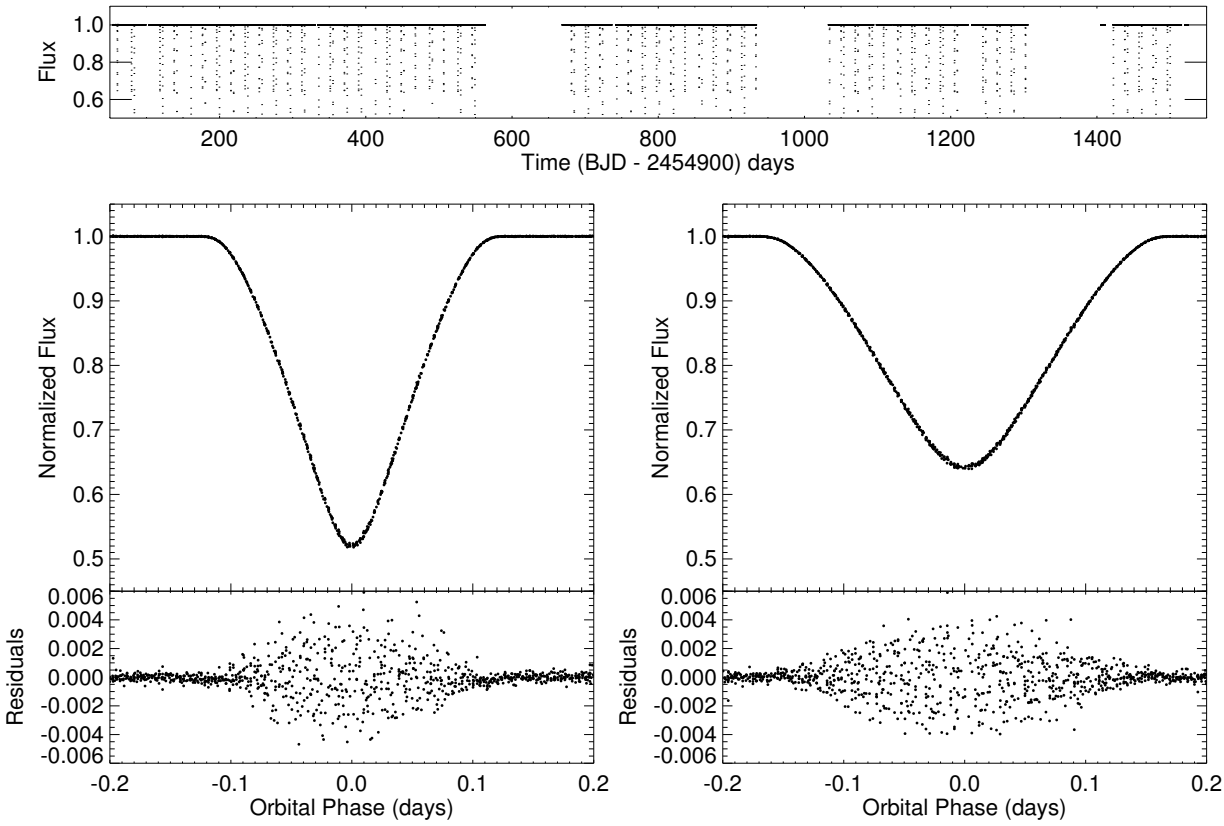

All primary (left) and secondary (right) eclipses phased together after ETV removal. Residuals to a nominal model of all this data illustrates the large scatter in eclipse due to starspot crossing events, as suggested in Figs. 6.3 and 6.4.The top panel shows the entire *Kepler* photometry data set after detrending.

photodynamic stellar eclipse model which have 'luckily' avoided passage over starspots to accurately find the stellar radii (Welsh et al., 2015). These are shown in Fig. 6.9. The application of these fits to the entire dataset reveals upwards spikes are consistent with the model of eclipse crossings of dark starspots (Fig. 6.10).

The second major effect is a result of the starspot crossing events producing an asymmetric eclipse shape. The 'U' shaped eclipse model is pushed away from the starspot crossing spike, causing the measured eclipse time to be biased away from the side of the eclipse with the starspot event (Alonso et al., 2009). If the binary pair orbits prograde relative to the stellar spin, then starspots that have just rotated into view will be occulted early in the

Figure 6.9: Photodynamical Model Data Including Starspot-Free Transits

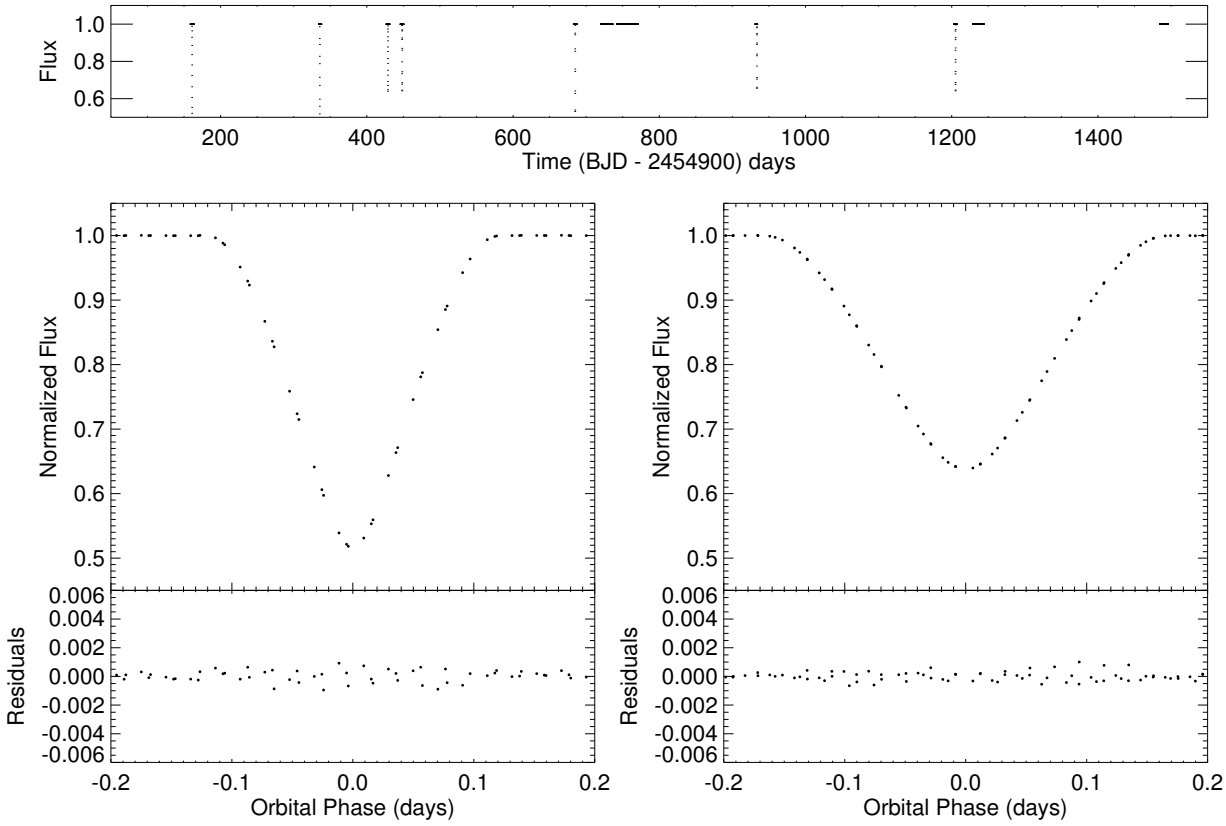

Similar to Fig. 6.8, except the eclipses of the primary (left) and secondary (right) stars have been selected as showing limited starspot activity. This data, along with the portions of the lightcurve near planet conjunctions, including the locations of observed transits and where transits are notably observed not to occur (see the top four panels of Fig. 6.7), is used for photodynamical modeling. The complete detrended dataset used in the photodynamical model shown in the top panel. The eclipse times of eclipses not included in the photometry are simultaneously fit to avoid starspot timing biases as described in the text.

Figure 6.10: Phased Eclipses and Best Fit Clean Model for All Eclipses

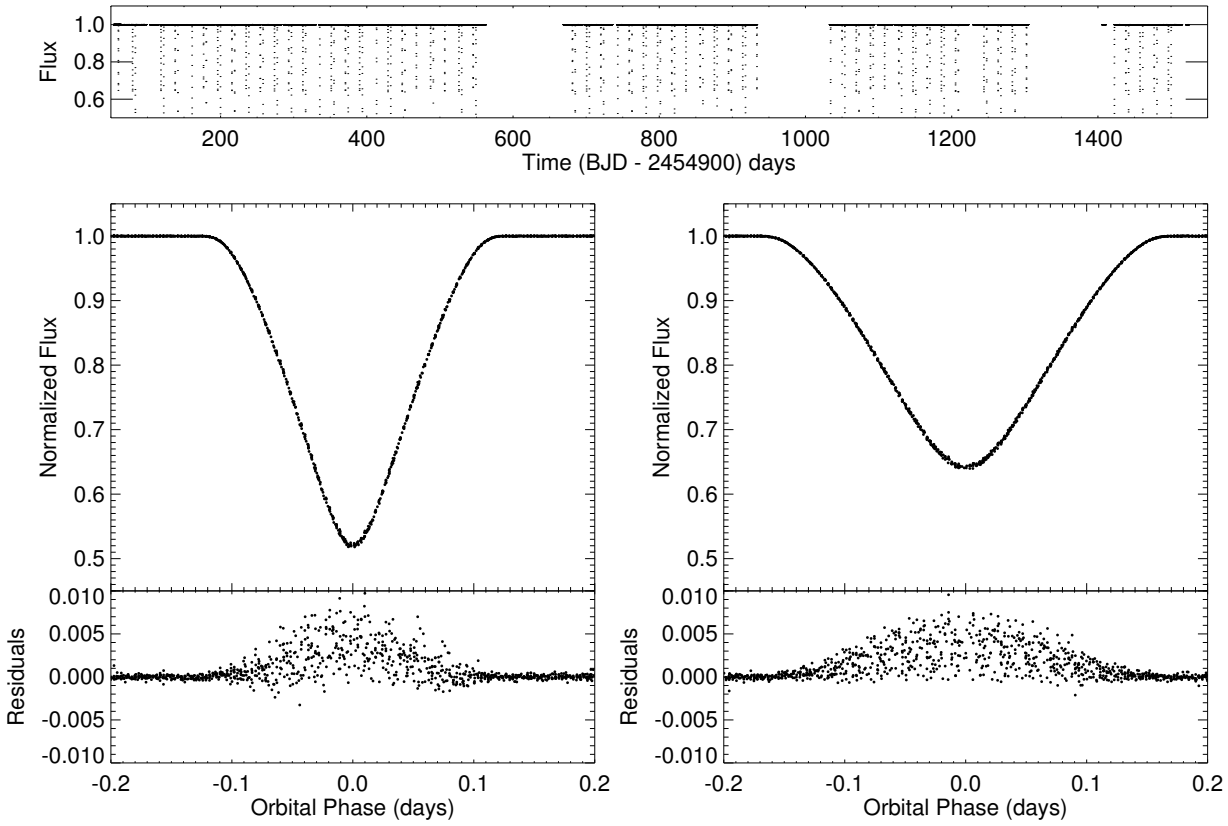

Similar to Fig. 6.8, all primary (left) and secondary (right) eclipses phased together after ETV removal. However, this stellar model and residuals are from a fit of the 'lucky' starspot-free transits as shown in Fig. 6.9. The vast majority of large residual excursions are now upwards, consistent with the darkening effect of starspot crossing, and suggesting these stellar models more accurately reflect the true radii of the stars.

eclipse, and spots that are rotating out of view will be occulted later in the eclipse (Fig. 1, Mazeh et al., 2015a). Spots rotating into view corresponds to a loss of flux due to the darker surface of the spot compared to the rest of the star, and therefore an overall downward flux trend in the lightcurve. Similarly, spots rotating out of view, and therefore appearing as a bump near the end of the eclipse lightcurve, will cause a corresponding increase in total measured flux out of eclipse. This leads to an anti-correlation between measured eclipse timing and the local lightcurve slope (Orosz et al., 2012a; Mazeh et al., 2015a; Welsh et al., 2015). Fig. 6.11 shows this effect for both primary and secondary eclipses – the first time this effect has been observed in both host stars of a CBP – and Fig. 6.12 graphically illustrates the reduction in ETV scatter.

Fitting a dynamical lightcurve model to the data without taking into account this effect may significantly bias the planetary parameters because the starspot induced ETVs would be interpreted as perturbations due to the planet (this effect was strong enough to cause Kepler-453 b to show a "negative" mass detection at 3-σ confidence for a naively applied photodynamic model on the uncorrected data; §6.2 Welsh et al., 2015). Therefore we adopt the strategy of fitting only the 'lucky' spot-free eclipses directly with the photodynamic model, as well as the portions of the data where transits are observed or expected (see Fig. 6.9)[2]. We will now address our approach to recovering information about the planetary perturber contained in the starspot affected eclipses rejected from the photodynamic model.

We initially measure individual eclipse times by fitting a time-binned transit model from Mandel & Agol (2002) with quadratic limb darkening to the *Kepler* photometry and the reported uncertainties. We simultaneously fit all of the eclipses of a given star so that the radius ratio, transit duration, limb darkening coefficients, and impact parameter are self-consistent across all transits. Additionally, we fit a midtransit time $t_{\mathrm{ETV},i}$ for each observed eclipse (i). We generate a model by multiplying the transit shape by a third order polynomial

2. This is somewhat analogous to 'lucky imaging,' where by taking many image observations (eclipses), occasionally one gets very good seeing and an image (eclipse) with minimal distortion is obtained (see, e.g., Hufnagel, 1966; Fried, 1978; Brandner & Hormuth, 2016)

Figure 6.11: Local Lightcurve Slope ETV Correlation

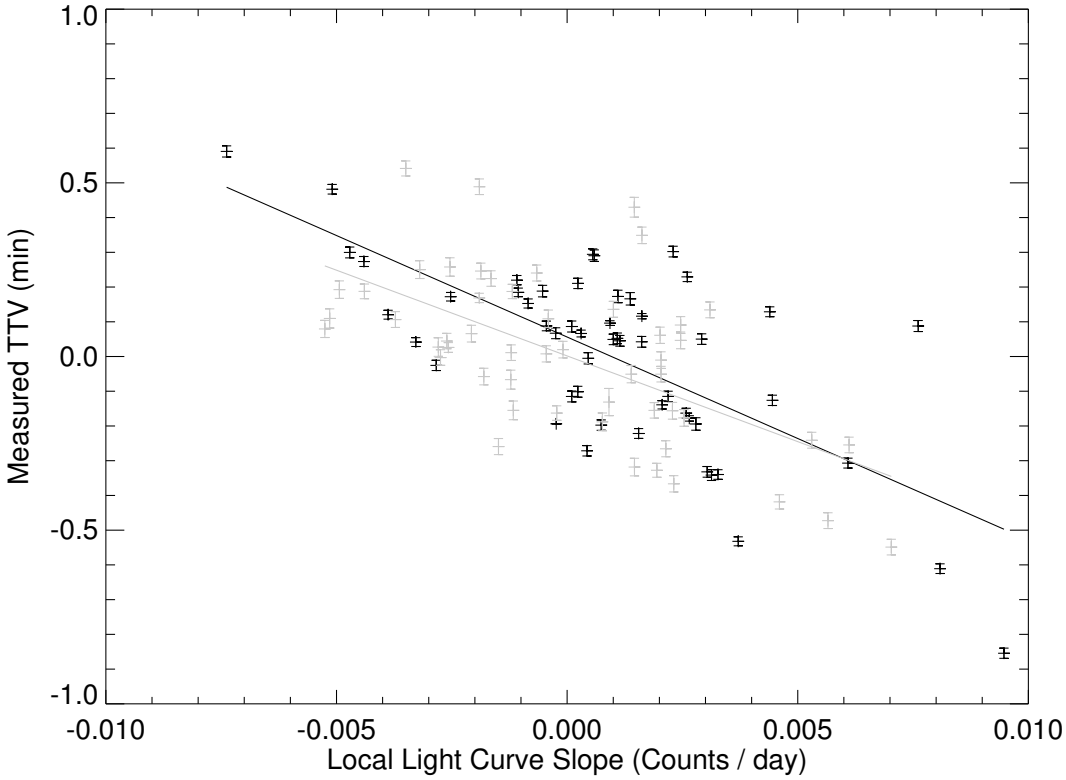

Measured ETVs of the primary (black) and secondary (gray) eclipses shown as a function of the local lightcurve slope (see Fig. 6.2). The anti-correlation expected for prograde rotation of both stars is observed, but significant scatter remains. This scatter is a combination of the planetary signal and residual starspot noise.

Figure 6.12: Linearly Corrected KIC 10753734 ETVs

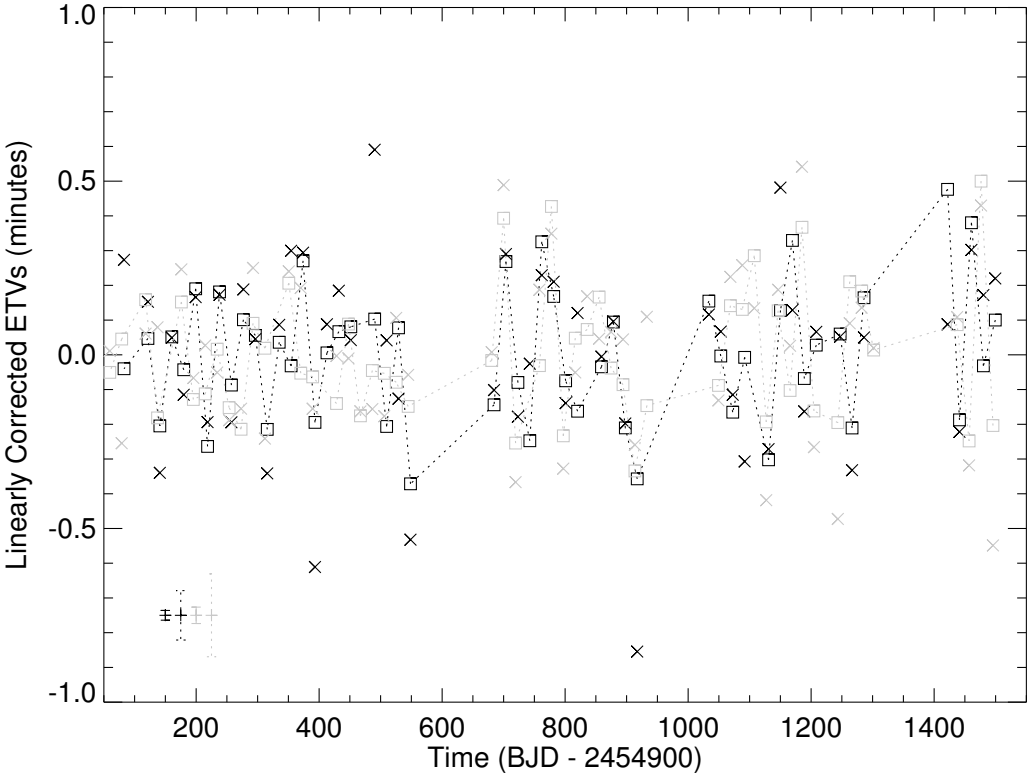

Measured ETVs of the primary (black) and secondary (gray) stars as measured initially (Xs) and after removing the linear trend shown in Fig. 6.11 (squares connected with dotted lines). The scatter in the ETVs is reduced, but structure remains. Typical measured uncertainties (solid) are shown in the lower right for primary (black) and secondary (gray), along with the inflated uncertainties (dashed) required for the planetary model to have $\chi^2_\nu = 1.0$. If all of the remaining ETV structure was due to planetary signal, it would not be necessary to rescale these uncertainties.

fit to a one-day segment of data surrounding each eclipse event with the eclipse masked out. We use a Levenberg-Marquardt algorithm to find the best fits and uncertainties. The reported uncertainties are substantially underestimated since they do not take into account stellar noise that the polynomial fit doesn't remove, such as the starspot eclipse effects. For preliminary fits with these times, we multiply our extracted uncertainties by a factor of 5.06 so $\chi^2_\nu = 1.00$ for a nominal model (see Fig. 6.12).

Using only the times rather than the lightcurve directly allows for the systematic correction of the local lightcurve slope effect, while losing only minimal information about the nature of the eclipsing stars since the 'lucky' eclipses contain all of the eclipse depth, duration, and shape information. While this technique has been successful in previous studies (Welsh et al., 2015), the residual scatter on the star-spot induced ETVs remains high (see Figs. 6.11). The local slope is not tightly correlated with ETV bias in this system due to both stars possessing spots. Thus the local lightcurve slope may be substantially affected by a star which is not being eclipsed.

Therefore, we take a new approach to measuring the ETVs of the spotty eclipses by modeling the spots directly. We use `spotrod`, a semi-analytic starspot transit lightcurve code with integrated MCMC capabilities (Béky et al., 2014; Foreman-Mackey et al., 2013). We choose this code because of its speed relative to purely numerical codes while maintaining accuracy and its ease of use. Each eclipse is fit individually, allowing complete freedom in starspot size, location, and flux deficit. In principle, a self-consistent model of the rotating spots on the surface of the star could be attempted, but changes in star spot latitudes, differential rotation, and other effects would make such a model computationally intensive and beyond the scope of this project. In order to keep the stellar properties self-consistent between starspot models, we apply a Guassian approximation of the posteriors of global parameter fits (R_A, $R_\mathrm{B}/R_\mathrm{A}$, $c_{1,A}$, $c_{2,A}$, $c_{1,B}$, $c_{2,B}$, P_AB, M_A, $M_\mathrm{B}/M_\mathrm{A}$, $e\cos\varpi$, $e\sin\varpi$, and i_B) from the clean eclipse fit (Figs. 6.9 and 6.10) as priors on each individual starspot eclipse. Each eclipse thus has 16 free parameters: each of the above with the strong priors

from the global fit, T_0 of each transit with a uniform prior, and four starspot parameters. The starspot parameters are the position on the eclipsed star (with uniform prior on the surface of a sphere), spot radius (circular spot assumed, uniform radius prior), and spot contrast (uniform prior). We use a 10-temperature parallel-tempered MCMC to avoid local minima and expedite convergence (Earl & Deem, 2005; Foreman-Mackey et al., 2013). Fig. 6.13 shows an example of models generated from draws from the MCMC posteriors of a `spotrod` fit to the primary eclipse at BJD 2456360.3 and residuals from each fit model. The significant residuals of the spot are largely captured by the model (Fig. 6.13, bottom panel), and the uncertainty in the transit midtime is comparable to the uncertainties of a spot-free fit after multiplicative increase of 5 as described above to yield $\chi^2_\nu = 1.00$ for a nominal model. This indicates that marginalizing over the effects of a single starspot on the eclipse timing accounts for the majority of the discrepancy between the N-body radially symmetric star model and the true system. We use these star-spot-marginalized eclipse times and uncertainties in our final full parameter fit.

In summary, to complete a modified photodynamic model, we detrend the *Kepler* photometric data with a polynomial of width 1 day after masking out eclipses and transits. We photodynamically fit only observed transits, closest planet-star approaches, and spot-free eclipses (Fig. 6.9). Some short-term correlated noise remains in this lightcurve, but detrending on shorter timescales is avoided to prevent introducing artificial variation to the transits or eclipses, whose duration is $\sim$0.2 days. We simultaneously fit this data and eclipse times of all remaining eclipses measured by marginalizing over the size, shape, and location of starspots. A 30 measurement RV data set spanning 30 days (Table 6.1) is also simultaneously fit. The 22 free parameters in the DEMCMC fit as described in §2 are $\{R_\mathrm{A}$, $c_{1,\mathrm{A}}$, $c_{2,\mathrm{A}}$, P_B, $T_{0,\mathrm{B}}$, $e_\mathrm{B}^{1/2}\cos(\omega_\mathrm{B})$, $e_\mathrm{B}^{1/2}\sin(\omega_\mathrm{B})$, i_B, $R_\mathrm{B}/R_\mathrm{A}$, $M_\mathrm{B}/M_\mathrm{A}$, $c_{1,\mathrm{B}}$, $c_{2,\mathrm{B}}$, $bright_\mathrm{B}$, P_p, $T_{0,\mathrm{p}}$, $e_\mathrm{p}^{1/2}\cos(\omega_\mathrm{p})$, $e_\mathrm{p}^{1/2}\sin(\omega_\mathrm{p})$, i_p, Ω_p, $R_\mathrm{p}/R_\mathrm{A}$, $M_\mathrm{p}/M_\mathrm{A}$, $C_\mathrm{RV}\}$ are all subject to uniform priors. In this model $dilute = \Omega_\mathrm{B} = 0$ and M_A is fixed at the spectroscopically measured value of $1.06 M_\odot$. This comprehensive model results in an accurate measurement

Figure 6.13: Starspot Marginalization Example

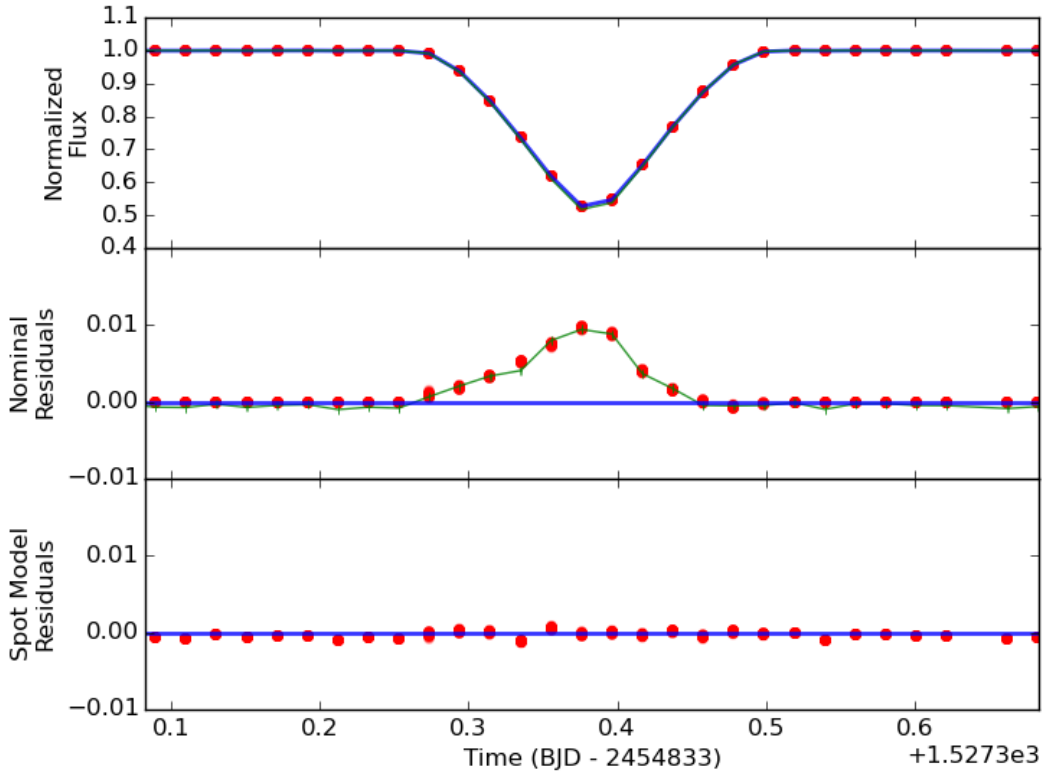

Eclipse fit including a four-free-parameter starspot. *Top:* The total eclipse shape after polynomial detrending as measured (blue), modeled using the clean-transit fit (green), and from 100 models drawn from the posterior of the starspot marginalization MCMC fits (red). *Middle:* Measured flux subtracted from the clean-transit model (green with *Kepler* uncertanities), and the starspot model subtracted from the clean-transit model (red). The starspot model reproduces the observed residual anomaly very well. *Bottom:* Residuals between the observed flux and the starspot model. While some scatter remains in transit, it is drastically reduced compared to the clean-transit model (middle panel) and comparable to out-of-transit scatter.

of the system's 3D architecture as well as a significant planetary mass detection.

6.1.4 Preliminary Results and Discussion

Full system posteriors are still in preparation, however a few key features can be confidently reported. The mass and radius of the stars are precisely measured by the transit and eclipse shapes and times, with $M_{\rm A} = 1.053 \pm 0.014 M_{\odot}$ and $R_{\rm A} = 1.063 \pm 0.005 R_{\odot}$. The has measured $M_{\rm p} \sim 0.25 M_{\rm Jupiter}$ and $R_{\rm p} = 0.61 \pm 0.02 R_{\rm Jupiter}$. The mutual inclination between the planet's and the binary's orbital planes is precisely measured by the precessing planet's transit depths at $I = 2.56^{\circ} \pm 0.02$. $P_{\rm crit} \approx 139$ days for KIC 10753734, and thus $P_{\rm p}/P_{\rm crit} \approx 1.8$. These values are all consistent with the previously measured population. Figs. 6.14 and 6.15 show preliminary DEMCMC fit results for all parameters, but explicit values are not tabulated here since the final analysis is ongoing. For full results see Mills et al. in prep. We expect the technique developed here combining starspot crossing models, photodynamic code, and RV data will be applicable to future high quality photometric data such as PLATO[3].

6.2 Kepler-453 b

This section summarizes the dynamical measurement work in the characterization of the tenth Kepler transiting circumbinary planet, Kepler-453 (KOI-1451 and KOI-3151) from Welsh et al. (2015, henceforth W15). For a complete discussion of all aspects of the system, refer directly to W15. Like KIC 10753734, the planetary transits of Kepler-453 b were identified by visual inspection of a known *Kepler* eclipsing binary KIC 9632895 (Prsa et al., 2011). Three transit events were identified with an approximate 230 day period, beginning at BJD 2455781.7 (Fig. 6.16). However the first transit occurs nearly halfway through the *Kepler* observing window. This is interpreted as significant precession changing the

3. see, e.g., http://sci.esa.int/plato/42730-scird-for-plato/.

Figure 6.14: KIC 10753734 DEMCMC Posteriors Part I

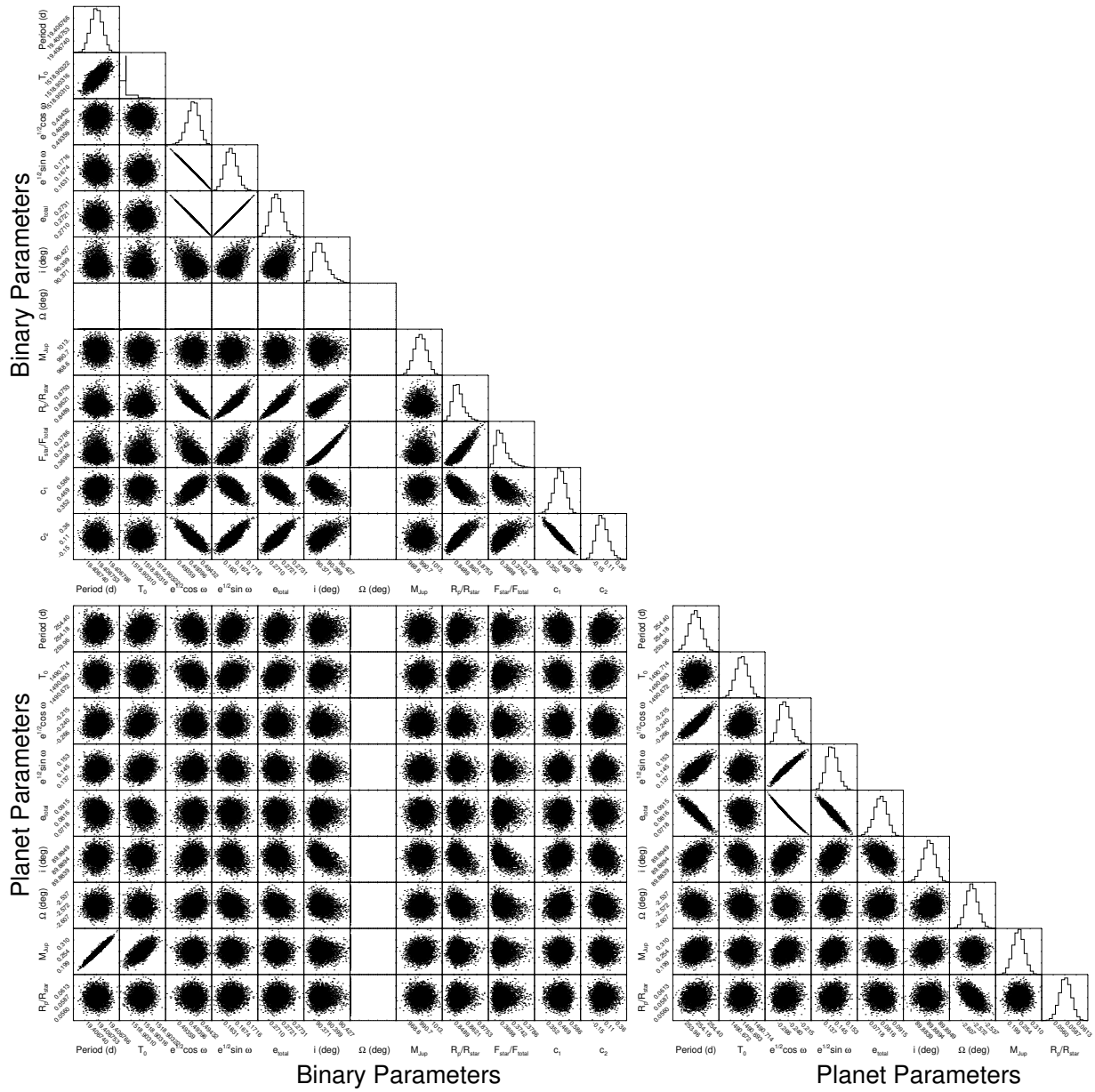

Posteriors and correlations between all pairs of DEMCMC parameters for the model described in §6.1.3.

Figure 6.15: KIC 10753734 DEMCMC Posteriors Part II

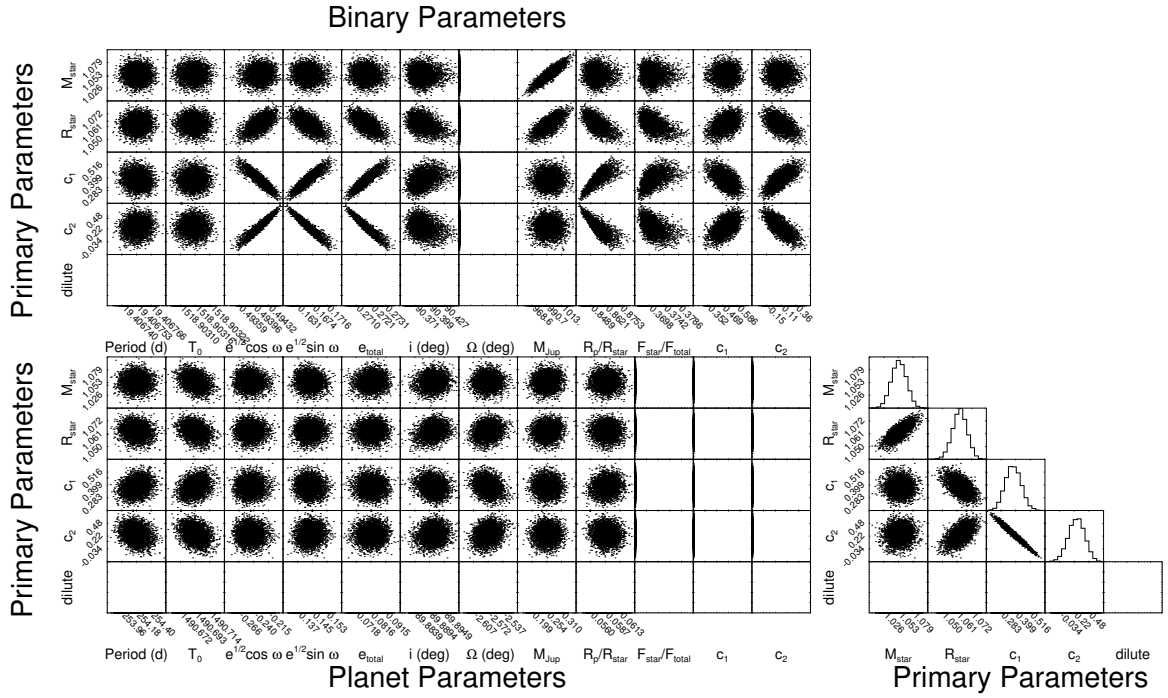

Identical to Fig. 6.14, but for remaining DEMCMC parameters.

transit geometry on the timescale of *Kepler* observational window. The change in transit durations and timings allows for precise measurement of the planet-binary mutual inclination. Additionally, the uncertainty in the planet's radius is only 0.63%, and the secondary star's radius uncertainty is 0.65%, making it one of the most precisely measured low-mass stars.

6.2.1 Photodynamic TTV Model

The binary consists of a G Dwarf ($M_1 = 0.944 \pm 0.01 M_\odot$) and an M Dwarf ($M_2 = 0.195 \pm 0.002 M_\odot$) in a relatively low eccentricity ($e = 0.0524 \pm 0.0037$) orbit of 27.3 days. The effects of starspots are clearly visible in eclipses of the brighter primary star (Fig. 6.17). Similar to the strategy discussed in §6.1.3, in order to get accurate and unbiased eclipse times only three primary eclipses without evidence of starspot activity were used directly in the photodynamic model (Fig. 6.18). The eclipses of the fainter secondary did not show signs of starspots so they are all included directly into the photodynamic model.

Individual eclipse times for all of the remaining primary eclipses were measured first by iteratively fitting the eclipse shape of the clean transits to a Mandel & Agol (2002) model. For all other eclipses, this shape was kept fixed and allowed to vary only in the specified midtime. The lightcurve was modeled by fitting a fifth-order polynomial multiplied by the eclipse shape to the *Kepler* photometry within three eclipse durations of each eclipse. The fits and 1-σ uncertainties were computed using the χ^2 statistic combined with a Levenberg-Marquardt minimization routine. The measured eclipse timing variations were then statistically corrected taking by linear regression with respect to the local light curve slope (see §6.1.3 and Mazeh et al., 2015a). After correction, no periodic trend in ETVs is observed (Fig. 6.19).

Our full photometric dataset thus includes the *Kepler* Simple Aperture Photometry (SAP) within a factor of three of the duration of three primary eclipses, each secondary eclipse, and the three observed transits. Additionally, three portions of the lightcurve near planet conjunction with the stars that do not show transit events were included to ensure

Figure 6.16: Kepler-453 b Transits and Conjunctions

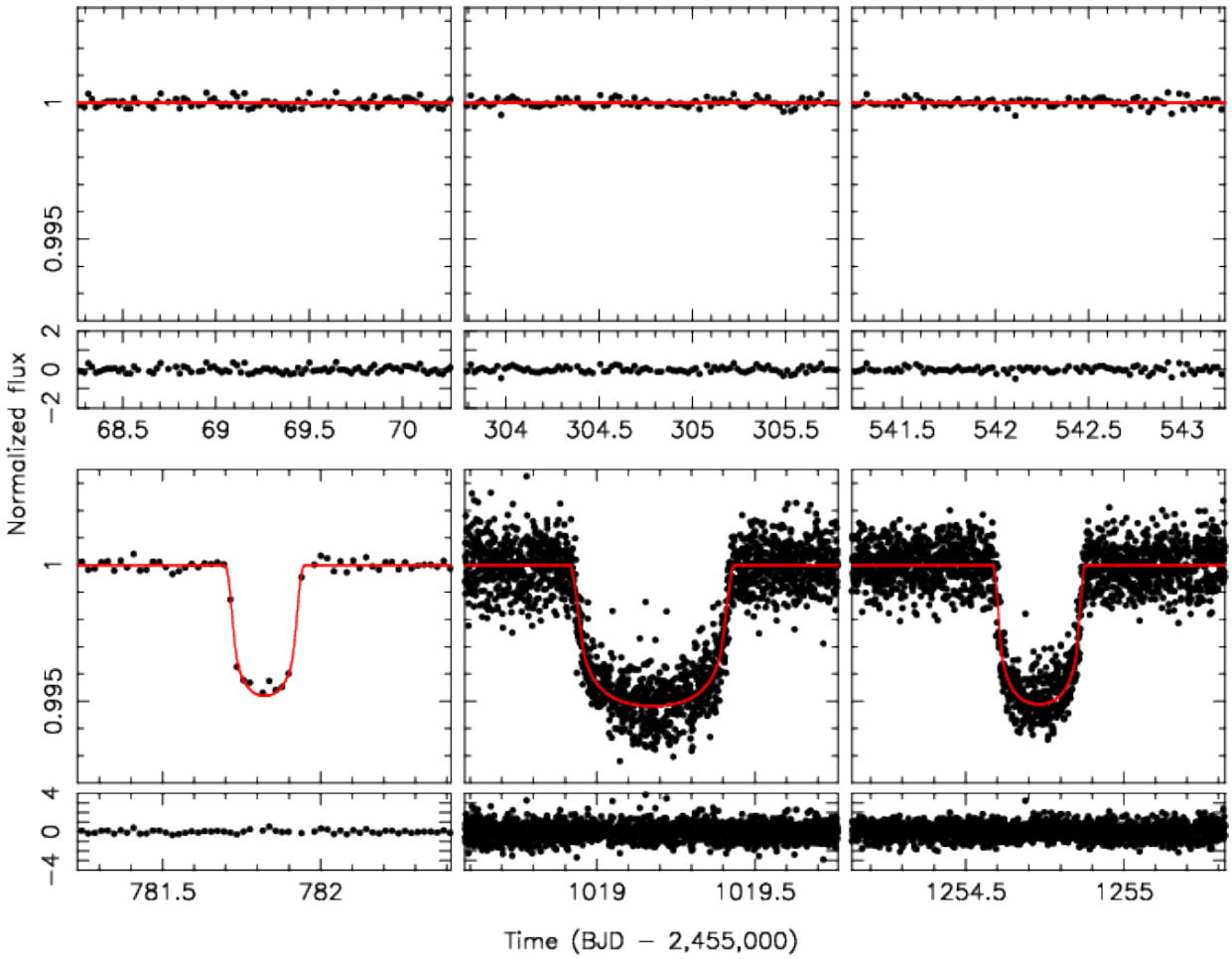

Observed planet transits (bottom row) and regions of the lightcurve near the closest sky-project star-planet approach which lack transits (top row) as predicted by the photodynamic model (red). The lower center and right panels contain short cadence data and thus have higher temporal cadence and more scatter around the model. Note the bottom three panels all have the same horizontal scale, emphasizing the significant changes in transit duration.

Figure 6.17: Kepler-453 Starspot Activity Examples

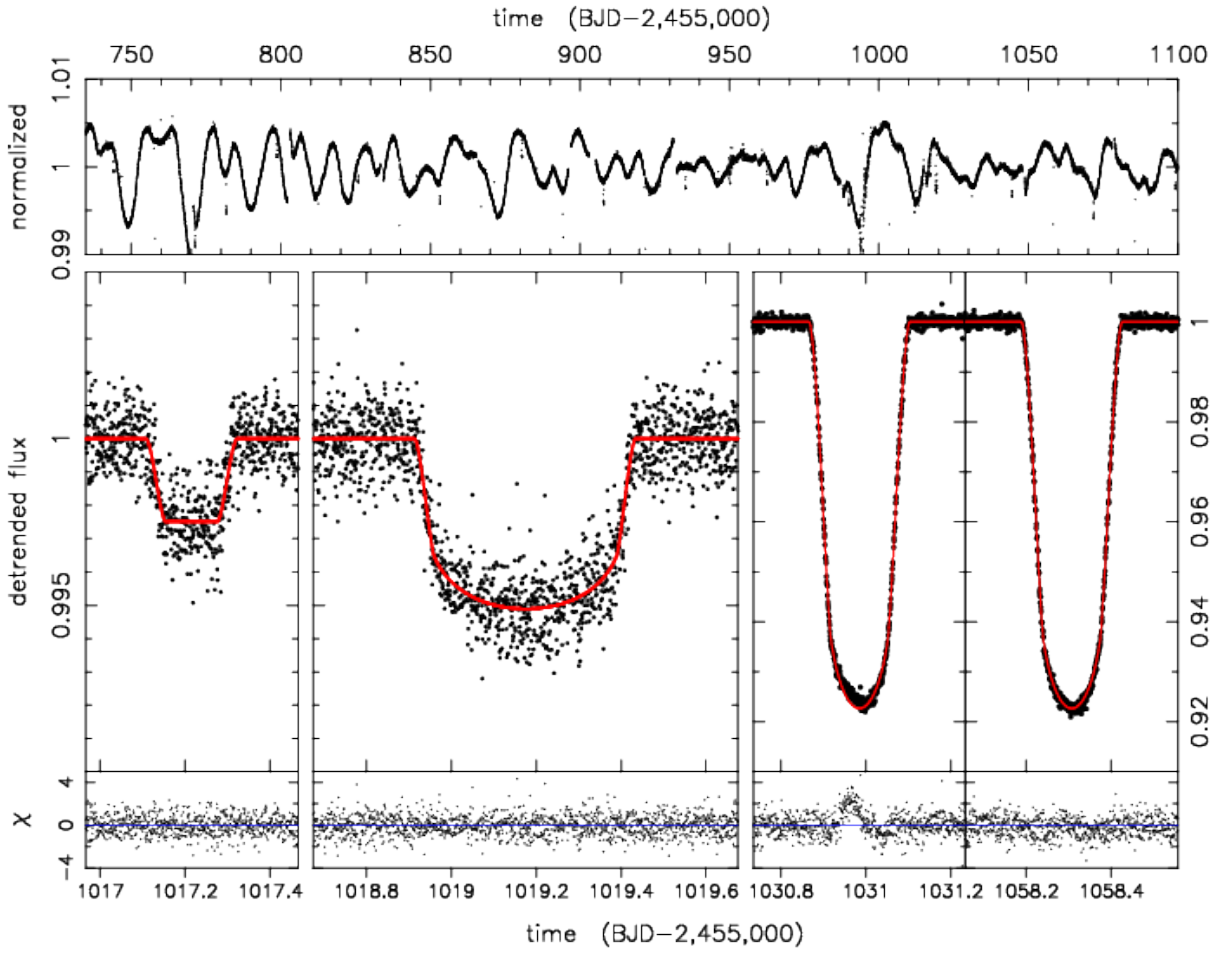

Top: One year of short cadence observation with instrument systematics removed showing residual percent-level variability due to star spot activity. *Bottom:* From left to right, an example of a secondary eclipse, planet transit, and two primary eclipses along with their residuals to a dynamical model (red). The second panel from the right shows a characteristic starspot crossing bump, which is present on the majority of primary eclipses and biases ETV measurement.

Figure 6.18: Eclipses Minimally Contaminated by Starspots

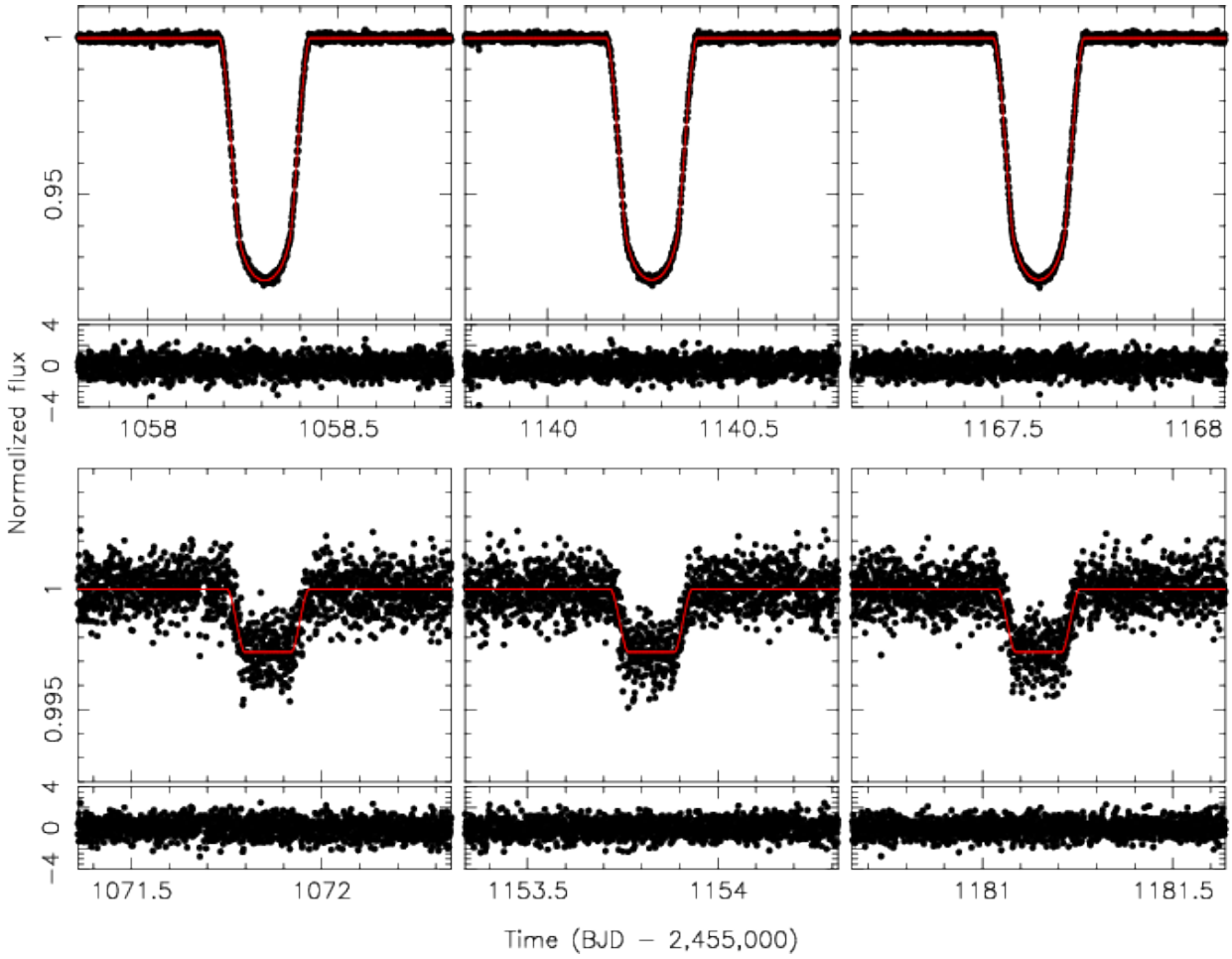

Top: The starspot-free primary eclipses that are directly fitted by the photodynamical model (red) to recover the geometric properties of the primary eclipse. Note the residuals in and out of transit are very similar for these three eclipses. *Bottom:* An example of three secondary eclipses. All secondary eclipses were used directly in the photodynamic model because no sign of starspot bias was present in the eclipses (again noting the residuals in and out of transit are statistically similar).

Figure 6.19: Corrected Eclipse Timing Variations

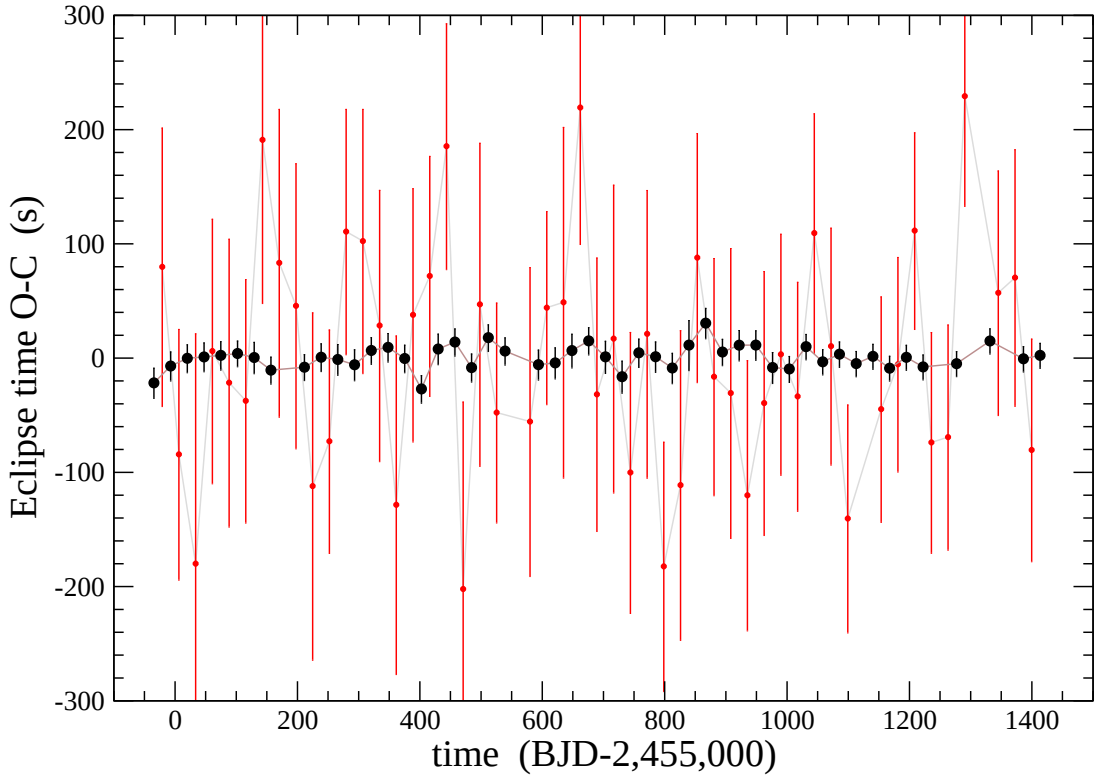

ETVs after removing the linear lightcurve-slope–ETV correlation. Primary ETVs are shown in black and the secondary ETVs are shown in red. No periodic variation or trend above the noise level is observed in either case.

the model did not introduce unobserved transits. The uncertainties reported in the *Kepler* data itself were increased by a multiplicative factor of 1.44 so that the reduced $\chi^2 = 1.0$ for a nominal model. This was necessary because the *Kepler* uncertainties underestimate the scatter of the data after fifth-order polynomial detrending was used in each lightcurve segment (with the eclipses masked out) to normalize the data and remove low frequency variations. We also include starspot statistically corrected ETVs for the remaining primary eclipses, and RV observations (see W15). We simultaneously fit these data to a photodynamic model. The tight constraints placed on the relative positions, velocities, and sizes of the three bodies in the system by the times, durations, and depths of the eclipses and transits allow very precise determinations of the geometric aspects of the system. The overall mass scale of the system was determined by fitting templates to high resolution spectroscopy in order to determine stellar mass, temperature, and metallicity (see W15).

6.2.2 Results and Discussion

MCMC photodynamic posteriors for the system are shown in Table 6.2. The starspot correction is highly significant for the interpretation of the mass of Kepler-453 b. A naive model which directly included all of the primary eclipses in the photodynamic code favored a $-90 M_{\rm Earth}$ planet at 3-σ significance because the starspots induced a periodic variation in primary eclipses that was out of phase with the planet detected by transit observations. The relatively larger uncertainties on the secondary eclipses due to lower signal to noise are permissive enough to allow the primary ETVs to dominate the fit. If the planet was forced to have a physically plausible positive mass, these uncorrected ETVs strongly preferred near zero mass for the planet. With the statistical starspot correction implemented, the flat ETVs (Fig. 6.19) are insufficiently precise to measure the planet mass, but result in a broad (± 16 $M_{\rm Earth}$ 1-σ range) posterior centered at zero mass as expected. This allows us to place a sensible upper bound on the planet's mass (ruling out a low-mass stellar companion), but does not require an anomalously low density planet (see, e.g., Lissauer et al., 2011b; Weiss

& Marcy, 2014; Mills & Mazeh, 2017).

The lack of transits early in the *Kepler* observing window as well as the precisely measured transit durations and depths in the latter half allow for an accurate measurement of the geometry of the system. The mutual inclination of the planet with respect to the binary is $2.258^\circ \pm 0.039$ and the planet's orbit is nearly circular $e = 0.0359 \pm 0.0088$ (see Fig. 6.20). Forward modeling reveals an inclination precession amplitude of 2.25° with a 103.5 year period. This geometry is consistent with models of circumbinary disk formation (Pierens & Nelson, 2008; Foucart & Lai, 2013).

This summary of the dynamical modeling of Kepler-453 is part of a broader analysis. For a complete discussion of stellar properties (including spectroscopic measurements), transit probabilities, and the binary habitable zone of Kepler-453, refer to W15 (Welsh et al., 2015).

Table 6.2: Kepler-453 Photodynamic MCMC Posteriors

Parameter Name[a]	Median	68% (1-σ) Uncertainty	Unit
	Binary Parameters[b]		
M_1	0.944	± 0.010	$M_\odot$
M_2	0.1951	± 0.0020	$M_\odot$
R_1	0.833	± 0.011	$R_\odot$
R_2	0.2150	± 0.0014	$R_\odot$
P	27.322037	± 0.000017	days
$T_{\rm conj}$	-34.574013	± 0.000060	BJD[c]
i	90.266	± 0.052	degrees
$e\ \sin\omega$	-0.0520	± 0.0037	
$e\ \cos\omega$	-0.006339	± 0.000016	
e[d]	0.0524	± 0.0037	
ω	263.05	± 0.48	degrees
$c_{1,1}$	0.41	± 0.06	
$c_{1,2}$	0.07	± 0.11	
$c_{2,1}$	0.33	± 0.11	
$c_{2,2}$	0.07	± 0.07	
T_2/T_1	0.584	± 0.015	K
dilute	0.02	± 0.02	
	Planet Parameters		
M_p	0.2	± 16.0	$M_{\rm Earth}$
R_p	6.204	± 0.039	$R_{\rm Earth}$
P_p	240.503	± 0.053	days
$T_{\rm conj}$	69.020	± 0.054	BJD[c]
inclination	89.4429	± 0.0091	degrees
$e\ \sin\omega$	-0.00322	± 0.00023	
$e\ \cos\omega$	-0.0358	± 0.0088	
e[d]	0.0359	± 0.0088	
ω	185.1	± 3.7	degrees
Ω	2.103	± 0.055	degrees
Mutual Inclination (I)	2.258	± 0.039	degrees

[a] The reported Keplerian parameters are the instantaneous (osculating) values at the reference epoch $T_{\rm epoch}$=2,454,964 BJD.

[b] Subscript 1 refers to the primary star and 2 the secondary star throughout.

[c] date with respect to BJD–2,455,000.

[d] This quantity is not directly fitted, but rather derived from the $e\cos\omega$ and $e\sin\omega$ values.

Figure 6.20: Kepler-453 System Geometry

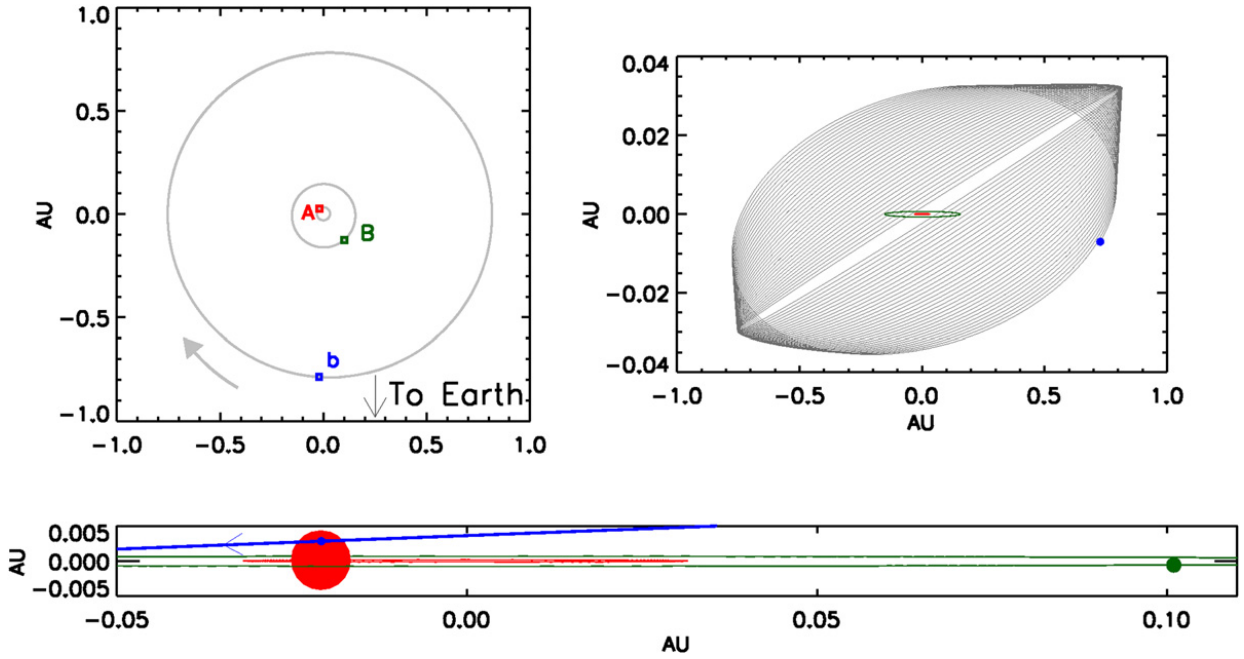

Views of the orbital geometry of Kepler-453, beginning with a top-down (face-on) view in the upper left. The bottom panel shows the transiting configuration as seen from Earth at BJD 2455781.8. The upper right panel shows the same edge-on orientation of the system as viewed from Earth, but with a stretched vertical axis. The predicted path of the planet Kepler-453 b for 10,000 days beginning from the *Kepler* observing window is shown in gray. The blue dot is the planet's location at BJD 24565000, on a path which is no longer transiting due to precession. The next transits are expected in year 2066.

CHAPTER 7

POPULATION ANALYSES

7.1 The Planetary Mass-Radius Relation and its Dependence on Orbital Period as Measured by Transit Timing Variations and Radial Velocities

The two most common techniques for measuring planetary masses—the radial velocity (RV) and the transit timing variations (TTVs) techniques, have been observed to yield systematically different masses for planets of similar radii. Following Steffen (2016), we consider the effects of the observational biases of the two methods as a possible cause for this difference. We find that at short orbital periods ($P < 11$ day), the two methods produce statistically similar results, whereas at long periods ($P > 11$ day) the RV masses are systematically higher than the TTV ones. We suggest that this is consistent with an RV detection-sensitivity bias for longer periods. On the other hand, we do find an apparently significant difference between the short and the long-period planets, obtained by both observing techniques—the mass-radius relationship parameterized as a power law has a steeper index at short periods than at long periods. We also point out another anticipated observational bias between the two techniques—multiple planet systems with derived RV masses have substantially larger period ratios than the systems with TTV mass derivation.

7.1.1 Introduction

Several thousand exoplanets have been discovered and characterized to date. The transit method has been the most numerically successful, with the *Kepler* survey alone characterizing the periods and radii of more than 4,000 planets and planet candidates (e.g., Coughlin et al., 2016; Morton et al., 2016). Usually, the transit light curves yield only the radii of the transiting planets, provided we know the radii of their parent stars. However, if a star

hosts multiple planets, the mutual gravitational perturbations of the planets may induce observable transit timing variations (TTVs), yielding constraints on the planetary masses (e.g., Agol et al., 2005; Holman & Murray, 2005; Deck & Agol, 2015; Jontof-Hutter et al., 2016; Hadden & Lithwick, 2017). The second most prolific method of planet observation is the radial velocity (RV) technique, in which the stellar reflex motion of the parent star is measured as the planet moves in its orbit (e.g., Udry & Santos, 2007; Mayor et al., 2011). Combined with transits, this method also yields planetary masses and radii.

The many planetary masses and radii derived from the RV and TTV techniques enabled us to study the mass-radius (M–R) relation of exoplanets (e.g., Weiss et al., 2013; Weiss & Marcy, 2014), which is crucial for our understanding planetary formation, evolution, and structure (e.g., Seager et al., 2007; Lopez & Fortney, 2014; Lee & Chiang, 2016). We use these findings to study the M–R relation below 8 $R_{\rm Earth}$ here. Above this limit the planetary radius depends only weakly on the mass, because of the dominance of electron degeneracy pressure (e.g., Zapolsky & Salpeter, 1969; Seager et al., 2007; Swift et al., 2012).

However, it has been pointed out that for planets of radii less than $\sim$8 $R_{\rm Earth}$, planetary masses measured via RVs seem to be systematically larger than the masses measured by TTVs (Steffen, 2016, henceforth S16). This observation can not be explained by the fact that the two techniques are sensitive to different radius regimes, because the difference between the two techniques holds true at any given specific radius, not merely for the distribution as a whole. This can be seen in the left panel of Figure 7.1, an update to Figure 1 of S16, with planets color-coded by the means of their mass characterization—blue color for the TTVs, red for RVs, and green for simultaneous characterization.

The planet data in the figure come from Jontof-Hutter et al. (2016) and references therein, as well as updates from Hadden & Lithwick (2016); Gettel et al. (2016); Mills et al. (2016); Dai et al. (2016); Petigura et al. (2016); MacDonald et al. (2016); Mills & Fabrycky (2017b), cases where masses are robustly inferred in Hadden & Lithwick (2017), and a more complete inclusion of all positive mass planets from Marcy et al. (2014). We do not include measured

Figure 7.1: TTV and RV Mass, Radius, and Period Relationships

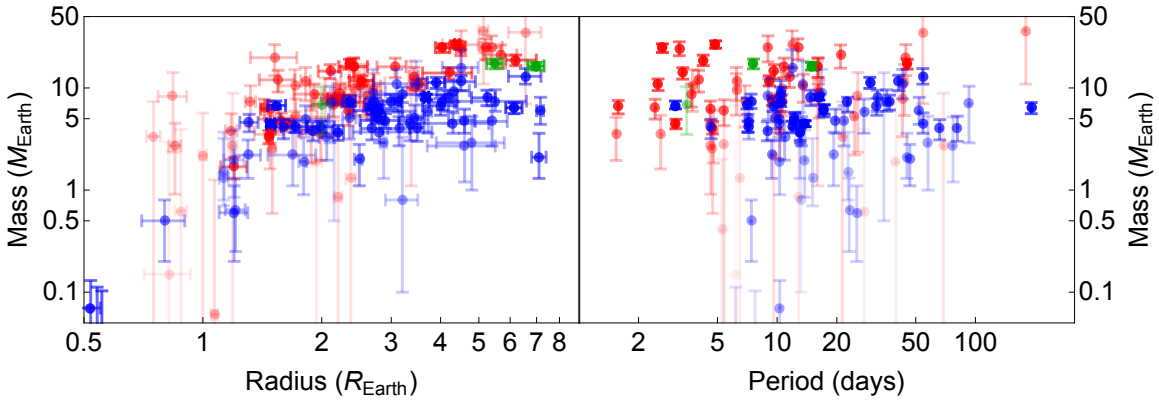

Masses, radii, and orbital periods (along with 1-σ uncertainties) for all planets as measured by RV (red), TTV (blue), or a combined RV-TTV analysis (green). The opacity of the points is decreased as the fractional uncertainties of the measurements rise so that points with large error bars do not distract the eye. Note that in both the left (M–R) panel and the right (M–P) panel, the red (RV) points generally lie above and to the left of the blue (TTV) points.

"negative mass" RV planets from Marcy et al. (2014), which are the result of statistical fluctuations, because a similar set of "negative mass" statistical planets from TTV data is not available. We also use the default prior masses from Hadden & Lithwick (2017) for consistency with all other measurements.

We show in Section 7.1.2 that for most of the systems with masses derived by the two techniques, the two resulting masses are consistent with each other. Therefore the mass difference can not be explained by assuming that one technique is systematically biased.

As pointed out by S16, one basic difference between the two techniques is their sensitivity as a function of the planetary orbital period. We discuss this difference in Section 7.1.3 and show that indeed the masses and radii coming from the two techniques have different period ranges. Furthermore, there seems to be a significant difference between the M–R relation for planets at short and long orbital periods. We show that these two effects, with an assumed threshold detection for the RV techniques for long orbital period, can account for the observed difference between the RV and TTV masses. Section 4 points to another difference, the period ratio of the orbital periods of adjacent planets, between the systems

studied by the two techniques. Section 7.1.7 briefly summarizes our findings.

7.1.2 Observational Overlap

Several exoplanet systems have both well-measured RV and TTV signals that allow for the determination of the mass of the same planet by both techniques. It is interesting to consider these systems to see if we can detect any significant difference between the masses derived by the two techniques. We restrict the discussion here to non-zero mass measurements at the 2-σ level published for both methods at the time of writing. In Table 7.1 we quote the RV and the TTV masses, in Earth masses, and the RV$-$TTV mass difference in units of σ for each planet. Our sample totals 8 planets including one hot Jupiter (Cochran et al., 2011; Masuda et al., 2013; Weiss et al., 2013; Barros et al., 2015; Dai et al., 2016; Hellier et al., 2012; Becker et al., 2015). We do not include Kepler-9 (Holman et al., 2010), since there are no published RV analyses independent of TTV analysis. We see that, excepting Kepler-89 d which differs at the 4-σ level, the mass measurements of both methods for an individual planets are all consistent at the 1- to 2-σ level. The mix of negative and positive difference values do not reveal any obvious systematic bias of the two methods relative to each other. A one-sample Kolmogorov-Smirnov Test of the offsets suggests that the distribution is not distinguishable from a Normal distribution—as one would expect if the two techniques are unbiased.

In Table 7.1 we also compare the reported mass values of small planets with RV masses based on measurements done by two different instruments, namely HIRES and HARPS-N, and again report their difference HIRES$-$HARPS-N. This sample contains 4 planets including Kepler-10 c, which has measured masses discrepant between different instruments at the 3-σ level (Weiss et al., 2016; Petigura et al., 2016; Dai et al., 2016). Thus the differences between different RV instruments performing mass measurements is similar to the differences between RV and TTV measurements. The similar scale of discrepancy suggests that the small difference between RV and TTV observations of individual systems is insufficient to claim

Table 7.1: Masses of Planets Measured with Both RVs and TTVs

Planet	RV Mass ($M_{\rm Earth}$)	TTV Mass ($M_{\rm Earth}$)	RV−TTV
Kepler-18 b	12 ± 5 [a]	18 ± 9 [a]	-0.58σ
Kepler-18 c	15 ± 5 [a]	17.3 ± 1.7 [a]	-0.44σ
Kepler-18 d	28 ± 7 [a]	8 ± 1.3 [a]	$+1.7\sigma$
Kepler-89 d	106 ± 11 [b]	$52.1^{+6.9}_{-7.1}$ [c]	$+4.2\sigma$
Kepler-89 e	35^{+18}_{-28} [b]	$13.0^{+2.5}_{-2.1}$ [c]	$+0.78\sigma$
K2-19 b	$31.8^{+6.7}_{-7.0}$ [d]	44 ± 12 [e]	-0.89σ
K2-19 c	$26.5^{+9.8}_{-10.8}$ [d]	$15.9^{+7.7}_{-2.8}$ [e]	$+0.80\sigma$
Wasp-47 b	362 ± 16 [f]	341^{+73}_{-55} [g]	$+0.28\sigma$
Planet	HIRES RV Mass ($M_{\rm Earth}$)	HARPS RV Mass ($M_{\rm Earth}$)	HIRES−HARPS
Kepler-10 b	4.61 ± 0.83 [h]	3.30 ± 0.49 [h]	$+1.4\sigma$
Kepler-10 c	$5.69^{+3.19}_{-2.90}$ [h]	17.2 ± 1.9 [h]	-3.1σ
K2-24 b	21.0 ± 5.4 [i]	$19.8^{+4.5}_{-4.4}$ [j]	$+0.17\sigma$
K2-24 c	27.0 ± 6.9 [i]	$26.0^{+5.8}_{-6.1}$ [j]	$+0.11\sigma$

[a] Cochran et al. (2011)
[b] Weiss et al. (2013)
[c] Masuda et al. (2013)
[d] Dai et al. (2016)
[e] Barros et al. (2015)
[f] Hellier et al. (2012)
[g] Becker et al. (2015)
[h] Weiss et al. (2016)
[i] Petigura et al. (2016)
[j] Dai et al. (2016)

one of the methods is systematically biased compared to the other.

7.1.3 Effect of Planet Period

7.1.4 Period Differences

A possible clue to the difference between the RV and TTV masses might be seen in the right panel of Figure 7.1, which shows mass determination versus the planetary orbital period. One can see that on the average, the TTV (blue) periods are substantially longer than the RV (red) ones. As pointed out by S16, this difference could be the result of the dependence of the SNR of the two techniques on the orbital period.

S16 showed that the SNR for an RV measurement is

$$\mathrm{SNR}_{\mathrm{RV}} \sim \frac{M_{\mathrm{p}}}{\sigma_{\mathrm{RV}} P^{1/3}} \ , \tag{7.1}$$

where σ_{RV} is the intrinsic uncertainty of a given RV measurement, M_{p} is the planetary mass and P is the orbital period of the planet. For a TTV measurement S16 obtained

$$\mathrm{SNR}_{\mathrm{TTV}} \sim \frac{M_{\mathrm{p}} R_{\mathrm{p}}^{3/2} P^{5/6}}{\sigma_{\mathrm{TTV}}} \ , \tag{7.2}$$

with R_{p} the radius of the planet and σ_{TTV} the uncertainty of a point in the light curve (S16).

We agree with these forms for an individual RV and TTV measurement, but point out that the vast majority of transiting exoplanets in the <8 R_{Earth} range of our interest have been discovered and characterized by the *Kepler* mission, whose observing window was 4 years. Therefore, when fitting, e.g., a sine curve to the TTV measurements, shorter period planets have more data points in the fixed observational window (Mazeh et al., 2013; Holczer et al., 2016). The number of transit (and thus TTV) observations, N, is $\propto P^{-1}$ and, assuming statistical white noise properties, SNR $\propto N^{1/2}$. Thus we suggest that Equation 7.2 need be multiplied by a factor $P^{-1/2}$ to yield

$$\mathrm{SNR}_{\mathrm{KEPLER}} \propto \frac{M_{\mathrm{p}} R_{\mathrm{p}}^{3/2} P^{1/3}}{\sigma_{\mathrm{TTV}}} \ . \tag{7.3}$$

The SNR of an RV data set also increases as $N^{1/2}$ after the first orbital period (S16). However, unlike TTV measurements which relied nearly exclusively on *Kepler*, there is not a clear practical limit to the length of time over which RV measurements may be made. Thus there is no period dependency on N, and the RV proportionality still holds when Equation 7.1 is multiplied by $N^{1/2}$ (excluding planets whose periods are so long that less than a few orbital periods have been observed). With or without our modification, it is

obvious that it is easier for the RV technique to obtain a short-period solution, all other parameters being equal, while the TTV techniques can obtain masses more easily for a longer period. The two relations can therefore account for the substantial period difference between the RV and TTV populations. A dependence of M–R relation of the orbital period might therefore explain the mass difference between the two populations.

7.1.5 M–R Relation for Different Periods for the RV and the TTV Masses

To study the mass-radius relationship and its dependence on observational technique, we fit all known masses and radii with a power-law M–R relation—$M_p \propto R_p^x$, where M_p and R_p are the planetary mass and radius. We then separated the data into RV and TTV measurements, and for each subsample we performed a weighted total (or orthogonal) least squares linear fit (e.g., York, 1966; Krystek & Anton, 2007) to the logarithmic mass and radius with a Markov chain Monte Carlo search. The linear best fits for all measurements (green), RV measurements (red), and TTV measurements (blue) are shown as straight lines in the upper panel of Figure 7.2 and listed in the first line of Table 7.2.

Table 7.2: Power Law Model Fits of the Form $M = 10^C \times R^E$

Period Range	Combined Data Fit		RV Fit		TTV Fit	
	Exponent	Constant	Exponent	Constant	Exponent	Constant
All	0.99 ± 0.04	0.45 ± 0.02	1.45 ± 0.07	0.41 ± 0.03	0.64 ± 0.06	0.50 ± 0.03
$P < 11$ days	1.46 ± 0.06	0.34 ± 0.03	1.50 ± 0.08	0.36 ± 0.03	1.34 ± 0.19	0.31 ± 0.07
$P > 11$ days	0.69 ± 0.06	0.51 ± 0.03	0.73 ± 0.19	0.83 ± 0.09	0.61 ± 0.06	0.49 ± 0.03

The upper panel of Figure 7.2 shows the linear logarithmic regressions obtained separately for the TTV and the RV masses using planets of all orbital periods. The linear fit for the RV mass measurements, with exponent of 1.45 ± 0.07, is substantially steeper than that of the TTV measurements, with exponent of 0.64 ± 0.06. The larger exponent could suggest that masses measured via the RV technique increase with radius significantly more quickly than the masses obtained by the TTV measurements.

To see if this is true, and based on the previous subsection, we divided the measurements

Figure 7.2: Mass Radius Relationship Power-Law Fits

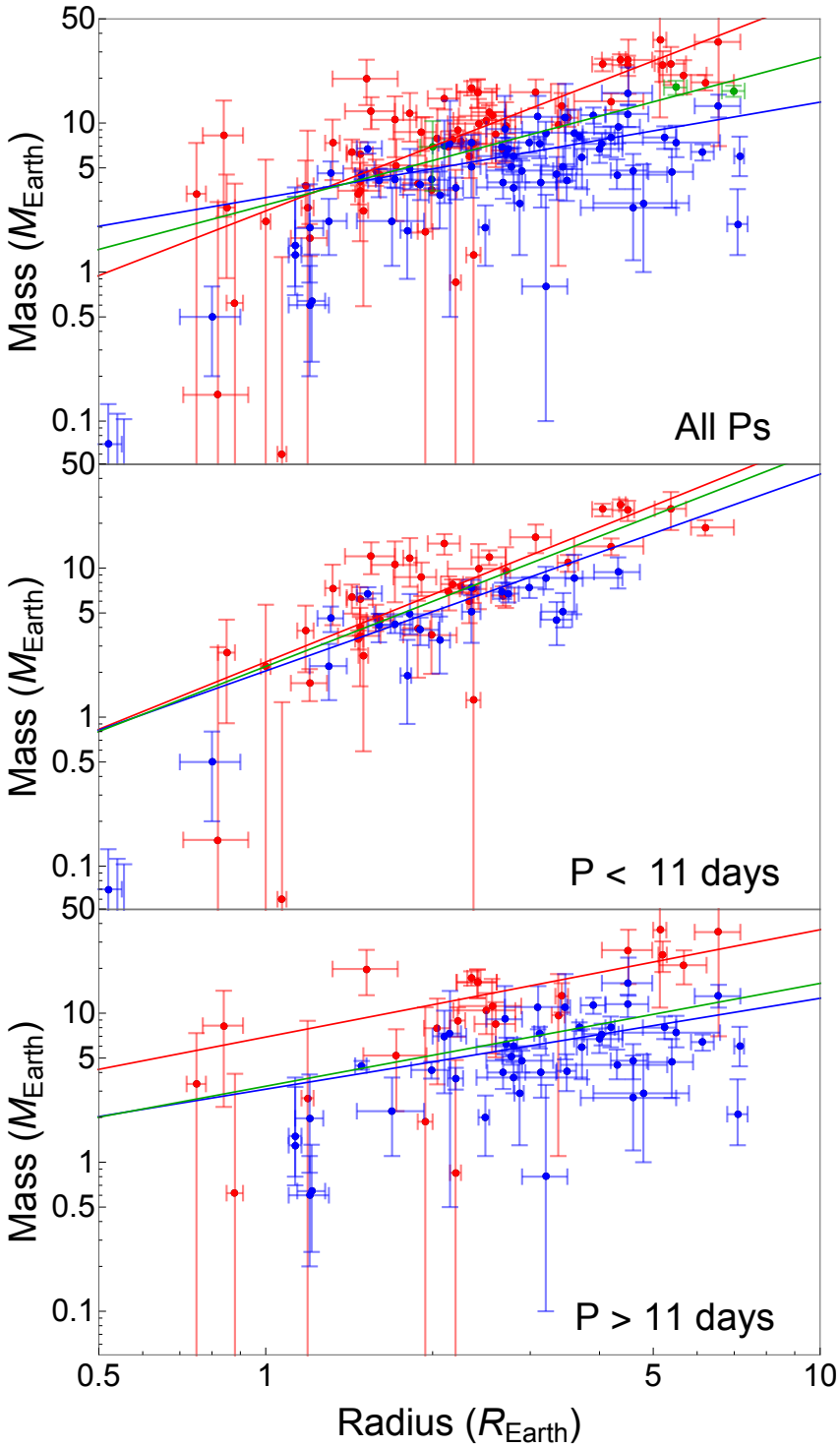

Power-law fits to the masses and radii of planets measured via RVs (red), TTVs (blue), and both (green) including all data (top panel) and then broken into short and long period bins (bottom 2 panels). Note that the slopes of the power laws are consistent in each period bin, but a constant offset is remains in the long period bin. Parameters of the fits can be found in Table 7.2.

into short- ($P < 11$ day) and long-period ($P > 11$ day) ranges. This period boundary was chosen empirically by identifying the maximum period for which planets with lower periods showed a similar M-R relationship. Figure 7.2 and the two lower lines of Table 7.2 reveal a clear difference in planet properties in each period bin. In each of these bins we again fitted linear regressions to the RV and TTV masses, and for these two data sets combined. Three surprising features emerged. First, the difference between the exponents of the M–R relation obtained for the TTVs and the RVs at the same period range disappeared. Second, there is a significant difference between the logarithmic slope of the M–R relation in the short-period range, 1.46 ± 0.06, and the long-period range, of 0.69 ± 0.06. These values are similar to the slopes obtained by the RV and TTV measurements individually over all period ranges, suggesting the different masses obtained by RVs and TTVs are probably a result of the different period range observed. As previously noted, this observational difference is due to the different period dependency of the methods' sensitivities (see Equations 7.1 and 7.3). Additionally, none of the measured M-R relationships agree with the frequently used power-law slope of 2.06 inspired by Solar System objects (Lissauer et al., 2011b). We also confirm that the few points at small R and M values do not dominate these effects by refitting the data while including a range of different minimum mass and radii cutoffs.

A third feature that emerged in Figure 7.2 lower panel is a statistically significant offset between the RV and TTV measurements in the long-period bin. Almost all the masses derived by RVs are higher than those derived by TTVs. In fact, there is no significant RV mass determination below 3–4$M_{\rm Earth}$. We attribute this difference to the fact that TTVs readily can detect long-period planets of low mass, whereas RV measurements are decreasingly sensitive to low-mass planets at longer orbital periods (see Equation 7.1). This decline in sensitivity could lead to a higher-mass threshold for the RV detection and the apparent observed mass discrepancy. Additionally, when the stellar rotation period ($\sim$10–50 days for main sequence FGKM stars) approaches the planetary orbital period, the RV amplitude detection threshold can worsen due to challenges distinguishing between star spot

activity and the planet signal. This degeneracy may prevent low-mass planets with long periods from being confidently detected by the RV technique even with a large amount of observational data.

7.1.6 Planet Period Ratios

The SNR of TTV signals depends strongly on the period ratio of the perturbing adjacent planet. The signal is greatest for compact systems near low-order mean motion resonances (e.g., Agol et al., 2005; Lithwick et al., 2012; Hadden & Lithwick, 2017, Figure 8), all else equal. On the other hand, RV mass detection of a planet is potentially hampered by the existence of another planet with a similar period. As a result, there is an inherent observational bias for more tightly-spaced planetary systems measured with TTVs compared to RVs, as shown in Figure 7.3. A two-sample Kolmogorov-Smirnoff test returns $\alpha = 4 \times 10^{-6}$, indicating a clear statistical difference between the two distributions. More RV observations of compact systems near MMR are necessary to shed light on the possibility that planets of a given radius in widely-spaced systems may have systematically different masses than those in more compact systems.

7.1.7 Summary

Following S16, we have shown that the difference between RV and TTV masses can be attributed to the different SNR dependence on orbital period between the two techniques. This difference causes a substantial difference in the period range of the two techniques—RV masses are mostly obtained for relatively short orbital periods, while the TTVs masses are weighted towards longer periods. When we divide the data into short- and long-period orbits, most of the differences between the masses of the two techniques disappear. This suggests that the underlying mass distribution measured by the RV and TTV techniques has similar properties.

We have found that the exponent in the power-law relation $M_p \propto R_p^x$ that presumably

Figure 7.3: RV and TTV Multiplanet Period Ratio Distributions

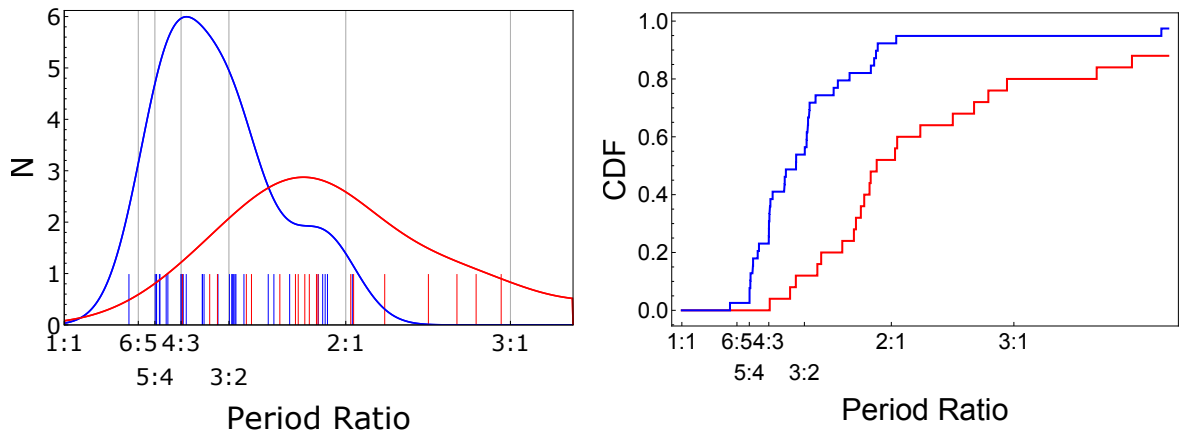

Left: The period ratios of pairs of planets with masses measured via TTV (blue) and RV (red) are marked as ticks on the horizontal axis with logarithmic scaling. A broad Gaussian kernel is used to produced a smooth histogram of both distributions. Note that many RV planets have no known companions and are therefore not included on this plot. *Right:* The cumulative distribution function (CDF) of the TTV and RV planet period ratios. There are a few very-widely spaced RV planets, which causes the RV (red) CDF to reach 1.0 beyond the limit plotted in this panel.

characterizes the M–R relation is substantially different for the short and the long orbital periods—the exponent best value is 1.46 ± 0.06 for the short-period planets and 0.69 ± 0.06 for the long-period range. Both values suggest that, on average, the density of the planets (proportional to M_p/R_p^3), is decreasing as a function of the planetary radius, as expected from considerations of planetary composition. However, our analysis suggests that the rate of density decrease depends on the orbital period. If confirmed, this has to be accounted for by planetary formation or evolution theories. We also demonstrate the expected more compact orbital period ratios of planets measured via TTVs compared to RVs.

7.1.8 Acknowledgements

We thank Jason Steffen for his seminal paper which inspired this study and for helpful discussions, and we thank Daniel Fabrycky, Jack Lissauer, William Welsh, and an anonymous reviewer for insightful comments which considerably improved this work. We greatly appreciate Daniel Jontof-Hutter for providing us with a tabulation of small exoplanet data through 2015 and illuminating comments. We also thank Josh Burkhart for making his Mathematica MCMC code publicly available (https://github.com/joshburkart/mathematica-mcmc). This research has made use of NASA's Astrophysics Data System. This research has received funding from the Israeli Centers for Research Excellence (I-CORE, grant No. 1829/12) and Grant NNX14AB87G issued through NASA's *Kepler* Participating Science Program.

7.2 Stochastic Migration of Low Mass Planets in a Turbulent Disk

7.2.1 Introduction

NASA's *Kepler* space observatory program is the most prolific exoplanet discovery mission to date, identifying over 4,000 confirmed planets and candidates likely to be actual planets (Coughlin et al., 2016; Morton et al., 2016). Of these, over 800 are found to be in multiplanet

systems with multiplicities ranging from 2 to 7. The distribution of the ratio of the periods of pairs of adjacent planets in multiplanet systems in the *Kepler* data set is broad, but has several significant features. Period ratios near first order mean motion resonances (MMRs: planet period ratios of the form $(j+1)/j$ where j is the integer 'rank' of the resonance) are preferred, particularly near 2:1, 3:2, and 4:3 (Fabrycky et al., 2014; Steffen & Hwang, 2015). Indeed, some systems have many planets in or near resonance (a "resonant chain," e.g., Goździewski et al., 2016; Mills et al., 2016; MacDonald et al., 2016). This, along with theoretical modeling, has been used to suggest that planets in the population discovered by *Kepler* formed via migration in a natal disk (Terquem & Papaloizou, 2007; Ida & Lin, 2008; Cossou et al., 2014; Mills et al., 2016). However, the majority of pairs of planets in *Kepler* multi-planet systems do not lie very close to resonances (Fabrycky et al., 2014). Guided by intuition based on our own inner Solar System, this has led others to suggest that these planets formed primarily in situ via giant impacts resulting in nearly random period ratios (Raymond et al., 2008; Hansen & Murray, 2012; Chiang & Laughlin, 2013). However, any theory that successfully describes the planet formation process of the multiplanet systems observed by *Kepler* must reproduce *both* a broad distribution of period ratios and the features near MMRs. Several solutions have been proposed, including considering dynamical effects which may sculpt the distribution near MMRs from a previously random distribution (Petrovich et al., 2013), dissipation away from resonance (Lithwick & Wu, 2012; Delisle et al., 2012; Batygin & Morbidelli, 2013), and migration processes which lead to planets not getting caught in MMRs permanently (Goldreich & Schlichting, 2014; Rein, 2012; Batygin & Adams, 2017; Pan & Schlichting, 2017). This paper focuses on the suggestion by Rein (2012, henceforth R12) that migration with stochastic forces, likely arising from MRI-induced turbulence in the disk (see, e.g., Balbus & Hawley, 1998), causes some planets to get trapped in MMRs but most to escape them (Adams et al., 2008).

R12 shows (Fig. 2) that the period ratio distribution (PRD) of *Kepler* can be closely matched by this method. We extend this result by considering the effects of this mechanism

on resonant chains and and with a slightly more sophisticated model. The existence of a subset of systems with 3- and 4-planet chains suggests that the level of turbulence must not be so great that all such chains are disrupted.

7.2.2 Methods

Our first step is to construct a set of multi-planet systems to numerically evolve and compare to the *Kepler* data set. We generate probability distribution functions (PDFs) of the multiplicity, masses, and period ratios of planet systems by convolving the observed *Kepler* distributions with a Gaussian kernel. This is straightforward for multiplicity and period ratio, as both quantities are well-measured, however the majority of *Kepler* planets do not have well known masses. Following R12, we therefore use the $M_p = R_p^{2.06} M_\oplus$ power law from Lissauer et al. (2011a) as nominal *Kepler* points, before applying the Gaussian kernel. We then produce a synthetic planet population by drawing a multiplicity and the appropriate number of masses and period ratios from their respective distributions, and setting each star to $1 M_\odot$. This method produces a sample which broadly resembles *Kepler* but does not have identically matching architectures or correlations between planet sizes (Lissauer et al., 2011b; Ciardi et al., 2013; Weiss et al., 2017). Finally, we scale the systems so that the innermost planet has a 100 day orbital period. This allows dissipative forces to move the planets inward to the presently observed short-period orbits.

We evolve the system using the REBOUND N-body code (Rein & Liu, 2012), with semi-major axis and eccentricity damping. While R12 applied damping forces only to the outermost planet, we extend this method to include damping on all planets. We set the semi-major axis damping timescale of the innermost planet ($\tau_{a,1}$) to 10^4 years, and its eccentricity damping timescale ($\tau_{e,1}$) to $10^{-2}\tau_{a,1}$. For every other planet (i), we set the damping timescales to

$$\tau_{a,i} = \tau_{a,1}(a_i/a_1)^{-3/2}(m_i/m_1)^{-1}, \tag{7.4}$$

and

$$\tau_{e,i} = 10^{-2}\tau_{a,i}. \tag{7.5}$$

This migration timescale is shorter than nominally expected for planets in the mass range of the majority observed by *Kepler* ($\tau_a \gtrsim 10^5$ years; see, e.g., Lubow & Ida, 2010), but produces similar inward migration behavior.

We use a parameterized turbulence model following R12, where the radial and azimuthal stochastic forces are independent Markov processes. The strength of turbulent forces is measured relative to the gravitational force from the central star and represented by $\alpha_{\rm T}$[1]. To prevent correlation timescales longer than an orbital timescale for inner planets of a system, we set the correlation timescale for the turbulence to be half of the orbital period of each planet, rather than the outermost planet as in R12 .

We also consider the effects of the disk evolution on these forces. We expect that for a large portion of a protoplanetary disk's evolution it is optically thick to ionizing radiation (Roberge & Kamp, 2010). This results in a dead zone in the mid-plane of the disk that is cooler and less susceptible to MRI turbulence. The dead zone is favorable for planet formation and, once formed, protoplanets remain there due to inclination damping. Planets in this region are likely to experience smoother migration due to the low turbulence levels very near the planet (Oishi et al., 2007; Armitage, 2015). Therefore, for $t = [0, \tau_{a,1}]$, we reduce the nominal stochastic force ($\alpha_{\rm T}$) in the model by a factor of $\beta = 10^3$. We find that most planets have already locked into resonant pairs or chains after $t = \tau_{a,1}$, and we have structured our initial conditions to yield planets entering the approximate period regime of observed *Kepler* planets at this time. Therefore, additional low-turbulence migration time is unlikely to have significant effect on the distribution of period ratios, but would require further numerical integration from greater starting semi-major axes in order to approximately reproduce the *Kepler* observations.

1. R12 uses α for this value. Here the subscript T is added to remove any ambiguity between this turbulence parameter and the Shakura-Sunyaev viscosity α parameter often used to describe disks.

As the disk dissipates, it eventually becomes thin to ionizing radiation, increasing turbulence into the disk midplane relative to the damping forces. Once the disk surface density is $\sim$ 100 g cm^{-2}, the approximate depth at which cosmic rays can penetrate to the disk midplane, MRI turbulence and eliminates the dead zone and the disk becomes fully turbulent (Gammie, 1996; Ciesla & Dullemond, 2010). Therefore, we set $\beta = 1$ and allow the full effects of the stochastic forcing to be felt over 10^4 years representing the final stages of disk dissipation. This may underestimate the amount of time which the disk spends fully turbulent, but the effects of turbulence are readily seen in our simulations at this timescale. Since the *Kepler* planets are in short period orbits ($P \lesssim 200$ days), we consider only disk properties inside a few AU. In this region the disk dissipates relatively evenly across the small range in semi-major axis spanned by a multiplanet system (as opposed to the disk at $\gtrsim$ 10AU which may dissipate more from the inside out; Ciesla & Dullemond, 2010). We are not concerned with the exact dissipation method, but fit the decay of the disk surface density as given in Ciesla & Dullemond (2010) at 0.1AU. We set the amplitude of the stochastic forcing relative to the gravitational force from the star proportional to the disk surface density. We also adjust the semi-major axis and eccentricity damping timescales inversely proportionally to the surface density of the remaining disk. Our surface density evolution follows

$$\log_{10} \Sigma = f_1(e^{f_2 t_f} - 1) + f_3 t_f, \tag{7.6}$$

where $f_1 = -3.281 \times 10^{-6}$, $f_2 = 13.824$, and $f_3 = -0.879$. t_f is the fractional amount of time which has passed since the beginning of the disk dissipation to the end after 10^4 years and thus ranges from 0 to 1 during the disk dissipation phase ($t_f = (t - 10^4 \text{ years})/(10^4 \text{ years})$). After the surface density reaches 0, we continue integrating the N-body equations of motion with no damping or stochastic forcing until time $t = 10^5$years.

We integrate 2,500 sets of initial conditions over a wide range of turbulences from $\alpha_{\rm T} = 5 \times 10^{-4}$ to 10^{-10}, spanning the range expected from a fully turbulent disk to that which is

Figure 7.4: Post Dead Zone Migration Period Ratio CDF.

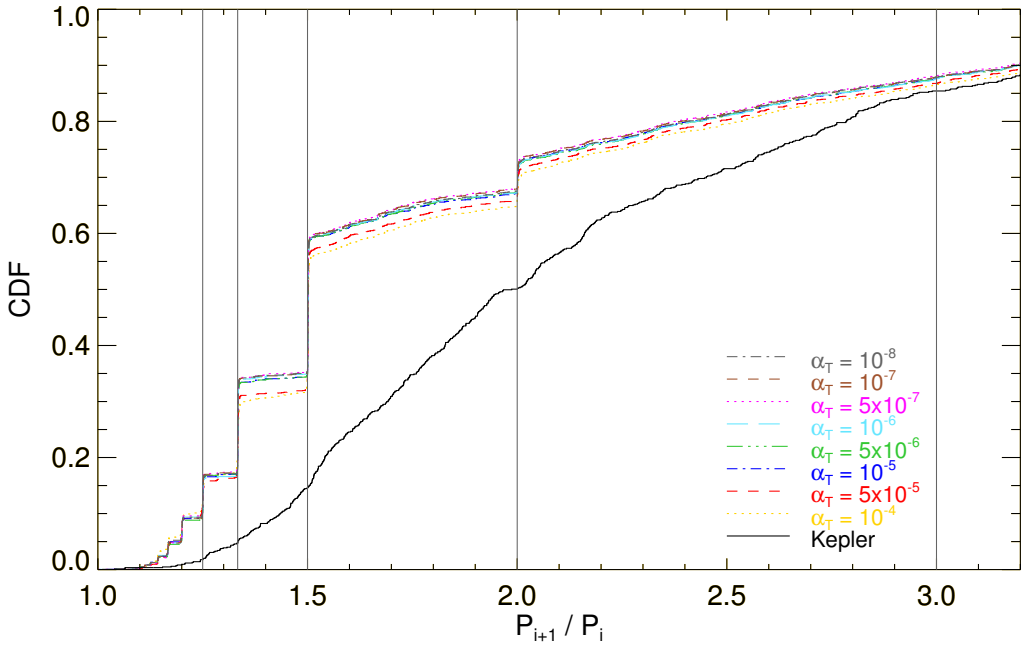

The cumulative distribution of period ratios of neighboring pairs of planets after the dead zone migration with $\beta = 10^3$ for a wide range of $\alpha_{\rm T}$ values (broken, colored lines) compared to the observed *Kepler* distribution (black, solid line). The majority of planets become trapped in resonances.

very smooth (Rein, 2012; Rein & Papaloizou, 2009). We also integrate 500 initial conditions over the same turbulence range, but stop integration after 10^6 years.

7.2.3 Results

During the dead zone migration (the first $t = \tau_{a,1}$ years), the planets consistently encounter, and get trapped in, mean motion resonances for all chosen values of $\alpha_{\rm T}$ (Fig. 7.4). These systems are compact compared to observed *Kepler* systems, stabilized by the damping forces in the disk. Due to the low levels of turbulence in the initial migration stage and the relatively widely-spaced initial conditions matching observed *Kepler* data, the MMRs in which migrating planet pairs get trapped are usually widely-spaced (low-rank).

After setting $\beta = 1$, i.e. assuming that the disk has becoming optically thin to ionizing

radiation, we allow the turbulent disk to dissipate as described in §7.2.2, which has a significant effect on the PRD. Figure 7.5 shows the PRDs after integration has been concluded. This represents the states of the systems after approximately 3×10^6 orbits of the inner planets without any damping or stochastic forces to allow short-term instabilities to occur, following disk dissipation. Very low level turbulence results in only a small effect on the final period distribution, with the resonant systems remaining stable. This is because at typical *Kepler* planet masses, the planets are many mutual Hill radii apart:

$$R_{\rm H,m} = \frac{a_1 + a_2}{2} \left(\frac{m_1 + m_2}{3M_\star} \right)^{1/3}, \tag{7.7}$$

where a_i and m_i are the semi-major axis and radius of the $i^{\rm th}$ planet. Scale-free separations can be described in units of mutual Hill radii:

$$\Delta_{\rm H} = (a_2 - a_1)/R_{\rm H,m}. \tag{7.8}$$

For instance, planets at a 2:1 orbital period ratio at 0.1 AU will have $\Delta_{\rm H} \approx 20$, for $m_1 \approx m_2 \approx 6M_{\rm Earth}$, near the peak of the assumed observed *Kepler* mass distribution. On Gyr timescales, planets at such great separations are unlikely to go unstable even accounting for the possible eccentricity excitation due to resonance and many-planet chains (Chambers et al., 1996; Smith & Lissauer, 2009; Obertas et al., 2017). However, the more tightly-spaced resonant planets may indeed subsequently go unstable (Obertas et al., 2017).

On the other hand, high levels of turbulence ($\alpha_{\rm T} \gtrsim 10^{-6}$) result in the removal of planets near resonance and fewer compact systems survive. Intermediate levels of turbulence ($\alpha_{\rm T} \sim 10^{-6}$) generate more compact systems on average than even low turbulent levels however (see Fig. 7.5 below the 3:2 period ratio). The turbulence helps break planet pairs out of MMR so that their relative contraction continues, but it is not so high that it allows them to skip over all MMRs or brings them into collisional trajectories. As a result, many of these systems get caught in higher-rank first-order MMRs than when there is no turbulence (see

Figure 7.5: Final Period Ratio CDF.

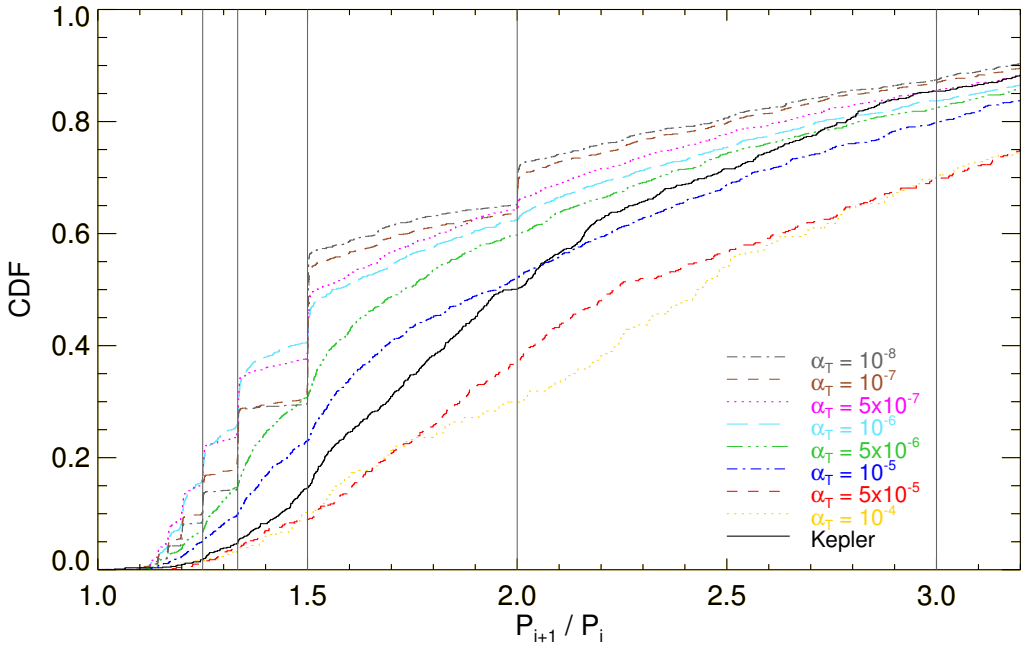

The cumulative distribution of period ratios of neighboring pairs of planets after the deadzone migration with $\beta = 10^3$, turbulent disk dissipation, and damping-free N-body integration after 10^5 years for a wide range of $\alpha_{\rm T}$ values (broken, colored lines) compared to the observed *Kepler* distribution (black, solid line).

Fig. 7.5). Additionally, the 2:1 resonance is nearly devoid of planet pairs as the turbulence allows planets to escape this resonance and move towards more compact resonances. This level of turbulence is consistent with that predicted to represent the forcing on a small planet in a fully turbulent disk (Rein & Papaloizou, 2009).

We also consider the length of resonant chains (3 or more planets in a series of 2-body resonances) for the different turbulence levels (see Fig. 7.6). We define a resonant chain as a sequence of 3 or more planets with each pair of planets within 0.5% of a nominal low-order MMR period ratio. We consider here the resonances 2:1, 3:2, 4:3, 5:4, and 3:1. For low eccentricity planets with $\mu = M_{\rm p}/M_\star = 10^{-5}$ (between $M_{\rm Earth}$ and $M_{\rm Neptune}$) the width of the low-rank, first-order MMRs is $\sim$0.1% (Petrovich et al., 2013). Thus for the *Kepler* planet mass distribution, which is dominated by sub-Neptune mass planets, the observed period ratios of resonant planets will be within a factor of a few of this value. For low levels of turbulence, virtually all neighboring pairs of planets get trapped in resonance, so resonance chains are a natural result (Fig. 7.6). For high turbulence levels, resonant chains are even more rare than resonant pairs, because they require multiple pairs of nearby planets to all maintain resonances.

We also consider the effect of observational bias on the PRD. We correct for this bias by taking the set of simulated multiplanet systems, picking a random system (with replacement) and observer orientation, and calculating how many planets in the system would have an impact parameter less than 1.0 from that perspective. We repeat this procedure until we have 3000 simulated observed multiplanet systems. As expected, compact systems become more strongly represented (Fig. 7.7).

We also run a sample of 500 systems at each turbulence level for 10^6 years after disk dissipation to test if dynamical instabilities would significantly change the PRD on this timescale. The PRD has no significant changes, with $<$2% of resonant chains destabilizing in this order of magnitude increase in integration time. This is likely due to the large dynamical spacing between low-mass planets in low rank MMRs.

Figure 7.6: Distribution of Resonant Chains.

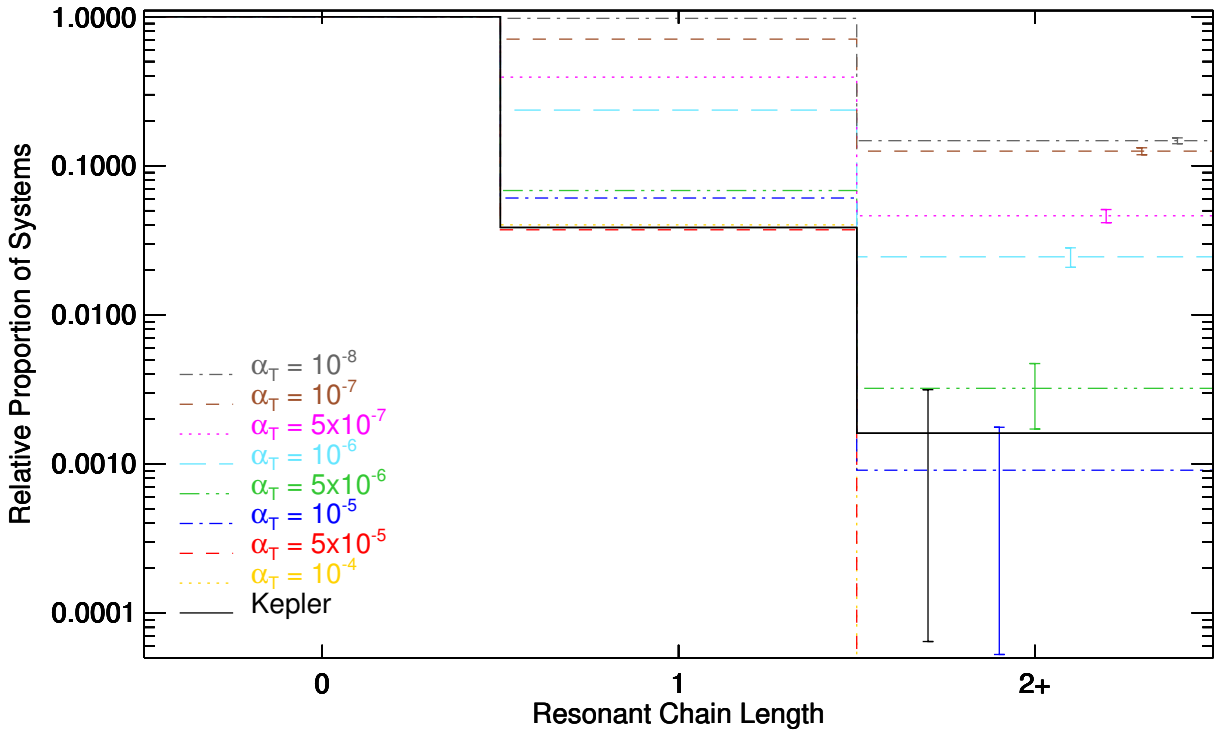

The distribution of the length of resonant chains neighboring pairs of planets after the deadzone migration with $\beta = 10^3$, turbulent disk dissipation, and damping-free N-body integration after 10^5 years for a wide range of α_T values (broken, colored lines) compared to the observed *Kepler* distribution (black, solid line). Binomial uncertainties are shown in the column showing resonant chains, slightly horizontally offset from each other for visual clarity.

Figure 7.7: PRD Corrected for Observational Bias

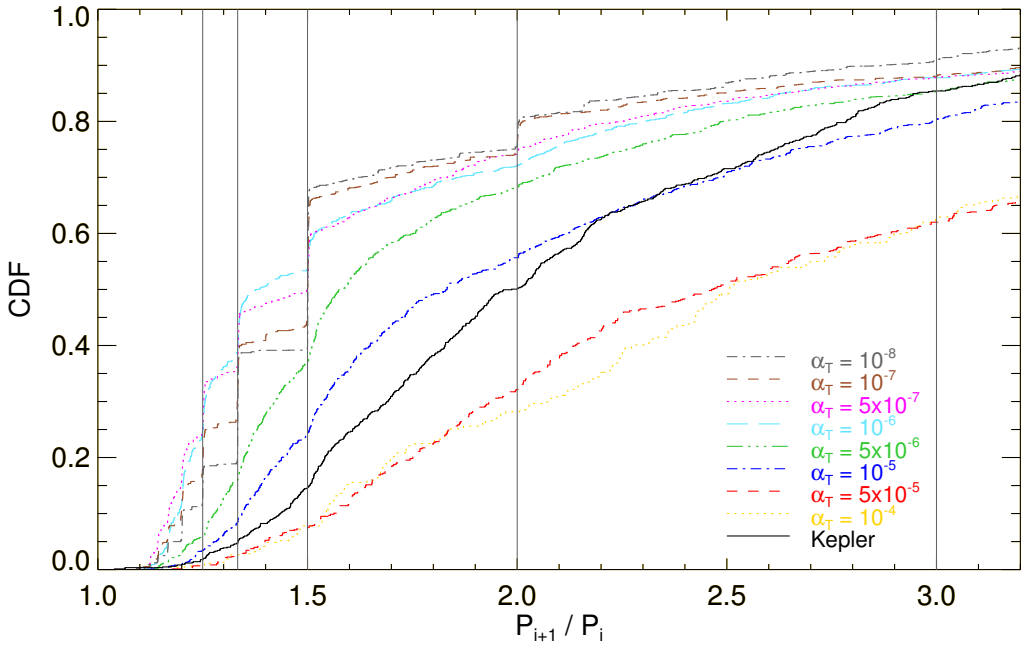

The same as in Fig. 7.5, except corrected for observing bias that results in systems with more compact planet spacings to more frequently be actually observed as a multiplanet system.

7.2.4 Discussion

We find that planet migration in a disk with turbulent strength $\alpha_{\rm T} \approx 10^{-5}$ reproduces both the PRD and the resonant chain production observed in *Kepler*. Planet pairs may have commonly entered resonance early in their migration histories, but are efficiently removed from resonance as turbulence sets in and the disk dissipates. Resonant trapping along with turbulence ensures that planets are fairly widely dynamically spaced, so that the systems do not dramatically change their PRD within Myr timescales after the disk dissipates due to dynamical instabilities.

Izidoro et al. (2017, henceforth I17) came to the conclusions that most systems do capture into resonance but subsequently go unstable, and that turbulence does not have significant effect on planet's migration histories. §7 of I17 suggests that R12 suffered from several deficiencies that led them to this different conclusion. I17 first questions R12's decision to

include stochastic forcing on all planets, but only semi-major axis and eccentricity damping on the outermost planet (which guarantees convergent migration). We address this issue by explicitly including these damping forces on all planets in theoretically predicted proportions (see Eqs. 7.4-7.5), along with the stochastic forces. They also argue that the length of the integration of the planets in the disk may have been insufficient in length to allow capture of planets into MMRs. In this study we demonstrate that after our initial dead-zone migration phase, the majority of planet pairs have indeed reached resonance. Lastly, I17 questions the turbulent force implementation. They comment that (1) the implementation is less sophisticated than their own, and (2) the levels of turbulence were chosen to explicitly to reproduce observations. We have a very similar turbulent scheme for numerical simplicity, but this work covers a broad range of resulting turbulences. Additionally, one may consider the simplicity of our turbulent scheme an advantage rather than a drawback, because it does not rely on the specifics of the parameterized density wave scheme employed (see Laughlin et al., 2004; Ogihara et al., 2007). By addressing these issues, we consider a comparison between results here and I17 to be valid.

In the stage where the disk is present our simulations are somewhat consistent with that found in I17; however, I17 produces systems that are even more compact (more than half of systems possess period ratios ≤ 1.25) and posses more planets. Whereas our initial conditions assume widely spaced protoplanets drawn from the observed *Kepler* distribution, I17 began with many compact embryo spacings in the disk of $\sim 5R_{\rm H,m}$. These embryos therefore often begin interior to low rank MMRs, and results in a population of extremely compact resonant systems post disk-dissipation. These often naturally go unstable on Myr timescales, but sub-Neptune planets in more widely spaced chains may remain stable for Gyrs (Obertas et al., 2017). This suggests that the present planetary architectures provides some insight into the natal spacings of the planetary embryos.

I17 concludes in part that N-body destabilization of compact resonant chains may lead to the observed *Kepler* PRD. However, their simulations produce too many planets in resonance

which do not go unstable after the disk dissipates, leading to a remnant population of resonant systems that has not been observed in abundant enough numbers by *Kepler*. For turbulence to have significant influence on the results of I17, it would need to occur at much higher levels than implemented by I17; however, Laughlin et al. (2004) suggests this may indeed be the case, with planets following a random walk more than an inward path in some regimes.

Our results indicate that a stage of significant turbulence during disk dissipation due to a fully turbulent disk may contribute to the PRD, as suggested in R12. This effect may result in (1) a larger fraction of planets away from resonance at the time of disk dissipation and (2) a set of resonant chains in 3:2, 4:3, and 5:4 MMRs but have few planets in 2:1 resonance, and that are likely to remain in stable resonant chains due to wide dynamical spacings. This would more faithfully reproduce the entire observed *Kepler* planet population – the sample of planets observed by *Kepler* suggest that 2:1 resonances among sub-Neptune resonant chains are rare (see, e.g., Goździewski et al. 2016; MacDonald et al. 2016; Mills et al. 2016; Luger et al. 2017, but cf. Lee & Peale 2002; Wright et al. 2011 for giant planets), with the excess of pairs near 3:2 much more statistically significant (Steffen & Hwang, 2015). Any model that produces resonant chains of sub-Neptune planets at a 2:1 orbital period ratio at $\sim$0.1 AU would require a robust destabilization method since such systems are likely to otherwise remain stable. On the other hand, the observed resonant chains – including the outstanding example Kepler-223 (Mills et al., 2016) – may be considered a natural part of the distribution of planetary systems without requiring any special circumstances in the disk to form.

7.2.5 Acknowledgements

I thank Hanno Rein for his seminal 2012 paper which inspired this work and for making his code publicly available (https://github.com/hannorein) - vastly improving the efficiency of this research. I also thank Daniel Fabrycky for invaluable guidance and insightful comments.

Funding for this work came in part from Grant No. NNX14AB87G. This work made use of NASA's astrophysical data system (ADS).

REFERENCES

Adams, F. C., Laughlin, G., & Bloch, A. M. 2008, ApJ, 683, 1117

Adams, J. C. 1846, MNRAS, 7, 149

Agnor, C. B., Canup, R. M., & Levison, H. F. 1999, Icarus, 142, 219

Agnor, C. B., & Lin, D. N. C. 2012, ApJ, 745, 143

Agol, E., & Deck, K. 2016, ApJ, 818, 177

Agol, E., Steffen, J., Sari, R., & Clarkson, W. 2005, MNRAS, 359, 567

Agol, E., & Steffen, J. H. 2007, MNRAS, 374, 941

Akaike, H. 1974, IEEE Transactions on Automatic Control, 19, 716

Almenara, J. M., Díaz, R. F., Mardling, R., et al. 2015, MNRAS, 453, 2644

Alonso, R., Aigrain, S., Pont, F., Mazeh, T., & CoRoT Exoplanet Science Team. 2009, in IAU Symposium, Vol. 253, Transiting Planets, ed. F. Pont, D. Sasselov, & M. J. Holman, 91–96

Ambikasaran, S., Foreman-Mackey, D., Greengard, L., Hogg, D. W., & O'Neil, M. 2014, ArXiv e-prints, arXiv:1403.6015

Angus, R., Aigrain, S., Foreman-Mackey, D., & McQuillan, A. 2015, MNRAS, 450, 1787

Armitage, P. J. 2010, Astrophysics of Planet Formation, 294

—. 2015, ArXiv e-prints, arXiv:1509.06382

Armstrong, D., Martin, D. V., Brown, G., et al. 2013, MNRAS, 434, 3047

Armstrong, D. J., Osborn, H. P., Brown, D. J. A., et al. 2014, MNRAS, 444, 1873

Asphaug, E., & Reufer, A. 2014, Nature Geoscience, 7, 564

Baglin, A. 2003, Advances in Space Research, 31, 345

Bailes, M., Bates, S. D., Bhalerao, V., et al. 2011, Science, 333, 1717

Bakos, G., Noyes, R. W., Kovács, G., et al. 2004, PASP, 116, 266

Balbus, S. A., & Hawley, J. F. 1998, Reviews of Modern Physics, 70, 1

Baranne, A., Queloz, D., Mayor, M., et al. 1996, A&AS, 119, 373

Barnes, S. A. 2003, ApJ, 586, 464

Barros, S. C. C., Almenara, J. M., Demangeon, O., et al. 2015, MNRAS, 454, 4267

Batalha, N. M., Borucki, W. J., Koch, D. G., et al. 2010, ApJ, 713, L109

Batalha, N. M., Rowe, J. F., Bryson, S. T., et al. 2013, ApJS, 204, 24

Batygin, K., & Adams, F. C. 2017, AJ, 153, 120

Batygin, K., Deck, K. M., & Holman, M. J. 2015, ArXiv e-prints, arXiv:1504.00051

Batygin, K., & Laughlin, G. 2015, Proceedings of the National Academy of Science, 112, 4214

Batygin, K., & Morbidelli, A. 2013, AJ, 145, 1

Becker, J. C., & Adams, F. C. 2016, MNRAS, 455, 2980

Becker, J. C., Vanderburg, A., Adams, F. C., Rappaport, S. A., & Schwengeler, H. M. 2015, ApJ, 812, L18

Bedell, M., Bean, J. L., Meléndez, J., et al. 2017, ApJ, 839, 94

Béky, B., Kipping, D. M., & Holman, M. J. 2014, MNRAS, 442, 3686

Binney, J., & Tremaine, S. 2008, Galactic Dynamics: Second Edition (Princeton University Press)

Bonfils, X., Mayor, M., Delfosse, X., et al. 2007, A&A, 474, 293

Borderies, N., & Goldreich, P. 1984, Celestial Mechanics, 32, 127

Borucki, W. J., & Summers, A. L. 1984, Icarus, 58, 121

Borucki, W. J., Koch, D., Basri, G., et al. 2010, Science, 327, 977

Borucki, W. J., Koch, D. G., Basri, G., et al. 2011, ApJ, 736, 19

Boss, A. P. 1997, Science, 276, 1836

Bourtembourg, R. 2013, Journal for the History of Astronomy, 44, 377

Bouvard, A. 1821, Tables astronomiques publiees par le Bureau des Longitudes de France

Boyajian, T. S., von Braun, K., van Belle, G., et al. 2012, ApJ, 757, 112

Brandner, W., & Hormuth, F. 2016, Astronomy at High Angular Resolution, 439, 1

Brooks, S. P., & Gelman, A. 1998, Journal of Computational and Graphical Statistics, 7, 434

Brown, T. M., Latham, D. W., Everett, M. E., & Esquerdo, G. A. 2011, AJ, 142, 112

Brown, T. M., Baliber, N., Bianco, F. B., et al. 2013, PASP, 125, 1031

Bruno, G. 1584, De l'infinito, universo e mondi (Ventia)

Bryson, S. T., Jenkins, J. M., Gilliland, R. L., et al. 2013, PASP, 125, 889

Burke, C. J., Bryson, S. T., Mullally, F., et al. 2014, ApJS, 210, 19

Butler, R. P., Marcy, G. W., Fischer, D. A., et al. 1999, ApJ, 526, 916

Butler, R. P., Marcy, G. W., Williams, E., et al. 1996, PASP, 108, 500

Campante, T. L., Barclay, T., Swift, J. J., et al. 2015, ApJ, 799, 170

Carter, J. A., Agol, E., Chaplin, W. J., et al. 2012, Science, 337, 556

Chambers, J. 2010, Terrestrial Planet Formation, ed. S. Seager, 297–317

Chambers, J. E. 2012, Mercury: A software package for orbital dynamics, ascl:1201.008

Chambers, J. E., & Migliorini, F. 1997, in Bulletin of the American Astronomical Society, Vol. 29, AAS/Division for Planetary Sciences Meeting Abstracts #29, 1024

Chambers, J. E., & Wetherill, G. W. 1998, Icarus, 136, 304

Chambers, J. E., Wetherill, G. W., & Boss, A. P. 1996, Icarus, 119, 261

Charbonneau, D., Brown, T. M., Latham, D. W., & Mayor, M. 2000, ApJ, 529, L45

Chatterjee, S., & Ford, E. B. 2015, ApJ, 803, 33

Chatterjee, S., Ford, E. B., Matsumura, S., & Rasio, F. A. 2008, ApJ, 686, 580

Chatterjee, S., & Tan, J. C. 2014, ApJ, 780, 53

Chiang, E., & Laughlin, G. 2013, MNRAS, 431, 3444

Chiang, E. I., Fischer, D., & Thommes, E. 2002, ApJ, 564, L105

Christiansen, J. L., Jenkins, J. M., Caldwell, D. A., et al. 2013, KSCI

Ciardi, D. R., Beichman, C. A., Horch, E. P., & Howell, S. B. 2015, ApJ, 805, 16

Ciardi, D. R., Fabrycky, D. C., Ford, E. B., et al. 2013, ApJ, 763, 41

Ciesla, F. J., & Dullemond, C. P. 2010, Evolution of Protoplanetary Disk Structures, ed. D. A. Apai & D. S. Lauretta, 66–96

Cochran, W. D., Hatzes, A. P., Butler, R. P., & Marcy, G. W. 1997, ApJ, 483, 457

Cochran, W. D., Fabrycky, D. C., Torres, G., et al. 2011, ApJS, 197, 7

Coelho, P., Barbuy, B., Meléndez, J., Schiavon, R. P., & Castilho, B. V. 2005, A&A, 443, 735

Copernicus, N. 1514, Commentariolus

Correa-Otto, J. A., Michtchenko, T. A., & Beaugé, C. 2013, A&A, 560, A65

Cossou, C., Raymond, S. N., Hersant, F., & Pierens, A. 2014, A&A, 569, A56

Coughlin, J. L., Mullally, F., Thompson, S. E., et al. 2016, ApJS, 224, 12

Cox, A. N. 2000, Allen's astrophysical quantities

Cresswell, P., & Nelson, R. P. 2006, A&A, 450, 833

Cumming, A., Marcy, G. W., & Butler, R. P. 1999, ApJ, 526, 890

Cuzzi, J. N., Hogan, R. C., Paque, J. M., & Dobrovolskis, A. R. 2001, ApJ, 546, 496

Dai, F., Winn, J. N., Albrecht, S., et al. 2016, ApJ, 823, 115

D'Angelo, G., Durisen, R. H., & Lissauer, J. J. 2010, Giant Planet Formation, ed. S. Seager, 319–346

Davies, M. B., Adams, F. C., Armitage, P., et al. 2013, ArXiv e-prints, arXiv:1311.6816

Dawson, R. I., & Fabrycky, D. C. 2010, ApJ, 722, 937

Dawson, R. I., Johnson, J. A., Fabrycky, D. C., et al. 2014, ApJ, 791, 89

Deck, K. M., & Agol, E. 2015, ApJ, 802, 116

Delfosse, X., Forveille, T., Mayor, M., et al. 1998, A&A, 338, L67

Delisle, J.-B., & Laskar, J. 2014, A&A, 570, L7

Delisle, J.-B., Laskar, J., Correia, A. C. M., & Boué, G. 2012, A&A, 546, A71

Demarque, P., Woo, J.-H., Kim, Y.-C., & Yi, S. K. 2004, ApJS, 155, 667

Diolaiti, E., Bendinelli, O., Bonaccini, D., et al. 2000, in Proc. SPIE, Vol. 4007, Adaptive Optical Systems Technology, ed. P. L. Wizinowich, 879–888

Dobrovolskis, A. R., & Borucki, W. J. 1996, in BAAS, Vol. 28, Bulletin of the American Astronomical Society, 1112

Doig, P. 1950, A concise history of astronomy.

Doyle, L. R., Carter, J. A., Fabrycky, D. C., et al. 2011, Science, 333, 1602

Dumusque, X., Santos, N. C., Udry, S., Lovis, C., & Bonfils, X. 2011a, A&A, 527, A82

Dumusque, X., Udry, S., Lovis, C., Santos, N. C., & Monteiro, M. J. P. F. G. 2011b, A&A, 525, A140

Duncan, M., Quinn, T., & Tremaine, S. 1989, Icarus, 82, 402

Dupuy, T. J., Kratter, K. M., Kraus, A. L., et al. 2016, ApJ, 817, 80

Earl, D. J., & Deem, M. W. 2005, Physical Chemistry Chemical Physics (Incorporating Faraday Transactions), 7, 3910

Eggenberger, A., Udry, S., Chauvin, G., et al. 2007, A&A, 474, 273

Everett, M. E., Howell, S. B., & Kinemuchi, K. 2012, PASP, 124, 316

Fabrycky, D., & Tremaine, S. 2007, ApJ, 669, 1298

Fabrycky, D. C. 2010, Non-Keplerian Dynamics of Exoplanets, ed. S. Seager, 217–238

Fabrycky, D. C., Lissauer, J. J., Ragozzine, D., et al. 2014, ApJ, 790, 146

Fernandez, J. A., & Ip, W. H. 1984, Icarus, 58, 109

Ferraz-Mello, S., Beaugé, C., & Michtchenko, T. A. 2003, Celestial Mechanics and Dynamical Astronomy, 87, 99

Fischer, D. A., Anglada-Escude, G., Arriagada, P., et al. 2016, PASP, 128, 066001

Ford, E. B., & Gregory, P. C. 2007, in Astronomical Society of the Pacific Conference Series, Vol. 371, Statistical Challenges in Modern Astronomy IV, ed. G. J. Babu & E. D. Feigelson, 189

Ford, E. B., Joshi, K. J., Rasio, F. A., & Zbarsky, B. 2000, ApJ, 528, 336

Foreman-Mackey, D., Hogg, D. W., Lang, D., & Goodman, J. 2013, PASP, 125, 306

Foucart, F., & Lai, D. 2013, ApJ, 764, 106

Fressin, F., Torres, G., Charbonneau, D., et al. 2013, ApJ, 766, 81

Fried, D. L. 1978, Journal of the Optical Society of America (1917-1983), 68, 1651

Galassi, M., & Gough, B. 2009, GNU Scientific Library: Reference Manual, GNU manual (Network Theory Limited)

Galle, J. G. 1846, MNRAS, 7, 153

Gammie, C. F. 1996, ApJ, 457, 355

García, R. A., Hekker, S., Stello, D., et al. 2011, MNRAS, 414, L6

Gaudi, B. S., & Winn, J. N. 2007, ApJ, 655, 550

Gelman, A., & Rubin, D. B. 1992, Statistical Science, 7, 457

Gettel, S., Charbonneau, D., Dressing, C. D., et al. 2016, ApJ, 816, 95

Gillon, M., Triaud, A. H. M. J., Demory, B.-O., et al. 2017, Nature, 542, 456

Girardi, L., Groenewegen, M. A. T., Hatziminaoglou, E., & da Costa, L. 2005, A&A, 436, 895

Gladman, B. 1993, Icarus, 106, 247

Goldreich, P., & Schlichting, H. E. 2014, AJ, 147, 32

Goldreich, P., & Soter, S. 1966, Icarus, 5, 375

Goldreich, P., & Tremaine, S. 1979, ApJ, 233, 857

—. 1980, ApJ, 241, 425

—. 1982, ARA&A, 20, 249

Goździewski, K., Bois, E., Maciejewski, A. J., & Kiseleva-Eggleton, L. 2001, A&A, 378, 569

Goździewski, K., & Migaszewski, C. 2014, MNRAS, 440, 3140

Goździewski, K., Migaszewski, C., Panichi, F., & Szuszkiewicz, E. 2016, MNRAS, 455, L104

Greenberg, R. J., Counselman, III, C. C., & Shapiro, I. I. 1972, Science, 178, 747

Hadden, S., & Lithwick, Y. 2014, ApJ, 787, 80

—. 2016, ApJ, 828, 44

—. 2017, AJ, 154, 5

Hansen, B. M. S., & Murray, N. 2012, ApJ, 751, 158

—. 2013, ApJ, 775, 53

Hayashi, C. 1981, Progress of Theoretical Physics Supplement, 70, 35

Hellier, C., Anderson, D. R., Collier Cameron, A., et al. 2012, MNRAS, 426, 739

Henrard, J. 1982, Celestial Mechanics, 27, 3

Henrard, J., & Lemaitre, A. 1983, Icarus, 55, 482

Herschel, W., & Watson, D. 1781, Philosophical Transactions of the Royal Society of London Series I, 71, 492

Hirano, T., Narita, N., Sato, B., et al. 2012, ApJ, 759, L36

Holczer, T., Shporer, A., Mazeh, T., et al. 2015, ApJ, 807, 170

Holczer, T., Mazeh, T., Nachmani, G., et al. 2016, ApJS, 225, 9

Holman, M., Touma, J., & Tremaine, S. 1997, Nature, 386, 254

Holman, M. J., & Murray, N. W. 2005, Science, 307, 1288

Holman, M. J., & Wiegert, P. A. 1999, AJ, 117, 621

Holman, M. J., Fabrycky, D. C., Ragozzine, D., et al. 2010, Science, 330, 51

Howard, A. W., Marcy, G. W., Bryson, S. T., et al. 2012, ApJS, 201, 15

Howell, S. B., Everett, M. E., Sherry, W., Horch, E., & Ciardi, D. R. 2011, AJ, 142, 19

Howell, S. B., Rowe, J. F., Bryson, S. T., et al. 2012, ApJ, 746, 123

Huber, D., Chaplin, W. J., Christensen-Dalsgaard, J., et al. 2013a, ApJ, 767, 127

Huber, D., Carter, J. A., Barbieri, M., et al. 2013b, Science, 342, 331

Huber, D., Silva Aguirre, V., Matthews, J. M., et al. 2014, ApJS, 211, 2

Hufnagel, R. E. 1966, in National Academy of Sciences, Vol. 3, Restoration of Atmospherically Degraded Images, 11

Hut, P. 1981, A&A, 99, 126

Ida, S., & Lin, D. N. C. 2008, ApJ, 673, 487

Inamdar, N. K., & Schlichting, H. E. 2015, MNRAS, 448, 1751

Izidoro, A., Haghighipour, N., Winter, O. C., & Tsuchida, M. 2014, ApJ, 782, 31

Izidoro, A., Ogihara, M., Raymond, S. N., et al. 2017, ArXiv e-prints, arXiv:1703.03634

Jenkins, J. M. 2002, ApJ, 575, 493

Jontof-Hutter, D., Rowe, J. F., Lissauer, J. J., Fabrycky, D. C., & Ford, E. B. 2015, Nature, 522, 321

Jontof-Hutter, D., Ford, E. B., Rowe, J. F., et al. 2016, ApJ, 820, 39

Kaib, N. A., & Chambers, J. E. 2016, MNRAS, 455, 3561

Kane, S. R., Ford, E. B., & Ge, J. 2008, in IAU Symposium, Vol. 249, Exoplanets: Detection, Formation and Dynamics, ed. Y.-S. Sun, S. Ferraz-Mello, & J.-L. Zhou, 115–118

Kant, I. 1755, Allgemeine Naturgeschichte und Theorie des Himmels

Kass, R. E., & Raftery, A. E. 1995, Journal of the american statistical association, 90, 773

Kepler, J. 1618, Epitome astronomiae copernicanae usitata forma quaestionum & responsionum conscripta, inque VII. libros digesta

Kepler, J., Brahe, T., & Eckebrecht, P. 1627, Tabvlae Rudolphinae, qvibvs astronomicae scientiae, temporum longinquitate collapsae restauratio continetur

Ketchum, J. A., Adams, F. C., & Bloch, A. M. 2011, ApJ, 726, 53

—. 2013, ApJ, 762, 71

Kipping, D. M. 2014, MNRAS, 440, 2164

Kiseleva, L. G., Eggleton, P. P., & Mikkola, S. 1998, MNRAS, 300, 292

Kley, W., & Haghighipour, N. 2014, A&A, 564, A72

—. 2015, A&A, 581, A20

Kley, W., & Nelson, R. P. 2012, ARA&A, 50, 211

Kokubo, E., & Ida, S. 1998, Icarus, 131, 171

Kostov, V. B., McCullough, P. R., Carter, J. A., et al. 2014, ApJ, 784, 14

Kostov, V. B., Orosz, J. A., Welsh, W. F., et al. 2016, ApJ, 827, 86

Kowal, C. T., & Drake, S. 1980, Nature, 287, 311

Krystek, M., & Anton, M. 2007, Measurement Science and Technology, 18, 3438

Kuiper, G. P. 1951, Proceedings of the National Academy of Science, 37, 1

Lagrange, J. L. 1778, Mémoires de lÀcadémie des Sciences de Paris

Lambrechts, M., & Johansen, A. 2012, A&A, 544, A32

Laplace, P. S. 1779, Histoire de l'Acadmie royale des sciences, avec les mmoires de mathmatique et de physique., Vol. 1776, 890

Laskar, J., & Gastineau, M. 2009, Nature, 459, 817

Laskar, J., & Petit, A. 2017, ArXiv e-prints, arXiv:1703.07125

Laughlin, G., Steinacker, A., & Adams, F. C. 2004, ApJ, 608, 489

Law, N. M., Morton, T., Baranec, C., et al. 2014, ApJ, 791, 35

Lawrence, A., Warren, S. J., Almaini, O., et al. 2007, MNRAS, 379, 1599

Le Verrier, U. J. 1846, Astronomische Nachrichten, 25, 85

Lecoanet, D., Adams, F. C., & Bloch, A. M. 2009, ApJ, 692, 659

Lee, E. J., & Chiang, E. 2016, ApJ, 817, 90

Lee, M. H., Fabrycky, D., & Lin, D. N. C. 2013, ApJ, 774, 52

Lee, M. H., & Peale, S. J. 2002, ApJ, 567, 596

Levison, H. F., Kretke, K. A., & Duncan, M. J. 2015, Nature, 524, 322

Levison, H. F., Morbidelli, A., Gomes, R., & Backman, D. 2007, Protostars and Planets V, 669

Levison, H. F., Morbidelli, A., Tsiganis, K., Nesvorný, D., & Gomes, R. 2011, AJ, 142, 152

Li, C.-H., Benedick, A. J., Fendel, P., et al. 2008, Nature, 452, 610

Li, G., Holman, M. J., & Tao, M. 2016, ApJ, 831, 96

Lin, D. N. C., & Ida, S. 1997, ApJ, 477, 781

Lin, D. N. C., & Papaloizou, J. 1986, ApJ, 309, 846

Lissauer, J. J., Hubickyj, O., D'Angelo, G., & Bodenheimer, P. 2009, Icarus, 199, 338

Lissauer, J. J., Fabrycky, D. C., Ford, E. B., et al. 2011a, Nature, 470, 53

Lissauer, J. J., Ragozzine, D., Fabrycky, D. C., et al. 2011b, ApJS, 197, 8

Lissauer, J. J., Jontof-Hutter, D., Rowe, J. F., et al. 2013, ApJ, 770, 131

Lissauer, J. J., Marcy, G. W., Bryson, S. T., et al. 2014, ApJ, 784, 44

Lithwick, Y., & Wu, Y. 2011, ApJ, 739, 31

—. 2012, ApJ, 756, L11

—. 2014, Proceedings of the National Academy of Science, 111, 12610

Lithwick, Y., Xie, J., & Wu, Y. 2012, ApJ, 761, 122

Liu, B., Ormel, C. W., & Lin, D. N. C. 2017, A&A, 601, A15

Lomb, N. R. 1976, Ap&SS, 39, 447

Lopez, E. D., & Fortney, J. J. 2014, ApJ, 792, 1

Lopez, E. D., & Rice, K. 2016, ArXiv e-prints, arXiv:1610.09390

Lovis, C., & Fischer, D. 2010, Radial Velocity Techniques for Exoplanets, ed. S. Seager, 27–53

Lubow, S. H., & Ida, S. 2010, Planet Migration, ed. S. Seager, 347–371

Luger, R., Sestovic, M., Kruse, E., et al. 2017, Nature Astronomy, 1, 0129

Lynden-Bell, D., & Kalnajs, A. J. 1972, MNRAS, 157, 1

MacDonald, M. G., Ragozzine, D., Fabrycky, D. C., et al. 2016, AJ, 152, 105

Mahajan, N., & Wu, Y. 2014, ApJ, 795, 32

Malhotra, R. 1993, Nature, 365, 819

—. 1996, AJ, 111, 504

—. 2015, ApJ, 808, 71

Malhotra, R., Black, D., Eck, A., & Jackson, A. 1992, Nature, 356, 583

Malmberg, D., Davies, M. B., & Chambers, J. E. 2007, MNRAS, 377, L1

Mamajek, E. E., & Hillenbrand, L. A. 2008, ApJ, 687, 1264

Mandel, K., & Agol, E. 2002, ApJ, 580, L171

Marcus, R. A., Sasselov, D., Hernquist, L., & Stewart, S. T. 2010, ApJ, 712, L73

Marcy, G., Butler, R. P., Fischer, D., et al. 2005, Progress of Theoretical Physics Supplement, 158, 24

Marcy, G. W., & Butler, R. P. 1996, ApJ, 464, L147

Marcy, G. W., Butler, R. P., Vogt, S. S., Fischer, D., & Lissauer, J. J. 1998, ApJ, 505, L147

Marcy, G. W., Isaacson, H., Howard, A. W., et al. 2014, ApJS, 210, 20

Martin, D. V., & Triaud, A. H. M. J. 2015, MNRAS, 449, 781

Masset, F., & Snellgrove, M. 2001, MNRAS, 320, L55

Masset, F. S., Morbidelli, A., Crida, A., & Ferreira, J. 2006, ApJ, 642, 478

Masuda, K. 2014, ApJ, 783, 53

Masuda, K., Hirano, T., Taruya, A., Nagasawa, M., & Suto, Y. 2013, ApJ, 778, 185

Mayor, M., & Queloz, D. 1995, Nature, 378, 355

Mayor, M., Queloz, D., Marcy, G., et al. 1995, IAU Circ., 6251

Mayor, M., Pepe, F., Queloz, D., et al. 2003, The Messenger, 114, 20

Mayor, M., Marmier, M., Lovis, C., et al. 2011, ArXiv e-prints, arXiv:1109.2497

Mazeh, T., Holczer, T., & Shporer, A. 2015a, ApJ, 800, 142

Mazeh, T., Krymolowski, Y., & Rosenfeld, G. 1997, ApJ, 477, L103

Mazeh, T., Perets, H. B., McQuillan, A., & Goldstein, E. S. 2015b, ApJ, 801, 3

Mazeh, T., Nachmani, G., Holczer, T., et al. 2013, ApJS, 208, 16

McArthur, B. E., Benedict, G. F., Barnes, R., et al. 2010, ApJ, 715, 1203

Melita, M. D., & Woolfson, M. M. 1996, MNRAS, 280, 854

Migaszewski, C., Słonina, M., & Goździewski, K. 2012, MNRAS, 427, 770

Mills, S. M., & Fabrycky, D. C. 2017a, AJ, 153, 45

—. 2017b, ApJ, 838, L11

Mills, S. M., Fabrycky, D. C., Migaszewski, C., et al. 2016, Nature, 533, 509

Mills, S. M., & Mazeh, T. 2017, ApJ, 839, L8

Minton, D. A., & Levison, H. F. 2014, Icarus, 232, 118

Minton, D. A., & Malhotra, R. 2009, Nature, 457, 1109

Miralda-Escudé, J. 2002, ApJ, 564, 1019

Montet, B. T., Tovar, G., & Foreman-Mackey, D. 2017, ArXiv e-prints, arXiv:1705.07928

Moore, A., Hasan, I., & Quillen, A. C. 2013, MNRAS, 432, 1196

Moore, A., & Quillen, A. C. 2013, MNRAS, 430, 320

Morbidelli, A., Chambers, J., Lunine, J. I., et al. 2000, Meteoritics and Planetary Science, 35, 1309

Morbidelli, A., Tsiganis, K., Crida, A., Levison, H. F., & Gomes, R. 2007, AJ, 134, 1790

Morton, T. D. 2015, isochrones: Stellar model grid package, ascl:1503.010

Morton, T. D., Bryson, S. T., Coughlin, J. L., et al. 2016, ApJ, 822, 86

Morton, T. D., & Johnson, J. A. 2011, ApJ, 738, 170

Mullally, F., Coughlin, J. L., Thompson, S. E., et al. 2015, ApJS, 217, 31

Murray, C., & Dermott, S. 1999, Solar System Dynamics (Cambridge University Press)

Murray, C. D., & Dermott, S. F. 1999, Solar system dynamics

Nelson, B. E., Robertson, P. M., Payne, M. J., et al. 2016, MNRAS, 455, 2484

Nesvorný, D., & Beaugé, C. 2010, ApJ, 709, L44

Nesvorný, D., Kipping, D. M., Buchhave, L. A., et al. 2012, Science, 336, 1133

Nesvorný, D., & Morbidelli, A. 2008, ApJ, 688, 636

Nesvorný, D., & Vokrouhlický, D. 2016, ApJ, 823, 72

Newton, I. 1687, Philosophiae Naturalis Principia Mathematica

—. 1717, Opticks, 2nd English Edition (London)

Newton, M. A., & Raftery, A. E. 1994, Journal of the Royal Statistical Society. Series B (Methodological), 3

Ngo, H., Knutson, H. A., Bryan, M. L., et al. 2017, AJ, 153, 242

Nutzman, P. A., Fabrycky, D. C., & Fortney, J. J. 2011, ApJ, 740, L10

Obertas, A., Van Laerhoven, C., & Tamayo, D. 2017, Icarus, 293, 52

Ogihara, M., Ida, S., & Morbidelli, A. 2007, Icarus, 188, 522

Oishi, J. S., Mac Low, M.-M., & Menou, K. 2007, ApJ, 670, 805

Ormel, C. W., Ida, S., & Tanaka, H. 2012, ApJ, 758, 80

Orosz, J. A., Welsh, W. F., Carter, J. A., et al. 2012a, Science, 337, 1511

—. 2012b, ApJ, 758, 87

Orosz, J., W., W., Haghighipour, N., Quarles, B., et al. in prep., ApJ

Oshagh, M., Santos, N. C., Boisse, I., et al. 2013, A&A, 556, A19

Pál, A. 2012, MNRAS, 420, 1630

Pál, A., & Kocsis, B. 2008, MNRAS, 389, 191

Pan, M., & Schlichting, H. E. 2017, ArXiv e-prints, arXiv:1704.07836

Papaloizou, J. C. B. 2011, Celestial Mechanics and Dynamical Astronomy, 111, 83

—. 2016, Celestial Mechanics and Dynamical Astronomy, 126, 157

Peale, S. J. 1976, ARA&A, 14, 215

—. 1986, Orbital resonances, unusual configurations and exotic rotation states among planetary satellites, ed. J. A. Burns & M. S. Matthews, 159–223

—. 1999, ARA&A, 37, 533

Penev, K., Jackson, B., Spada, F., & Thom, N. 2012, ApJ, 751, 96

Petigura, E. A., Marcy, G. W., & Howard, A. W. 2013, ApJ, 770, 69

Petigura, E. A., Howard, A. W., Lopez, E. D., et al. 2016, ApJ, 818, 36

Petrovich, C., Malhotra, R., & Tremaine, S. 2013, ApJ, 770, 24

Pierens, A., & Nelson, R. P. 2007, A&A, 472, 993

—. 2008, A&A, 483, 633

—. 2013, A&A, 556, A134

Plavchan, P., Latham, D., Gaudi, S., et al. 2015, ArXiv e-prints, arXiv:1503.01770

Plavchan, P. P., Anglada-Escude, G., White, R., et al. 2013, in Proc. SPIE, Vol. 8864, Techniques and Instrumentation for Detection of Exoplanets VI, 88641J

Poisson, S. D. 1809, Journal de lÉcole polytechnique, VIII, 1

Pollacco, D. L., Skillen, I., Collier Cameron, A., et al. 2006, PASP, 118, 1407

Pollack, J. B., Hubickyj, O., Bodenheimer, P., et al. 1996, Icarus, 124, 62

Prsa, A., Batalha, N., Slawson, R. W., et al. 2011, AJ, 141, 83

Pu, B., & Wu, Y. 2015, ApJ, 807, 44

Queloz, D., Mayor, M., Weber, L., et al. 2000, A&A, 354, 99

Quillen, A. C. 2006, MNRAS, 365, 1367

—. 2011, MNRAS, 418, 1043

Rajpaul, V., Aigrain, S., Osborne, M. A., Reece, S., & Roberts, S. 2015, MNRAS, 452, 2269

Rappaport, S., Sanchis-Ojeda, R., Rogers, L. A., Levine, A., & Winn, J. N. 2013, ApJ, 773, L15

Rasio, F. A., & Ford, E. B. 1996, Science, 274, 954

Rasio, F. A., Nicholson, P. D., Shapiro, S. L., & Teukolsky, S. A. 1992, Nature, 355, 325

Rasio, F. A., Tout, C. A., Lubow, S. H., & Livio, M. 1996, ApJ, 470, 1187

Raymond, S. N., Armitage, P. J., & Gorelick, N. 2009, ApJ, 699, L88

Raymond, S. N., Barnes, R., Armitage, P. J., & Gorelick, N. 2008, ApJ, 687, L107

Rein, H. 2012, MNRAS, 427, L21

Rein, H., & Liu, S.-F. 2012, A&A, 537, A128

Rein, H., & Papaloizou, J. C. B. 2009, A&A, 497, 595

Rein, H., Papaloizou, J. C. B., & Kley, W. 2010, A&A, 510, A4

Remus, F., Mathis, S., Zahn, J.-P., & Lainey, V. 2012, A&A, 541, A165

Rivera, E. J., Laughlin, G., Butler, R. P., et al. 2010, ApJ, 719, 890

Roberge, A., & Kamp, I. 2010, Protoplanetary and Debris Disks, ed. S. Seager, 269–295

Roell, T., Neuhäuser, R., Seifahrt, A., & Mugrauer, M. 2012, A&A, 542, A92

Rogers, L. A. 2015, ApJ, 801, 41

Rowe, J. F., Bryson, S. T., Marcy, G. W., et al. 2014, ApJ, 784, 45

Rowe, J. F., Coughlin, J. L., Antoci, V., et al. 2015, ApJS, 217, 16

Roy, A. E. 1988, Orbital motion (3rd revised and enlarged edition)

Sanchis-Ojeda, R., Fabrycky, D. C., Winn, J. N., et al. 2012, Nature, 487, 449

Scargle, J. D. 1982, ApJ, 263, 835

Schlaufman, K. C., Lin, D. N. C., & Ida, S. 2010, ApJ, 724, L53

Schwamb, M. E., Orosz, J. A., Carter, J. A., et al. 2013, ApJ, 768, 127

Seager, S., Kuchner, M., Hier-Majumder, C. A., & Militzer, B. 2007, ApJ, 669, 1279

Seager, S., & Mallén-Ornelas, G. 2003, ApJ, 585, 1038

Sinclair, A. T. 1972, MNRAS, 160, 169

Sing, D. K. 2010, A&A, 510, A21

Sinukoff, E., Fulton, B., Scuderi, L., & Gaidos, E. 2013, Space Sci. Rev., 180, 71

Skumanich, A. 1972, ApJ, 171, 565

Smith, A. W., & Lissauer, J. J. 2009, Icarus, 201, 381

Soderhjelm, S. 1975, A&A, 42, 229

Southworth, J. 2008, MNRAS, 386, 1644

Southworth, J., Bruntt, H., & Buzasi, D. L. 2007, A&A, 467, 1215

Steffen, J. H. 2016, MNRAS, 457, 4384

Steffen, J. H., & Agol, E. 2005, MNRAS, 364, L96

Steffen, J. H., & Hwang, J. A. 2015, MNRAS, 448, 1956

Steffen, J. H., Batalha, N. M., Borucki, W. J., et al. 2010, ApJ, 725, 1226

Storch, N. I., & Lai, D. 2015, MNRAS, 450, 3952

Struve, O. 1952, The Observatory, 72, 199

Swift, D. C., Eggert, J. H., Hicks, D. G., et al. 2012, ApJ, 744, 59

Tadeu dos Santos, M., Correa-Otto, J. A., Michtchenko, T. A., & Ferraz-Mello, S. 2015, A&A, 573, A94

Tal-Or, L., Mazeh, T., Alonso, R., et al. 2013, A&A, 553, A30

Tenenbaum, P., Jenkins, J. M., Seader, S., et al. 2013, ApJS, 206, 5

Ter Braak, C. J. F. 2005, Wageningen UR, Biometris, 010404, 556

Terquem, C., & Papaloizou, J. C. B. 2007, ApJ, 654, 1110

Thorsett, S. E., Arzoumanian, Z., & Taylor, J. H. 1993, ApJ, 412, L33

Toomre, A. 1964, ApJ, 139, 1217

Touma, J. R., & Sridhar, S. 2015, Nature, 524, 439

Tremaine, S., & Zakamska, N. L. 2004, in American Institute of Physics Conference Series, Vol. 713, The Search for Other Worlds, ed. S. S. Holt & D. Deming, 243–252

Tsiganis, K., Gomes, R., Morbidelli, A., & Levison, H. F. 2005, Nature, 435, 459

Twicken, J. D., Jenkins, J. M., Seader, S. E., et al. 2016, AJ, 152, 158

Udry, S., & Santos, N. C. 2007, ARA&A, 45, 397

Valenti, J. A., & Fischer, D. A. 2005, ApJS, 159, 141

van Saders, J. L., Ceillier, T., Metcalfe, T. S., et al. 2016, Nature, 529, 181

Veras, D., & Armitage, P. J. 2004, Icarus, 172, 349

Vogt, S. S., Allen, S. L., Bigelow, B. C., et al. 1994, in Society of Photo-Optical Instrumentation Engineers (SPIE) Conference Series, Vol. 2198, Instrumentation in Astronomy VIII, ed. D. L. Crawford & E. R. Craine, 362

Walsh, K. J., Morbidelli, A., Raymond, S. N., O'Brien, D. P., & Mandell, A. M. 2011, Nature, 475, 206

Wang, J., Fischer, D. A., Xie, J.-W., & Ciardi, D. R. 2015, ApJ, 813, 130

Ward, W. R. 1997, Icarus, 126, 261

Weidenschilling, S. J. 1977, MNRAS, 180, 57

Weiss, L. M., & Marcy, G. W. 2014, ApJ, 783, L6

Weiss, L. M., Marcy, G. W., Rowe, J. F., et al. 2013, ApJ, 768, 14

Weiss, L. M., Rogers, L. A., Isaacson, H. T., et al. 2016, ApJ, 819, 83

Weiss, L. M., Marcy, G. W., Petigura, E. A., et al. 2017, ArXiv e-prints, arXiv:1706.06204

Welsh, W. F., Orosz, J. A., Carter, J. A., et al. 2012, Nature, 481, 475

Welsh, W. F., Orosz, J. A., Short, D. R., et al. 2015, ApJ, 809, 26

Wetherill, G. W. 1985, Science, 228, 877

Winn, J. N. 2010, Exoplanet Transits and Occultations, ed. S. Seager, 55–77

Winn, J. N., Fabrycky, D., Albrecht, S., & Johnson, J. A. 2010, ApJ, 718, L145

Winn, J. N., & Fabrycky, D. C. 2015, ARA&A, 53, 409

Wisdom, J. 1980, AJ, 85, 1122

Wolszczan, A. 1994, Science, 264, 538

Wolszczan, A., & Frail, D. A. 1992, Nature, 355, 145

Wright, J. T., Marcy, G. W., Howard, A. W., et al. 2012, ApJ, 753, 160

Wright, J. T., Upadhyay, S., Marcy, G. W., et al. 2009, ApJ, 693, 1084

Wright, J. T., Veras, D., Ford, E. B., et al. 2011, ApJ, 730, 93

Wu, Y., & Lithwick, Y. 2011, ApJ, 735, 109

Xie, J.-W. 2013, ApJS, 208, 22

Xu, W., & Lai, D. 2016, MNRAS, 459, 2925

Yi, X., Vahala, K., Li, J., et al. 2016, Nature Communications, 7, 10436

Yoder, C. F., & Peale, S. J. 1981, Icarus, 47, 1

York, D. 1966, Canadian Journal of Physics, 44, 1079

Zapolsky, H. S., & Salpeter, E. E. 1969, ApJ, 158, 809

Zhang, X., Liu, B., Lin, D. N. C., & Li, H. 2014, ApJ, 797, 20

Zhou, J.-L., Lin, D. N. C., & Sun, Y.-S. 2007, ApJ, 666, 423